UNIVERSITY OF OKLAHOMA
GRADUATE COLLEGE

DIFFUSE OPTICAL TOMOGRAPHY OF SPONTANEOUS BRAIN FLUCTUATIONS IN HUMANS

A DISSERTATION

SUBMITTED TO THE GRADUATE FACULTY

in partial fulfillment of the requirements for the

Degree of

DOCTOR OF PHILOSOPHY

By
ALI FAHIM KHAN
Norman, Oklahoma
2022

DIFFUSE OPTICAL TOMOGRAPHY OF SPONTANEOUS BRAIN FLUCTUATIONS IN HUMANS

A DISSERTATION APPROVED FOR THE
STEPHENSON SCHOOL OF BIOMEDICAL ENGINEERING

BY THE COMMITTEE CONSISTING OF

Dr. Lei Ding, Chair

Dr. Han Yuan

Dr. Ari Berkowitz

Dr. Joseph Havlicek

Dr. William Sonntag

Acknowledgments

In the name of Allah, the Almighty, Who is the most Beneficent and the most Merciful.

I would first like to acknowledge Allah (God), Who gave me the knowledge and strength to undertake this doctoral journey.

It has been my privilege to have been advised by Dr. Ding and co-advised by Dr. Yuan, two wonderful mentors who provided academic support, financial support, and valuable advice throughout my doctoral journey at the University of Oklahoma.

Besides, I would like to thank my dissertation committee members, Dr. Ari Berkowitz, Dr. Joseph Havlicek, and Dr. William Sonntag, who provided constructive suggestions on my research. All our meetings helped me to grow professionally and scientifically.

I would like to thank Yuan Lab for their assistance with the collection of experimental data. A special thanks to Fan Zhang from the Yuan Lab for helping with the preprocessing of the data. I would like to also thank Dr. Guofa Shou for his mentorship and support in my studies. In addition, I would like to thank Chuang Li for useful discussions.

I would like to thank the staff and faculty at OU who supported me. I also want to thank everyone who reviewed my publications.

I want to thank everyone who financially supported and funded my doctoral journey.

Finally, but not least, I would like to thank my family and friends. They supported me physically, mentally, and emotionally throughout these years. My life is incomplete without them.

Dedication

I dedicate this dissertation to the memory of my brave and patriotic father, Major Fahim-Ur-Rahim Khan. His battle with pancreatic cancer was a significant source of inspiration for me to research in the field of biomedical engineering. Also, I dedicate this dissertation to the unprivileged strata of the world who deserve access to healthcare and education.

Table of Contents

Acknowledgements iv
Dedication v
Table of Contents vi
List of Tables x
List of Figures xi
List of Abbreviations xiii
List of Peer-Reviewed Publications xvi
Abstract xvii
1. Introduction 1
2. Background 6
2.1 Functional near-infrared spectroscopy 6
2.2 Diffuse optical tomography 10
2.2.1 Forward problem 12
2.2.2 Inverse problem 15
2.3 Resting-state functional connectivity 16
2.4 DOT RSNs 23
3. Brain-wide diffuse optical tomography 29
3.1 Introduction 29
3.2 The forward problem 29
3.2.1 Spectral DOT model 29
3.2.2 Numerical models for head tissue volumes and surfaces 32
3.2.3 Optode co-registration 38
3.2.4 Sensitivity profile of head model 39
3.3 Inverse source reconstruction 41
3.4 Processes in controlling numerical errors 44
3.4.1 Removal of non-neuronal signals 44
3.4.2 Conditioning of Jacobian matrices 46
3.4.3 Temporal smoothing of the regularization parameters 46
3.5 Group-level spatial ICA for pattern recognition 47
3.6 Spatiotemporal regression 51

3.7 Statistical correlation tomography 52
3.8 Summary and discussion 53
4. Evaluation of BW-DOT using simulation and experimental data 59
4.1 Introduction 59
4.2 Methods 60
4.2.1 DOT reconstructions using simulated fNIRS data 60
4.2.2 Localizing motor activity 64
4.2.3 Data analysis protocols 66
4.3 Results 67
4.3.1 DOT reconstructions using simulated data 67
4.3.2 DOT reconstructions using motor task experimental data 72
4.4 Summary and discussion 77
5. DOT resting-state networks 80
5.1 Introduction 80
5.2 Materials and methods 81
5.2.1 Experimental protocols 81
5.2.2 Data analysis protocols 82
5.2.3 Evaluation and validation protocols 84
5.2.3.1 Spatial similarity of DOT RSNs to fMRI RSN templates 84
5.2.3.2 HbO vs. HbR DOT RSNs 85
5.2.3.3 Reproducibility of DOT RSNs 86
5.3 Results 87
5.3.1 Spatial patterns of DOT RSNs 87
5.3.2 Spatial match of DOT RSNs to fMRI RSNs templates 91
5.3.3 HBR DOT RSNs and their comparisons with HBO DOT RSNs 95
5.3.4 Reproducibility of DOT RSNs along time and across participants 102
5.4 Discussion 103
5.4.1 Reconstruction of multiple brain-wide RSNs 104
5.4.2 HbO vs. HbR DOT RSNs 107
5.4.3 Reproducibility of DOT RSNs 108
6. Coactivation pattern analysis of DOT resting-state data 110
6.1 Introduction 110

6.2 Materials and Methods 111
6.2.1 Participants, experimental and data protocols 111
6.2.2 Preprocessing of fNIRS data 111
6.2.3 Brain-wide DOT resting-state networks 113
6.2.4 Estimations of CAPs and their spatial, temporal, and transitional properties 114
6.2.5 Relationship between CAPs and GS 118
6.3 Results 119
6.3.1 Brain-wide DOT CAPs 119
6.3.2 Temporal, dynamic, and spectral measures of DOT CAPs 122
6.3.3 Global CAPs phase-locked to GS 126
6.3.4 Plausible neuronal relevance for global CAPs 127
6.3.5 Brain-wide CAPs at individual participants 133
6.4 Discussion 135
6.4.1 Brain-wide coactivations indicating recurring brain states 135
6.4.2 Spatiotemporal metrics of CAPs indicate structured transitions among brain states 138
6.4.3 Plausible origins of CAPs and GS 140
6.4.4 Relationship among coactivations, structured propagations, and global activity patterns 143
7. Spatiotemporal differences between HbO and HbR CAPs 145
7.1 Introduction 145
7.2 Materials and Methods 147
7.2.1 Participants, experimental and data protocols 147
7.2.2 fNIRS data preprocessing 148
7.2.3 Estimation of brain-wide resting-state networks 148
7.2.4 Quantitative comparison between HbO and HbR DOT RSN spatial maps 149
7.2.5 Estimations of CAPs 149
7.2.6 Quantitative comparison between the spatiotemporal properties of HbO and HbR CAPs 150
7.2.7 Reproducibility of spatiotemporal properties of CAPs 151
7.3 Results 152
7.3.1 Spatial patterns of HbO and HbR DOT RSNs 152

7.3.2 Significant differences exist between spatial topographies of HbO and HbR CAPs 155
7.3.3 HbR CAPs exhibit a more structured transitional organization than HbO CAPs. 160
7.3.4 Reproducibility of HbO and HbR CAPs..... 163
7.4 Discussion 164
8. Summary..... 168
8.1 Summary of results..... 168
8.2 Limitations and future work..... 172
Bibliography 175

List of Tables

Table 2-1 Examples of DOT resting-state studies 22
Table 3-1 Baseline chromophore concentrations in the FEM model. 37
Table 4-1 PSF-based metrics of a realistic head geometry. 71
Table 4-2 PSF-based metrics of a high-resolution head model with high-density optode cap..... 72
Table 5-1 Two-way ANOVA tests on TD and SC metric values. 101

List of Figures

Figure 1-1 Relationship of multiple projects comprising the dissertation 4
Figure 2-1 Schematic diagram of fNIRS measurements. 7
Figure 2-2 Examples of head caps used in DOT studies 8
Figure 2-3 General framework of Diffuse Optical Tomography. 11
Figure 2-4 Resting-state networks templates. 17
Figure 2-5 Schematic for seed-based correlation analysis. 18
Figure 3-1 Brain-wide Diffuse Optical Tomography framework. 30
Figure 3-2 Example of contrasts issue in MRI image. 33
Figure 3-3 Examples of manifold errors and disadvantaged topological features on surface meshes and their correction. 34
Figure 3-4 Example of disadvantaged topological features. 35
Figure 3-5 Tetrahedral head model mesh examples. 36
Figure 3-6 Optode co-registration. 38
Figure 3-7 Sensitivity profile of HbO for 760 nm. 40
Figure 3-8 Volumetric source space of the inverse solution. 42
Figure 3-9 Spatial smoothing in the volumetric domain. 43
Figure 3-10 Jacobian conditioning example for an example FEM mesh. 47
Figure 3-11 Schematic diagram of group-level spatial ICA. 49
Figure 3-12 Schematic diagram of group-level spatial ICA with PCA reduction. 50
Figure 4-1 A realistic head geometry for evaluation of BW-DOT. 60
Figure 4-2 PSF-based metrics defined on a realistic head geometry. 62
Figure 4-3 High-density cap montage. 64
Figure 4-4 Experimental paradigm for hand-clenching task. 65
Figure 4-5 Simulation-based DOT reconstruction of localized concentration change. 66
Figure 4-6 Simulation-based DOT reconstructions of temporal concentration changes in the motor cortex. 68
Figure 4-7 PSF-based metrics of HbO and HbR. 69
Figure 4-8 PSF-based metrics of HbO and HbR of high-density cap. 70
Figure 4-9 Motor task data reconstructions of a representative participant. 73
Figure 4-10 Motor task data reconstructions for other participants. 74
Figure 4-11 Dynamics of motor reconstructions. 76
Figure 5-1 Spatial patterns of group-level HbO DOT RSNs. 88
Figure 5-2 Spatial patterns of group-level HbR DOT RSNs. 89
Figure 5-3 Group-level HbO confusion matrices between d-RSNs and f-RSNs template maps. 92
Figure 5-4 Comparison of participant-level HbO d-RSNs and f-RSNs template maps. 93
Figure 5-5 Comparison of participant-level HbR d-RSNs and f-RSNs template maps. 94
Figure 5-6 Comparison of the regional and distributed DOT RSNs. 95
Figure 5-7 Comparison between HbO and HbR DOT RSNs. 96
Figure 5-8 Quantitative comparison of group-level HbO and HbR d-RSNs using TD. 97
Figure 5-9 Quantitative comparison of group-level HbO and HbR d-RSNs using SC. 98
Figure 5-10 Quantitative comparison of participant-level HbO and HbR d-RSNs using TD. 99

Figure 5-11 Quantitative comparison of participant-level HbO and HbR d-RSNs using SC. ... 100
Figure 5-12 Spatial correlations between group-level and participant-level DOT RSNs. 102
Figure 6-1 CAP framework. 112
Figure 6-2 Brain-wide DOT CAPs. 117
Figure 6-3 Group-level HbR DOT ICs. 118
Figure 6-4 Group-level DOT CAPs using different cluster sizes. 120
Figure 6-5 Temporal and dynamic measures of DOT CAPs. 122
Figure 6-6 PSD of GS and DOT CAPs. 123
Figure 6-7 Effect of temporal discontinuity on the temporal and dynamic metrics of CAPs. ... 124
Figure 6-8 The spatiotemporal properties of CAPs (k = 6) in the absence of global signal. 125
Figure 6-9 GS phase histograms of DOT CAPs. 126
Figure 6-10 Investigation of neuronal origins of global CAPs. 128
Figure 6-11 Percentage ratio of global CAPs (PRGC). 130
Figure 6-12 Exemplar illustrations of occurrences of four global CAPs in Figure 6-10A. 133
Figure 6-13 Participant-level brain-wide DOT CAPs. 134
Figure 6-14 Bar plots of means and standard deviations of spatial correlations (SCs) between the group-level and participant-level spatial maps of CAPs in Figure 6-10A. 135
Figure 7-1 ICA-based HbO and HbR DOT RSN maps have similar spatial topographies. 153
Figure 7-2 Complete set of group-level HbO DOT RSNs. 154
Figure 7-3 Complete set of group-level HbR DOT RSNs. 155
Figure 7-4 Quantitative comparison of spatial maps of HbO and HbR DOT RSNs. 156
Figure 7-5 Spatial topographies of HbO and HbR DOT CAPs. 157
Figure 7-6 HbO and HbR DOT CAPs for k=8. 158
Figure 7-7 HbR CAPs exhibit a structured transitional organization than HbO CAPs. 159
Figure 7-8 Group-level spatial maps of HbO and HbR DOT CAPs for session 1 and session 2. 161
Figure 7-9 3D distance map and occurrence rates of CAPs across sessions. 162
Figure 7-10 One-step transitions of HbO and HbR DOT CAPs for session 1 and session 2. 163

List of Abbreviations

AP	Anterior-Posterior
BOLD	Blood Oxygenation Level-Dependent
BW-DOT	Brain-Wide Diffuse Optical Tomography
CAP	Co-activation Pattern
CSF	Cerebrospinal Fluid
CSU	Coefficient of Spatial Uniformity
CW	Continuous-Wave
CW-fNIRS	Continuous-Wave Functional Near-Infrared Spectroscopy
DA	Diffusion Approximation
DAN	Dorsal Attention Network
dFC	Dynamic Functional Connectivity
DOF	Degrees of Freedom
DOT	Diffuse Optical Tomography
DMN	Default Mode Network
d-RSN	DOT Resting-State Network
DV	Dorsal-Ventral
EEG	Electroencephalography
FC	Functional Connectivity
FEF	Frontal Eye Fields
FEM	Finite Element Method
fMRI	Functional Magnetic Resonance Imaging
fNIRS	Functional Near-Infrared Spectroscopy
f-RSN	fMRI Resting State Network
FPN	Frontoparietal Network
FOV	Field of View
FWHM	Full Width at Half Maximum
gSICA	Group Level Spatial Independent Component Analysis

GLM	General Linear Model
GS	Global Signal
GVTD	Global-Variance in Temporal Derivative
GUI	Graphical User Interface
HbO	Oxygenated Hemoglobin
HbR	Deoxygenated Hemoglobin
HD-DOT	High-Density Diffuse Optical Tomography
IC	Independent Component
ICA	Independent Component Analysis
IFG	Inferior Frontal Gyrus
IOD	Interoptode Distance
L	Limbic
LCD	Liquid Crystal Display
LED	Light Emitting Diode
LS	Long Separation
M1	Primary Motor Cortex
MATLAB	Matrix Laboratory
MBLL	Modified Beer-Lambert Law
MEG	Magnetoencephalography
MNE	Minimum Norm Estimate
mPFC	Medial Prefrontal Cortex
MRI	Magnetic Resonance Imaging
NIRS	Near-Infrared Spectroscopy
NVC	Neurovascular Coupling
OD	Optical Density
OL	Overlap Metric
PCA	Principal Component Analysis
PCC	Posterior Cingulate Cortex

PET	Positron Emission Tomography
PMC	Premotor Cortex
PRGS	Percentage Ratio of Global CAPs
PSD	Power Spectral Density
PSF	Point Spread Function
ROI	Region of Interest
RSN	Resting-State Network
RTE	Radiative Transfer Equation
SC	Spatial Correlation
SCA	Seed-Based Connectivity Analysis
SCT	Statistical Correlation Tomography
S-D	Source-Detector
SFG	Superior Frontal Gyrus
SICA	Spatial Independent Component Analysis
SM	Somatomotor
SMA	Supplementary Motor Area
SNR	Signal-to-Noise Ratio
SS	Short Separation
STR	Spatiotemporal Regression
TD	Temporal-Matching Degree
TICA	Temporal Independent Component Analysis
TPN	Task-Positive Network
V	Visual
VAN	Ventral Attention Network
WCOR	Windowed Co-occurrence Ratio

List of Peer-Reviewed Publications

Khan, A. F., Fan Zhang, Guofa Shou, Han Yuan, and Lei Ding. "Hemoglobin concentration in reduced state captures a more structured spatiotemporal organization of resting-state brain activity than in the oxygenated state" (Manuscript in preparation).

Khan, A. F., Fan Zhang, Guofa Shou, Han Yuan, and Lei Ding. "Transient brain-wide coactivations and structured transitions revealed in hemodynamic imaging data" (Under review in Neuroimage).

Khan, A. F., Fan Zhang, Han Yuan, and Lei Ding. "Brain-wide functional diffuse optical tomography of resting state networks," Journal of Neural Engineering 18, no. 4 (2021): 046069.

Khan, A. F., Fan Zhang, Han Yuan, Lei Ding, "Brain-Wide Diffuse Optical Tomography Based on Cap-Based, Whole-Head fNIRS Recording," 43rd EMBC, virtual, Oct-Nov 2021.

Khan, A. F., Fan Zhang, Han Yuan, Lei Ding. "Dynamic Activation Patterns of the Motor Brain Revealed by Diffuse Optical Tomography," 41st International EMBC, Berlin, Jul 23-27, 2019.

Zhang F, **Khan, A. F**, Ding L, Yuan H. "Network organization of resting-state cerebral hemodynamics and their aliasing contribution" (Manuscript in preparation).

Zhang F, **Khan, A. F**, Ding L, Yuan H. "Neurovascular Coupling in Human Brain Measured by Simultaneous fNIRS and EEG" (Manuscript in preparation).

Zhang, F., Cheong, D., **Khan, A. F**., Chen, Y., Ding, L., & Yuan, H. "Correcting Physiological Noise in Whole-Head Functional Near-Infrared Spectroscopy," Journal of Neuroscience Methods, 109262, 2021.

Zhang, Daniel Cheong, Yuxuan Chen, **Khan, A. F**., Lei Ding, Han Yuan. "Superficial Fluctuations in Functional Near-infrared Spectroscopy," 41st International EMBC, Berlin, Jul 23-27, 2019.

Abstract

In the absence of tasks or external stimuli, the human brain produces recordable spontaneous low-frequency fluctuating hemodynamic signals, which show temporally-correlated activity among brain regions forming so-called resting-state networks (RSNs). Multiple RSNs have been identified using functional neuroimaging modalities across species and behavioral states. They are nonstationary over a scan time. These networks collectively cover almost the entire brain and play significant roles in human behaviors. Moreover, abnormalities in RSNs have been identified in major neurological and psychiatric disorders.

RSNs have been studied primarily using the blood oxygenation level-dependent (BOLD) signal generated from functional magnetic resonance imaging (fMRI). Despite numerous studies on these networks, several questions remain partially answered. For example, what is the spatiotemporal structure of networked brain activity obtained from other imaging contrasts such as oxygenated (HbO) and deoxygenated (HbR) hemoglobin signals? Are there observable spatiotemporal differences between these two contrasts? Does the controversial global signal contain neuronally relevant information? This dissertation attempts to answer some of these questions using diffuse optical tomography (DOT). DOT is a non-invasive functional neuroimaging technique based on functional near-infrared spectroscopy (fNIRS) that is more accessible than fMRI, making it available to patients, for example, requiring portability and having resistance to head motion.

Several task-based DOT studies have shown a promise in studying the human brain's functional connectivity (FC). However, DOT resting-state studies remain sparse. These studies have imaged limited cortical areas and have assumed that the brain's FC remains stationary over a scan despite increasing evidence that resting-state FC is a brain-wide nonstationary phenomenon.

These limitations were specifically addressed in this dissertation. A significant part of this dissertation involves developing a novel brain-wide DOT (BW-DOT) framework that integrates a cap-based whole-head optode placement system with multiple computational approaches, including finite-element modeling, inverse source reconstruction, data-driven pattern recognition, and statistical correlation tomography, to study brain-wide networked activity in dual contrasts of HbO and HbR. The spatiotemporal resolution of this framework was quantitatively evaluated using simulation and task-based fNIRS experimental data. RSNs were then reconstructed using resting-state data from healthy human participants. The brain's functional connectivity (FC) was then studied as regions coactivating and/or co-deactivating at fine timescales down to a single frame, using the so-called coactivation pattern (CAP) analysis for both HbO and HbR contrasts.

The evaluation results suggest that BW-DOT has the spatiotemporal resolution to study brain-wide networked activity in human adults. Applying BW-DOT to resting-state data revealed multiple RSNs, covering almost the entire neocortical surface. The spatial patterns of these networks suggest statistically significant similarities to fMRI RSN (f-RSN) templates. Furthermore, RSNs obtained from HbO and HbR suggests similarity in the number of RSN types reconstructed and their corresponding spatial patterns. At the same time, HbR RSNs show more similarity to f-RSN templates statistically, and HbO RSNs indicate more bilateral patterns over two hemispheres. In addition, the BW-DOT framework allowed consistent reconstructions of RSNs across individuals and recording sessions, indicating its high robustness and reproducibility, respectively.

The results from CAP analysis show that a small number, i.e., six, of transient brain-wide CAPs describe major spatiotemporal dynamics of DOT signals. These CAPs represent recurring brain states, have bilaterally symmetrical spatial topographies and exist in highly anticorrelated

pairs. Moreover, a structured transitional pattern among six brain states is identified in which two CAPs of anterior-posterior (AP) spatial patterns are in preferred positions, potentially mediating transitions among all brain states. The results further reveal two brain states showing global positive and negative patterns over the entire cortex. These two global brain states are responsible for generating a subset of peaks and troughs in global signals (GS), supporting the recent reports on the neuronal relevance of hemodynamic GS. Collectively, these results suggest that transient brain events (i.e., CAPs), global brain activity, and brain-wide structured transitions co-exist in humans. They are closely related to and extended the observations of similar neuronal events recently reported in animals. The CAP analysis further revealed several differences between the spatiotemporal properties of HbO and HbR DOT CAPs, with the latter contrast having a more structured transitional organization. Overall, this dissertation establishes a novel DOT-based framework and reveals insights into the spatiotemporal functional organization of networked brain activity from multiple hemodynamic contrasts in healthy humans under resting conditions.

1. Introduction

The human brain is a complex interconnected structure that forms networks that efficiently communicate (Ward, 2003) to achieve brain function (Park and Friston, 2013). The brain remains active in the absence of tasks or external stimuli, i.e., resting state (Buckner et al., 2008). Based on fMRI signals recorded under resting-state, numerous experimental works have demonstrated that spontaneous low-frequency fluctuations in these signals exhibit temporal correlations across multiple brain regions, forming so-called resting-state network (RSNs) (Biswal et al., 1995). Multiple RSNs span regional and distributed cortical areas (Bressler and Menon, 2010, Riedl et al., 2016) and are reproducible in healthy individuals (Damoiseaux et al., 2006b). Alterations of RSNs have been reported in major neurological and psychiatric disorders (Agosta et al., 2012, Buckner et al., 2008), which suggests significant clinical value in further studying and understanding RSNs (Fox and Raichle, 2007).

In the functional neuroimaging field, RSNs are often characterized by second-order statistical relationships between recordable brain signals, typically referred to as functional connectivity (FC). Recently, increasing evidence from fMRI data suggests that the brain's FC is nonstationary over a scan involving dynamic reconfiguration into transient states resulting in temporal changes in RSNs (Preti et al., 2017, Allen et al., 2014a, Chang and Glover, 2010, Liu et al., 2013, Hutchison et al., 2013a). This idea of the brain being a dynamic system under resting conditions is further supported by studies on electrical brain signals in animals (Matsui et al., 2019) and humans (Lei Ding, 2021). The dynamic FCs (dFCs) have neurobehavioral significance (Allen et al., 2014b, Hutchison et al., 2013b, Rosenberg et al., 2016, Kelly et al., 2008) and relevance to vigilance (Thompson et al., 2013a), sustained attention (Zuberer et al., 2021), and clinical issues, especially

in understanding altered connectivity in schizophrenic (Damaraju et al., 2014), Alzheimer's (Jones et al., 2012), and depression (Demirtaş et al., 2016) patients.

Although the spatiotemporal properties of FCs have been studied using different functional imaging modalities, resting-state fMRI remains the de facto gold standard in this field. This dominance of fMRI in studying FCs is attributed to its ability to image the whole human brain with a high spatial resolution (at the millimeter level) and reproducibility (Chen et al., 2008, Damoiseaux et al., 2006b). However, the technical limitations of fMRI are increasingly acknowledged in the research community, requesting more accessible imaging modalities. Firstly, from the perspective of signals, the fMRI's BOLD signal is primarily sensitive to concentration changes of HbR (Buxton, 2013), thus only providing one contrast. Secondly, the sampling rate of a conventional fMRI machine is low (typically about 0.5 to 1 Hz). This low sampling rate makes it difficult to resolve the aliasing noise problem (Lowe et al., 1998) in hemodynamic signals caused by non-neuronal but systematic sources from respiration and blood circulation (Lowe et al., 1998, Tong et al., 2011). Thirdly, MRI scanners have a loud operating noise due to the energization of the coils. The background noise of an MRI device can exceed 120 dB (Price et al., 2001). Such a loud pulsating noise is potentially disturbing to the participant. It also activates parts of the brain (Rondinoni et al., 2013), thus introducing bias in estimating RSNs (Gaab et al., 2008). Fourthly, fMRI machines are prone to head motion, which mandates that the participant's head be strapped. Thus, it becomes challenging to scan children and infants without sedation which may itself alter RSNs (Stamatakis et al., 2010). Fifthly fMRI devices are typically not portable and are usually expensive to procure, operate and maintain, thus limiting their use cases to a laboratory setting. Sixthly, the population with body implants that are not MRI compliant cannot undergo an MRI scan, nor patients with claustrophobia.

DOT, an optical-based technology, is used as a complementary functional neuroimaging modality to fMRI (Wheelock et al., 2019). It is a noninvasive tomographic modality based on functional near-infrared spectroscopy (fNIRS) instruments (Ferrari and Quaresima, 2012). DOT can reconstruct cortical signals from surface recordings, which is mathematically an inverse problem and usually requires modeling light propagation within head tissues (see Section 2.2). The sampling rate of a DOT system is about 5 to 10 times higher than a typical fMRI machine (Ferrari and Quaresima, 2012), which gives DOT the capability to address the aliasing noise (Lowe et al., 1998) in hemodynamic signals as described above. Typically, DOT equipment is portable, low-cost, and not as bulky as fMRI scanners and, therefore, more accessible to diverse populations, including individuals with non-MRI-compliant implants (Bortfeld, 2019), neonates (Mintzer and Moore, 2019), bedridden patients (Mathieu et al., 2020), and patients undergoing surgeries (Frogel et al., 2019, Serraino and Murphy, 2017). Establishing a capacity to use DOT equipment to study the brain's FC can thus significantly extend our capabilities to investigate new basic and clinical questions about the functions of the human brain.

Taking advantage of the portability of fNIRS instruments, DOT has been reported in multiple resting-state studies in adults (White et al., 2009, Eggebrecht et al., 2014, Aihara et al., 2020) and neonates (White et al., 2012, Ferradal et al., 2016). These studies have collectively demonstrated the ability of DOT to image functional brain networks under resting conditions and have further demonstrated the similarities between RSNs obtained by DOT and fMRI (Eggebrecht et al., 2014). However, most of these studies have used limited spatial coverage (see Table 2-1).

To further establish DOT-based technologies in studying resting-state brain activity beyond the existing literature, we need to achieve a whole-head optode coverage to reconstruct brain-wide distributed networks because resting-state brain activity is a brain-wide phenomenon (Bressler and

Menon, 2010). Furthermore, the similarity and difference between RSNs obtained from HbR and HbO should be quantitatively compared comprehensively. Such a comparison has not been sufficiently addressed, while the sensitivity to both HbR and HbO is one of the important advantages of fNIRS signals over fMRI signals. Finally, DOT RSN studies have primarily focused on generating static cortical maps. In contrast, there is increasing evidence that the brain's FC is nonstationary, as described above. Therefore, there is potential for studying the temporal structure of the networked brain activity of resting-state DOT data.

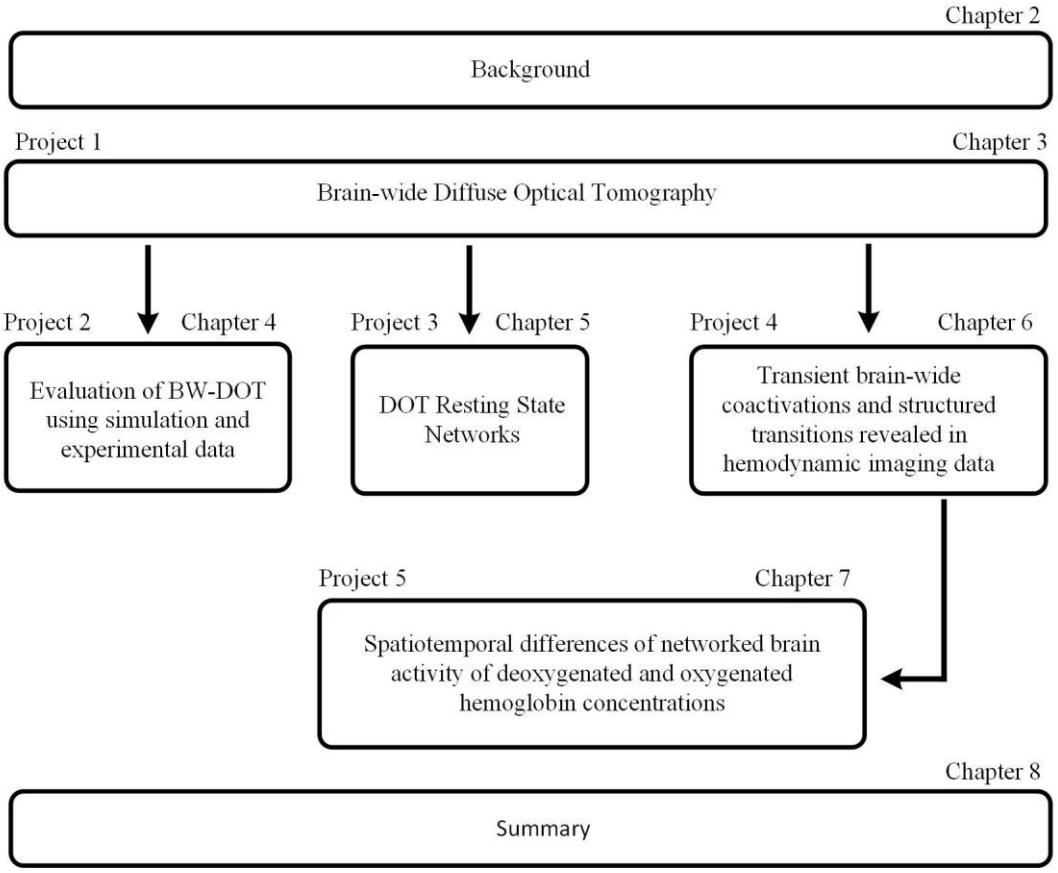

Figure 1-1 Relationship of multiple projects comprising the dissertation

This dissertation comprises several projects that are reported in different chapters. The relationship between these chapters and projects is illustrated in Figure 1-1. ***Chapter 2*** gives a brief

introduction to the technique of DOT. First, the fundamental principles of fNIRS followed by DOT are described. Then, a brief literature review of RSNs followed by RSNs reconstructed using DOT imaging is provided. ***Chapter 3*** introduces a new computational framework for studying networked brain activity using fNIRS data. The proposed framework integrates a cap-based whole-head optode placement system with multiple computational approaches to reconstruct brain networks in dual contrasts of HbO and HbR. ***Chapter 4*** provides the evaluation of the framework. First, using simulation data, point-spread function-based metrics are used to quantify the system's spatial resolution. Later, the spatiotemporal patterns of brain activations involving motor control are studied using task-based experimental data.

Chapter 5 applies the framework to resting-state fNIRS data from healthy participants reconstructing multiple RSNs in HbO and HbR contrasts. The spatial patterns of these networks from the two contrasts are quantitatively compared with each other and to f-RSN templates. ***Chapter 6*** studies the brain's FC using the method of co-activation patterns (CAPs). The results provide valuable insights into the spatiotemporal functional organization of the brain at rest. ***Chapter 7*** investigate differences between the spatiotemporal properties of CAPs obtained from resting-state HbO and HbR DOT data. C***hapter 8*** summarizes the major work presented in this dissertation and discusses its significance.

2. Background

2.1 Functional near-infrared spectroscopy

The possibility of using near-infrared (NIR) light to detect cerebral oxygenation in adults noninvasively was first described in a transillumination spectroscopic experiment (Jobsis, 1977). Since then, his idea has culminated in the well-known fNIRS technique used to noninvasively study brain tissue oxygenation using NIR light in the range of 650-950 nm. See (Chen et al., 2020b, Lloyd-Fox et al., 2010, Boas et al., 2014, Scholkmann et al., 2014, von Lühmann et al., 2021, Yeung, 2021, Pinti et al., 2020, Ferrari and Quaresima, 2012, Quaresima and Ferrari, 2019) for reviews on studying brain function using fNIRS.

The principle of fNIRS is illustrated in Figure 2-1. Light emanating from a light source enters the head and passes through multiple layers of head tissues such as the scalp, cranium, brain-protective membranes, and cerebrospinal fluid (CSF). After much absorption, reflection, and scattering, light photons penetrate the cortex and interact with chromophores such as hemoglobin molecules in their oxygenated (HbO) and deoxygenated (or reduced) (HbR) states. The concentrations of these chromophores are coupled to cerebral hemodynamics and neuronal activity by a cascade of metabolic processes in what is known as neurovascular coupling (NVC) (Buxton, 2009). The photons eventually move away from the cortex towards the scalp and emit out of the head, where they are detected using sensitive photodetectors and converted to voltage signals. These signals are fed to a computer and are used to estimate relative changes in the concentration of HbO and HbR in the region being interrogated. Under resting state, the fNIRS signal represents a mixture of (i) non-evoked (spontaneous) neurovascular coupling and (ii) systemic physiological processes, for example, respiration and heart pulsation, etc. (Scholkmann et al., 2014).

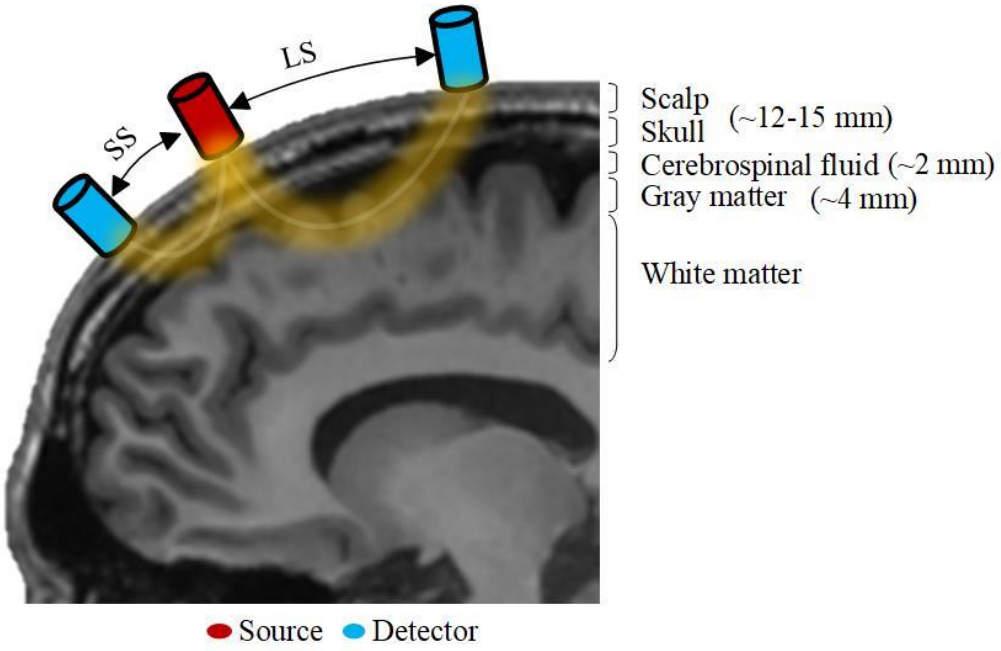

Figure 2-1 Schematic diagram of fNIRS measurements.
NIRS light emits from an LED/laser source, enters the head, travels across multiple tissue layers in a "banana-shaped" path, emits out of the head and is detected by a NIRS detector. The light measurement at a point on the light path is called a channel. SS: Short-separation channel, LS: Long-separation channel.

Usually, the fNIRS detector is a photodiode, and the source is an LED or a laser. Figure 2-2 shows examples of how these optodes can be arranged on a participant's head. The optode arrangement can be in the form of patches (Figure 2-2A-D) or distributed across the head (Figure 2-2A-D). The inter-optode distance (IOD) defines the distance between the source and detector and is critical to obtaining a neuronally relevant signal. Generally, a larger IOD enables a deeper head region to be interrogated. However, too large an IOD will render the fNIRS signal useless as it will represent mostly noise due to severe attenuation of light. Hence, the IOD is carefully chosen to strike a balance between depth and signal-to-noise ratio (SNR). While an IOD of about 2 cm is sufficient for imaging an infant cortex (Duncan et al., 1995), an IOD of about 3 cm is typically used for imaging the adult cortex (Van der Zee et al., 1992).

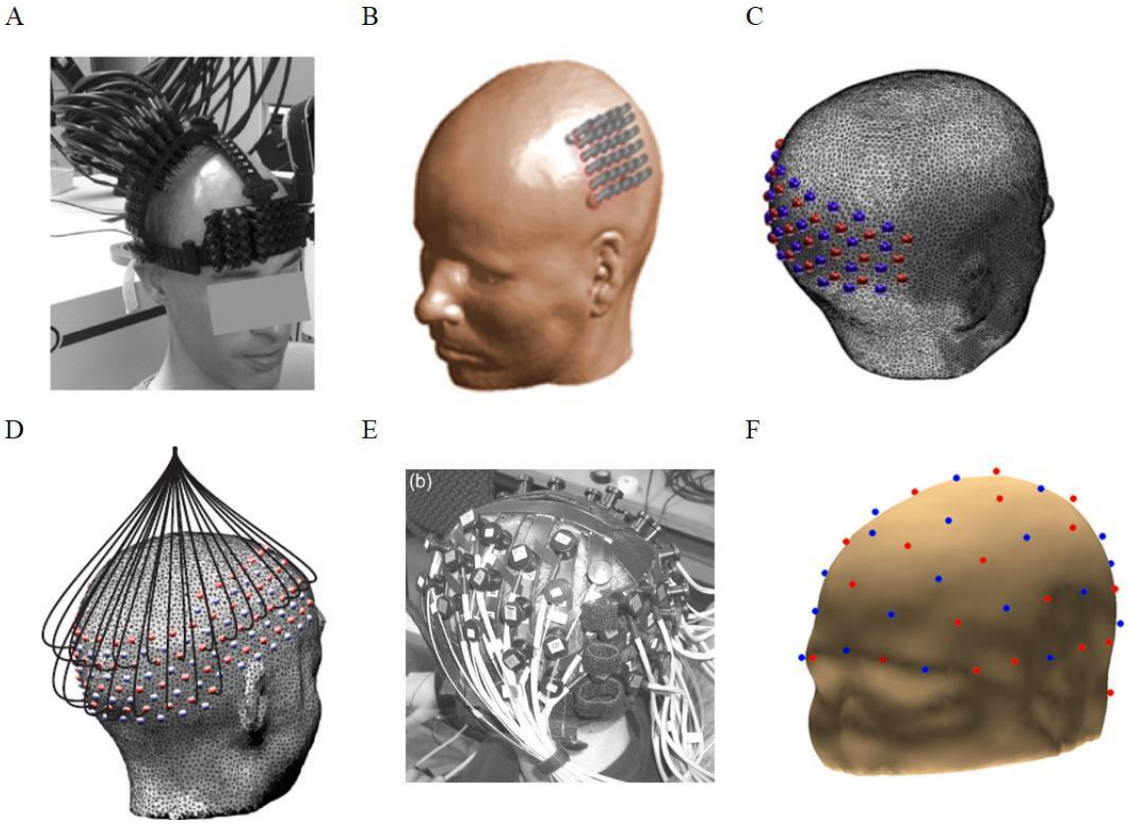

Figure 2-2 Examples of head caps used in DOT studies
(A) Multi-area patch-based system (Koch et al., 2010) (B) patch-based system on somatomotor area (Habermehl et al., 2012), with permission from Elsevier (C) patch-based system on the visual area (Eggebrecht et al., 2012), with permission from Elsevier (D) patch-based system on a large FOV (Eggebrecht et al., 2014), with permission from Springer Nature (E) whole-head DOT system (Franceschini et al., 2006), and (F) whole-head DOT system (Khan et al., 2021), with permission from IOP Publishing.

Most fNIRS systems, known as CW-fNIRS systems, continuously emit light at multiple wavelengths and measure the light intensity at the detectors. The light measurement on the photon path (Figure 2-1) is called a channel. This measurement is usually done at the midpoint between the source and detector at a depth of half the IOD (Patil et al., 2011). By comparing the emitted light intensity I_0 to the detected light I intensity, one can measure the light attenuation A (unitless):

$$A = -log\frac{I}{I_0} \qquad 2\text{-}1$$

The light attenuation is related to the chromophore concentrations via a relationship known as the Beer-Lambert Law (BLL) (Ingle Jr and Crouch, 1988):

$$A = \varepsilon . c . d \tag{2-2}$$

where ε is the molar extinction coefficient ($L\, mol^{-1} cm^{-1}$), c is chromophore concentration ($mol\, L^{-1}$) and d is the path length (cm). BLL assumes that the light is attenuated by absorption and follows a straight line. However, this is not suitable for biological tissues such as the brain, where scattering dominates the absorption (Boas et al., 2001). To accommodate for the scattering and change in photon path length, a modified form of the BLL called modified BLL (MBLL) (Delpy and Cope, 1997) is used.

$$A = \varepsilon_{\lambda} . c . d . DPF_{\lambda} + G \tag{2-3}$$

where DPF (unitless) is the differential pathlength factor that adjusts for the actual path length, which is longer than d and is about 6.53±0.99 (Duncan et al., 1995). The term G accounts for light attenuation due to scattering and is not known. Because CW-fNIRS is used in this dissertation, we are interested in relative changes in chromophore concentrations rather than absolute concentrations, we can cancel out this term and obtain a differential (relative to the baseline state) expression:

$$\Delta A = \varepsilon_{\lambda} . \Delta c . d . DPF_{\lambda} \tag{2-4}$$

Using two wavelengths λ_1, λ_2, and assuming that HbO and HbR chromophores are used, we can obtain the following system of linear equations:

$$\begin{aligned} \Delta A_{\lambda 1} &= d . DPF_{\lambda 1} \left(\varepsilon_{HbR,\lambda 1} . \Delta c_{HbR} + \varepsilon_{HbO,\lambda 1} . \Delta c_{HbO} \right) \\ \Delta A_{\lambda 2} &= d . DPF_{\lambda 2} \left(\varepsilon_{HbR,\lambda 2} . \Delta c_{HbR} + \varepsilon_{HbO,\lambda 2} . \Delta c_{HbO} \right) \end{aligned} \tag{2-5}$$

where the unknowns Δc_{HbO}, and Δc_{HbR} are the changes in HbO and HbR concentrations relative to the baseline concentrations. The total hemoglobin concentration change can be calculated as a sum of these values:

$$\Delta c_{Total} = \Delta c_{HbO} + \Delta c_{HbR} \quad 2\text{-}6$$

Over the last two decades, fNIRS has found numerous applications, including basic neuroscience research questions (Hoshi and Tamura, 1993, Villringer et al., 1994, Kato et al., 1993, Meek et al., 1995, Niu and He, 2014), psychology (Cutini et al., 2012), neurodevelopment (Lloyd-Fox et al., 2010), psychiatry (Ehlis et al., 2014), neurorehabilitation (Strangman et al., 2006), economics (Kopton and Kenning, 2014), and brain-computer interface (Naseer and Hong, 2015), etc. Because of its robustness against movement and high portability, fNIRS has been used to study brain activity under naturalistic use cases such as walking (Takeuchi et al., 2016) and navigation (McKendrick et al., 2016), and yoga (Dybvik and Steinert, 2021), etc. Furthermore, because of its accessibility to diverse populations, fNIRS has been used by individuals with non-MRI compliant implants (Bortfeld, 2019), neonates (Mintzer and Moore, 2019), bedridden patients (Mathieu et al., 2020), and patients undergoing surgeries (Frogel et al., 2019, Serraino and Murphy, 2017).

2.2 Diffuse optical tomography

Despite the immense usefulness demonstrated by the fNIRS as described above, it nevertheless has several limitations. For example, light measurements from a source-detector pair are sensitive to a broad bulk photon path between a source and a detector. Hence, these measurements are sensitive to a combination of cerebral and extracerebral tissues. Secondly, each fNIRS channel provides only one measurement location. Increasing the number of source-detectors (SD) pairs can increase measurements. However, the total number of measurement points

is still limited. Thirdly, fNIRS channels usually use a relatively constant IOD which probes the head at a constant depth from the scalp. Hence fNIRS produces functional topographic maps that are not sensitive to depth.

These limitations are addressed to an extent by DOT, a more advanced algorithmic form of fNIRS. DOT uses fNIRS overlapping measurements to reconstruct functional tomographic images of the brain (Arridge, 1999, Yodh and Chance, 1995, Bluestone et al., 2001) with spatial resolution approaching fMRI (Eggebrecht et al., 2014, Ferradal et al., 2016). DOT offers a relatively cheaper, safer, and more portable alternative to conventional functional neuroimaging modalities such as fMRI and PET. See (Jacques and Pogue, 2008, Gibson and Dehghani, 2009), and (Wheelock et al., 2019) for a review on DOT.

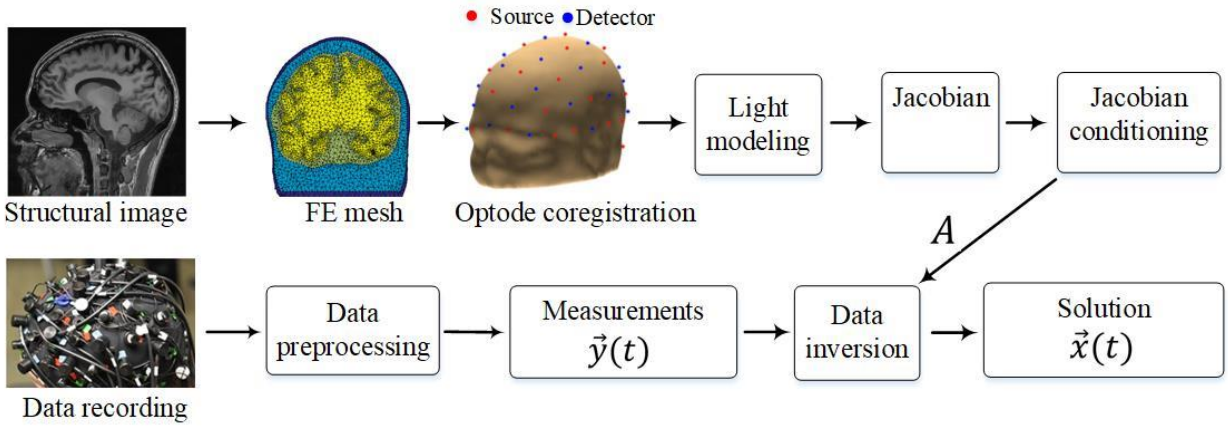

Figure 2-3 General framework of Diffuse Optical Tomography.
MRI structural scan or an age-corrected template is used to create a FEM head model. Optical properties are assigned to each tissue type and digitized 3D locations of the optodes are co-registered onto the model. The Jacobian (also known as sensitivity matrix) is calculated using a light-modeling software and is then conditioned. fNIRS measurements are recorded and undergo preprocessing such as artifactual channel/segment removal (or correction), and band-pass filtering, etc. These processed measurements are inverted using a regularized estimation framework. The solution of the inversion is a volumetric time-series at each node/voxel of the head model, which can undergo further processing such as smoothing, data reduction, etc.

A general framework of DOT is illustrated in Figure 2-3. Mathematically, DOT is an inverse problem and can be described by a linear equation:

$$\vec{y}(t) = A\vec{x}(t) \qquad 2\text{-}7$$

where the forward operator A describes how the changes in optical properties $\vec{x}(t)$ are mapped to the changes in observed fNIRS light measurements $\vec{y}(t)$. Therefore, a typical DOT algorithm consists of (1) a forward problem and (2) an inverse problem. In the context of imaging the human brain, the forward model approximates the aggregate photon propagation within the different layers of the head tissues starting from a light source to a light detector.

A finite-element-method (FEM) model is usually generated by segmenting an MRI structural image of an individual to model the human head. The FEM head model is parameterized by the spatial distribution of optical tissue properties such as absorption and scattering coefficients, etc. A relationship between the changes in these optical properties to the changes in surface light measurements on the scalp is calculated in a Jacobian, also called a sensitivity matrix. This matrix is the forward operator A in Eq. 2-7. In the inverse problem, the head's optical properties are estimated such that the predicted or simulated measurements match the physical measurements from the fNIRS device, using light measurements and the forward model. These estimates in the form of tomographic functional maps are further used to infer brain activity.

2.2.1 Forward problem

This section will briefly describe how to arrive at Eq. 2-7. A set of partial differential equations (PDE), collectively called the radiative transport equation (RTE), can be used to model light transport in biological tissues as a flow of energy emitted from an isotropic light source (Arridge, 1999). For computational ease, the diffusion approximation (DA) to the RTE is used. The frequency-domain form of the DA equation is given by:

$$-\nabla \cdot \kappa(\vec{r})\nabla\Phi(\vec{r},w) + \left(\mu_a(\vec{r}) + \frac{iw}{c_m(\vec{r})}\right)\Phi(\vec{r},w) = q_0(\vec{r},w) \quad \text{2-8}$$

where $\kappa(\vec{r}) = 1/3(\mu_a(\vec{r}) + \mu_s'(\vec{r}))$ is the diffusion coefficient (also known as the diffusion length coefficient (Jacques and Pogue, 2008), $\mu_a(\vec{r})$ and $\mu_s'(\vec{r})$ are the absorption and scattering coefficients respectively at location $\vec{r}$. The reduced form of the scattering coefficient $\mu_s'(\vec{r}) = \mu_s(\vec{r}) \cdot (1-g)$ is typically used instead of the $\mu_s(\vec{r})$ since the biological tissues provide a highly scattering anisotropic media for near-infrared light, where g is the anisotropy coefficient. The photon fluence rate $\Phi(\vec{r},w)$ at location $\vec{r}$ is a scalar function (unit: power/area) of the angular modulation frequency w. The speed of light in the medium is $c_m(\vec{r}) = c/n(\vec{r})$, where c is the speed of light in a vacuum and $n(\vec{r})$ is the index of refraction at the location $\vec{r}$. The isotropic light source, represented by light intensity $q_0(\vec{r},w)$, is used to ensure the validity of DA assumption. Furthermore, the DA is valid provided the following assumptions are met (Jacques and Pogue, 2008): isotropic light radiance; changes of light fluence are much slower than a photon's travel time over the mean free path (MFP), where MFP=$3\kappa(\vec{r})$; and much more scattering than absorbing, i.e. $\mu_s'(\vec{r}) \gg \mu_a(\vec{r})$. These conditions are sufficiently met in imaging the human brain. The brain tissues inside the skull are away from the light sources on the scalp at the depth sufficiently larger than the MFP, beyond which the light radiance is isotropic. Moreover, light fluence changes modulated by the slow hemodynamic variations are on the order of seconds compared to the travel time of photons which is on the order of picoseconds.

Since a CW-NIRS system is used in this dissertation, where $w = 0$, the Eq. 2-8 can be simplified to:

$$\left(\nabla^2 - \frac{\mu_a}{\kappa(\vec{r})}\right)\Phi(\vec{r}) = -\frac{q_0(\vec{r})}{\kappa(\vec{r})} \quad \text{2-9}$$

Since the human head has a complex geometrical shape and contains optically

inhomogeneous tissues, the Eq. 2-9 can be solved numerically using the FEM approach (Arridge, 1999) that builds linearized approximations to PDEs based on the volumetric meshes derived from a structural 3D MRI head image. Subject-specific structural MRI scan data or age-corrected atlases may be used to create the FEM mesh (Ferradal et al., 2014). A FEM mesh of a human head (see Section 3.2.2) typically has hundreds of thousands of tetrahedral elements. A smaller sized-element results in a more accurate solution but at the cost of increased computational time (Doulgerakis-Kontoudis et al., 2017).

The Rytov approximation and Green's functions method (Arridge, 1999, O'Leary et al., 1995) are used to solve Eq. 2-9. The solution is discretized into a set of SD pair measurements (Wheelock et al., 2019):

$$y(\lambda) = -\ln\frac{\Phi}{\Phi_0} = -\sum_{i}^{N}\frac{V_i}{\kappa(\vec{r}_i)}\cdot\frac{G(\vec{r}_s,\vec{r}_i,\lambda)\cdot G(\vec{r}_d,\vec{r}_i,\lambda)}{G(\vec{r}_s,\vec{r}_d,\lambda)}\Delta\mu_a(\vec{r}_i) \qquad 2\text{-}10$$

where,Φ_0 is the baseline fluence rate, V_i is the tetrahedron volume at the location $\vec{r}_i$, and N is the total number of nodes in the volume mesh. The terms $G(\vec{r}_s,\vec{r}_i,\lambda)$ and $G(\vec{r}_d,\vec{r}_i,\lambda)$ are the Green's functions that represent the spatial sensitivity at the location $\vec{r}_i$ due to the sources and detectors placed at locations $\vec{r}_s$and $\vec{r}_d$, respectively. Green's functions are dependent on the geometry of the media. The normalizing term $G(\vec{r}_s,\vec{r}_d)$ is the Green's function of the source evaluated at the detector's location d. Note that $G(\vec{r}_s,\vec{r}_d) \equiv G(\vec{r}_d,\vec{r}_s)$ due to the reciprocity theorem of electromagnetic radiation (Case and Zweifel, 1967). The Rytov approximation $\delta\Phi = \ln\left(\frac{\Phi}{\Phi_0}\right)$ provides a normalizing effect for the small errors in the optical properties. For CW-fNIRS, $\delta\Phi = \ln\left(\frac{I}{I_0}\right)$ where A is the amplitude of measured fNIRS light intensity. Eq. 2-7 is a time-dependent form of Eq. 2-10, where, $\vec{y}(t) = -\ln\left(\frac{I(t)}{I_0(t)}\right)$ are differential light measurements (also known as

optical density, OD), $A = -\sum_i^N \frac{V_i}{\kappa(\vec{r}_i)} \cdot \frac{G(\vec{r}_s,\vec{r}_i,\lambda)\cdot G(\vec{r}_d,\vec{r}_i,\lambda)}{G(\vec{r}_s,\vec{r}_d,\lambda)}$, and $\vec{x}(t) = \Delta\vec{\mu}_a(t)$ represents a vector of changes in absorption coefficients at each node of the FEM mesh, which is unknown and estimated. The Jacobian is a $NM \times NN$ matrix having the following structure:

$$A = \begin{bmatrix} \frac{\delta \ln I_1}{\delta \mu_{a1}} & \cdots & \frac{\delta \ln I_1}{\delta \mu_{aNN}} \\ \vdots & \ddots & \vdots \\ \frac{\delta \ln I_{NM}}{\delta \mu_{a1}} & \cdots & \frac{\delta \ln I_{NM}}{\delta \mu_{aNN}} \end{bmatrix} \quad \text{2-11}$$

where N is the number of FEM mesh nodes, and M is the number of fNIRS measurements. This matrix can be calculated using publicly-available FEM modeling software such as Nirfast (Dehghani et al., 2009a) and TOAST++(Schweiger and Arridge, 2014). The matrix A can also be calculated using Monte Carlo Methods (MCM) (Wang et al., 1995, Boas et al., 2002). MCM provides a more accurate solution than DA, mainly corresponding to the superficial layers of the FEM model, however, at an increased computational cost. Whereas DA-based solutions are computationally-efficient and can handle large FEM mesh size and channel size (Wu et al., 2015). Notice that $\vec{y}(t)$ and A are wavelength-dependent and so, the Jacobian must be calculated separately for both wavelengths. Furthermore, the Jacobian must be smoothed prior to be used for inversion (Section 2.2.2).

2.2.2 Inverse problem

The objective of the inverse problem is to estimate the changes in optical properties at every node of the FEM mesh in the solution source space using fNIRS measurements and the Jacobian A. This inverse problem is typically solved using a single-step inversion (Wheelock et al., 2019). The inversion can also be iterative (Dehghani et al., 2009a), resulting in a more accurate solution but is computationally more expensive. The single-step inversion (e.g., Eq. 3-6) is computationally

feasible and has been used successfully in several studies (Culver et al., 2003, Eggebrecht et al., 2014, White et al., 2009, Eggebrecht et al., 2012, Ferradal et al., 2016). The DOT problem is highly ill-posed and underdetermined (Wheelock et al., 2019). Therefore, irrespective of which technique of inversion is utilized, the inversion must be regularized to avoid overfitting the solution to the data. Once the changes in optical properties are estimated for each wavelength, the changes in concentrations of chromophores relative to the baseline concentrations can be calculated using a constrained least-squares fit to the Beer-Lambert Law relation:

$$\vec{\mu}_a = \mathrm{E}\vec{c} \qquad 2\text{-}12$$

where $\vec{\mu}_a$ is the vector containing absorption coefficients of the chromophores (HbO and HbR), $\vec{c}$ is the vector containing the concentration of these chromophores, and E is the molar extinction coefficients matrix. These coefficients are experimentally found for chromophores at different wavelengths (Prahl, 1999).

2.3 Resting-state functional connectivity

The phenomenon of RSNs was discovered using fMRI in the bilateral regions of the somatomotor (SM) cortex in the low-frequency band (<0.1Hz) (Biswal et al., 1995). Although this seminal report discovered a regional network, there is growing evidence that RSNs are a brain-wide phenomenon (Bressler and Menon, 2010, Miltner et al., 1999), leading to the idea of large-scale RSNs. An example of a large-scale RSN is that of the so-called default-mode network (DMN) (Raichle et al., 2001, Greicius et al., 2003) (Figure 2-4), which is activated when a person is thinking about themselves, others, past events or performing future planning (Buckner et al., 2008). This network comprises distributed cortical areas, including the posterior cingulate cortex (PCC), medial prefrontal cortex (mPFC), angular gyrus, and medial temporal regions.

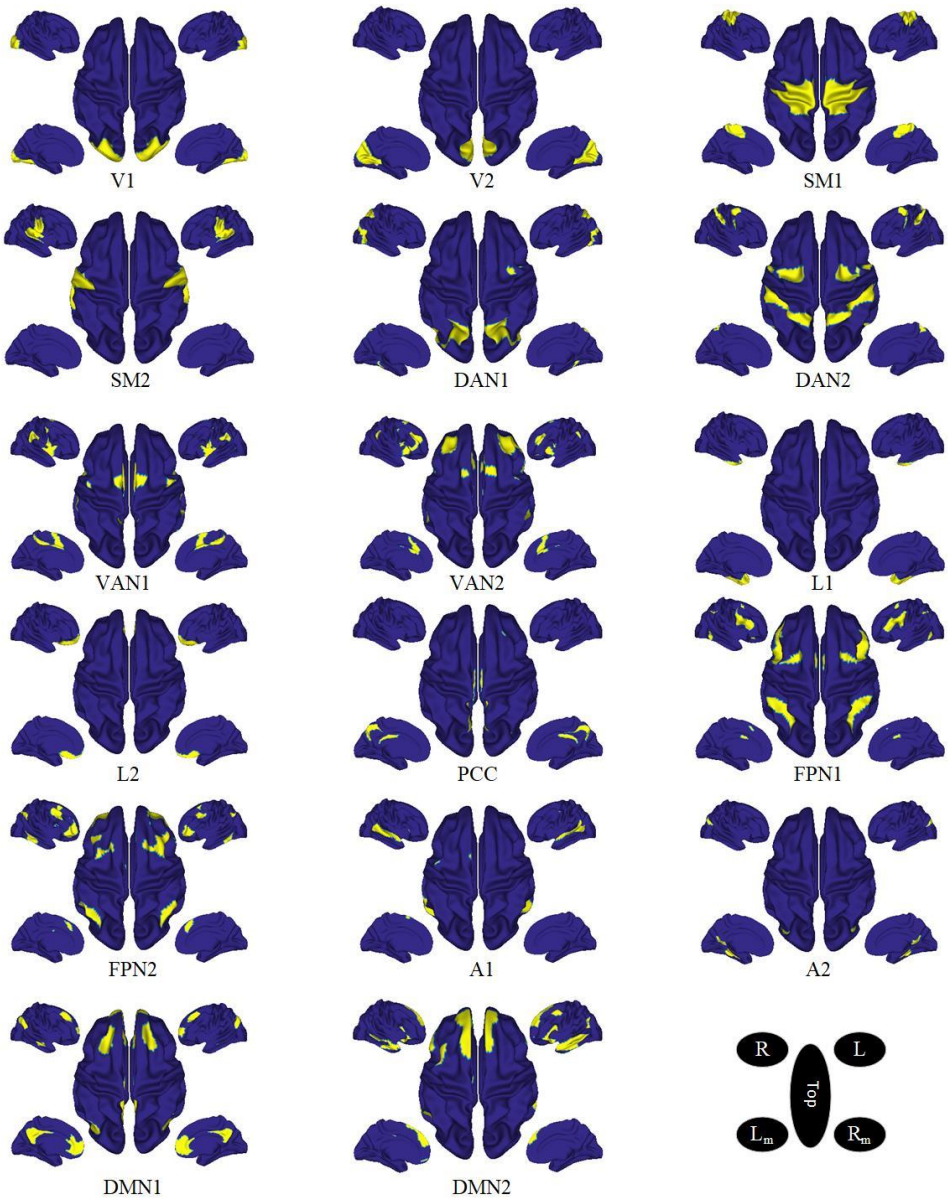

Figure 2-4 Resting-state networks templates.

All spatial maps are shown on the standard FreeSurfer cortical surface (gray/white matter interface). V = visual, SM = somatomotor, DAN = dorsal attention network, VAN = ventral attention network, L = limbic, PCC = posterior cingulate cortex, FPN = frontoparietal network, A = auditory, DMN = default mode network, A = anterior, L/R = left/right, Lm/Rm = left/right medial wall. Numbers: subnetworks (Yeo et al., 2011).

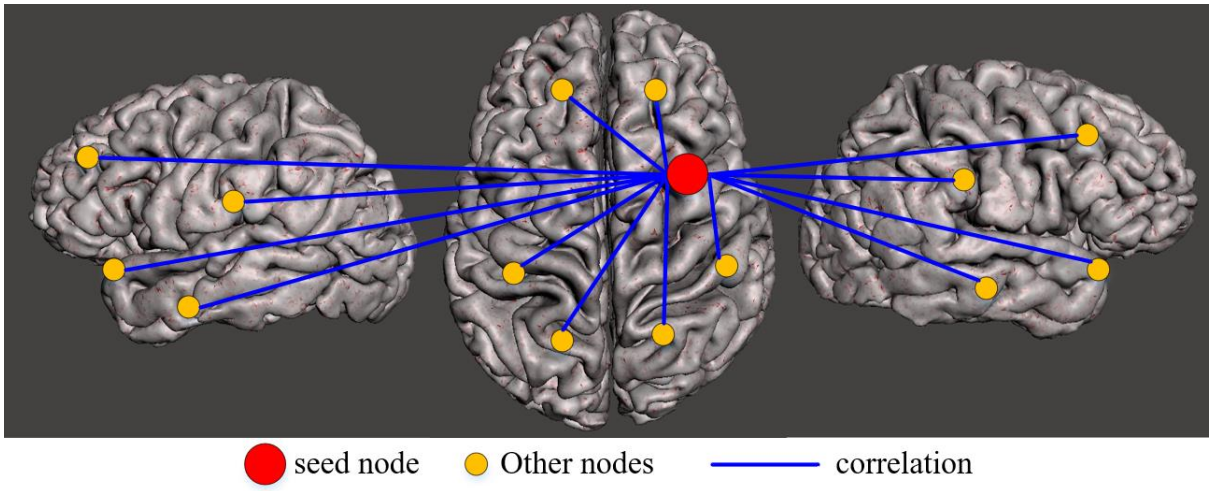

Figure 2-5 Schematic for seed-based correlation analysis.

Other examples of distributed large-scale RSNs include frontoparietal network (FPN), dorsal-attention network (DAN), and ventral-attention network (VAN) (Figure 2-4). It has been extensively reported that RSNs exhibit consistencies across participants (Damoiseaux et al., 2006a, Yeo et al., 2011) and show significant behavioral correlates (Allen et al., 2014b, Hutchison et al., 2013b, Rosenberg et al., 2016, Kelly et al., 2008) as well as clinical abnormalities in major neuropsychiatric disorders (Fox and Greicius, 2010).

A popular and relatively straightforward method of calculating RSNs is the so-called seed-based connectivity analysis (SCA). In SCA, a "seed" is first chosen, which can be a voxel time series or an average of the timeseries of a region-of-interest (ROI), i.e., a collection of co-located voxels in the imaging area of the participant's head (Figure 2-5). Then the correlation between the seed's timeseries and the timeseries of all other voxels or ROI is calculated. Statistically thresholded maps of these correlations describe the RSN (Brookes et al., 2016). SCA is highly dependent on the seed location, thereby biasing the RSN to this choice (Cole et al., 2010). Thus, the total number of RSNs becomes equal to the number of seed choices. Although this number can be reduced by using only the ROIs, it introduces another problem; defining the ROI. On the other

hand, the data-driven independent component analysis (ICA) approach is not dependent on the selection of seed locations and can simultaneously reconstruct multiple RSNs (Calhoun et al., 2001, Chen et al., 2008, Damoiseaux et al., 2006b, Brookes et al., 2011, Smith et al., 2009a, Beckmann et al., 2005). RSNs calculated from ICA analysis have been shown to be similar to SCA-derived RSNs, although these two are not identical (Van Dijk et al., 2010, Joel et al., 2011).

Although the brain's FC at rest is extensively studied, the exact neurophysiological mechanisms underlying these correlations remain elusive. In fMRI, increasing evidence has been documented that such resting-state FCs are nonstationary over a scan (Preti et al., 2017, Allen et al., 2014b, Chang and Glover, 2010). In contrast to static FCs over the entire scanning window, estimations of FCs over sequential sliding-time windows (either partially overlapped or non-overlapped) within a scan have led to the so-called dynamic FCs (dFC). It has been further suggested that dFCs potentially have higher sensitivities than static FCs for correlating with behavioral and disease conditions (Damaraju et al., 2014, Hutchison et al., 2013a). FCs are time-varying and have motivated numerous animal and human studies to identify potential neurophysiological events responsible for correlation-based FCs observed in brain signals, leading to several candidate hypotheses.

Brain-wide propagating activity, characterized by wave-like recurring patterns (at mesoscopic and macroscopic levels), is one of these hypotheses behind FCs (Muller et al., 2018). Propagating wave dynamics of large-scale spontaneous neural networks have been reported in animals (Huang et al., 2010, Stroh et al., 2013, Steriade et al., 1993, Luczak et al., 2007) and humans (Halgren et al., 2019, Gu et al., 2021, Raut et al., 2021, Massimini et al., 2004). For example, globally distributed cortical waves have been recorded using optical imaging in mice at a timescale of seconds (Matsui et al., 2016). Similarly, lateral-to-medial propagating waves in rats (Majeed et al.,

2011, Majeed et al., 2009) and global wave patterns in humans (Raut et al., 2021) have been reported in blood-oxygen-level-dependent (BOLD) signals. In humans, more types of propagating activities have been observed, including alternating activation waves between the DMN and task-positive networks (TPNs) (Majeed et al., 2011, Yousefi et al., 2018) and directionally constrained waves along the spatial axis representing the cortical hierarchical organization (Gu et al., 2021). These waves may be the underpinnings of correlational structures in resting-state FCs (Matsui et al., 2019), or at least critical in shaping the dynamics in resting-state FCs (Gu et al., 2021), and potentially with novel information about brain functional organizations in parallel to correlational FCs (Majeed et al., 2011).

The second hypothesis proposes that resting-state FCs are driven by short-lived coactivation patterns (CAPs) (Liu and Duyn, 2013). These CAPs are obtained via a point process analysis focusing on selected fMRI frame data surrounding regional peaks (Tagliazucchi et al., 2011, Cifre et al., 2020). Strong correspondences between these transient events and resting-state FCs are reflected in their spatial patterns (Liu et al., 2013), and CAPs account for significant variances describing resting-state FCs (Tagliazucchi et al., 2016). Recent clustering studies on the entire fMRI frame data further indicate that similar coactivation patterns exist beyond local peaks of fMRI activity in predefined regions-of-interests, leading to the detection of the so-called manifold recurring brain-wide CAPs (Gutierrez-Barragan et al., 2019), while their relationship to resting-state FCs is yet to be established. Moreover, CAPs have been recently reported in neuronal electrical signals in both animals (Matsui et al., 2019) and humans (Ding et al., 2021). An obvious advantage of CAP-based analysis is to allow interrogation of dFCs at fine temporal scales down to single timeframes (Liu et al., 2018b), eliminating the need for a priori selected sliding windows as typically required in correlational methods. Moreover, CAP studies have shown clinical

relevance (Liu et al., 2018b, Yang et al., 2021, Marshall et al., 2020, Rey et al., 2021, Kaiser et al., 2019, Zhuang et al., 2018).

The third hypothesis is global brain activity, linked to a well-known phenomenon in fMRI data analysis that is currently still under debate (Liu et al., 2017), i.e., global signal (GS). The anticorrelated DMN and TPNs, for example, have shown a strong positive correlation under the influence of GS, resulting in global brain activity patterns (Yousefi et al., 2018). Furthermore, global brain activity has been observed as transient brain states during brain-wide propagating waves (Matsui et al., 2019). GS is defined as the time series of intensity averaged across imaging voxels in fMRI, which is usually regressed out in the preprocessing of fMRI data (Desjardins et al., 2001, Aguirre et al., 1998), as it is believed that physiological noise substantially contributes to it (Liu et al., 2017). However, recent studies have demonstrated that GS may contain neuronally relevant information (Murphy and Fox, 2017, Schölvinck et al., 2010) and is primarily modulated by the fluctuating state of arousal (Wong et al., 2013, Chang et al., 2016, Liu et al., 2018). While GS is known for affecting FC analysis (Murphy et al., 2009, Fox et al., 2009, Murphy and Fox, 2017), it also drives dFC patterns (Chang et al., 2009). All these facts support the potential role of global brain activity in generating resting-state FCs.

Table 2-1 Examples of DOT resting-state studies

Study	N	State	Age (Year)	Con.	Type	#S-D	#Ch	SR (Hz)	BPF (Hz)	GSR	Short channel (mm)	λ(nm)	Acq. Time (min)	FOV	FEM model	Forward solver	Inverse method	Chrom.	#RSNs	RSFC method	Dim
(White et al., 2009)	5	EO/Sit	24-27	Healthy	CW	V:24S/28D SM:18S-28D	NR	10	0.009-0.5	Y	13	750/850	10-15	SM, V	2-layer	Nirfast	MPGISPR	HbO/R,total	2	SBCA	SP
(White et al., 2012)	8	Sleep	<10w	3Healhty 5preterm with different conditions	CW	18S/16D	106	10.78	0.009–0.08	Y	10	750/850	10-20	V	Infant T2 atlas,	Nirfast	MPGISPR	HbO/R, total	1	SBCA ICA	SP
(Eggebrecht et al., 2014)	8	EO/Sit	21-45	Healthy	CW	96S/92D	~1200	10	0.009–0.08	Y	13	750/850	10	O, parts bilateral Parietal, temporal, frontal cortex	Sub. T1/T2 5-layer	Nirfast	MPGISPR	HbO/R	6	SBCA	SP
(Ferradal et al., 2016)	9	Sleep	<2days neonates	Healthy	CW	32S/34D	NR	10	0.009–0.08	Y	10	750/850	20-60	O, T, IP	Sub. T1/T2 4-layer	Nirfast	NR	HbO/R	3	SBCA ICA	SP
(Aihara et al., 2020)	20	EO/sit	21-38	Healthy	CW	32S/32D	LS:96 SS:56	18.5	0.009-0.08	N	13	780/805 830	10	Bilateral Frontal parietal	Sub. T1 5-layer	MCX	HB-DOT	HbO/R	19	ROI based correlation analysis	SP
(Khan et al., 2021)	13	EO/sit	31.7	Healthy	CW	34S/31D	LS:109 SS:8	6.25	0.009-0.2	Y	8	760/850	6	Whole	4-layer	Nirfast	MNE	HbO/R	11	ICA	SP

λ: wavelength, EO: Eyes-Closed, EO: Eyes-Open, FOV: Field-of-View, ICA: Independent component analysis, IP: Inferior parietal, MPGISPR: Moore-Penrose generalized inverse with spatially variant regularization, N: Number of participants, NR: Not reported, O: Occipital, SBCA: Seed-based correlation analysis, S-D: Source-Detector, SM: Somatomotor, SP: Spatial, T: temporal, V: Visual, Y: Yes

It is important to note that these three phenomena (i.e., propagating waves, CAPs, and global brain activity) have shown linkages among each other. As discussed above, propagating waves are of global nature (Stroh et al., 2013). Manifold recurring brain-wide CAPs have been suggested to be phase-locked to GS in rodents (Gutierrez-Barragan et al., 2019, Ma et al., 2020). Furthermore, a recent mice study (Matsui et al., 2016) using wide-field optical imaging concurrently monitoring calcium and hemodynamic signals indicates all three phenomena in both neuronal spiking and hemodynamic data in which transient CAPs are embedded in globally propagating waves. These three phenomena have been studied separately in both animals and humans. Studies indicating their potential connections have been largely performed on animal models (Gutierrez-Barragan et al., 2019, Matsui et al., 2016, Ma et al., 2020), and the understanding of their interactions in humans remains sparse.

2.4 DOT RSNs

DOT is gaining an interest in the functional neuroimaging community to study brain activity due to its high accessibility. However, a majority of DOT studies have utilized a task-based paradigm, while resting-state studies remain sparse. A list of major DOT resting-state studies is provided in Table 2-1. Most of these studies are reported using CW-fNIRS instruments with patch-based optode montages providing limited brain coverage. Interestingly, these studies have assumed that brian's FC across a scan is stationary. Therefore, these studies have reported only static RSNs. In contrast, whole-head DOT dFCs have not been reported to the best of our knowledge.

DOT RSNs were first reported in a seminal work, demonstrating the feasibility of studying RSNs in human adults using DOT technology (White et al., 2009). They used a two-layer head model with high-density optode patches (smallest IOD: 13 mm) on the SM and visual cortical areas. Using regularized single-step inversion and SCA, they obtained RSNs of HbO, HbR, and

total hemoglobin contrasts covering bilateral areas in the SM and visual cortices. They also demonstrated that while there was a strong correlation within a network's bilateral regions, there was little correlation between regions of the two networks. Furthermore, these RSNs could be obtained at the participant level and across sessions.

The work of White et al. (2009) was later extended, via creating new configurations of rectangular high-density optodes (smallest IOD: 13 mm) for curved head surfaces, to cover an even larger area of the underlying cortex and achieve gyrus-level spatial resolution for mapping cortical activations (Eggebrecht et al., 2014). Their optode cap (Figure 2-2D) included 96 sources and 92 detectors using about 1200 channels. Using SCA, this study mapped six RSNs, including the visual, ventral motor, auditory, frontoparietal control (FPC), DAN, and DMN. The spatial maps of these networks shared correspondences with those obtained from fMRI data. However, the mPFC and precuneus nodes for DMN and dorsal nodes for the motor network were missing as no optodes covered those corresponding surface measurement areas. Both of the above-mentioned studies utilized customized patch-based configurations for equal-distance optode placements, which could effectively control the density of optodes and precisely assess their performances based on calculable metrics such as localization error and effective resolution, etc. (Wheelock et al., 2019).

Departing from the patch-based approach, a DOT RSN study used a cap-based configuration for optode placements using 32 sources and detectors effectively covering bilateral frontal and parietal areas (Aihara et al., 2020). Because of limited coverage, only about 20 regions were studied for connectivity analysis. Nevertheless, the study demonstrated that DOT could be used to image functional brain networks under resting conditions and further demonstrated the similarities between RSNs obtained by DOT and fMRI. This work also provided evidence that the cap-based

optode placement, which usually could not control inter-optode distances to be equal to the patch-based optode placement, could be used for DOT-based RSN studies.

Taking advantage of the portability of fNIRS instruments, DOT-RSNs have also been reported in bedside monitoring of preterm neonates under intensive care. For example, (White et al., 2012) used a high-density (smallest IOD: 10 mm) rectangular optode patch with 18 sources and 16 detectors covering the posterior part of the head. This study involved monitoring three full-term healthy babies and five preterm babies with medical conditions of varying degrees. Using SCA, their results showed strong bilateral correlations in the visual cortex in healthy babies but unilateral correlation patterns in a preterm baby with an occipital stroke, demonstrating the sensitivity of DOT to neuronal injury. Furthermore, because the SCA method is sensitive to the choice of seed location (see Section 2.3 of this dissertation), the authors of this study also reconstructed the RSNs using the ICA method, which showed results similar to those obtained using the SCA method.

The work of White et al. (2012) was later extended in another study (Ferradal et al., 2016) on full-term neonates to study their neurodevelopment. They used a larger high-density (smallest IOD: 10 mm) rectangular optode patch with 32 sources and 34 detectors covering more functional brain areas. Using SCA to obtain RSNs showed strong bilateral correlation patterns in the visual, middle temporal, and auditory networks. These results also showed similarity to ICA-based reconstructions and SCA-based reconstructions using fMRI.

These studies have collectively demonstrated the ability of DOT to image functional brain activity under resting conditions and have further demonstrated the similarities between RSNs obtained by DOT and fMRI (White et al., 2012, Eggebrecht et al., 2014, Ferradal et al., 2016, Aihara et al., 2020). However due to the limited spatial coverage of optodes, these studies either

reported missing nodes for distributed networks (Eggebrecht et al., 2014) or limited functional connectivity between pre-selected anatomical regions (Aihara et al., 2020). Mapping a large number of brain-wide RSNs has the significance in 1) providing a better perspective on the membership of distributed nodes for individual RSNs; 2) building the possibility of mapping whole-brain inter-RSN connectivity maps as in fMRI (Bressler and Menon, 2010), which have demonstrated insights to basic neuroscience questions (De Luca et al., 2006, Damoiseaux et al., 2006b) and potential for clinical use (Bressler and Menon, 2010).

To further establish DOT-based technologies in studying RSNs beyond the existing literature, we need to demonstrate that DOT-RSN can simultaneously reveal more brain-wide distributed networks under resting conditions, close to the common number of RSNs as revealed by fMRI data, e.g., 10 (Damoiseaux et al., 2006b) or 17 (Yeo et al., 2011), as well as to demonstrate the sensitivity of detecting all nodes for an RSN. Brain-wide reconstructions are necessary as extensive fMRI literature has indicated that most RSNs are widely distributed over the cortex (Bressler and Menon, 2010). No missing node is the basic requirement in providing a complete picture of each RSN. For example, the missing mPFC node of DMN in a previous DOT RSN study (Eggebrecht et al., 2014) is a hallmark in aging or Alzheimer's disease-related connectivity changes (Buckner et al., 2008). Missing nodes also hinder the investigation of inter-node connectivity, which is critical in studying pathopsychology in schizophrenia (Du et al., 2016). In addition, simultaneous detections of multiple RSNs offer the opportunity to study cross-RSN functional connectivity (Power et al., 2011), which has been demonstrated in fMRI with higher sensitivity than individual RSNs in detecting abnormal alterations in neuropsychiatric disorders (Bressler and Menon, 2010).

Furthermore, the similarity and difference between RSNs obtained from HbR and HbO should be quantitatively compared comprehensively as such a comparison has not been sufficiently addressed while the sensitivity to both HbR and HbO is one of the important advantages of fNIRS signals over fMRI signals. Finally, DOT RSN studies have primarily focused on generating static cortical maps, whereas there is increasing evidence that the brain's FC is nonstationary, as described above. Therefore, there is potential for studying the temporal structure of the networked brain activity of resting-state DOT data.

In this dissertation, we proposed a new framework termed BW-DOT to simultaneously reconstruct multiple dual-contrast brain-wide RSNs over the cortex, using a cap-based whole-head configuration for optode placements (Figure 2-2F, Figure 3-1). The CW-fNIRS system consisted of adjustable head caps mounting 73 dual-wavelength optodes that provided a field-of-view (FOV) covering the majority of the cortex. High-quality FEM models derived from individual MRI scans were used to accurately calculate forward light propagations in head tissues. Peripheral sensors, together with eight dedicated SS fNIRS channels, were employed to assist in the removal of non-neuronal signal sources before RSN reconstructions. The utility of FEM models and additional channels (both SS channels and peripheral sensors) was to compensate for the limitations of the cap-based optode placement configuration in sensitivity profiling and non-neuronal signal rejections, respectively, as compared to the patch-based configuration with high-density optode placements (Wheelock et al., 2019). Relative concentration changes in HbO and HbR chromophores were estimated simultaneously in a single-step joint regularized inverse reconstruction procedure. We then used a data-driven approach, i.e., spatial ICA (SICA) (Calhoun et al., 2001), to derive a cortical representation of HbO and HbR RSNs. Furthermore, we adopted a process of multi-step statistical analyses from our previous work to reconstruct genuine

tomography of RSNs with statistical meaning (Li et al., 2018). The BW-DOT framework is subsequently applied to resting-state fNIRS data to reconstruct brain-wide RSNs. Moreover, the brain's FC is analyzed using the method of co-activation patterns, which provide valuable insights into the spatiotemporal functional organization of the brain at rest.

3. Brain-wide diffuse optical tomography

This chapter has been adapted from the following peer-reviewed publication with permission from IOP Publishing:

Khan, A. F., Fan Zhang, Han Yuan, and Lei Ding. "Brain-wide functional diffuse optical tomography of resting state networks," Journal of Neural Engineering 18, no. 4 (2021): 046069, DOI: https://doi.org/10.1088/1741-2552/abfdf9).

3.1 Introduction

In this chapter, we proposed a new framework termed BW-DOT to simultaneously reconstruct multiple dual-contrast brain-wide RSNs over the cortex, using a cap-based whole-head configuration for optode placements (Figure 3-1). This framework is an amalgamation of several technologies, which are described one by one in this chapter.

3.2 The forward problem

3.2.1 Spectral DOT model

Like fMRI, where RSNs are obtained from relative fluctuations of hemodynamic signals (Buxton, 2013), we focus on CW-DOT advancements in imaging relative changes of HbO and HbR concentrations. To estimate concentration changes for both HbR and HbO, two light wavelengths of 760 nm ($\lambda 1$) and 850 nm ($\lambda 2$) with the optimal sensitivity to HbR and HbO, respectively, were used. Therefore, Eq. 2-10 needs to be solved as an inverse problem (see Section 2.2.2) twice to estimate $\Delta\mu_a(t)$ under two wavelengths. After that, changes in HbR and HbO concentrations are found using the spectral decomposition as in Eq. 2-12, where E is the matrix of the extinction coefficients of HbR and HbO, and $\Delta C(t) = [\Delta HbR(t);\ \Delta HbO(t)]$ are the vectors of time-varying chromophore concentration changes.

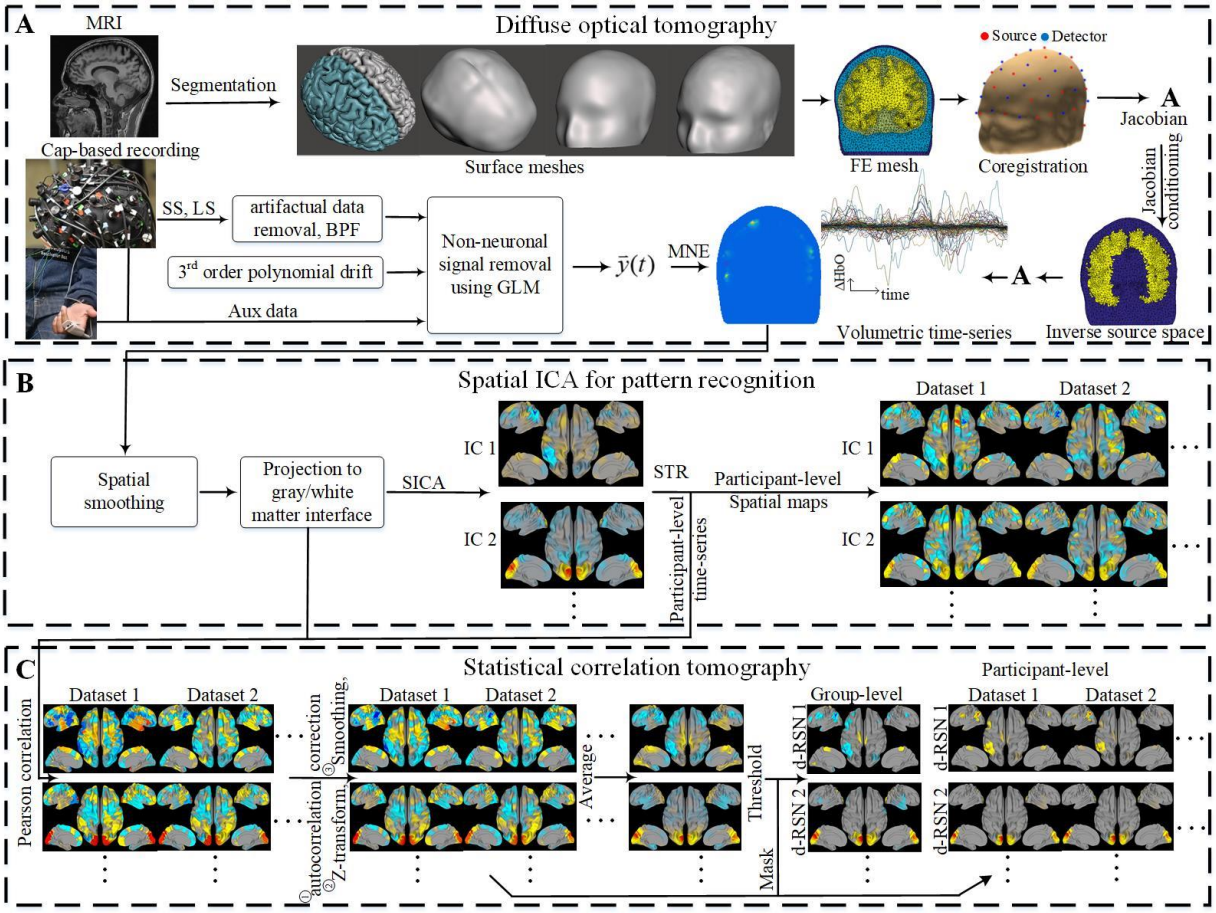

Figure 3-1 Brain-wide Diffuse Optical Tomography framework.
(A) Diffuse optical tomography. Measurements: MRI structural scans, fNIRS recordings from cap-based system, auxiliary data from a pneumatic respiratory belt, accelerometer, and photoplethysmography sensor; Preprocessing: artifactual channel/segment data removal, band-pass filtering, and general linear model; Forward modeling: tissue segmentation, generation of surface meshes, generation of FE mesh, coregistration of optodes on FE mesh, and generation and conditioning of Jacobian matrix; Inverse reconstruction: regularized joint-estimation using minimum norm estimation. **(B) Spatial ICA for pattern recognition:** volumetric spatial smoothing, volume to cortical surface projection, group-level spatial ICA, and spatiotemporal regression to obtain participant-level spatial maps and time series of ICs. **(C) Statistical correlation tomography** is derived by correlational analysis between the time series of ICs and sources at both group-level and participant-level. (Figure adapted from Khan et al. (2021)).

In the present framework, a spectrally-constraint approach was instead used, which related light intensity changes directly to chromophore concentration changes, leading to an inverse system less sensitive to measurement noise (Srinivasan et al., 2005) and a single step for joint

estimation of HbR and HbO concentration changes relativeto the baseline concentrations (Section 3.3). Eq. 2-10 is thus modified as:

$$\begin{bmatrix} \Delta\vec{y}_{\lambda 1}(t) \\ \Delta\vec{y}_{\lambda 2}(t) \end{bmatrix} = \begin{bmatrix} A_{HbR,\lambda 1} & A_{HbO,\lambda 1} \\ A_{HbR,\lambda 2} & A_{HbO,\lambda 2} \end{bmatrix} \begin{bmatrix} \Delta\overrightarrow{HbR}(t) \\ \Delta\overrightarrow{HbO}(t) \end{bmatrix} \quad 3\text{-}1$$

where $\Delta\overrightarrow{HbR}(t)$and $\Delta\overrightarrow{HbO}(t)$ are the vectors of time-varying HbR and HbO changes, respectively. $\overrightarrow{\Delta y}_{\lambda 1}(t) = -\ln\left(\frac{\vec{I}_{\lambda 1}(t)}{I_{\lambda 1,base}}\right)$, and the Jacobian A consists of four submatrices where the submatrix $A_{HbR,\lambda 1}$ is a $M \times N$ matrix:

$$A_{HbR,\lambda 1} = \begin{bmatrix} \frac{\delta \ln I_{\lambda 1,1}}{\delta \mu_{a1}} \varepsilon_{HbR,\lambda 1} & \cdots & \frac{\delta \ln I_{\lambda 1,1}}{\delta \mu_{aN}} \varepsilon_{HbR,\lambda 1} \\ \vdots & \ddots & \vdots \\ \frac{\delta \ln I_{\lambda 1,M}}{\delta \mu_{a1}} \varepsilon_{HbR,\lambda 1} & \cdots & \frac{\delta \ln I_{\lambda 1,M}}{\delta \mu_{aN}} \varepsilon_{HbR,\lambda 1} \end{bmatrix} \quad 3\text{-}2$$

where $\varepsilon_{HbR,\lambda 1}$ is the molar absorption coefficient for HbR at wavelength $\lambda 1$. The $\frac{\delta \ln I_{\lambda 1,i}}{\delta \mu_{aj}}$ entry defines the log-ratiometric amplitude of the ith (i = 1, …, M) light measurement arising from a small change in μ_{aj} at the jth (j = 1…M) source node. The other submatrices i.e. $A_{HbR,\lambda 2}$, $A_{HbO,\lambda 1}$, and $A_{HbO,\lambda 2}$ could be similarly defined. These submatrices can be calculated using the Nirfast software (Dehghani et al., 2009a) via Green's functions with realistic tissue boundaries, baseline optical properties (chromophore concentrations), and locations of light sources and detectors using the Adjoint method (Arridge and Schweiger, 1995). This leads to the linear forward model:

$$\vec{y}(t) = A\vec{x}(t) \quad 3\text{-}3$$

where, the known measurements $\vec{y}(t) = \begin{bmatrix} \Delta\vec{y}_{\lambda 1}(t) \\ \Delta\vec{y}_{\lambda 2}(t) \end{bmatrix}$ and the unknown chromophore concentration changes $\vec{x}(t) = \begin{bmatrix} \Delta\overrightarrow{HbR}(t) \\ \Delta\overrightarrow{HbO}(t) \end{bmatrix}$. The forward operator A thus relates the changes in concentrations at

each node of a FEM head model to the changes in log-ratiometric light intensities measured on the scalp.

3.2.2 Numerical models for head tissue volumes and surfaces

A FEM head model can be constructed using a relatively simple head geometry, for example, a two-layer head model (White et al., 2009) or a realistic five-layer head model (Eggebrecht et al., 2014). A realistic head model obtained from individual structural images such as MRI scan, along with accurate optode location digitization, generally provides better spatial *a priori* information resulting in a more accurate forward and inverse solution. I have used a four-layer FEM volumetric mesh head model from participant-specific MRI structural images in my dissertation.

Firstly, the FreeSurfer software (Jenkinson et al., 2012) was used to perform tissue segmentation on participants' T1-weighted MRI images. This segmentation yielded triangular surface meshes for the boundaries of the scalp (10,242 nodes), skull (10,242 nodes), CSF (10,242 nodes), and pial surface (306,091±19,289 nodes), each representing a boundary enclosing the head tissue with a unique set of optical properties. For each participant, the cortical surface, defined as the gray matter/white matter interface (20,484 nodes), was also generated using FreeSurfer for the purpose of statistical analysis and visualization (see Chapter 5).

Secondly, non-manifold errors (e.g., intersection, self-intersection, duplicate nodes, gaps, etc.) and disadvantaged topological features (e.g., dents and high aspect-ratio elements, etc.) presented on these derived surfaces meshes, especially the pial surface due to its highly convoluted nature, were identified. These unwanted surface mesh features can subsequently create volume mesh elements of undesired shapes and sizes and thus lead to numerical errors in computing Jacobian matrices. Some of these errors arise because of poor contrast areas in the structural image. Figure 3-2 shows an example of poor image contrast in a structural image around the temporal

bones. This produces poor tissue segmentation of the skin and outer skull surfaces resulting in intersection and dents on these surface meshes (Figure 3-3A).

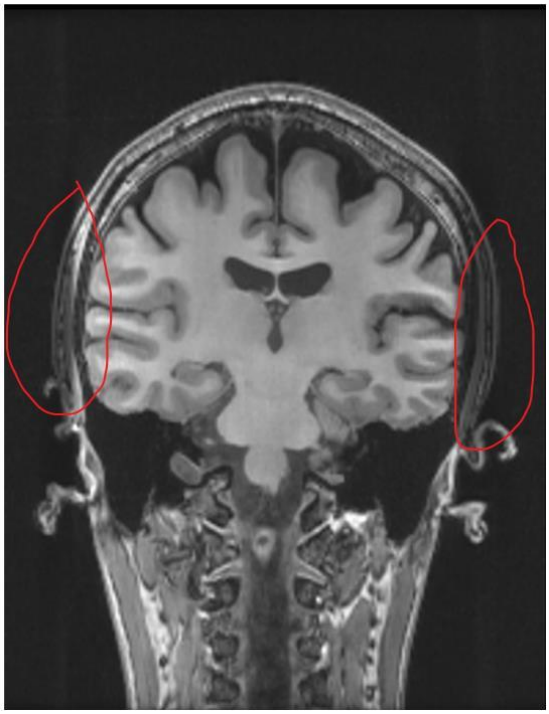

Figure 3-2 Example of contrasts issue in MRI image.
Coronal slice showing poor contrast areas encircled in red, responsible for poor tissue segmentation shown in Figure 3-3A

A postprocessing pipeline was developed using the Autodesk Meshmixer software (meshmixer.com) and the Iso2mesh toolbox (Fang and Boas, 2009) to remove these non-manifold errors and minimize disadvantaged topological features on these surface meshes. Figure 3-3B shows the surface mesh in Figure 3-3A after applying the correction. Another typical mesh-related problem is the high-aspect-ratio (ratio of the longest edge to shortest edge) triangular elements shown as red areas in the Figure 3-3C, E. Using our postprocessing pipeline, we were able to improve these elements so they could have a lower aspect ratio (Figure 3-3D, F). Figure 3-4 provides an example of mesh-related problems on the pial surface and the respective corrections.

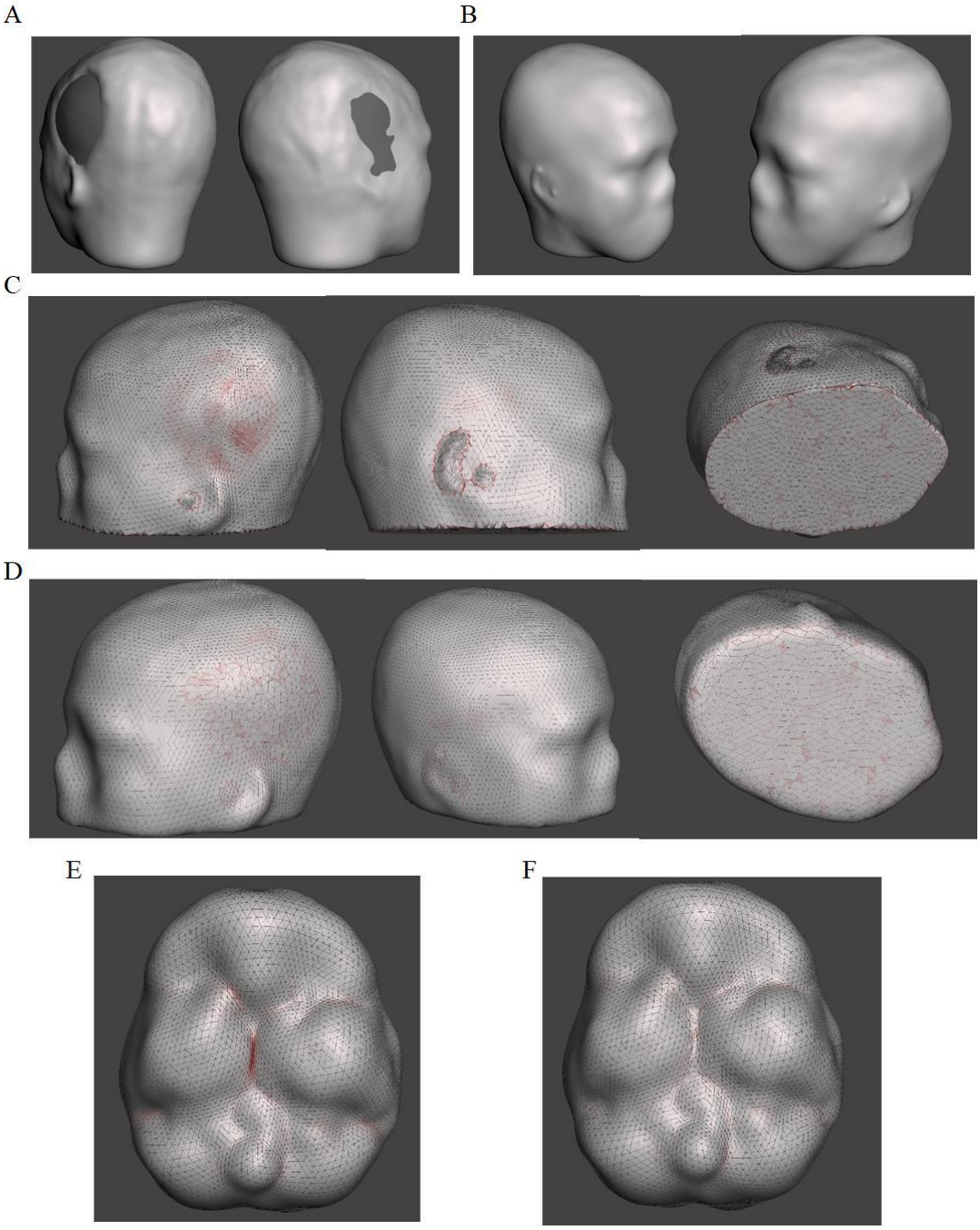

Figure 3-3 Examples of manifold errors and disadvantaged topological features on surface meshes and their correction.

(A) Intersection of skin surface with outer skull layer before correction and (B) after correction. (C) high-aspect ratio triangles illustrated in red color present on the scalp surface before and (D) after correction (E) high-aspect ratio triangles present on the skull surface before and (F) after correction.

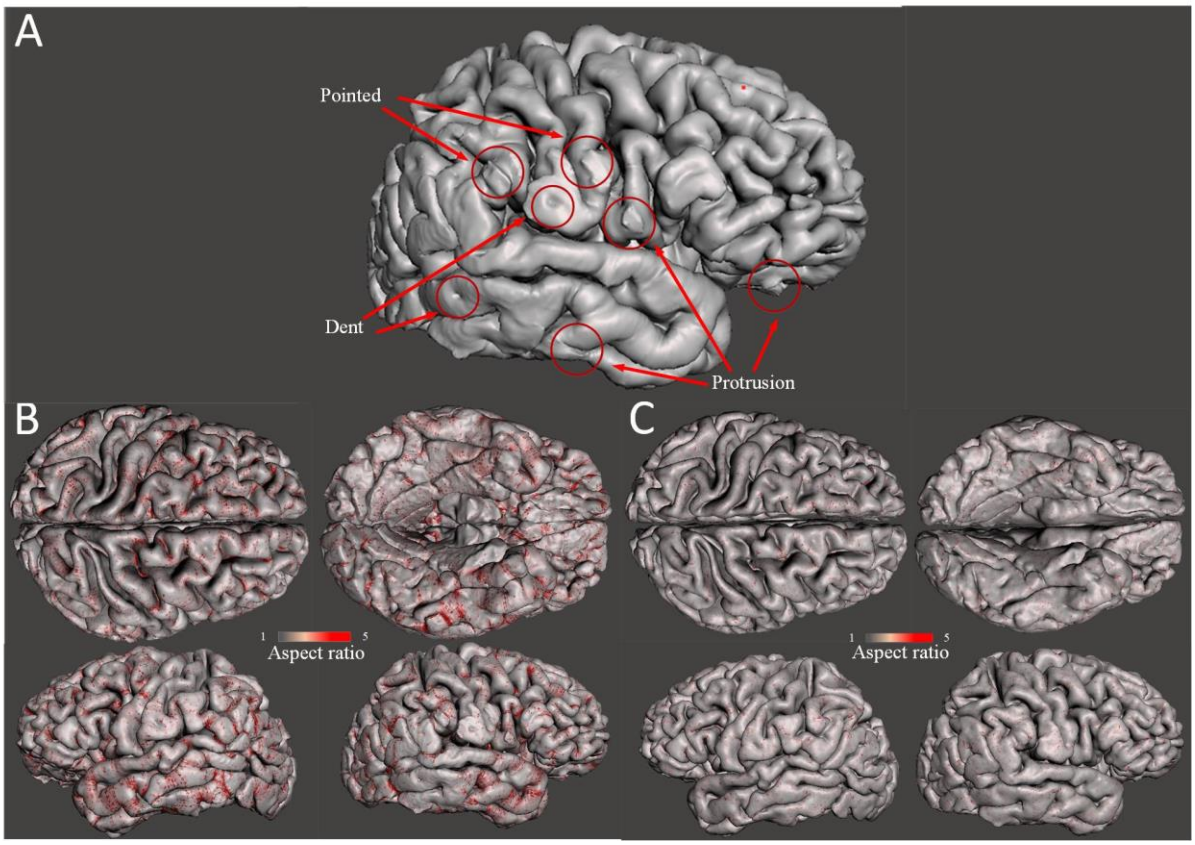

Figure 3-4 Example of disadvantaged topological features.
(A) Examples of disadvantaged topological features on pial surface meshes generated by FreeSurfer: protrusions, dents, and pointed features; An example of the spatial distribution of aspect ratio on the cortical surface mesh before (B) and after (C) the mesh postprocessing.

After postprocessing the surface meshes, to reduce computational demands, the volume below the nose of these surface meshes was removed since this volume was far away from the scalp and was not expected to have an observable influence on surface light measurements (See Figure 3-3C).

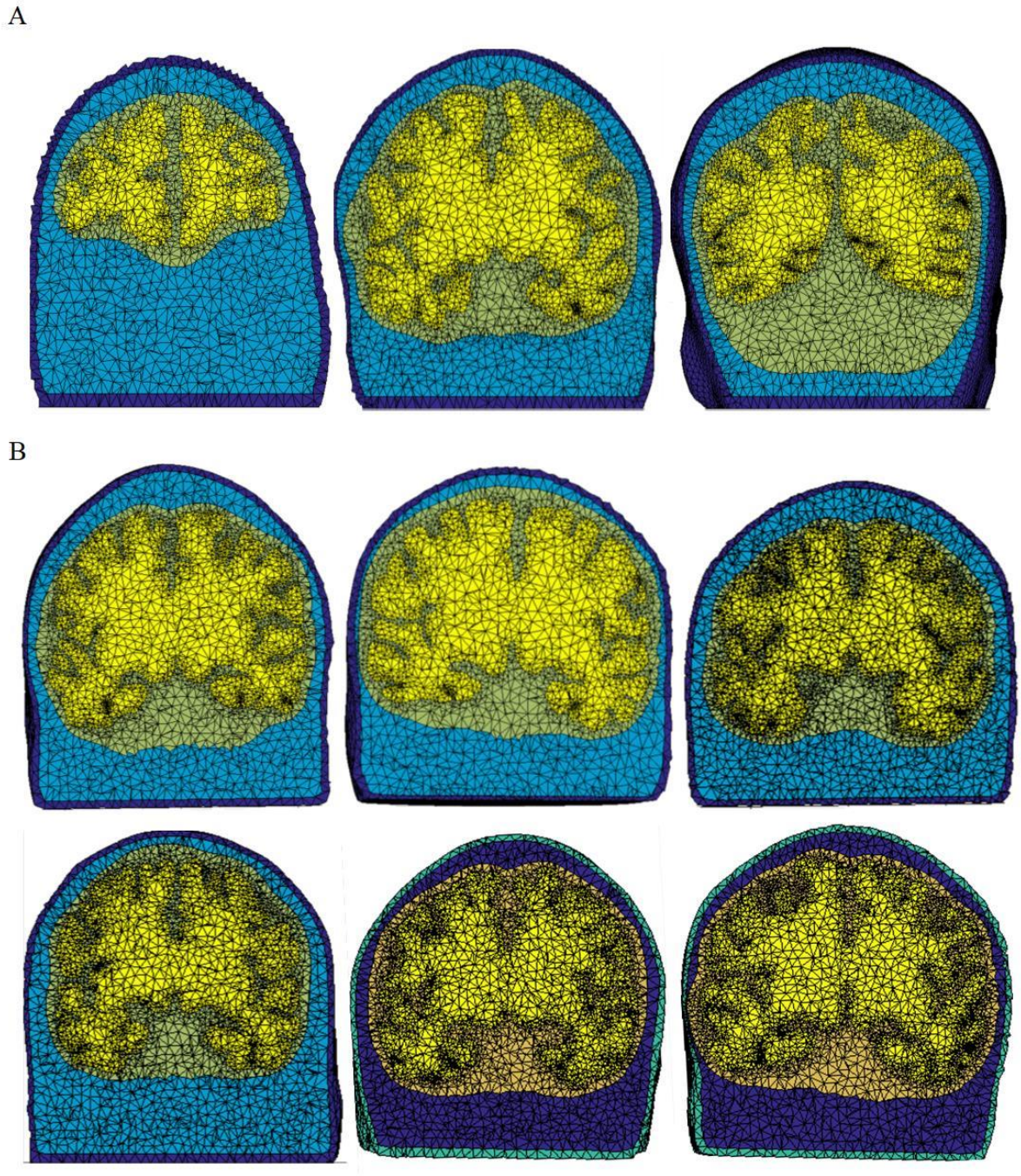

Figure 3-5 Tetrahedral head model mesh examples.
(A) coronal view of an example tetrahedral mesh of an individual with about 186 k nodes. The coronal slice is placed roughly at the (left) anterior, (middle) center, and (right) posterior parts of the head (B) more mesh examples from individuals.

Next, these participant-level surface meshes were combined and converted into a tetrahedral FEM volume mesh using the Iso2mesh toolbox. Figure 3-5 shows several FEM head models. Note that a variable size of mesh elements was used to balance the computational demands and accuracies. Specifically, large spaces (e.g., deep brain tissues) had relatively large elements, thin volumes (e.g., the scalp) had relatively small elements, and the complex brain structures (i.e., tissues close to the pial surface) had the smallest elements. This strategy resulted in FEM volume meshes with reduced mesh nodes (~100k nodes). At the same time, it maintained fine meshing near the highly convoluted pial surface across which the optical property changed dramatically between CSF and brain tissues. The preservation of the complex, convoluted cortical structures is critical in characterizing networked brain activity as only HbO, and HbR concentration changes in the vasculature of the cortical tissues are believed to be caused by neuronal electrical activity (Obrig and Villringer, 2003, Scholkmann et al., 2014).

Optical parameters for the scalp, skull, CSF, and brain tissues are then assigned according to the values from the literature. The baseline chromophore concentrations (Human head models tutorial at milab.host.dartmouth.edu/nirfast/) were assigned to the head tissues as shown in Table 3-1. These baseline concentrations were used throughout this dissertation unless otherwise stated.

Table 3-1 Baseline chromophore concentrations in the FEM model.

Tissue type	HbO (μmol/L)	HbR (μmol/L)	Scatter Amplitude	Scatter Power
Scalp	45.0	15.0	2	0.5
Skull	39.2	9.8	1.4	1.4
CSF	0.9	0.1	0.5	0.2
Brain	54.0	22.0	0.76	0.54

3.2.3 Optode co-registration

The next step in creating the FEM head model is to co-register the optode locations on the mesh. The locations of the optodes can be obtained by using a handheld digitizer such as a Polhemus electromagnetic pen (polhemus.com) or using photogrammetric-based digitizer techniques (www.ant-neuro.com/products/xensor). Alternatively, a template of 3D locations of optodes may also be used if a digitizer is unavailable or if the digitization is of poor quality. In this work, we digitized the locations of EEG electrodes, optodes, and landmarks (nasion, inion, and preauricular areas) using a handheld Polhemus digitizer. These 3D locations were co-registered onto the FEM mesh using a custom-written graphical user interface (GUI) in Matlab software (The Mathworks, Natick, MA).

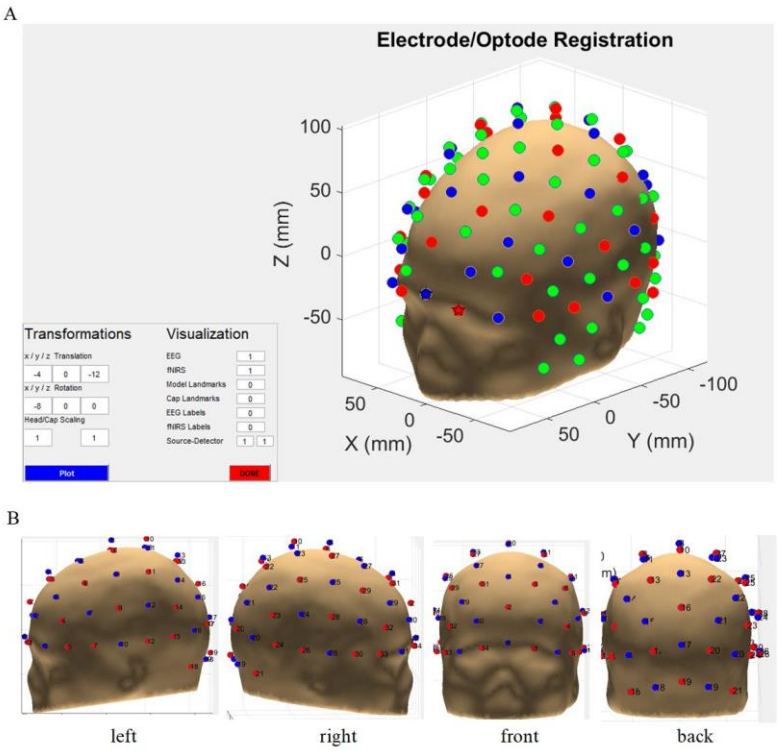

Figure 3-6 Optode co-registration.
(A) Custom-built graphical user interface for co-registering optode and electrode locations onto a FEM mesh (B) after co-registration. Only optodes are shown for the sake of clarity.

The co-registration process is semi-automatic. Firstly, the program estimates a rough orientation of the 3D points based on the landmarks. Then the operator adjusts the 3D locations making sure it fits onto the head as best as possible. Then, the 3D locations are mapped onto the scalp using a nonlinear transformation such that these locations are mapped to a point on the scalp with the shortest Euclidean distance. Figure 3-6 shows a snapshot of this GUI and an example of co-registered optodes onto the FEM mesh. The last step in the FEM mesh creation is to convert the mesh into a Nirfast-compatible spectral FEM mesh using Nirfast in-built tools.

3.2.4 Sensitivity profile of head model

The so-called sensitivity profile is a valuable method to understand which set of nodes in the FEM model provides meaningful data. Nodes with low sensitivity, e.g., deep nodes, effectively provide noise, and their data may be discarded in the analysis. To visualize the sensitivity of each FEM node to all light measurements for a specific wavelength and chromophore, the so-called sensitivity profile can be calculated from $A_{chrom,\lambda}$ in Eq. 3-2 using the following relation (Dehghani et al., 2009b):

$$J_i^{total} = \frac{\sum_{i=1}^{NM} J_{ij}}{\left(abs\left(\sum_{i=1}^{NM} J_{ij}\right)\right)_{max}} \qquad 3\text{-}4$$

where, J_{ij} is the sensitivity at node j of the FEM head model mesh due to S-D pair i for NM S-D pairs. The J_i^{total} is hence the total normalized sensitivity at each node j. In this dissertation, for the purpose of visualizations, an absolute of the numerator in Eq. 3-4 is taken and multiplied by 100 % to calculate the percentage of total normalized sensitivity, which is referred to as the sensitivity or sensitivity profile.

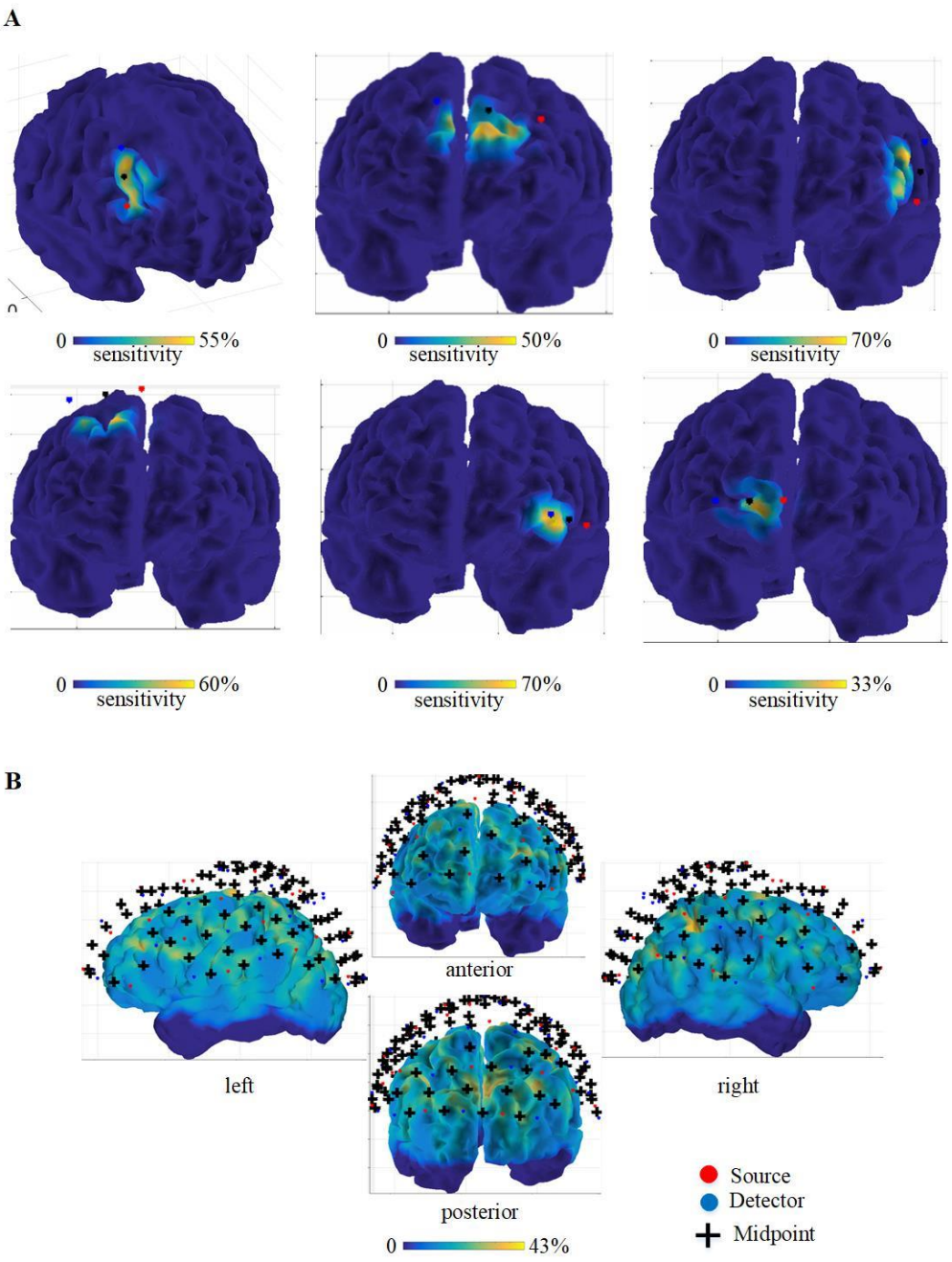

Figure 3-7 Sensitivity profile of HbO for 760 nm.
(A) Examples of sensitivity profile of single channels (B) total sensitivity profile.

Figure 3-7 shows the sensitivity profile of HbO for 760 nm wavelength for individual channels (Figure 3-7A) and all channels combined (Figure 3-7B). For individual channels, the nodes near the optodes have large sensitivities. On the other hand, nodes away from the path or deep in the

model have very low sensitivities. The overall sensitivity profile shows a brain-wide sensitivity except for ventral parts of the brain, mainly the inferior temporal cortex and the middle wall.

3.3 Inverse source reconstruction

The source domain for the inverse reconstruction, hereafter referred to as the inverse source space, was determined according to (1) the sensitivity profile (from $\boldsymbol{A}$ in Eq. 3-3), (2) the cortical structure of interest in investigating brain networks, and (3) the number of unknowns to lessen the ill-posedness of the inverse problem. Thus, the volumetric inverse sourcespace was constituted with nodes inside the brain (enclosed by the pial surface) and no deeper than 45 mm from the scalp, beyond which the sensitivity had dramatically decreased. Note that the data analyses of RSNs are performed on the cortical data projected from volumetric source data. In contrast, the use of the volumetric source space here considered the contributions of all brain tissues to the light propagation pathway. Also, note that I have used different depth criteria for different experiments and 45 mm is the maximum allowable depth. The reduction in the source space led to a reduced-size $\boldsymbol{A}$ while retaining the portion corresponding to the major cortical structures of interest. Figure 3-8 shows an example of volumetric source space defined at 40 mm from the scalp.

The reduced sensitivity matrix $\boldsymbol{A}$ was then smoothed (see Section 3.4.2). The inverse problem was solved via a minimum-norm estimate (MNE) (Bertero et al., 1988) with the Tikhonov regularization (Tikhonov, 1963, Calvetti et al., 2000) as in

$$min(\|\vec{y}(t) - \boldsymbol{A} \cdot \vec{x}(t)\|_2^2 + \lambda(t) \cdot \|\vec{x}(t)\|_2^2) \qquad 3\text{-}5$$

where the first term $\|\vec{y}(t) - \boldsymbol{A} \cdot \vec{x}(t)\|_2^2$ denotes the residual errors in fitting measurement data, $\|\vec{x}(t)\|_2^2$ is the L2 norm regularization term (Michel et al., 2004), and $\lambda(t)$ is the regularization parameter, which was estimated at each time point using the L-curve method (Hansen and O'Leary, 1993) implemented in the Regularization Tools toolbox (Hansen, 2007).

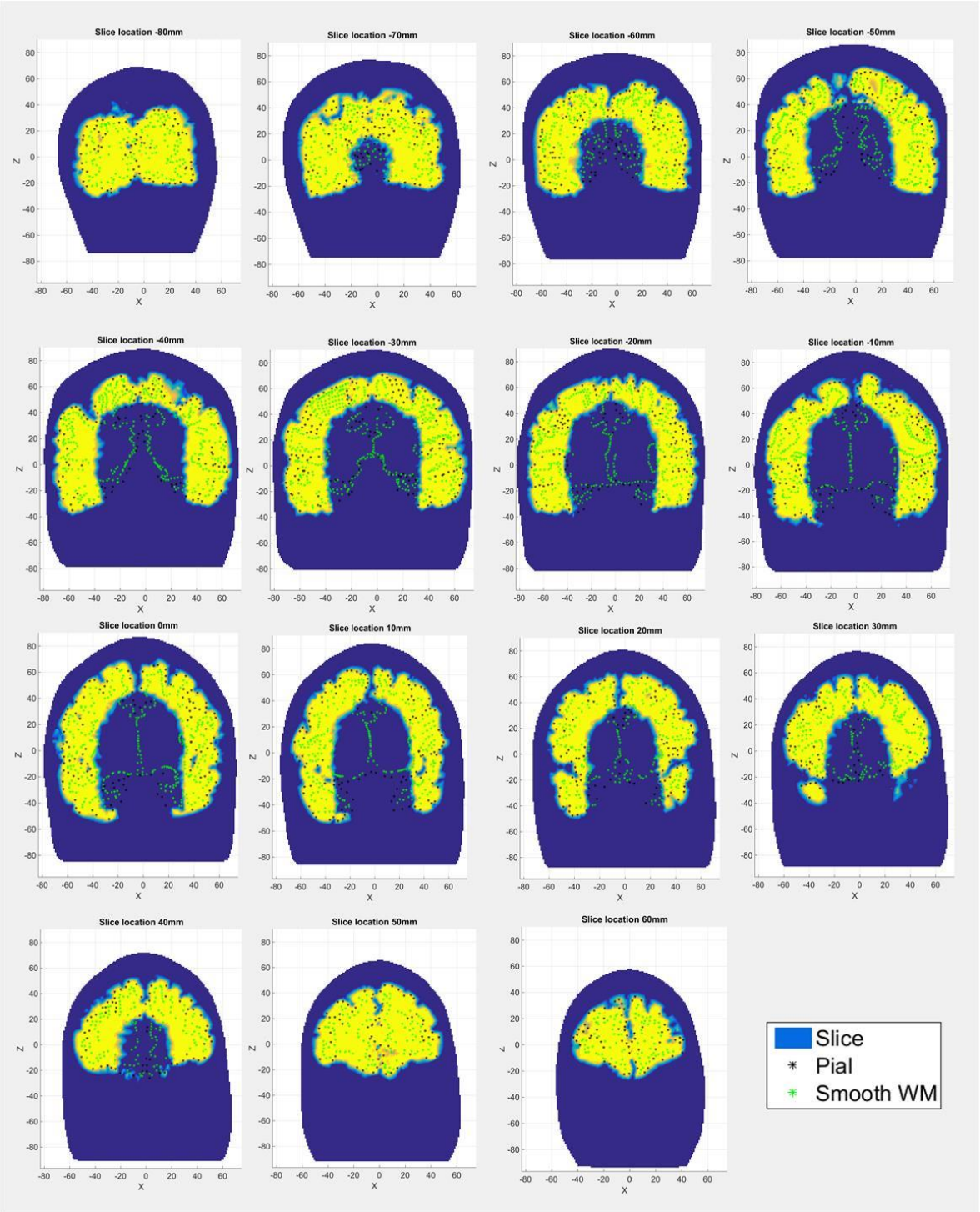

Figure 3-8 Volumetric source space of the inverse solution.

An example of volumetric source space defined at 40 mm from the scalp. Coronal slice views are shown at different locations. WM= white matter. Negative and positive slice locations represent the posterior and anterior parts of the head model respectively.

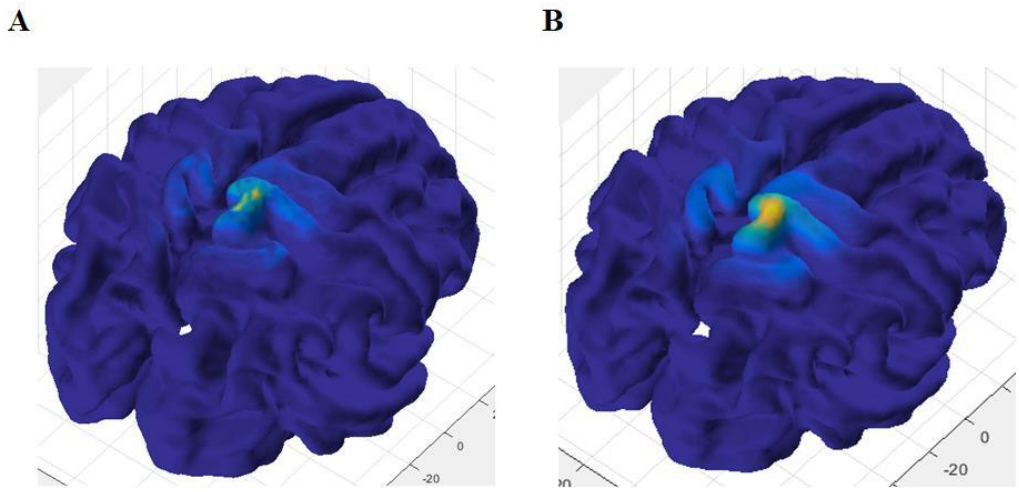

Figure 3-9 Spatial smoothing in the volumetric domain.
(A) Before and (B) after spatial smoothing. All results are projected on the interface between gray and white matter.

The minimization of Eq. 3-5 yielded the inverse solution:

$$\vec{\hat{x}}(t) = \boldsymbol{A}^T(\boldsymbol{A} \cdot \boldsymbol{A}^T + \lambda(t) \cdot \boldsymbol{I})^{-1}\vec{y}(t) \qquad 3\text{-}6$$

where $\boldsymbol{I}$ is the identity matrix and the inverse solution $\vec{\hat{x}}(t)$ is a vector of joint estimates of HbR and HbO concentration changes relative to the baseline concentrations. These volumetric data are spatially smoothed using a spherical kernel (6 mm diameter). Figure 3-9 shows the effect of spatial smoothing on a localized DOT reconstruction in volumetric space.

To prepare for group-level SICA (gSICA) analysis (Section 3.5), inverse volumetric data $\vec{\hat{x}}_k(t)$ of individuals from Eq. 3-6 are firstly mapped to individual cortical surfaces (interface between the gray and white matter) as only HbO and HbR concentration changes close to the gray matter are believed to reflect neuronal activity (Obrig and Villringer, 2003, Scholkmann et al., 2014), and definitions of fMRI RSNs have been reported mainly on the cortical surface as well (Desjardins et al., 2001). The projection is performed by assigning data on the nearest FEM source node in the inverse source space to each node on the cortical surface. Cortical source space was

defined by keeping nodes on the cortical surface within a certain depth from the skin. Nodes deeper than this depth are assigned a value of zero.

Similar to fMRI RSN studies (Desjardins et al., 2001), the global signal as a function of time is calculated by spatially summing projected data over the cortical surface for each participant and then regressed out from time courses of individual cortical nodes.

3.4 Processes in controlling numerical errors

The proposed BW-DOT is a complex multi-step framework that involves large-scale numerical calculations, i.e., FEM forward light modeling and inverse reconstructions, etc. The numerical accuracy of its outcome, i.e., RSNs, is dependent on the quality of data, e.g., inverse reconstructions sensitive to recording noises, and selected parameters, e.g., FEM shapes/sizes for FEM (Eggebrecht et al., 2012) and regularization parameters for inverse calculations (Eggebrecht et al., 2014), at each step of the framework. Thus, we have developed multiple processes to control their qualities. These processes are integrative parts of the entire framework and the computational algorithms discussed in Sections 3.4.1- 3.4.3.

3.4.1 Removal of non-neuronal signals

Non-neuronal signals in fNIRS measurements include superficial scalp responses (Saager and Berger, 2005) and systematic physiological fluctuations, i.e., cardiac pulsation, blood pressure, respiration, autonomic nervous system activity, and body movements (Kirilina et al., 2013, Tachtsidis and Scholkmann, 2016, Schecklmann et al., 2017), which could potentially impact the accuracy of the proposed framework. For example, signals generated by extracerebral tissues (e.g., the scalp) could be forcibly projected onto the cerebral tissues during the inverse source reconstruction, and these non-neuronal signals mean more fluctuations that potentially violate the assumption behind Eq. 2-10 (i.e.,$\Delta\mu_a \ll \mu_{a,base}$).

Considering that non-neuronal signals exhibit global spatial patterns due to systematic physiological fluctuations and regional modulations due to the downstream effect from heterogeneously distributed blood flows (Kirilina et al., 2013, Schuenke et al., 2007) and relatively localized facial muscles activity (Schecklmann et al., 2017, Novi et al., 2020), we adopted a revised version of our previously developed fully-automatic denoising procedure, named principal-component-analysis-based general linear model (PCA-GLM) (Zhang et al., 2019), for the cap-based whole-head high-density fNIRS recordings. We used auxiliary sensors for breath, motion, and pulsation to capture physiological activity and eight SS channels (IOD: 8 mm) distributed across the scalp to capture superficial activity. PCA was applied to OD data from long-separation (LS) channels (mean IOD: 3.65 ± 0.44 cm). The spatial uniformity of each PCA component was assessed by the metric of coefficient of spatial uniformity (CSU) (Kohno et al., 2007). A principal component of LS channels (PC-LS) with the highest CSU was identified, which was believed, based on the spatial pattern, to represent contributions in OD data mostly from non-neuronal signals. However, the time course of PC-LS was not directly removed from LS data, as in PCA filtering (Zhang et al., 2005), since neuronally-relevant responses with global spatial patterns have been reported in hemodynamic signals from fMRI studies (Chen et al., 2020a). Instead, the PC-LS was used to identify a component from the SS channels, which was believed to be only sensitive to responses from superficial tissues (Saager and Berger, 2005). Specifically, PCA was applied to OD data from SS channels, and then the principal component (PC-SS) with the highest temporal correlation with PC-LS was defined as the global activity generated by extracerebral tissues. The time course of PC-SS and filtered auxiliary recordings (i.e., acceleration, respiration, cardiac pulsation), together with a third-order polynomial drift, were used as regressors in a GLM to remove non-neuronal signals and instrumental noises in data from LS channels.

3.4.2 Conditioning of Jacobian matrices

While the postprocessing pipeline has been developed to improve the quality of FEM meshes (Section 3.2.2), certain resultant tetrahedral FEM mesh elements could still be of poor quality, e.g., of high aspect ratios. Such elements can cause abnormally large-value entries in the Jacobian matrix $\boldsymbol{A}$ (Eq. 3-3), leading to estimation errors in the inverse solution (Eq. 3-6). Figure 3-10 illustrates an example of large values in a jacobian despite performing post-processing on the surface meshes required to create the FEM head model (see Section 3.2.2). These values were located in a region rather than being dispersed around the head model, possibly indicating the presence of poor tetrahedral elements. The values of these elements are shown in Figure 3-10B. Thus, the matrix $\boldsymbol{A}$ was conditioned using local smoothing since, usually, only a few abnormal entries in individual Jacobian matrices exist. Specifically, Jacobian entries greater than a threshold determined from the histogram were spatially smoothed using the mean operation over a spherical kernel of size 5 mm (increased to 7 mm if no neighboring elements were not found within the kernel of 5 mm). Then, all smoothed jacobian values greater than the threshold were given the threshold value, for example, 5 in Figure 3-10C. Figure 3-10D shows that only a fraction of the original jacobian entries was thresholded at 5.

3.4.3 Temporal smoothing of the regularization parameters

Implementing the L-curve method (Hansen and O'Leary, 1993) to estimate the regularization parameter in Eq. 3-6 involves repeating matrix inversions in Eq. 3-6 and numerically searching for corners L-curves, both of which are not immune from numerical errors. After computing $\lambda(t)$ values using the Regularization Tools toolbox (Hansen, 2007), the estimated $\lambda(t)$ values may contain outliers. These outlier values must be smoothed to avoid more outliers from appearing in the subsequent numerical calculations. Different smoothing strategies were tested to correct these

outliers, including moving average, local linear regression (loess() and lowess() functions in Matlab and use first degree and second-degree polynomial fits, respectively), and robust linear regression (rlowess() function in Matlab). Thus, we smoothed the regularization parameters from individual participants using the robust linear regression (Harrell, 2015) using Matlab's smooth() function with a span of 5, i.e., the number of data points for calculating the smoothed value.

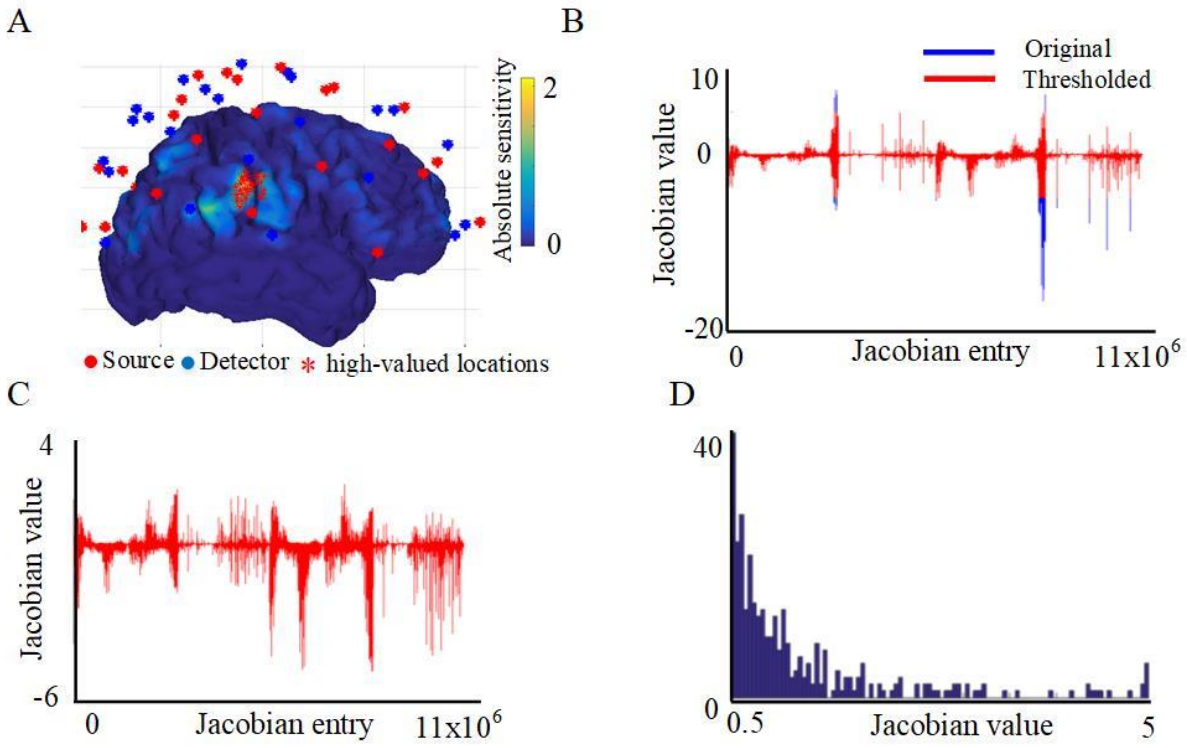

Figure 3-10 Jacobian conditioning example for an example FEM mesh.
(A) Locations of 39 high value of a jacobian greater than 5, projected on the pial surface. Sensitivity profile of HbO is overlaid on to the pial surface (B) a plot of vectorized jacobian (C) a plot of vectorized jacobian after smoothing (D) histogram of absolute jacobian values greater than 0.5.

3.5 Group-level spatial ICA for pattern recognition

At this point, we have a timeseries of HbO and HbR concentrations changes relative to the baseline concentrations defined on the cortical surface from different participants (Section 3.3). The next step is to find spatiotemporal patterns in these timeseries data using the ICA approach,

as detailed in this section. The ICA approach has been shown to outperform the SCA method in an fNIRS RSN study in terms of sensitivity and specificity, especially in the presence of large noise (Zhang et al., 2010). Thus, the selection of ICA is suitable for the cap-based optode placement configuration used in this dissertation, which lacks uniform sensitivity and has increased noise compared to a high-density DOT patch-based optode configuration.

ICA is a linear transformation of data that maximizes the independence and non-gaussianity of its components (Comon, 1994). In a typical ICA analysis, the N linear data mixtures $[x_1, x_2, \dots x_N]$ are assumed to be a linear mixture of N independent components (ICs):

$$x_j = a_{j1}s_1 + a_{j2}s_2 + a_{j3}3 + \cdots + a_{jn}s_N, \text{ for all j.} \quad 3\text{-}7$$

Eq. 3-7 can be written in a matrix notation as:

$$X = A.S \quad 3\text{-}8$$

where the ICs in S linearly mix according to the weights defined in the so-called mixing matrix A to generate the data mixture X. Eq. 3-8 is called the ICA model. It is a generative model in the sense that it describes how the observed data X are generated by the mixing of ICs. Note that it is assumed that X and S are zero-mean. If they are not, then they can be zero-centered by subtracting their respective means. The problem of the ICA is thus to find A which can then be used to find $\hat{S}$ i.e., an estimate of the true sources in S. This can be written as:

$$\hat{S} = W.X \quad 3\text{-}9$$

where the unmixing matrix W is the inverse of the mixing matrix, i.e., $W = A^{-1}$. Note that (1) there must be at least N number of observations where N is the number of ICs, (2) the ICs need to

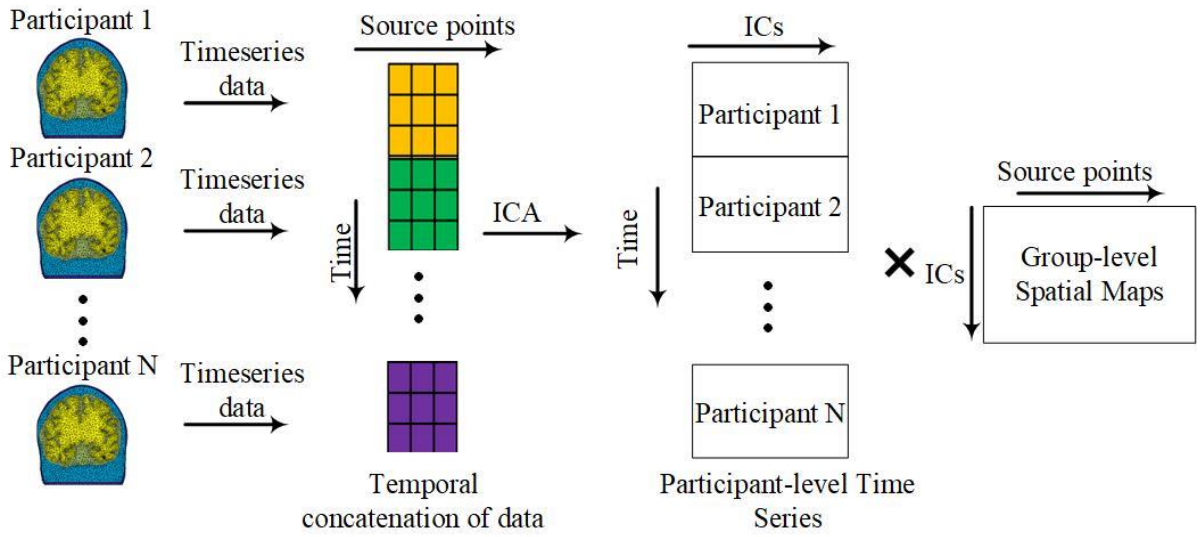

Figure 3-11 Schematic diagram of group-level spatial ICA.

be non-gaussian but not their mixtures, (3) there is a sign, variance, and order ambiguity in $\hat{S}$ since both $\hat{S}$ and W are estimated.

Typically, functional neuroimaging experiments (including experiments in this dissertation) involve the analysis of several participant data. This leads to the use of gSICA, which performs ICA on several participant data simultaneously (Calhoun et al., 2009). A general schematic of gSICA is shown in Figure 3-11. First, the observed data (obtained in Section 3.3) are temporally concatenated along a common spatial dimension (Schmithorst and Holland, 2004), yielding a two-dimensional (2D) matrix as shown in Figure 3-11. Although there are different methods of concatenations (see Calhoun et al. (2009) for a review), the temporal concatenation of individual participant data works well with fMRI data since there are greater temporal variations than spatial variations (Schmithorst and Holland, 2004). It has been used widely in gSICA of fMRI data (Calhoun et al., 2009). Since the spatiotemporal dimensions of fMRI data are similar to fNIRS data, we have used temporal concatenation in gSICA of fNIRS data in our previous study (Khan et al., 2021) and throughout this dissertation.

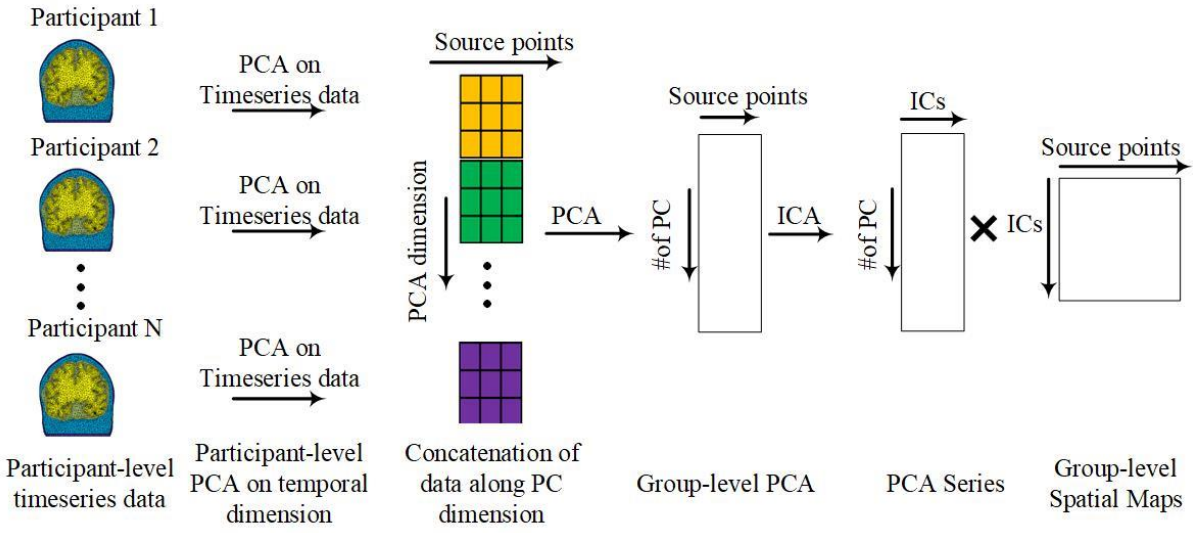

Figure 3-12 Schematic diagram of group-level spatial ICA with PCA reduction.

Following the data concatenation, the 2D matrix is decomposed into its constituent spatiotemporal components as in Eq. 3-9 (Figure 3-11). Specifically, each spatial component, i.e., spatial IC (a row vector in $\hat{S}$ in Eq. 3-9) represents the cortical map of brain activities as a network of mutually dependent source nodes at the group level. The spatial ICs can be normalized in the spatial dimension using a z-score to minimize inter-IC spatial variations. Moreover, the temporal component, i.e., each temporal IC (a part of the column vector in A in Eq. 3-9), represents an IC time course of an individual participant. The gSICA can also be performed using PCA on individual data in the temporal domain prior to the data concatenation and after concatenation to reduce the computational load (Calhoun et al., 2009, Erhardt et al., 2011), as illustrated in Figure 3-12. This data reduction avoids overlearning, which otherwise can be observed in ICA (Hyvärinen et al., 1999).

In the BW-DOT framework, gSICA analysis (Calhoun et al., 2009) is performed on the mapped surface data $\vec{\hat{x}}_k(t)$ in Eq. 3-6 (Figure 3-1) where k represents a participant. Firstly, the data $\vec{\hat{x}}_k(t)$ from individuals are normalized (in the temporal domain) using z-score to minimize

inter-participant variations. Secondly, PCA (with the dimension of 40) is applied to temporal data from individuals to reduce the computational load. Then, data from individuals are temporally concatenated along the dimension of principal components yielding a group-level 2D source matrix X. Lastly, the FASTICA algorithm (Hyvarinen, 1999) from the EEGLAB toolbox (Delorme and Makeig, 2004) was applied to X as in Eq. 3-9, where each component in $\hat{S}$ represents the estimated cortical maps of brain activities as a network of mutually dependent source nodes in the FEM mesh head model. The matrix $\hat{S}$ is normalized in the spatial dimension using a z-score to minimize inter-IC spatial variations.

3.6 Spatiotemporal regression

The next step in the BW-DOT is a back-projection step performed on the gSICA ICs to estimate participant-level spatiotemporal ICs (Calhoun et al., 2001, Calhoun et al., 2008). This back-projection is done via the so-called spatiotemporal regression (STR), which uses least-squares via a two-step multi-regression method to estimate participant-level spatiotemporal ICs (Beckmann et al., 2009). Specifically, first, the participant-level timeseries T_k (k is a participant) are calculated as:

$$T_k = \vec{\hat{x}}_k \hat{S}^{-1} \tag{3-10}$$

where, $\vec{\hat{x}}_k$is a participant's timeseries data and $\hat{S}^{-1}$ is the inverse of $\hat{S}$ which contains the estimated group-level spatial maps. In the second step, the participant-level spatial maps S_k (k is a participant) are calculated as:

$$S_k = {T_k}^{-1} \vec{\hat{x}}_k \tag{3-11}$$

Note that since $\hat{S}$ and T_k are non-square, I have used MATLAB's Moore-Penrose pseudoinverse function i.e., pinv() to calculate ${TC_k}^{-1}$ in Eq. 3-11.

3.7 Statistical correlation tomography

The fNIRS and DOT technologies have an inherent problem of being superficial (Dehghani et al., 2009b). To make matter worse, it has been well documented that inverse solutions based on a minimum norm estimation (Section 3.3) favor superficial source reconstructions (Pascual-Marqui, 1999). To improve the depth issue, recently, a technique called statistical correlation tomography (SCT) was described and implemented on EEG source imaging data (Li et al., 2018) that makes use of correlation analysis (Yuan et al., 2016). This technique efficiently minimizes the effect of magnitude-causing superficial source reconstructions and leads to the recovery of RSNs in relatively deep cortical structures, e.g., PCC. SCT has been shown to be more effective than the weighting matrix of ICA at defining large-scale EEG RSNs with high spatial resolution and similarity to fMRI RSNs (Li et al., 2018). SCT was used as the next step in the BW-DOT framework.

First, correlation coefficients (CC) between an IC time course $\vec{T}_k(t)$ and a source node time course $\vec{\hat{x}}_k(t)$ was calculated at lag zero for individual participants:

$$CC_k(j,n) = corr\left(\vec{\hat{x}}_k(j,t), \vec{T}_k(n,t)\right), j = 1,\ldots,20; n = 1,\ldots,\mathrm{N}_{sourcespace} \qquad 3\text{-}12$$

where $\mathrm{N}_{sourcespace}$ denotes the total number of nodes in the source space (see Section 3.3). Secondly, Fisher's Z-transform (Fisher, 1915) was applied to CC values to obtain z-values as:

$$z_k(j,n) = \frac{1}{2} ln\left(\frac{1 + CC_k(j,n)}{1 - CC_k(j,n)}\right) \qquad 3\text{-}13$$

where, $z_k(j,n)$ has a normal distribution with zero expectation and variance $1/(df - 3)$, where df is the effective degrees of freedom (DOF) and is equal to the sample size under the assumption of independence (Bartlett, 1946). This assumption of independence is often not met in the presence of autocorrelated time series (Friston et al., 1994), and the DOF must be

corrected. Our experience was that these autocorrelations were high in the reconstructed DOT data. Hence, the DOF was corrected as follows. The autocorrelations of $\vec{T}_k(t)$ and $\vec{\hat{x}}_k(t)$ were calculated as, i.e., ρ_C and ρ_T, respectively, and were used to correct the z-values from Eq. 3-13 using the approximation {Valencia, 2009 #839} :

$$N_k'(j,n) \approx \frac{N_k(j,n)}{1 + 2\sum_{\tau=1}^{N_k(j,n)-1} \rho_C(j,n)(\tau).\rho_T(j,n)(\tau)} \quad 3\text{-}14$$

where $N_k(j,n)$ is the number of time points (Valencia et al., 2009) for participant k and IC j at node n and τ is lag. All z-value maps for all time points and participants were then individually smoothed using the heat kernel with FWHM of 6 mm (Chung et al., 2005, Chung et al., 2010). These smoothed z-values were converted to a z-score (Vincent et al., 2007a) as:

$$\bar{z}_k(j,n) = \frac{z_k(j,n)}{\sqrt{N_k'(j,n) - 3}} \quad 3\text{-}15$$

The group-level z-score maps were then calculated using (Silver and Dunlap, 1987, Alexander, 1990):

$$\bar{z}_{group}(j,n) = \frac{\sum(N_k'(j,n) - 3) \cdot z_k(j,n)}{\sum(N_k'(j,n) - 3)} \quad 3\text{-}16$$

These group-level SCTs were thresholded (at $p < .01$) using t-tests on z-scores from individual nodes with participants as samples, which resulted in thresholded spatial maps that define DOT-derived cortical RSNs (d-RSNs) for both HbO and HbR chromophores.

3.8 Summary and discussion

A new computational framework of DOT is proposed, termed BW-DOT, for reconstructing resting-state brain networks based on near-infrared spectroscopy with a cap-based whole-head optode montage. It is noted that DOT RSN studies have either used high-density optode patches with small FOV (White et al., 2009) or sparsely placed optodes for a relatively large FOV

(Franceschini et al., 2006). One recent work has reported a circular montage covering the sides and back of the head to provide high-density optode placements and large FOV at the same time to achieve spatial resolution at the level of a gyrus fold (Eggebrecht et al., 2014). Their optode montage, however, still does not cover the entire scalp, particularly the anterior and dorsal parts of the scalp. In the present study, we used a cap-based optode montage that covers almost the entire scalp while still providing sufficiently high spatial (73 optodes with IOD of 3.65 ± 0.44 cm) and temporal resolution (6.25 Hz) (Khan et al., 2019) to reconstruct multiple brain-wide RSNs simultaneously. Beyond providing a brain-wide FOV to map distributed brain function, another reason to adopt whole-head cap-based optode montages is to standardize the recording montage of the DOT RSN imaging modality. Specifically, obtaining time-series data from standard locations on the scalp provides an opportunity to integrate datasets from different researchers for analysis that promotes data sharing and increases statistical power for discoveries (Biswal et al., 2010).

In theory, a high-density DOT system has superior imaging metrics (i.e., point spread functions, localization error, and spatial resolution) than a sparse DOT system (Wheelock et al., 2019, Fishell et al., 2020) (see Chapter 4). It should, however, be noted that having a high-density cap that covers the entire scalp raises critical technical challenges and requires many trade-offs. For example, an extension of high-density DOT from a regional patch to the entire scalp could inevitably cause significantly increased bulk mass on the head of participants, a non-trivial experimental logistical problem. This can also potentially increase the scalp temperature (Bozkurt and Onaral, 2004), which increases blood flow to the scalp (Guyton, 2000) and non-neuronal hemodynamic signals into fNIRS recordings. Moreover, a large number of optodes decrease the portability of data acquisition equipment and increase experimental preparation time. Irregular

head shapes also raise difficulties in keeping the inter-optode distance constant over the entire scalp, which could impact the superior imaging metrics that have been demonstrated in patch-based systems (Wheelock et al., 2019). Achieving the whole-head coverage with high-density placements further leads to possibly reduced temporal sampling rate as more optical sources need to be excited, and close distances between sources inevitably worsen optical interference if turned on simultaneously. Keeping these challenges in view, in our resting-state study, we selected a LED fNIRS system with 34 sources, 31 detectors, and 8 SS detectors that led to 109 long channels and 8 SS channels, a number similar to electrodes in a typical high-density EEG source imaging system (Yuan et al., 2016). In order to achieve a high sampling rate to effectively avoid aliasing effects in fNIRS data (see Section 3.4.1), we used parallel source illumination for those sources that were far apart (greater than 9 cm), which led to a sufficient temporal sampling rate at 6.25 Hz. Furthermore, in contrast to the HD patch-based optode placement, which has SS optodes naturally integrated into high-density systems (the smallest IOD: 1.3 mm) (Eggebrecht et al., 2014), our optode cap used dedicated SS channels to record signals for rejecting non-neuronal signals (see 3.4.1 and below for more discussions). Despite these challenges, the BW-DOT can still reconstruct brain-wide RSNs (Chapter 5) using the whole-head cap-based system. We attribute this ability of BW-DOT to several methodological innovations discussed below to counteract trade-offs made on measurements.

The proposed framework mainly utilizes a data-driven approach (i.e., ICA) for pattern recognition of RSNs, which is not dependent on the selection of seed locations and simultaneously reconstructs multiple RSNs. The ICA approach has been shown to outperform the seed-based correlation method in an fNIRS RSN study in terms of sensitivity and specificity, especially in the presence of large noise (Zhang et al., 2010). Thus, the selection of ICA is suitable for the cap-

based optode placement configuration that lacks uniform sensitivity and has increased noise as compared to a high-density DOT patch-based optode configuration. It has been well documented that inverse solutions based on minimum norm estimation favor superficial source reconstructions (Pascual-Marqui, 1999). Therefore, we have further supplemented ICA with a correlation analysis (Yuan et al., 2016) to create SCT (Li et al., 2018). This efficiently minimizes the effect of magnitude-causing superficial source reconstructions and leads to the recovery of RSNs in relatively deep cortical structures, e.g., PCC (Chapter 5). The same SCT has been shown to be more effective than the weighting matrix of ICA at defining large-scale EEG RSNs with high spatial resolution and similarity to fMRI RSNs (Li et al., 2018). Furthermore, because the oscillatory behavior nature of fNIRS data leads to high autocorrelation in data, the reconstructions of DOT d-RSNs are susceptible to false cross-correlations caused by autocorrelation (Woolrich et al., 2001, Roy et al., 2008). Thus, correction on cross-correlations due to these autocorrelations is also implemented in the SCT framework.

It has been suggested that hemodynamic signals originating from extracerebral tissues can elicit spatial patterns that resemble putative RSNs in fMRI (Chen et al., 2020a). For DOT, non-neuronal signals raise even more challenges. Specifically, the hemodynamic signals generated from extracerebral tissues (e.g., the scalp) may forcibly be projected onto the cerebral tissues during inverse source reconstruction. Consequently, these additional signal fluctuations riding on top of neuronal signals could potentially violate the basic assumption behind Eq. 2-10 (i.e.,$\Delta\mu_a \ll \mu_{a,base}$). Therefore, removal of non-neuronal signals before the inverse step is critical for the proposed framework, especially for the whole-head high-density systems, as discussed above.

In DOT RSN studies, typically, a combination of temporal filtering and GLM-based SS signal regression is used to remove non-neuronal signals (Wheelock et al., 2019). Temporal filtering,

typically bandpass filtering (Pinti et al., 2019), is effective in removing high-frequency noises, e.g., cardiac pulsation (0.8-1.6 Hz) and respiration (0.2-0.6 Hz), but is not effective in removing non-neuronal signals mixed with neuronal signals in the same frequency bands, i.e., low-frequency oscillations (0.04-0.2 Hz) and very-low-frequency oscillations (0.01-0.04 Hz) (Stefanovska et al., 1999, Tong et al., 2011). A spatial filter, i.e., PCA, has been used to separate non-neuronal components from neuronal components. In contrast, it has been suggested that the methodology is prone to over-remove useful signal components that result in a reduction of activations in task data (Zhang et al., 2005, Zhang et al., 2016, Boas et al., 2004). On the other hand, GLM using signals from SS channels with IOD less than 1.5 cm as regressors has been demonstrated to be effective in removing non-neuronal signals generated by extracerebral tissues like the scalp (Saager and Berger, 2005, Gagnon et al., 2011, Gagnon et al., 2012). It is known that blood flow in the scalp tissues is heterogeneously distributed (Schuenke et al., 2007). Therefore, assuming heterogeneous scalp hemodynamics in GLM could result in more effective removal of non-neuronal signals (Wyser et al., 2020). In the present framework, we have implemented eight dedicated optodes as SS channels (Sato et al., 2016) distributed symmetrically across the scalp to estimate global non-neuronal components with slow spatial variations. These optical channels were placed strategically to capture the heterogeneity of the scalp hemodynamics by targeting the superficial blood vasculature (e.g., superior temporal and occipital arteries/veins). Furthermore, auxiliary data from peripheral sensors and 3rd-order-polynomial drift were used to filter out non-neuronal signals related to systematic variations. Note that ICA could further identify residual non-neuronal noise in the BW-DOT framework as the ICA algorithm is inherently sensitive to the pattern of noise (Zhang et al., 2010).

The strategies to compensate trade-offs in recordings also involve other computation-intensive

approaches, including FEM modeling to accurately model head volumes for light propagation, especially the highly convoluted pial structure to maintain the accuracy of the diffusion approximation; spectrally-constraint approach for calculating Jacobian matrices concurrently for HbO and HbR; and L-curve method for regularization parameter selections. All of these approaches, together with ICA, SCT, and GLM discussed above, collectively form the proposed framework, leading to the reconstruction of multiple brain-wide RSNs. An important characteristic of these computation-intensive processes is that they are vulnerable to numerical errors. Since numerical errors usually generate sparse but abnormally large artifacts in data and could be amplified during the data flow of the analysis pipeline, processes in managing numerical errors are thus an integrative part of our proposed framework. These processes include quality control of FEM meshes, conditioning of Jacobian matrices, and conditioning of regularization parameters.

4. Evaluation of BW-DOT using simulation and experimental data

This chapter has been adapted from the following peer-reviewed publications:

Khan, A. F., Fan Zhang, Han Yuan, Lei Ding. "Brain-Wide Diffuse Optical Tomography Based on Cap-Based, Whole-Head fNIRS Recording," 43rd EMBC, virtual, Oct-Nov 2021.

Khan, A. F., Fan Zhang, Han Yuan, Lei Ding. "Dynamic Activation Patterns of the Motor Brain Revealed by Diffuse Optical Tomography," 41st International EMBC, Berlin, Jul 23-27, 2019.

4.1 Introduction

The ground truth eliciting the observed resting-state brain activity is typically unknown. Functional neuroimaging technologies intended to study resting-state brain activity are typically validated against carefully designed stimuli that elicit known brain responses. Therefore, once it is determined that a DOT system can accurately reconstruct a putative cortical activity, one can assume that the same system can also accurately reconstruct resting-state brain activity. For example, to test their patch-based DOT system in reconstructing distributed brain activity, Eggebrecht et al. (2014) evaluated their system against tasks including hearing words, covert reading, and imagined reading. These tasks elicited brain responses well-reported in the fMRI literature and provided confidence that their DOT system was also capable enough to reconstruct resting-state brain activity accurately. Similarly, other DOT systems were tested using, for example, stimulation of the visual (Zeff et al., 2007) and motor (Koch et al., 2010, Habermehl et al., 2012) cortical areas in which they accurately reconstructed brain activity in the visual and motor cortices respectively. Using a similar approach, known ground truths were used to evaluate the spatiotemporal resolution of the BW-DOT framework using simulated and experimental data in this chapter.

4.2 Methods

4.2.1 DOT reconstructions using simulated fNIRS data

A four-layer FEM head model for the simulation-based experiments was used (see Section 3.2.2). This model was obtained using the procedure described in Chapter 3 to an MRI structural image of Bert, a fictitious participant, available from FreeSurfer tissue segmentation software. The head model consisted of 100,942 nodes and 597,605 tetrahedrons. Figure 4-2B shows a coronal slice view of this head model, illustrating the tetrahedral elements representing four tissues, including scalp, skull, CSF, and brain. Each tissue region of the head model was assigned baseline optical properties and chromophore concentrations as in Table 3-1. The optode cap co-registered (see Section 3.2.3) on the head model (Figure 4-2A) consisted of 34 sources, 31 detectors distributed across the entire scalp (IOD mean: 3.65 ± 0.44 cm, mode: 2.98 cm, min: 2.98 cm, max: 4.56 cm). This configuration of the optodes was also used in the actual fNIRS experiments.

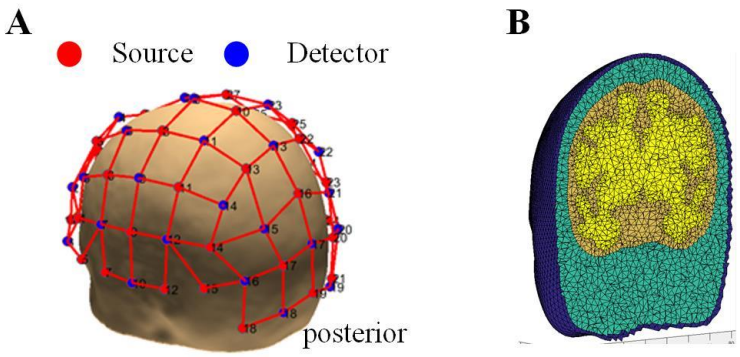

Figure 4-1 A realistic head geometry for evaluation of BW-DOT.
(A) PSF-based metric definitions (B) cap-based optode montage Figure adapted from Khan et al. (2021).

The Jacobian (see Section 3.4.2) was calculated using Nirfast software. The DOT forward model (see Section 3.2) was run to obtain the baseline optical fNIRS data for each wavelength separately (760 nm and 850 nm). Note that these baseline data correspond to the denominator in the OD term in Eq. 3-1. Different values of OD are then obtained by inducing relative changes to

the chromophore concentrations at different locations in the brain and running the forward model. Using the OD and Jacobian, the inverse solution (see Section 3.3) was calculated to jointly estimate the changes in the concentration of HbO and HbR relative to the baseline concentrations.

Three simulation-based experiments were performed and are presented here in order of increasing complexity. In the first experiment, a localized (sphere of 3 mm diameter) change of -6.5% in the concentration of HbO on the right motor cortex (Figure 4-5A) was induced, and the fNIRS optical data were calculated. Then the inverse solution was estimated, i.e., the change in the concentration of HbO relative to the baseline concentrations.

In the second experiment, HbO and HbR concentration changes relative to the baseline concentrations, following physiologically reasonable-valued temporal waveforms, were induced, as shown in Figure 4-6A. The simulated optical fNIRS data were calculated for each time point, followed by the inverse solution to estimate the change in the concentration of HbO and HbR relative to the baseline concentrations. In the third experiment, a localized (sphere of 3 mm diameter) change of a +10% and -10% in HbO and HbR concentration, respectively, was induced at 2879 locations in the brain. These testing locations were distributed randomly, and their projections on the cortical surface are shown as red dots in Figure 4-2B. The forward model for concentration change at each test location was run, thus obtaining 2879 whole-head fNIRS optical data measurements for each wavelength. The inverse solution was then calculated to estimate the change in the concentration of HbO and HbR relative to the baseline concentrations for each location separately.

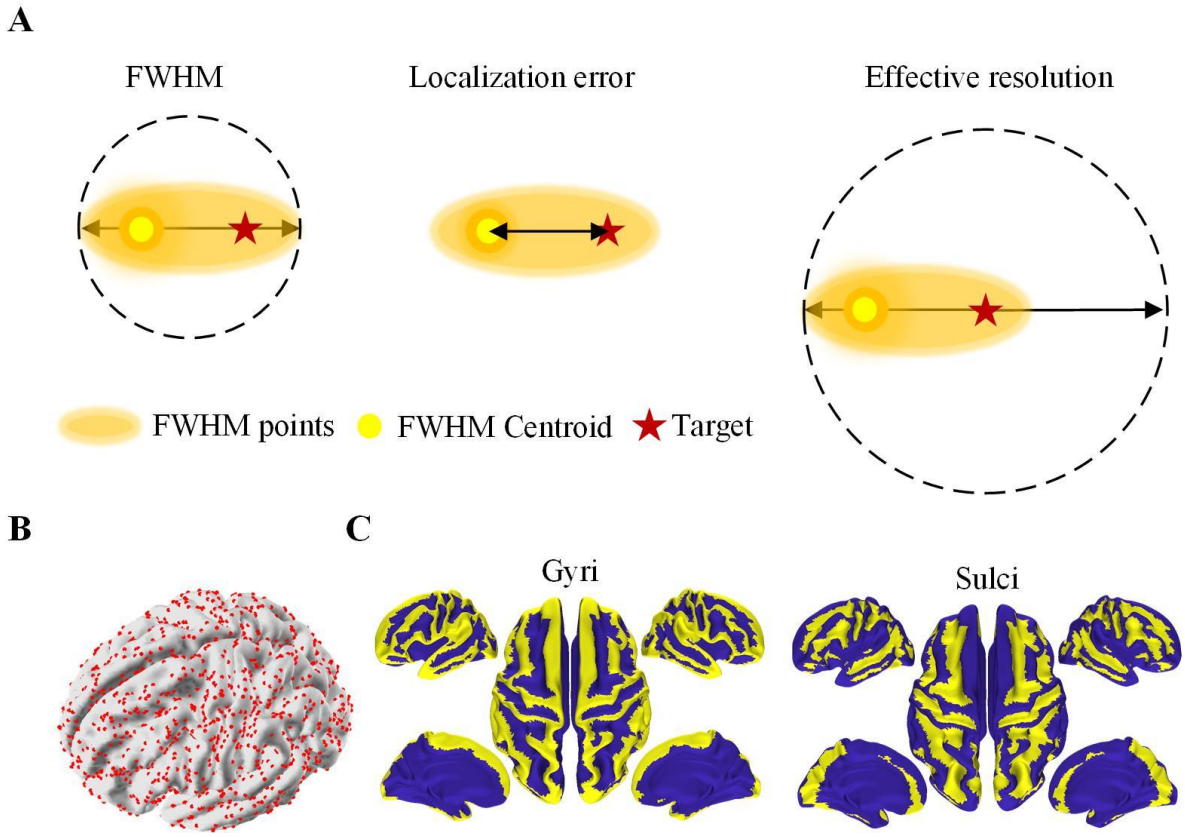

Figure 4-2 PSF-based metrics defined on a realistic head geometry.
(A) PSF-based metric definitions (B) locations (red dots) projected on the pial surface that were chosen for the calculation of metrics (C) definitions of shallow (summation of gyri) and deep (summation of sulci) cortical areas in yellow color. Figure adapted from Khan et al. (2021).

The spatial resolution of these inverse reconstructions was quantitatively evaluated using metrics calculated from each reconstruction's point-spread function (PSF) (White, 2012). ThePSF describes the response of an imaging system to a point input change, i.e., a change of chromophore at a single node or a localized region of the FEM mesh. Three PSF-based metrics were utilized as shown in Figure 4-2A; FWHM, localization error, and effective resolution. Briefly, FWHM describes the maximum Euclidean distance between the nodes with half the amplitude of the maximum-valued node. Localization error represents the mean Euclidean distance between all

FWHM points and the simulated node with chromophore changes (target node). The effective resolution is twice the Euclidean distance between the target node and the furthest FWHM node. In determining FWHM nodes, those nodes that were separated more than 4 mm apart were considered outliers and excluded.

The sensitivity of the mesh nodes to the source-detector pair is typically greater near the optodes than the nodes farther from the optodes (see Figure 3-7 for an example). Therefore, to investigate the effect of distance from the optodes on the metrics, histograms of the PSF-based metrics were calculated, including only those nodes within a Euclidean distance of 25 mm from either a source or a detector. Furthermore, to investigate the effects of depth on the PSF-based metrics, all metric values for head model nodes within deep cortical regions (represented as a summation of sulci) and shallow cortical regions (represented as a summation of gyri) were determined. The sulci and gyri were defined using an atlas (Destrieux et al., 2010). The resultant representation of deep and shallow cortical regions is illustrated in yellow in Figure 4-2C. This cortical surface is the intersection between the brain's gray and white matter.

In the fourth experiment, the third experiment was repeated on a higher resolution FEM head model (324,328 nodes and 1,898,862 tetrahedral elements) (Figure 4-3B) and a higher density optode cap (Figure 4-3A). The optode cap comprised 67 sources and 61 detectors placed on the standard 10-5 system (Oostenveld and Praamstra, 2001). A total of 515 channels were used with the mean±standard deviation, minimum, and maximum IOD of 47.5±15.1 mm, 21.1 mm, and 69.8 mm, respectively. A total of 1000 locations at the white matter and gray matter interface were used. These test locations are shown in Figure 4-3C as yellow and blue dots representing shallow and deep locations, respectively. The PSF-based metrics were calculated as described in experiment 3.

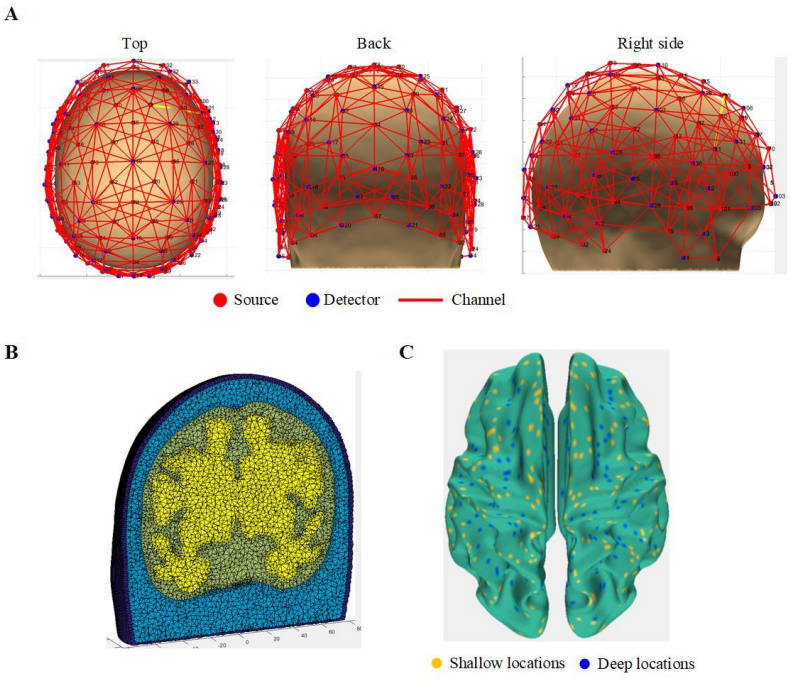

Figure 4-3 High-density cap montage.
(A) Cap montage, (B) coronal slice view of the high-resolution FEM head model, and (C) locations for inducing concentration changes on the interface between gray and white matter.

4.2.2 Localizing motor activity

The next step was to determine the ability of the BW-DOT to localize brain activity against an explicit stimulus, for example, hand-clenching, which is known to elicit pronounced activity in the contralateral motor cortex as reported in fMRI (Rao et al., 1993), EEG, fNIRS (Lee et al., 2019), and DOT (Habermehl et al., 2012) studies.

This study was approved by the University of Oklahoma Health Sciences Center (OUHSC) Institutional Review Board (IRB). Seven healthy adult participants (3 females, 4 males, age: 25-50 years) were recruited without any neurological or neuropsychiatric disorders. Written informed consent was obtained from every participant before the study. Individual participants sat in a comfortable dark and sound-damped room for four sessions. E-Prime (Psychology Software Tools, Sharpsburg, PA) software was used to program the visual cues (black arrows on a gray

background) and instructions displayed on an LCD monitor located about 90 cm from the participant. In each session, participants performed a right-hand clenching task in six blocks as shown in Figure 4-4.

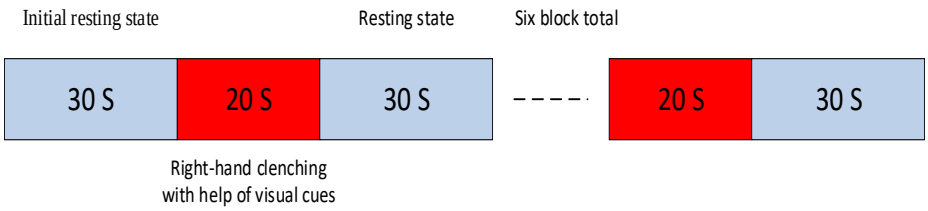

Figure 4-4 Experimental paradigm for hand-clenching task.

Nirscout extended, a commercially available dual-wavelength (760/850nm) CW-fNIRS device (nirx.net), was used to collect fNIRS data with 32 LED emitters and 32 avalanche photodiode detectors. The optodes were placed on an elastic cap (EASYCAP GmbH, Herrsching, Germany) designed with the 10-5 system (Oostenveld and Praamstra, 2001). These optodes were uniformly distributed across the entire scalp (IOD: mean: 30.7±7.6 mm) to maximize FOV while maintaining high density. The FOV, represented by the spread of the sensitivity profile from the Jacobian matrix (Dehghani et al., 2009a), is dependent on the quantity and position of the optodes. Consequently, the sensitivity profile of the optode cap covered the most superficial cortical structures. The 3D locations of the optodes and head landmarks (nasion, left, and right preauricular areas) were recorded using the Polhemus Patriot handheld digitizer (polhemus.com).

Structural head MRI of participants was acquired using a GE Discovery MR750 whole-body 3-Tesla MRI scanner (GE Healthcare, Milwaukee, WI, USA). The following parameters were set: FOV = 240 mm, axial slices per slab = 180, slice thickness = 1 mm, image matrix = 256×256, TR/TE = 8.45/3.24 ms. FEM head models were created as described in Chapter 3. The peripheral measurements included a triaxial MEMs accelerometer, photoplethysmography sensor, and pneumatic respiratory belt that was worn by participants on the forehead, left index finger, and

abdomen to record head motions, cardiac rhythms, and chest movements, respectively. Data from these peripheral sensors were recorded by connecting to the auxiliary input ports of a 64-channel EEG amplifier (Brain Vision, NC, USA) at a sampling rate of 500 Hz.

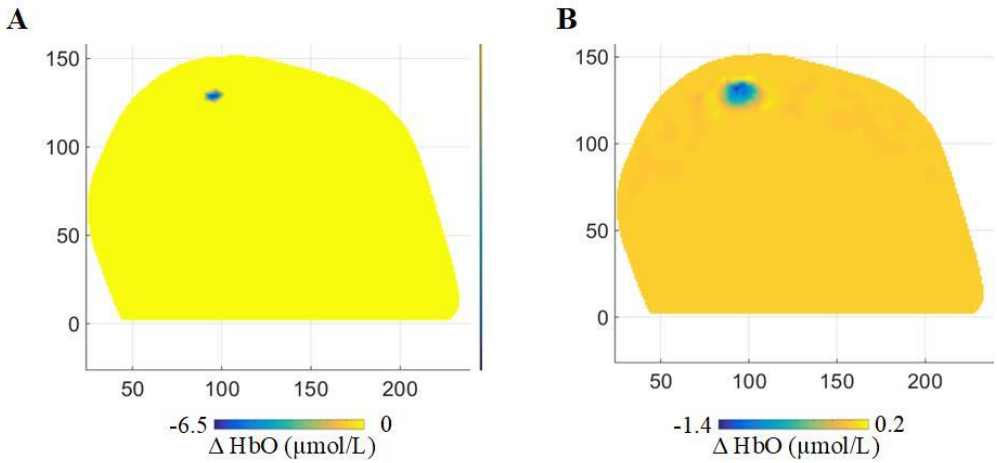

Figure 4-5 Simulation-based DOT reconstruction of localized concentration change. (A) A -6.5 % localized change in HbO concentration used as synthetic data (B) recovered concentration change following tomographic reconstruction plotted on a sagittal slice view.

4.2.3 Data analysis protocols

The following data analysis protocol was applied to task-based fNIRS data. The fNIRS data were pre-processed with the HOMER2 fNIRS toolbox (Huppert et al., 2009) and our proprietary MATLAB® scripts. The fNIRS data were block-averaged to increase SNR, then log-ratioed (mean of the channel taken as the baseline) and bandpass filtered (0.02~0.5 Hz). The PSD of the OD data was calculated using Welch's method (window length: 60 s, 50 % overlapping). Channels that lacked the heartbeat frequencies (0.8–1.6 Hz) in the OD PSD data (indicating potential poor optode-scalp contact) were rejected. A total of 105 channels were retained. Bad time segments corresponding to excessive head movements were removed. Then, the OD data were subject to the inverse reconstruction procedure, yielding the volumetric inverse solution, which was spatially smoothed (6 mm spherical kernel) to reject high-frequency spatial noise (Friston et al., 1995).

These smoothed volumetric data were projected to the cortical surfaces. Reconstruction results were also stored as time-stamped movies to study the dynamics of the motor cortex corresponding to the hand-clenching task.

4.3 Results

4.3.1 DOT reconstructions using simulated data

For the first simulation-based experiment (Section 4.2.1), the reconstructed concentration change closely followed the simulated concentration change of HbO relative to the baseline tissue HbO concentrations (Figure 4-6B). However, unlike the induced concentration change contained in a sphere of 3mm, the reconstruction change was spread out of the 3mm spherical boundary. For the second simulation-based experiment (Section 4.2.1), the reconstructed concentration changes followed the temporal patterns of the induced chromophore concentration changes of HbO Figure 4-6C and HbR Figure 4-6E. Due to the spatial spread of the inverse solution, the reconstructed activity spread out to parts of the somatosensory and premotor cortices.

Figure 4-7 shows the PSF-based metrics projected on a cortical surface (Figure 4-7A, D) and their histograms (Figure 4-7B, E). To better visualize the spatial distribution of the metrics on the cortical surface, spatial interpolation of these metrics on the cortical surfaces for HbO (bottom row in Figure 4-7A) and HbR (bottom row in Figure 4-7D) was performed. The first and second moments of these metrics are also presented in Table 4-1. For HbO, a mean of (31.3±11.9) mm, (12.2±7.8) mm, and (48.1±16.1) mm of FWHM, localization error, and effective resolution, respectively. For HbR, superior metrics were obtained, i.e., a mean of (29.2±9.7) mm, (11.9±6.5) mm, and (44.8±13.6) mm of FWHM, localization error, and effective resolution, respectively.

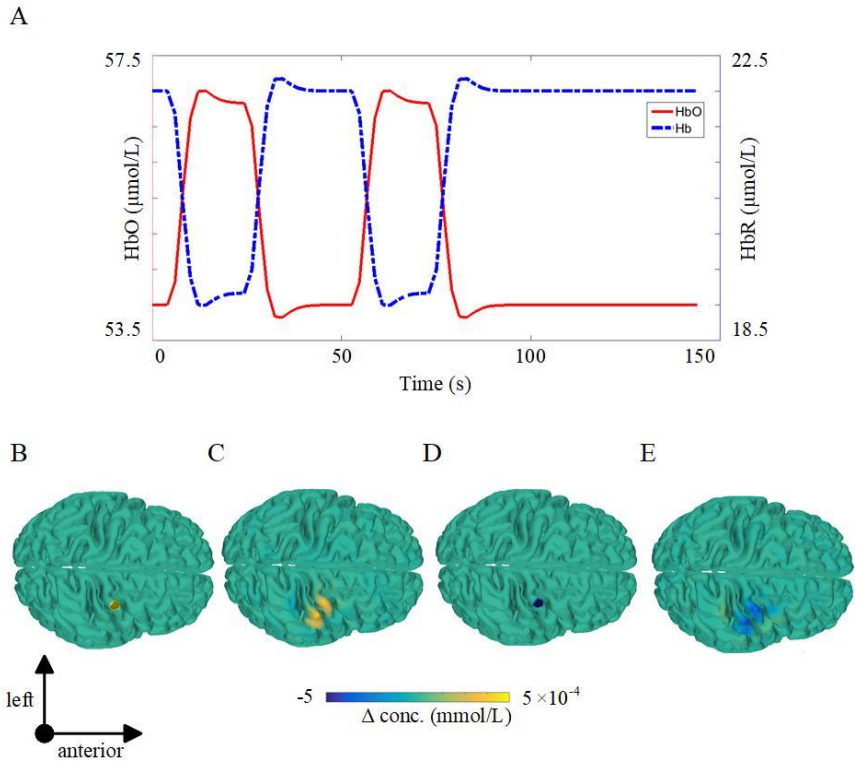

Figure 4-6 Simulation-based DOT reconstructions of temporal concentration changes in the motor cortex.

(A) Localized variations in concentration of HbO and HbR induced in a 3 mm diameter sphere on the right primary motor cortex. (B) input HbO (C) reconstructed HbO (D) input HbR (E) reconstructed HbR. Input and reconstruct Input and reconstructed simulation concentration changes in the concentration of chromophores are shown at T=14 s projected onto the pial surface. Figure adapted from Khan et al., (2019).

All metrics for nodes within the defined FOV were significantly smaller than those away from the optodes. For the nodes within FOV, the differences in the metrics between the deep and shallow regions were much smaller than those outside FOV (Table 4-1). For the within-FOV nodes of HbO, the overall mean and standard deviation of FWHM, localization error, and effective resolution were (26.2±9.1) mm, (5.7±3.7) mm, and (37.8±11.1) mm, respectively. For HbR, the overall mean and standard deviation of FWHM, localization error, and effective resolution were (27.3±9.1) mm, (5.5±3.2) mm, and (36.4±10.5) mm, respectively.

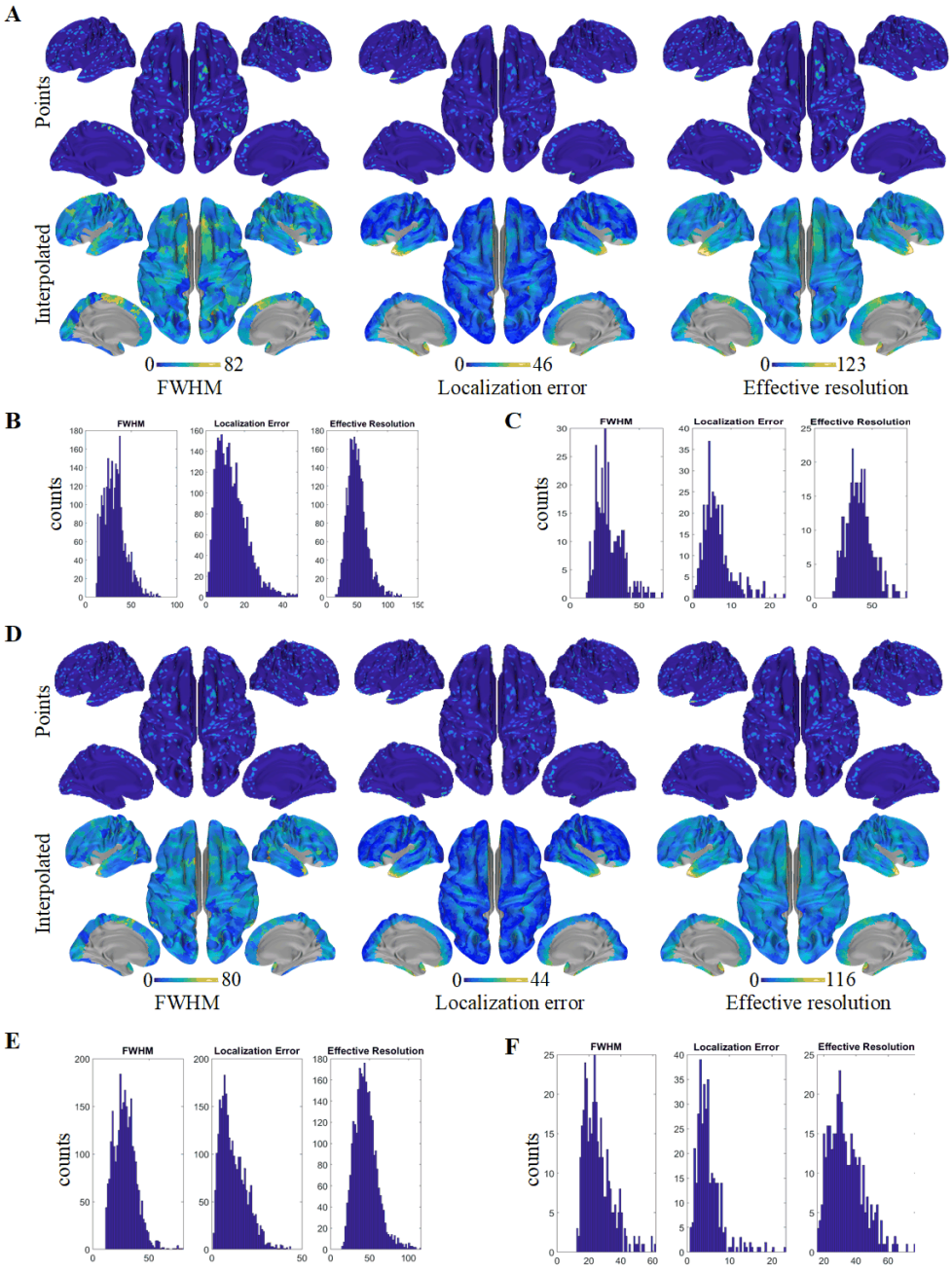

Figure 4-7 PSF-based metrics of HbO and HbR.

(A) Visualization of PSF-based metrics on cortical surface of HbO and their (B) histograms, (C) histogram of PSF-based metrics within the FOV of 25 mm (D) Visualization of PSF-based metrics on cortical surface of HbR and their (E) histograms, (F) histogram of PSF-based metrics within the FOV of 25 mm.

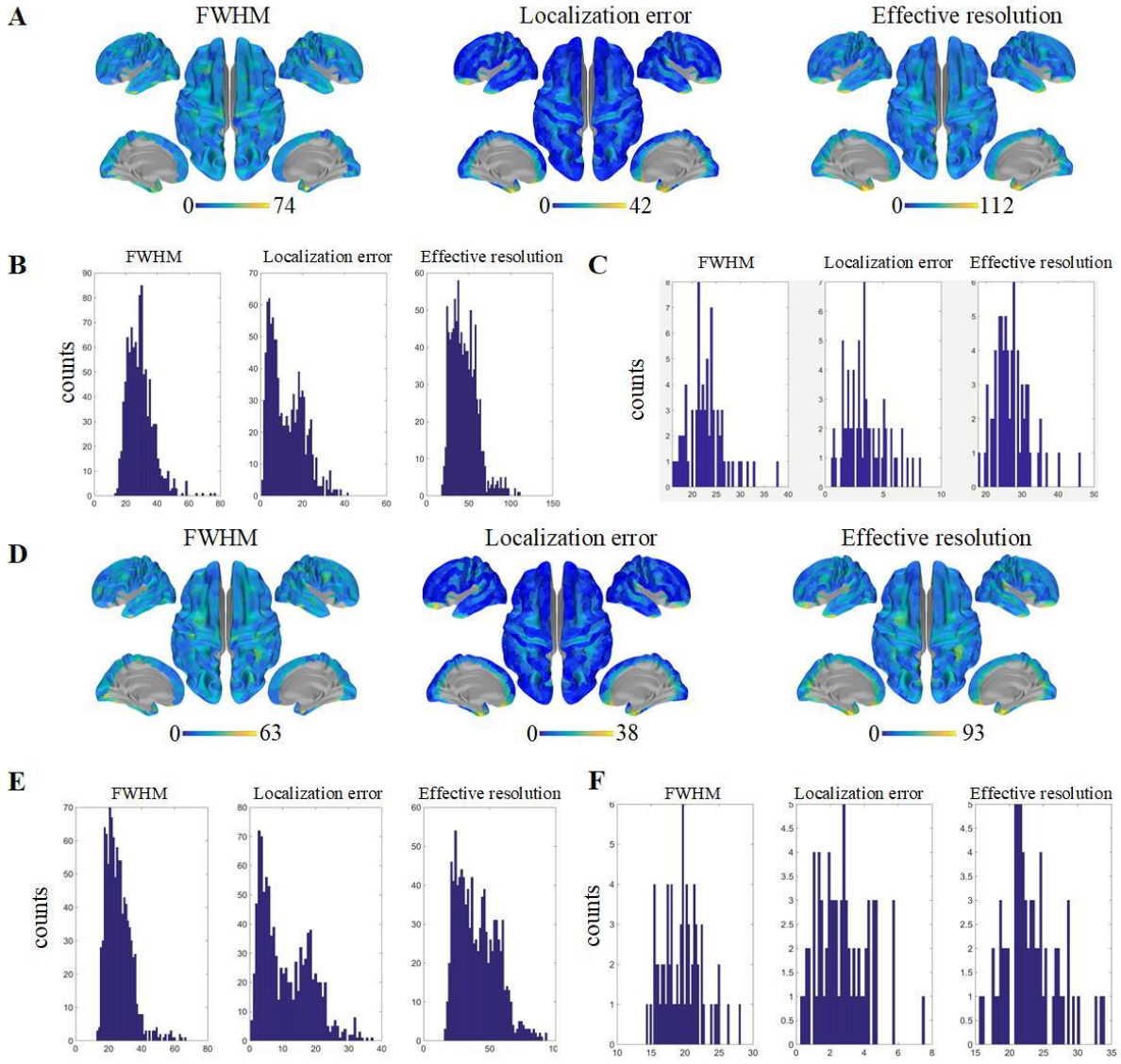

Figure 4-8 PSF-based metrics of HbO and HbR of high-density cap.
(A) Visualization of PSF-based metrics on cortical surface of HbO and their (B) histograms, (C) histogram of PSF-based metrics within the FOV of 25 mm (D) Visualization of PSF-based metrics on cortical surface of HbR and their (E) histograms, (F) histogram of PSF-based metrics within the FOV of 25 mm.

Table 4-1 PSF-based metrics of a realistic head geometry.

	Node Location	HbR			HbO		
		FWHM (mm)	Localization error (mm)	Effective resolution (mm)	FWHM (mm)	Localization error (mm)	Effective resolution (mm)
All nodes	Shallow	(28.1±9.4)	(9.7±6.2)	(41.6±13.8)	(31.7±11.6)	(11.2±7.0)	(46.7±15.9)
	Deep	(30.2±9.8)	(14.4±6.0)	(48.3±12.5)	(33.1±11.2)	(15.4±6.2)	(52.3±13.3)
	Overall	(29.1±9.7)	(11.9±6.5)	(44.8±13.6)	(31.3±11.9)	(12.2±7.8)	(48.1±16.1)
Within FOV	Shallow	(27.2±8.7)	(5.3±2.9)	(36.0±10.3)	(29.8±10.3)	(7.1±4.0)	(41.2±11.3)
	Deep	(27.5±9.5)	(5.7±3.4)	(36.8±10.6)	(30.0±10.4)	(7.5±4.1)	(42.1±11.0)
	Overall	(27.3±9.1)	(5.5±3.2)	(36.4±10.5)	(26.2±9.6)	(5.7±3.7)	(37.8±11.1)
Sparse patch: FWHM (21.6±4.6), Localization error (5.3±2.0), Effective resolution (29.9±5.2) (White, 2012)							

Generally, the deeper cortical regions showed higher-valued metrics than shallow cortical regions. Some areas with exceptionally high metrics values included the temporal pole, posterior part of the temporal lobe, ventral parts of the inferior frontal gyrus (IFG), and ventral-medial regions of the superior frontal gyrus (SFG). These parts were mainly outside the optode cap's FOV (see Figure 3-7) (note that the optode cap's FOV is defined from the sensitivity profile and is different from the optode FOV, which is defined as the Euclidean distance of 25 mm from any optode). The spatial patterns of all three metrics were bilaterally symmetric with some exceptions, for example, parts of SFG and IFG (Figure 4-7D). Among these nodes, the shallow nodes for HbR had the highest quality metrics, i.e., (27.2±8.7) mm, (5.3±2.9) mm, and (36.0±10.3) mm for FWHM, localization error, and effective resolution, respectively. These metrics were comparable to the sparse patch-based HD-DOT system in the literature (White, 2012) (see Table 4-1). Figure 4-8 shows the PSF-based metrics interpolated on the cortical surface (Figure 4-8A, D) and their histograms (Figure 4-8BC, E, F) for the higher-resolution head model and higher density cap montage. The first and second moments of these metrics are also presented in Table 4-2. Some areas with exceptionally high metrics values included mainly the temporal pole and ventral-medial

regions of the SFG. However, overall, these metrics were superior to the previous case (Figure 4-7) as described above for both HbO and HbR.

Table 4-2 PSF-based metrics of a high-resolution head model with high-density optode cap.

	Node Location	**HbR**			**HbO**		
		FWHM (mm)	Localization error (mm)	Effective resolution (mm)	FWHM (mm)	Localization error (mm)	Effective resolution (mm)
All nodes	Shallow	(22.8±5.4)	(6.4±5.5)	(31.7±11.4)	(26.8±6.9)	(7.6±6.3)	(36.9±13.4)
	Deep	(27.0±6.7)	(11.6±5.8)	(41.8±11.4)	(30.2±7.3)	(12.9±6.1)	(45.5±11.1)
	Overall	(24.8±6.4)	(8.9±6.2)	(36.5±12.5)	(28.4±7.3)	(10.1±6.7)	(41.0±13.1)
Within FOV	Shallow	(19.5±2.7)	(2.5±1.4)	(22.7±3.3)	(23.3±4.4)	(3.3±1.5)	(28.0±6.4)
	Deep	(19.7±2.8)	(2.6±1.4)	(23.0±3.5)	(23.2±4.1)	(3.5±1.6)	(27.8±5.6)
	Overall	(19.6±2.7)	(2.5±1.4)	(22.8±3.4)	(23.3±4.3)	(3.4±1.6)	(27.9±6.1)
Sparse patch: FWHM (21.6±4.6), Localization error (5.3±2.0), Effective resolution (29.9±5.2) (White, 2012)							

The metrics for nodes within the defined FOV were significantly smaller than those away from the optodes. Also, for the nodes within FOV, the differences in the metrics between the deep and shallow regions were much smaller than those outside FOV (Table 4-2). For the within-FOV nodes of HbO, the overall mean and standard deviation of FWHM, localization error, and effective resolution were (23.3±4.3) mm, (3.4±1.6) mm, and (27.9±6.1) mm, respectively. For HbR, the overall mean and standard deviation of FWHM, localization error, and effective resolution were (19.6±2.7) mm, (2.5±1.4) mm, and (22.8±3.4) mm, respectively.

4.3.2 DOT reconstructions using motor task experimental data

Inspection of the movies of reconstructed inverse results revealed pronounced activity in the contralateral motor cortex in response to the right-hand hand clenching. These brain activations are shown in Figure 4-9 as window-averaged (10-25 s) spatial maps projected on a cortical surface for four sessions of a representative participant. Data from all four sessions were averaged and used for reconstruction to improve localization further. This yielded a more localized

reconstruction, as shown in Figure 4-9E, and reduced variations outside the primary motor cortex (M1) in individual session data. Results from all sessions showed consistent spatial activation patterns in Figure 4-9. Additional participant reconstruction results for session-averaged data are shown in Figure 4-10. These maps also exhibit pronounced brain activity in the contralateral motor cortex. These results on the experimental motor task data provide confidence that the BW-DOT can accurately localize brain activity.

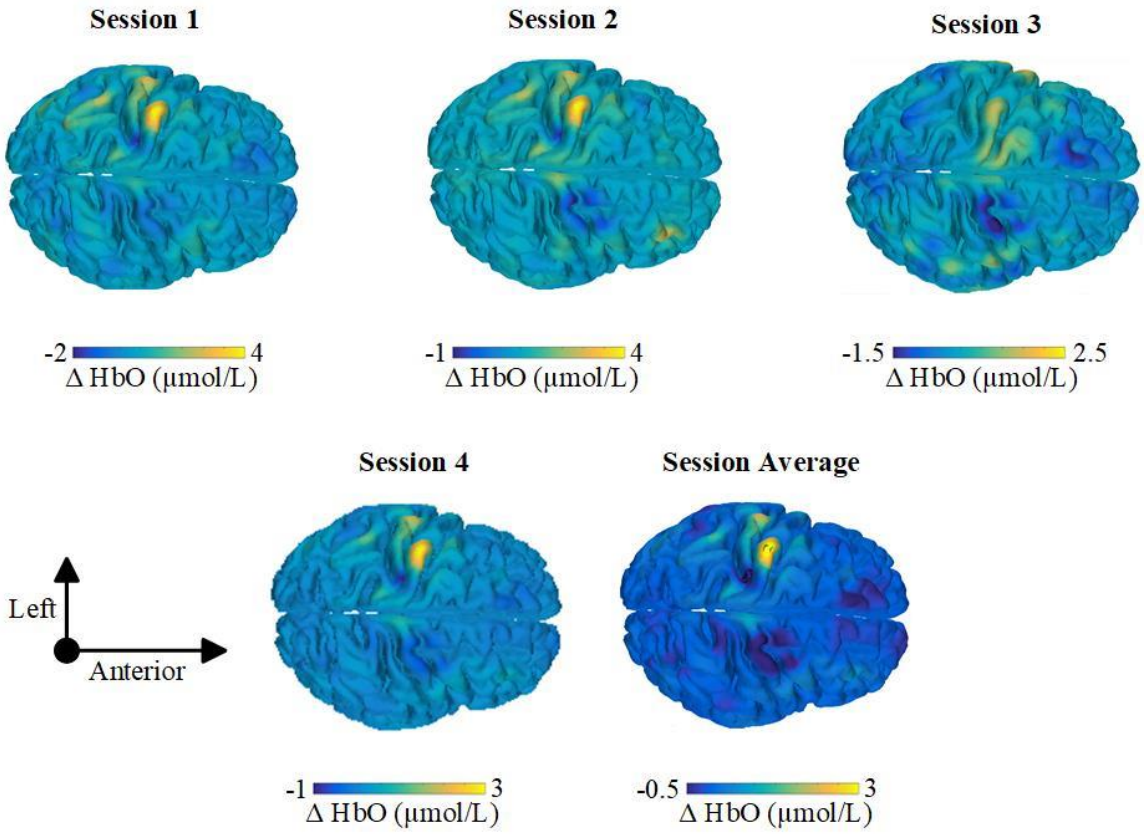

Figure 4-9 Motor task data reconstructions of a representative participant.
Volume to cortical surface projection of reconstructed changes in concentration of HbO for a right-hand clenching block-design motor task. Each projection was time-averaged (10-25 s window) for all four sessions (a-d) and session-averaged data (e). Figure adapted from Khan et al. (2019).

To study dynamic changes in brain activity behind efforts to clench the hand repetitively, reconstruction results from the experimental data were further analyzed. Figure 4-11 shows the timing maps revealing temporal dynamics of three brain areas: (1) M1, (2) premotor cortex (PMC), and (3) supplementary motor area (SMA). These maps showed timing information (columns) across sessions (rows) and session average (the last row). Through qualitative visual inspection, time was recorded when brain areas of interest displayed pronounced activation. The first column represented recorded times at which cortical activations became observable in any brain area. Interestingly, some activity could be seen in the PMC and SMA for S2, S3, and session average (visually not apparent because of a uniform colorbar). This could be attributed to the motor preparation for upcoming movements.

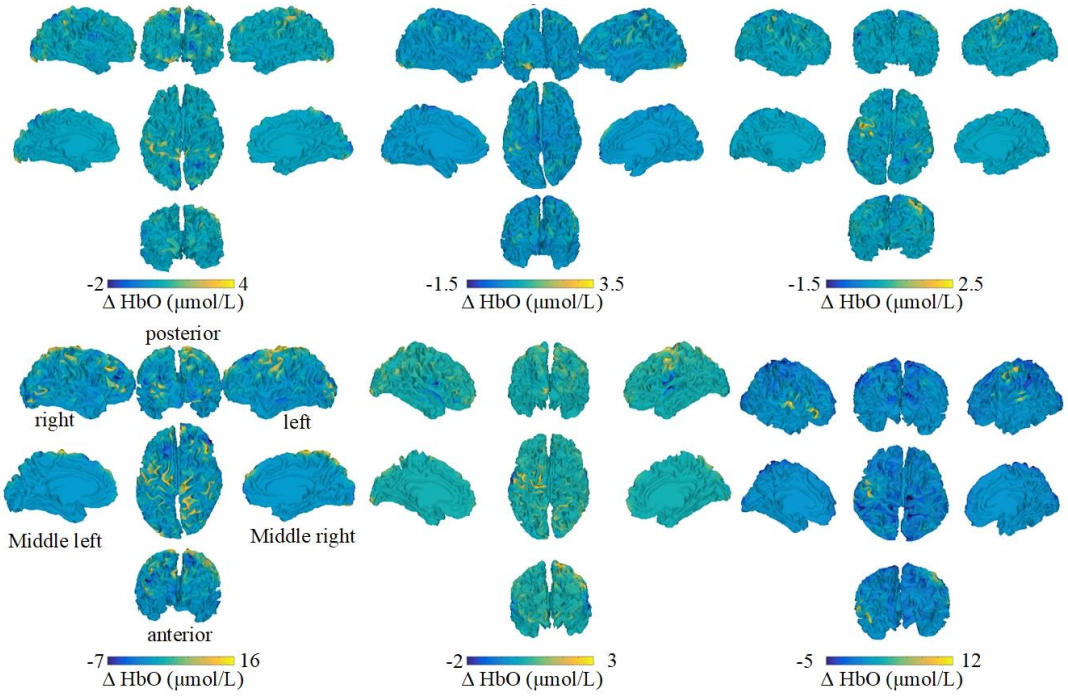

Figure 4-10 Motor task data reconstructions for other participants.
Volume to cortical surface projection of reconstructed changes in concentration of HbO for a right-hand clenching block-design motor task. Session-averaged data was used for reconstruction. Each projection was time-averaged (10-25 s window).

M1 started to show lateralized activations (3.4±0.4) s following hand clenching. The delay can be attributed to neurovascular coupling, in which the hemodynamic activity lags the neural activity by a few seconds. At this time, PMC displayed lateralized suppression. However, it started to display lateralized activity (5.1±0.9) s after M1. Interestingly, some ipsilateral activity was also observed. For example, there was an increase in HbO concentration in the M1 area for S1 and session-averaged data. In addition, a decrease in HbO concentration was seen in M1 at the time of activation of SMA (see the fourth column) across all sessions and PMC (S1 and S2). The bilateral role of M1 in motor control is well reported in neuroimaging data. The variance in ipsilateral brain activity across sessions could be attributed to individual differences in control strategies, usually active brain processes. This is consistent with previous experiments, for example, studies involving EEG (Ding et al., 2011). SMA was also active before M1 activation (S2 and S3) and during M1 activation (all sessions except S1). This is consistent with previous literature where SMA is thought to be related to motor planning and coordination. Interestingly, SMA also started to show activity several seconds after stopping hand clenching. Although, at the onset, this activity was predominantly lateralized contralateral to the clenching, later, however, bilateral activations (Gerloff et al., 1998) soon followed.

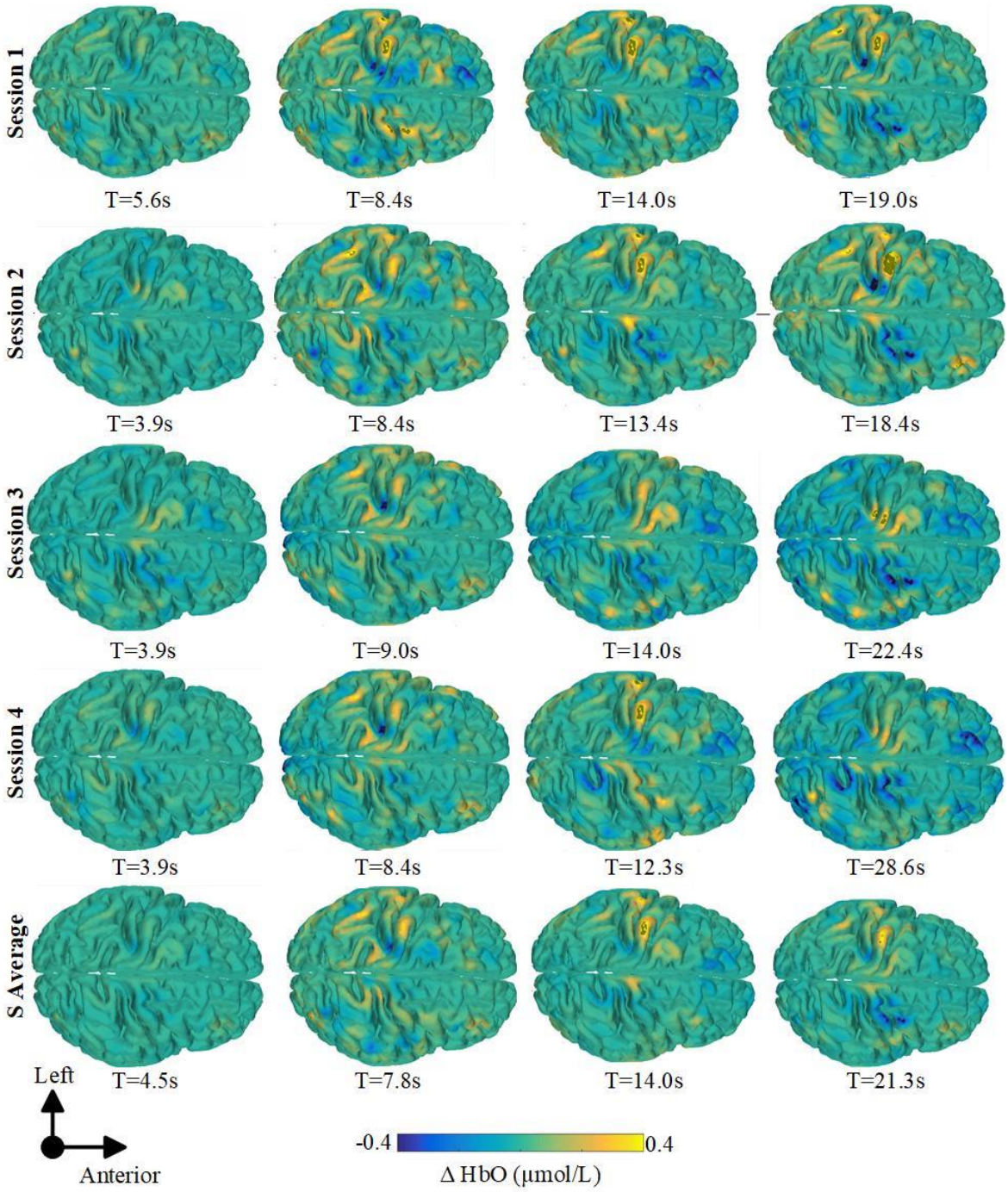

Figure 4-11 Dynamics of motor reconstructions.

Timing map showing temporal dynamics of the sensorimotor and adjacent areas for four sessions (row 1-4) and session-averaged (row 5) data. First column represents recorded time at which significant activity started to display in the sensorimotor area. M1, PMC and SMA started to show significant activations as seen in columns 2-4 respectively. Figure adapted from Khan et al. (2019).

4.4 Summary and discussion

In this chapter, the performance of the BW-DOT framework was evaluated in reconstructing changes in concentrations of HbO and HbR using simulation and motor task experimental data. These reconstructions, or in other words, inverse solutions, closely followed the known ground truths in each experiment described in the methods part of this chapter. To quantify the spatial spread of the reconstructions, a study was conducted to understand the distribution of the PSF-based metric values on a realistic head geometry constructed from high-quality surface meshes. Such an evaluation of these metrics was previously reported using patch-based regional DOT systems on a simple two-layer head geometry (White, 2012). Our current evaluation of these metrics on cap-based whole-head systems provided useful knowledge of the distribution of these metrics on a realistic head geometry with different resolutions and with whole-cap optode montage of different densities.

Our results show that the localization errors (Section 4.2.1) are almost identical to data reported from a patch-based DOT only covering limited cortical regions. At the same time, the FWHM and effective resolution metrics are comparable to metrics reported from the patch-based DOT system calculated on a relatively simpler head geometry, i.e., a regional epicortical surface patch (White, 2012), but still relatively inferior because of the brain-wide coverage and the consideration of realistic cortical structures, both of which are not considered in the patch-based DOT. Note that while using a FEM model with higher resolution and higher optode density resulted in superior metrics, however, the improvement in these metrics is not enough to outweigh the logistic challenges and potential problems involved with increasing the optode density to such as level (See Section 3.8 for a discussion on these challenges and problems).

The PSF-based metrics showed a dependence on depth, i.e., the metrics were lower in quality in deeper cortical regions (i.e., sulci) than the shallow regions (i.e., gyri). This depth effect was more prominent in cortical areas away from the optodes (outside FOV). This effect was expected due to the reduced sensitivity at nodes outside FOV. A possible solution to this problem is to include more optodes in the cap montage. It is noted that this FOV (within 25 mm) includes parts of the cortical sulcus structures but could not reach deep brain areas like the insular cortex and thalamus. The capability of mapping relatively deep structures (i.e., cortical sulci) might be enabled by long-distance emitter-receiver pairs used for recordings. However, as PSF-based metrics are sensitive to the factors influencing reconstruction performances, these metrics could be used in a future study to optimize the proposed BW-DOT system.

Since we used only one head model, a comprehensive simulation-based assessment based on multiple head models is worth investigating. Moreover, only a subset of mesh locations (2879) was used for calculating the metrics due to the computational demands. In the future, we expect to include more if not all locations in the head model's FEM mesh. The potential strategies to further improve BW-DOT performance include the use of higher-quality FEM meshes, improved inverse procedures, and optimized optode placement schemes. An investigation of PSF-based metrics on realistic head geometries for our proposed cap-based whole-head diffuse optical tomography system suggest comparable performance over sparse optodes patch-based regional systems. These metrics are sensitive to factors that influence reconstruction qualities associated with diffuse optical tomography.

The performance of the BW-DOT method in reconstructing motor brain activation patterns evoked by a simple motor task was also evaluated. Data from several participants in multiple repeated sessions were analyzed. Using experimental data, BW-DOT could accurately localize

motor sources, consistent with previously reported literature (White et al., 2009, Ding et al., 2011). Moreover, these results were reliable because they were consistent over four sessions, and we obtained these results from several participants (Figure 4-10). In addition, to block averaging data, we also used session-averaged data, which resulted in more localized reconstructions.

Finally, a timing analysis of reconstructed results was performed, revealing rich temporal information of three brain areas within the motor network for motor control. Pleasingly, these results were consistent with previously reported literature, e.g., Ding et al. (2011). It is worth noting that EEG is not efficient at reconstructing SMA sources because of its close-vicinity and bilateral nature on the middle wall that tends to cancel off current dipoles (Ding et al., 2011). However, since DOT is principally based on blood hemodynamics, it is not susceptible to these canceling effects. Overall, these experiments collectively demonstrate that the proposed BW-DOT framework can accurately reconstruct brain activity with a large FOV covering the majority of the cortex. These results provide the confidence that the proposed framework has the spatiotemporal resolution to reconstruct brain-wide resting-state activity.

5. DOT resting-state networks

This chapter has been adapted from the following peer-reviewed publication with permission from IOP Publishing:

Khan, A. F., Fan Zhang, Han Yuan, and Lei Ding. "Brain-wide functional diffuse optical tomography of resting state networks." Journal of Neural Engineering 18, no. 4 (2021): 046069. DOI: https://doi.org/10.1088/1741-2552/abfdf9)

5.1 Introduction

The BW-DOT framework was introduced in Chapter 3. In Chapter 4, we evaluated the DOT part of this framework using known ground truth consisting of simulation and experimental data. The results from these experiments suggested that the BW-DOT framework has sufficient spatiotemporal resolution to reconstruct brain-wide RSNs. In this chapter, we tested the BW-DOT framework using resting-state data from healthy human participants to reconstruct brain-wide RSNs.

Our results revealed a comprehensive set of RSNs and their subnetworks, which collectively cover almost the entire neocortical surface of the human brain, both at the group level and among individual participants. The spatial patterns of these DOT RSNs suggest statistically significant similarities to fMRI RSN templates. Our results also reported the networks involving the mPFC and precuneus that had been missed in previous DOT RSN studies. Furthermore, RSNs obtained from HbO and HbR suggest similarity in terms of the number of RSN types reconstructed and their corresponding spatial patterns, while HbR RSNs show statistically more similarity to fMRI RSN templates and HbO RSNs indicate more bilateral patterns over two hemispheres. In addition, the BW-DOT framework allowed consistent reconstructions of RSNs across individuals and recording sessions, indicating its high robustness and reproducibility, respectively.

5.2 Materials and methods

5.2.1 Experimental protocols

This study was approved by the OUHSC IRB. Thirteen healthy adult participants (Age: 31.7 ± 9.3 years) were recruited without any neurological or neuropsychiatric disorders. Written informed consent was obtained from every participant before the study.

Two same-day data recording sessions were performed on each participant sitting in a comfortable dark and sound-damped room. Recording data on the same day attempted to reduce the possibility of changes to RSNs because of factors such as sleep deprivation (Kaufmann et al., 2016, De Havas et al., 2012, Yeo et al., 2015) and stress (Soares et al., 2013). E-Prime (Psychology Software Tools, Sharpsburg, PA) software was used to program the visual cues (black arrows on a gray background) and instructions displayed on an LCD monitor located about 90 cm from the participant. In each session, participants performed a task section of right-hand clenching for about 4 minutes and a resting-state section for about six minutes. Only the resting-state data from the two sessions were analyzed in the present study, as our goal was to reconstruct RSNs.

Structural head MRI of participants was acquired using a GE Discovery MR750 whole-body 3-Tesla MRI scanner (GE Healthcare, Milwaukee, WI, USA). The following parameters were set: FOV = 240 mm, axial slices per slab = 180, slice thickness = 1 mm, image matrix = 256×256, TR/TE = 8.45/3.24 ms. FEM head models were created as described in Chapter 3. Data from fNIRS optodes, auxiliary sensors, and EEG sensors (not analyzed in the present study) were simultaneously recorded. fNIRS data were collected by a dual-wavelength (760/850 nm) CW-fNIRS system (NIRx GmbH, Germany) at a sampling rate of 6.25 Hz. The fNIRS system comprised 34 LED sources, 31 avalanche photodetectors, and 8 SS detectors (IOD: 8 mm), which jointly formed 109 LS and 8 SS channels. The FOV, represented by the spread of the sensitivity

profile from the Jacobian matrix, is dependent on the quantity and position of the optodes (Dehghani et al., 2009a). The optodes were placed on an elastic cap (EASYCAP GmbH, Herrsching, Germany) designed with the 10-5 system (Oostenveld and Praamstra, 2001). These optodes were uniformly distributed across the entire scalp to maximize FOV while maintaining high density (IOD mean: 3.65 ± 0.44 cm, mode: 2.98 cm, min: 2.98 cm, max: 4.56 cm). Consequently, the sensitivity profile of the optode cap covered the most superficial cortical structures. The 3D locations of the optode and head landmarks (nasion, left, and right preauricular areas) were recorded using the Polhemus Patriot handheld electromagnetic digitizer (polhemus.com). The peripheral measurements included a triaxial MEMs accelerometer, photoplethysmography sensor, and pneumatic respiratory belt that were worn by participants on the forehead, left index finger, and abdomen to record head motions, cardiac rhythms, and chest movements, respectively. Data from these peripheral sensors were recorded by connecting to the auxiliary input ports of a 64-channel EEG amplifier (Brain Vision, NC, USA) at a sampling rate of 500 Hz.

5.2.2 Data analysis protocols

The following data analysis protocol was applied to resting-state fNIRS data, separately, for HbO and HbR and two recording sessions from thirteen participants. fNIRS data were pre-processed with the HOMER2 fNIRS toolbox (Huppert et al., 2009) and our proprietary MATLAB® scripts. Specifically, the raw light intensity data were converted to OD by taking their log ratios to the average of the time courses. Power spectral densities (PSD) of the OD data were calculated using Welch's method (window: 60 s, 50% overlapping). Long channels that lacked the heartbeat frequencies (0.8-1.6 Hz) in the OD PSD data (indicating potential poor optode-scalp contact) were rejected. The OD data were then bandpass filtered (0.009 Hz to 0.08 Hz).

Bad data segments corresponding to excessive head movements were removed using the metric of global variance in temporal derivative (GVTD) (Sherafati et al., 2017, Sherafati et al., 2020a). The time points that had GVTD values larger than 3 times the mean GVTD value across all time points were identified. Then time windows of 16 s centered at these time points were masked as bad time segments and excluded from further analyses. The PC-SS that represented the global physiological activity (see Section 3.4.1) was calculated. The auxiliary measurements, including triaxial acceleration, respiration, and cardiac activity, were bandpass filtered (0.009 Hz to 0.08 Hz) to generate nuisance regressors that accounted for physiological activity. The PC-SS, auxiliary regressors, and a 3rd-order polynomial drift were then included in the design matrix as nuisance regressors in a GLM procedure to remove non-neuronal signals (see Section 3.4.1). Then, the regressed OD data were subject to the inverse reconstruction procedure (see Section 3.3), yielding the volumetric inverse solution data $\vec{\hat{x}}_k(t)$ (k: index of participants), which were spatially smoothed (using 6 mm spherical kernel) to reject high-frequency spatial noise (Friston et al., 1995). These smoothed data were subjected to gSICA analysis (see Section 3.5) and SCT reconstruction (see Section 3.7) to estimate spatial patterns of IC from inverse OD data.

Obtained spatial patterns of independent components were then matched (via visual inspection) to a set of previously reported fMRI RSN (f-RSN) templates (Yeo et al., 2011) to define d-RSNs, while those independent components that could not be matched to any of the f-RSN templates were excluded from further analysis. These binary template spatial maps (i.e., 1 for nodes inside the spatial coverage of an f-RSN and 0 for outside nodes) were defined on the standard FreeSurfer cortical model allowing direct spatial comparison to obtained independent components. Matched d-RSNs set included the visual (V), somatomotor (SM), DMN, FPN, DAN,

VAN, auditory (A), limbic (L), and PCC networks. Multiple d-RSNs matched to a single f-RSN template map were defined as subnetworks differentiated by numerical indices.

5.2.3 Evaluation and validation protocols

5.2.3.1 Spatial similarity of DOT RSNs to fMRI RSN templates

The matching of d-RSNs and their corresponding template maps was quantitatively evaluated using two spatial matching metrics, i.e., template-matching degree (TD) (Greicius et al., 2007) and spatial correlation (SC) (Noda and Ozaki, 2005). For both matching metrics, z-score values defining d-RSNs (Eq. 3-16) were first converted to absolute values since the binary f-RSN templates did not carry sign information. The TD metric was defined as follows:

$$TD(i,j) = \frac{Z_{in}(i,j) - Z_{out}(i,j)}{Z_{in}(i,j) + Z_{out}(i,j)} \quad 5\text{-}1$$

where i and j represented the indices for f-RSN and d-RSN, respectively. $Z_{in}(i,j)$ and $Z_{out}(i,j)$ were z-scores of the d-RSN j (Eq. 3-16) averaged over all source nodes inside and outside the f-RSN template i, respectively. The SC metric was calculated between the vectorized z-score values of a d-RSN and the vectorized binary values of an f-RSN template. Higher positive TD and SC values indicated greater spatial similarity between the two compared spatial maps. TD and SC metrics were calculated for all possible pairs of f-RSN templates and d-RSNs to build confusion matrices (see Figure 5-3 for an example) for both HbO and HbR at the group and individual participant levels. For each group-level confusion matrix, the diagonal values (matched pairs) were compared with the off-diagonal values (unmatched pairs) for statistical significance testing (t-test with Bonferroni correction). Spatially matching a d-RSN to a target f-RSN template may also result in a partial match to other f-RSN templates that are close neighbors of the target f-RSN template, resulting in positive off-diagonal values of a confusion matrix. Thus, diagonal values

from the confusion matrix were further statistically compared with the positive-only off-diagonal values to test whether the similarities of matched pairs were statistically significantly higher than those of unmatched pairs but had spatial closeness. For participant-level confusion matrices, the metric values of the matched, unmatched, and positive-only unmatched pairs were calculated separately for individual d-RSNs and statistically compared (t-test with Bonferroni correction) for each type of d-RSN using data from all participants as samples.

5.2.3.2 HbO vs. HbR DOT RSNs

Based on the group-level confusion matrices (built-in Section 5.2.3.1) corresponding to HbO and HbR, the differences between HbO and HbR d-RSNs were quantitatively evaluated for TD and SC metric values from both data recording sessions. Specifically, the metric values of HbO were statistically (t-test with Bonferroni correction) compared with the metric values of HbR for the matched pairs (the diagonals of confusion matrix) and, separately, for the unmatched pairs (the off-diagonals of confusion matrix). The comparison was then extended to the participant level, where, based on the participant-level confusion matrices (also built from Section 5.2.3.1), the metric values of HbO and HbR were statistically compared (t-test with Bonferroni correction) for each type of d-RSN using data from all participants as samples. HbO and HbR d-RSN spatial maps were further directly compared with each other without first matching them to the f-RSN templates. Since no binary template was involved, an alternative metric to TD, i.e., spatial overlap (OL) (Gomaa and Fahmy, 2016), was used to quantitatively assess the extent of spatial overlap between the HbO and HbR d-RSNs together with SC. The metric OL was defined as:

$$OL\ (a,b) = \frac{|a \cap b|}{min(\ |a|, |b|)} \qquad 5\text{-}2$$

where a and b were binarized (using thresholded spatial maps of group-level d-RSNs as masks, see Figure 5-1and Figure 5-2) sets corresponding to HbO and HbR d-RSNs, respectively. SC and OL metrics were calculated for all possible pairs of HbO and HbR d-RSNs to build confusion matrices (see Figure 5-7 for an example) at the group and individual participant levels. Statistical comparisons between diagonal and off-diagonal metric values with all d-RSNs combined from the group-level confusion matrices and separately for individual d-RSNs from the participant-level confusion matrices were similarly conducted as in Section 5.2.3.1.

5.2.3.3 Reproducibility of DOT RSNs

To assess the repeatability of reconstructed d-RSNs, we hypothesized that the HbO and HbR d-RSNs were consistent across the two data recording sessions. To test this hypothesis, two-factor analysis of variance (ANOVA) tests (Glantz et al., 1990) with independent variables of Pairs, i.e., matched and unmatched, and Sessions were applied separately on TD and SC metric values corresponding to participant-level confusion matrices (built-in Section 5.2.3.1) for HbO and HbR d-RSNs resulting in a total of four tests. To test whether d-RSNs from individual participants were consistent with the group-level d-RSNs (Chen et al., 2008), it was hypothesized that spatial correlations between participant-level d-RSNs and their corresponding group-level d-RSNs should be positive and statistically higher than zero correlations. Unthresholded participant-level d-RSNs ($\bar{z}_k(j,n)$ in 3-15) were correlated to the corresponding unthresholded group-level d-RSNs ($\bar{z}_{group}(j,n)$ in 3-16) using the SC metric for all participants. A non-parametric approach was used to test the significance of these SC values (t-test with Bonferroni correction) to the distribution of SC values for null correlations created by calculating all combinations of unmatched group-level and participant-level d-RSNs. The process was repeated separately for HbO and HbR d-RSNs and data from two recording sessions.

5.3 Results

5.3.1 Spatial patterns of DOT RSNs

Using BW-DOT, we reconstructed nineteen brain-wide HbO d-RSNs at the group level, yielding eleven unique d-RSNs, and seven suggested subnetworks (Figure 5-1). Note that only one independent component (data not shown) could not be matched to the template set. Three d-RSNs were identified as two subnetworks (V1a, V1b, and V2) belonging to the visual network. These identified subnetworks primarily covered the superior occipital gyrus (V2), middle occipital gyrus (V1a, V1b), dorsal part of the inferior occipital gyrus (V1a, V1b, V2), and rostral part of the inferior occipital gyrus (V1a, V1b). V1a and V1b covered mostly the lateral part of the visual cortex and part of the ventral visual stream, while V2a covered the medial part of the visual cortex. The subnetwork V1 showed hemispheric dominance, while V2 exhibited bilateral symmetry. These two subnetworks cut across the calcarine fissure, with V1 and V2 more dominant ventral and dorsal to the fissure, respectively. Two d-RSNs were identified as the SM network. The identified SM d-RSNs primarily covered the postcentral gyrus (SMa and SMb), precentral gyrus (SMa and SMb), and inferior parietal lobule (SMa). Unlike SMb, SMa was bilateral. Interestingly, the lateral and medial parts of the SMa showed a negative correlation with each other. The sensory and motor cortices were joined together. They mainly were separated from their association cortices, which is consistent with the literature (Yeo et al., 2011).

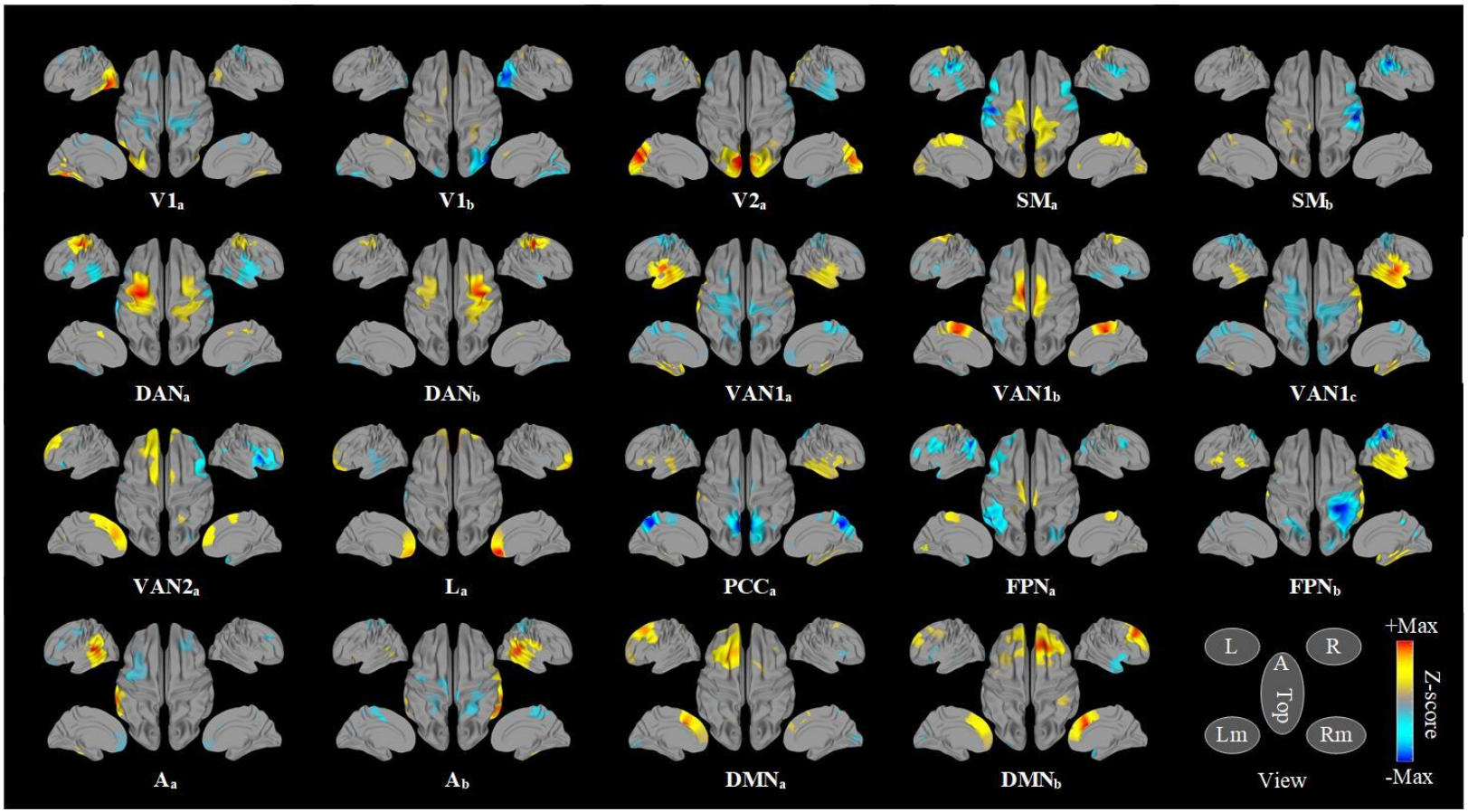

Figure 5-1 Spatial patterns of group-level HbO DOT RSNs.

Spatial patterns of 11 group-level HbO d-RSNs and their subnetworks. All spatial maps are shown on the standard FREESURFER cortical surface (gray/white matter interface) and thresholded ($p < .01$). V = visual, SM = somatomotor, DAN = dorsal attention network, VAN = ventral attention network, L = limbic, PCC = posterior cingulate cortex, FPN = frontoparietal network, A = auditory, DMN = default mode network, A = anterior, L/R = left/right, Lm/Rm = left/right medial wall. Numbers: subnetworks; Letter subscripts: multiple detection of subnetworks.

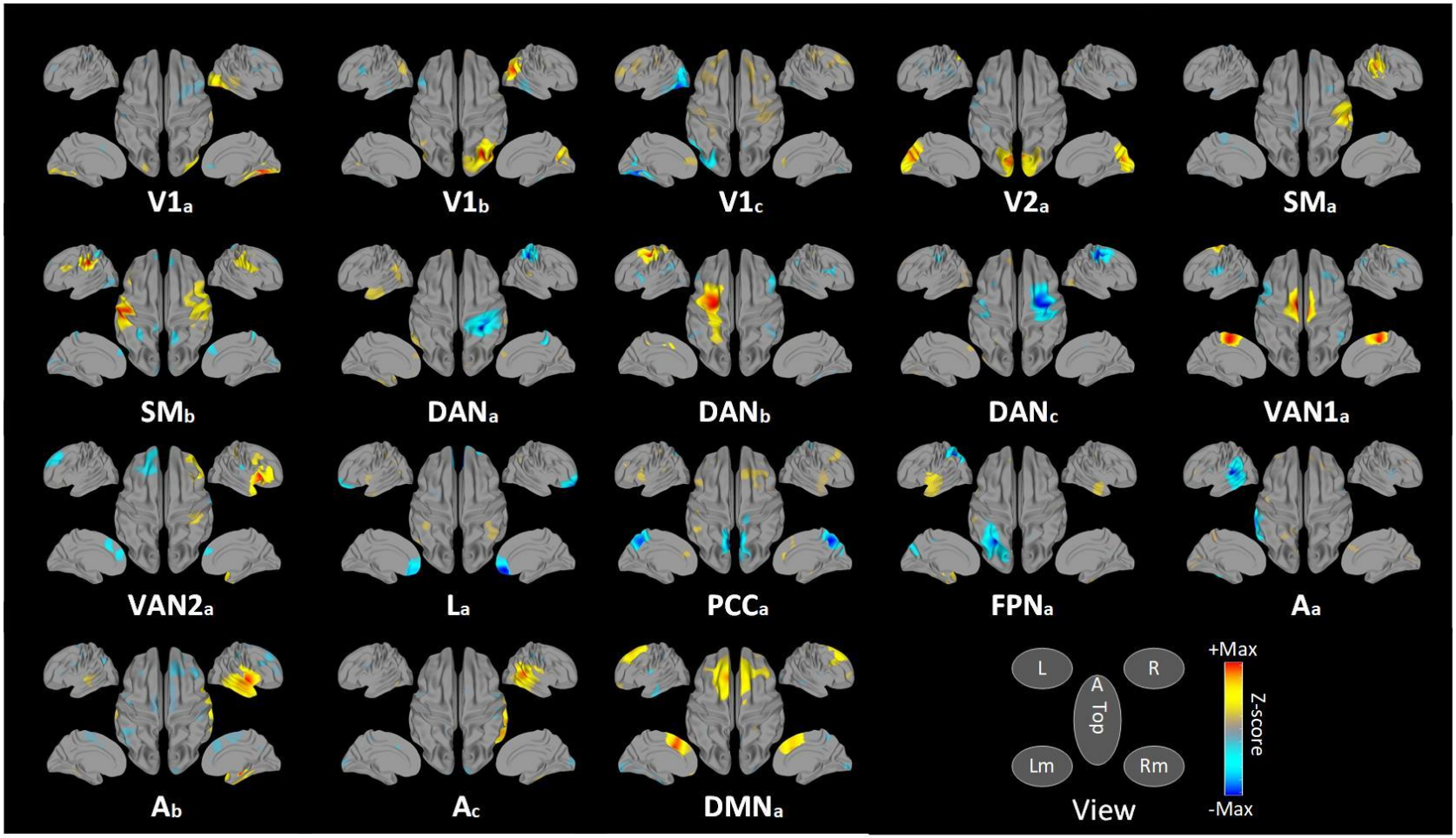

Figure 5-2 Spatial patterns of group-level HbR DOT RSNs.
Spatial patterns of 11 group-level HbR d-RSNs and their subnetworks illustrated in the same way as Figure 5-1.

Only one RSN was identified as the limbic RSN (L), which consisted of the ventral part of the SFG and the frontal pole. Bilateral symmetry was observed for this network with slight right hemispheric dominance. Similarly, only one RSN was identified covering the PCC. The reconstructed PCC primarily covered the precuneus with some spread to parts of the cuneus and paracentral lobule. Although the auditory regions were also present as active in a few d-RSNs, it was exclusively present in two d-RSNs with high left (Aa) and right (Ab) hemispheric dominance, respectively.

More distributed networks were also reconstructed beyond the regional networks described above. Two symmetric d-RSNs were identified as DAN, which primarily covered the frontal eye fields (DANa and DANb) bilaterally but had hemispheric dominance. A closely coordinating network with DAN to achieve attentional control is VAN which comprises the temporoparietal junction (TPJ), ventral frontal cortex (VFC) (Vossel et al., 2014), and parts of SFG (Yeo et al., 2011). Four d-RSNs were identified as two VAN subnetworks (VAN1 and VAN2). These d-RSNs primarily covered the TPJ (VAN1), VFC (VAN1a, VAN2a), and dorsal (VAN1) and ventral (VAN2) parts of SFG. VAN1a and VAN1b had bilateral symmetric patterns, whereas VAN1c and VAN2a showed hemispheric dominance.

As suggested by fMRI data, two d-RSNs were identified as FPN, a large-scale and widely distributed RSN (Yeo et al., 2011). These reconstructed d-RSNs primarily covered anterior brain regions: middle frontal gyrus (MFG) (FPNa) and IFG (FPNa); and posterior brain regions: inferior parietal lobe (FPNa and FPNb) and dorsal part of SFG (FPNa). The FPNa showed a bilateral network with both anterior and posterior nodes. In contrast, FPNb showed pronounced dominance in the right hemisphere and the absence of anterior nodes.

Finally, two d-RSNs were identified as the DMN, a large-scale and widely distributed network in fMRI, and the most widely studied f-RSN (Yeo et al., 2011). Both reconstructed DMN d-RSNs primarily covered parts of mPFC, the medial part of MFG, and the dorsal part of IFG. They showed left (DMNa) and right (DMNb) hemispheric dominance, respectively. Some spatial extent of the network was also present on the temporal pole (DMNb). These results demonstrate that the reconstructed d-RSNs and their subnetworks span regional cortical areas (mainly for basic sensory functions) as well as widely distributed cortical areas (mainly for higher-order functions). The spatial distributions of these d-RSNs collectively cover almost the entire superficial structures of the cortex, reach the depth as much as of PCC, and resemble f-RSNs in literature.

5.3.2 Spatial match of DOT RSNs to fMRI RSNs templates

The group-level spatial matching of HbO d-RSNs to f-RSNs templates yielded color-coded confusion matrices for the quantitative metrics of TD (Figure 5-3A) and SC (Figure 5-3C). Large positive TD and SC values for diagonal elements (boxed with black lines) confirmed the spatial similarity between the matched reconstructed d-RSN (horizontal axis) and the corresponding f-RSN template (vertical axis). Positive off-diagonal entries indicated possible confusion due to a d-RSN overlapping partially with the unmatched f-RSN template(s). This confusion is more prominent in closely spaced d-RSNs such as between SM and A, between PCC and V2, and between VAN/L and DMN.

Statistically, both TD and SC values from all matched pairs of d-RSNs and f-RSNs (white bars in Figure 5-3B and Figure 5-3D, respectively) were found to be significantly higher ($p < 1e-17$ and $p < 1e-34$ respectively, corrected) than those metric values from all unmatched pairs (blue bars in Figure 5-3B and Figure 5-3D), indicating that overall the group-level d-RSNs (Figure 5-1) were spatially similar to their matched templates.

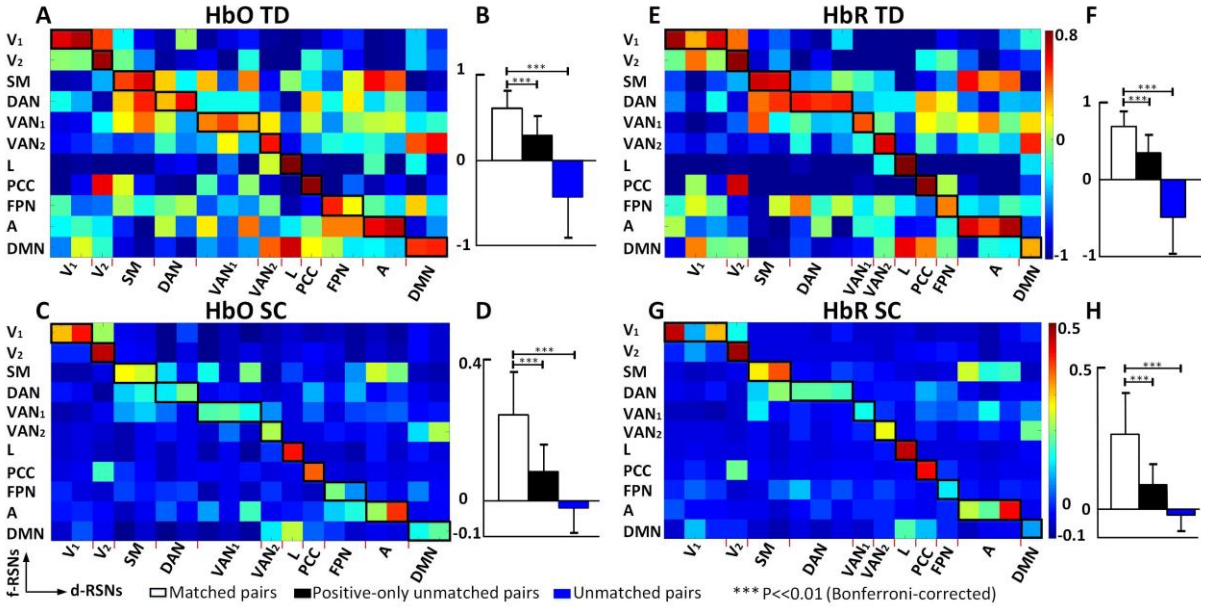

Figure 5-3 Group-level HbO confusion matrices between d-RSNs and f-RSNs template maps. (A) and (C) and HbR (E) and (G) chromophores and the quantitative metrics of TD (A) and (E) and SC (C) and (G). Means and standard deviations of metric data calculated from each confusion matrix for matched pairs (boxed by thick solid lines in diagonals), positive-only unmatched pairs, and unmatched pairs are presented for HbO TD (B), HbO SC (D), HbR TD (F), and HbR SC (H), together with their statistical differences tested using t-test (Bonferroni-corrected).

Furthermore, both TD and SC values from all matched pairs of d-RSNs and f-RSNs were found to be statistically significantly higher ($p < 1e\text{-}5$ and $p < 1e\text{-}7$ respectively, corrected)than those from positive-only unmatched pairs (black bars in Figure 5-3B and Figure 5-3D), which indicated that matched d-RSN and f-RSN pairs still had the highest spatial matching metric values in general. At the same time, there were some spatial overlaps between neighbored d-RSNs.

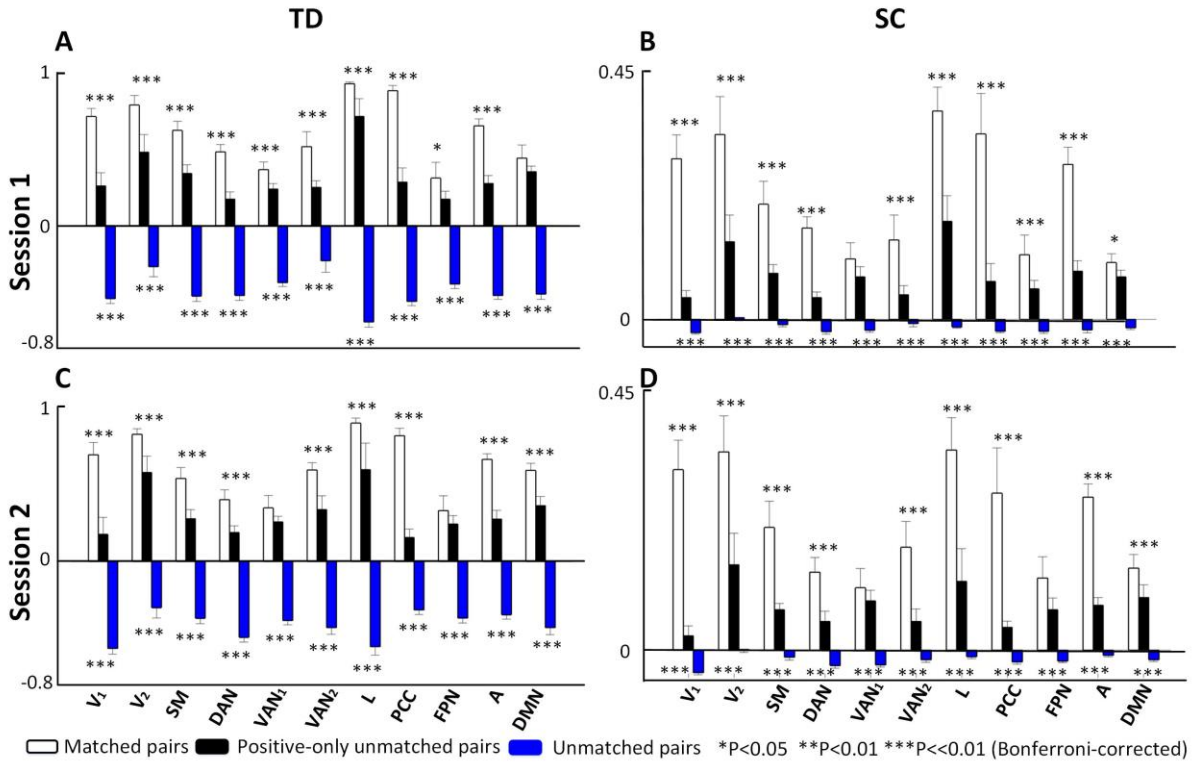

Figure 5-4 Comparison of participant-level HbO d-RSNs and f-RSNs template maps. Means and standard deviations of metric data for individual d-RSNs calculated from all participant-level confusion matrices for matched pairs (white bars), positive-only unmatched pairs (black bars), and unmatched pairs (blue bars) are plotted for TD (A and C) and SC (B and D) for two recording sessions, together with their statistical differences tested using t-test (Bonferroni-corrected).

Next, all TD and SC metric data were broken down for individual d-RSNs (see Section 5.2.3.1). The means and standard deviations of TD (Figure 5-4A and Figure 5-4C for sessions 1 and 2, respectively) and SC values (Figure 5-4B and Figure 5-4D for sessions 1 and 2, respectively) for matched pairs (white bars), unmatched pairs (blue bars), and positive-only unmatched pairs (black bars) were calculated from participant-level confusion matrices for each HbO d-RSN (horizontal axes). Mean values of both the TD and SC metrics from all matched pairs were significantly (at least $p < 1e\text{-}7$, corrected) higher than those from all corresponding unmatched

pairs in all d-RSNs and in both sessions, indicating that overall, the participant-level d-RSNs were spatially similar to their matched templates.

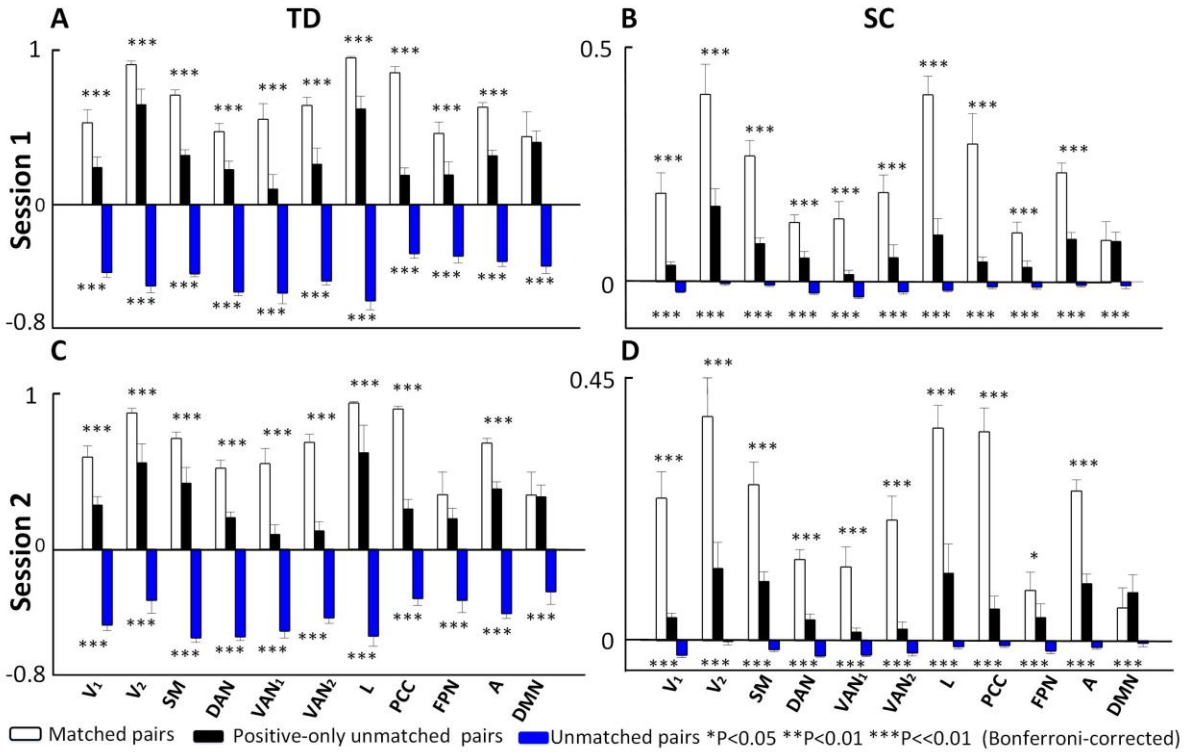

Figure 5-5 Comparison of participant-level HbR d-RSNs and f-RSNs template maps.

Means and standard deviations of metric data for individual d-RSNs calculated from all participant-level confusion matrices for matched pairs (white bars), positive-only unmatched pairs (black bars), and unmatched pairs (blue bars) are plotted for TD (A, C) and SC (B, D) for two recording sessions, together with their statistical differences tested using t-test (Bonferroni-corrected).

Moreover, in most d-RSNs from both recording sessions, the mean values of both the TD and SC metrics from the matched pairs were significantly (at least $p < .05$ with the majority of $p << .01$, corrected) higher than those from the positive-only unmatched pairs. It is noted that data from only three out of four conditions (two sessions and two metrics) for DMN, two out of four for FPN, and one out of four for VAN1 survived the Bonferroni correction, where all these d-RSNs involved more distributed spatial patterns. Furthermore, the d-RSNs with regional patterns (i.e., V, SM, L,

PCC, and A) exhibited higher TD and SC metric values (Figure 5-4) in general as compared to d-RSNs with distributed patterns (i.e., DAN, VAN, FPN, and DMN). A quantitative analysis (Figure 5-6) confirmed that these differences were statistically significant ($p < .01$, corrected) in HbO d-RSNs for both data sessions and metrics.

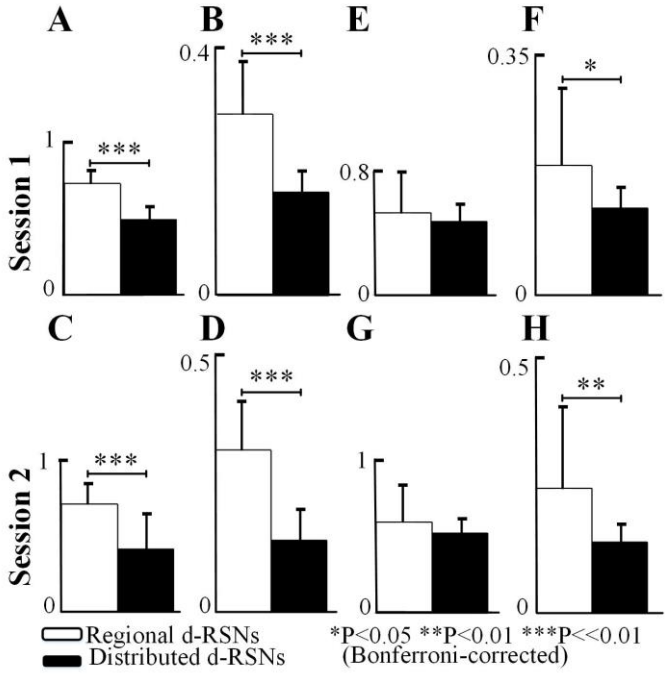

Figure 5-6 Comparison of the regional and distributed DOT RSNs.
Means and standard deviations of quantitative metric data for regional (white bar) and distributed (black bar) d-RSNs calculated from each group-level confusion matrix for matched pairs are plotted for two contrasts, two recording sessions, and two metrics, together with their statistical differences tested using t-test (Bonferroni-corrected). (A) HbO, session 1, TD; (B) HbO, session 1, SC; (C) HbO, session 2, TD; (D) HbO, session 2, SC; (E) HbR, session 1, TD; (F) HbR, session 1, SC; (G) HbR, session 2, TD; (H) HbR, session 2, SC.

5.3.3 HBR DOT RSNs and their comparisons with HBO DOT RSNs

Eighteen brain-wide d-RSNs were identified from HbR data (see Section 5.2.2), yielding a total of eleven unique d-RSNs, and five of them suggest subnetworks (Figure 5-2). Note that only two IC (data not shown) could not be matched to the template set. Generally, the spatial patterns

of HbR d-RSNs resembled those of HbO d-RSNs. Meanwhile, some minor differences were also observed. Firstly, the HbR d-RSNs exhibited less crosstalk between RSNs than HbO d-RSNs. For example, HbO DANa, VAN1a, VAN1c, PCCa, and FPNb included more of the lateral temporal lobe (Figure 5-1) than the corresponding HbR d-RSNs (Figure 5-2). Secondly, some bilateral HbO d-RSNs, such as DANa and DANb, were observed as less bilateral in HbR d-RSNs, i.e., DANb and DANc, respectively.

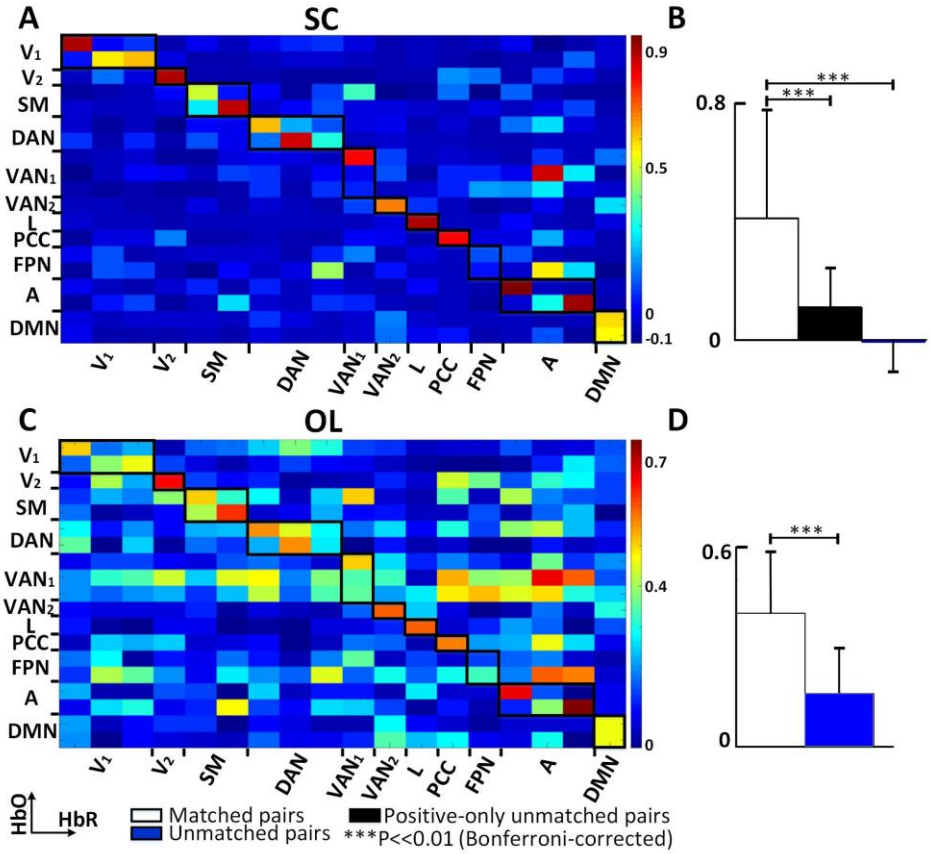

Figure 5-7 Comparison between HbO and HbR DOT RSNs.
Group-level confusion matrices between HbO and HbR d-RSNs for two quantitative metrics of SC (A) and OL (C). Means and standard deviations of metric data calculated from each confusion matrix for matched pairs (boxed by thick solid lines in diagonals), positive-only unmatched pairs (not available for OL), and unmatched pairs are plotted for SC (B) and OL (D), together with their statistical differences tested using t-test (Bonferroni-corrected).

Similar to HbO (see Section 5.3.2), at the group level, the spatial similarities between matched

reconstructed d-RSNs and corresponding f-RSN templates were found in both TD (diagonal elements in Figure 5-3E) and SC metrics (diagonal elements in Figure 5-3G). The confusions observed among the closely spaced HbO d-RSNs, i.e., between SM and A, PCC ad V2, and VAN/L and DMN, are also similarly observed in HbR d-RSNs. Similar to HbO, both the TD and SC values from all matched pairs of d-RSNs and f-RSNs (white bars in Figure 5-3F and Figure 5-3H, respectively) were found to be significantly higher ($p < 1e\text{-}19$ and $p < 1e\text{-}39$, respectively, corrected) than metric values from all unmatched pairs (blue bars in Figure 5-3F and Figure 5-3H), indicating that overall the group-level HbR d-RSNs (Figure 5-2) were spatially similar to their assigned templates.

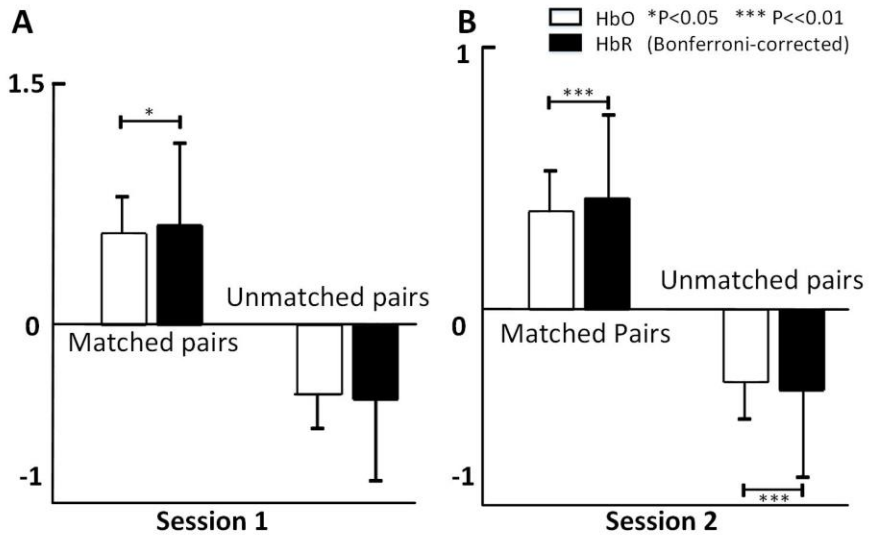

Figure 5-8 Quantitative comparison of group-level HbO and HbR d-RSNs using TD. Means and standard deviations of TD metric data for HbO d-RSNs (white bars) and HbR d-RSNs (black bars) calculated from group-level confusion matrices (Figure 5-3) for matched pairs and unmatched pairs are plotted for recording session 1 (A) and session 2 (B), together with their statistical differences tested using t-test (Bonferroni-corrected).

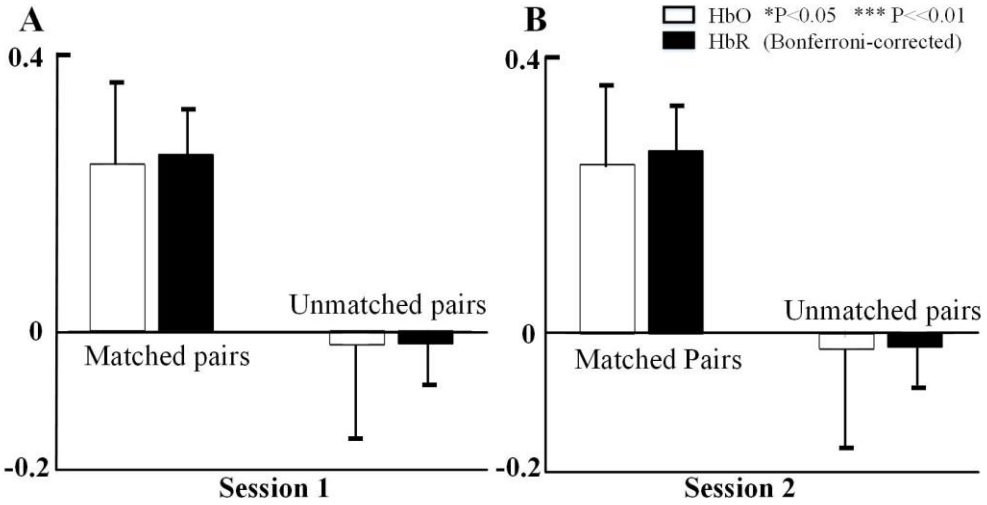

Figure 5-9 Quantitative comparison of group-level HbO and HbR d-RSNs using SC. Means and standard deviations of SC metric data for HbO d-RSNs (white bars) and HbR d-RSNs (black bars) calculated from group-level confusion matrices (Figs. 3B and E) for matched pairs and unmatched pairs are plotted for recording session 1 (A) and session 2 (B), together with their statistical differences tested using t-test (Bonferroni-corrected).

Furthermore, both the TD and SC values from all matched pairs of d-RSNs and f-RSNs were found to be statistically significantly higher ($p < 1e\text{-}5$ and $p < 1e\text{-}5$, respectively, corrected) than those from positive-only unmatched pairs (black bars in Figure 5-3F and Figure 5-3H), which indicated that matched HbR d-RSN and f-RSN pairs had the highest spatial matching metric values in general. At the same time, there were some spatial overlaps between neighbored d-RSNs.

When TD and SC metric data were broken down for individual d-RSNs (Figure 5-5), similar to HbO RSNs, mean TD and SC values from all matched pairs were significantly (at least $p < 1e\text{-}3$, corrected) higher than those from all unmatched pairs in all d-RSNs and both sessions. Moreover, for most d-RSNs from both data recording sessions, the mean TD and SC values from the matched pairs were significantly ($p << .01$ with one $p < .05$, corrected) higher than those from the positive-only unmatched pairs. It is noted that data from none of the four conditions (two sessions and two metrics) for DMN and only three out of four for FPN survived the Bonferroni

correction, where all these d-RSNs involved more distributed spatial patterns. Also, similar to HbO d-RSNs, the networks with regional patterns (i.e., V, SM, L, PCC, and A) exhibited high TD and SC metric values in general as compared to the d-RSNs with distributed patterns (i.e., DAN, VAN, FPN, and DMN) (Figure 5-5). A quantitative analysis (Figure 5-6) confirmed that these differences in the SC metric were statistically significant in both sessions (at least p< .05, corrected).

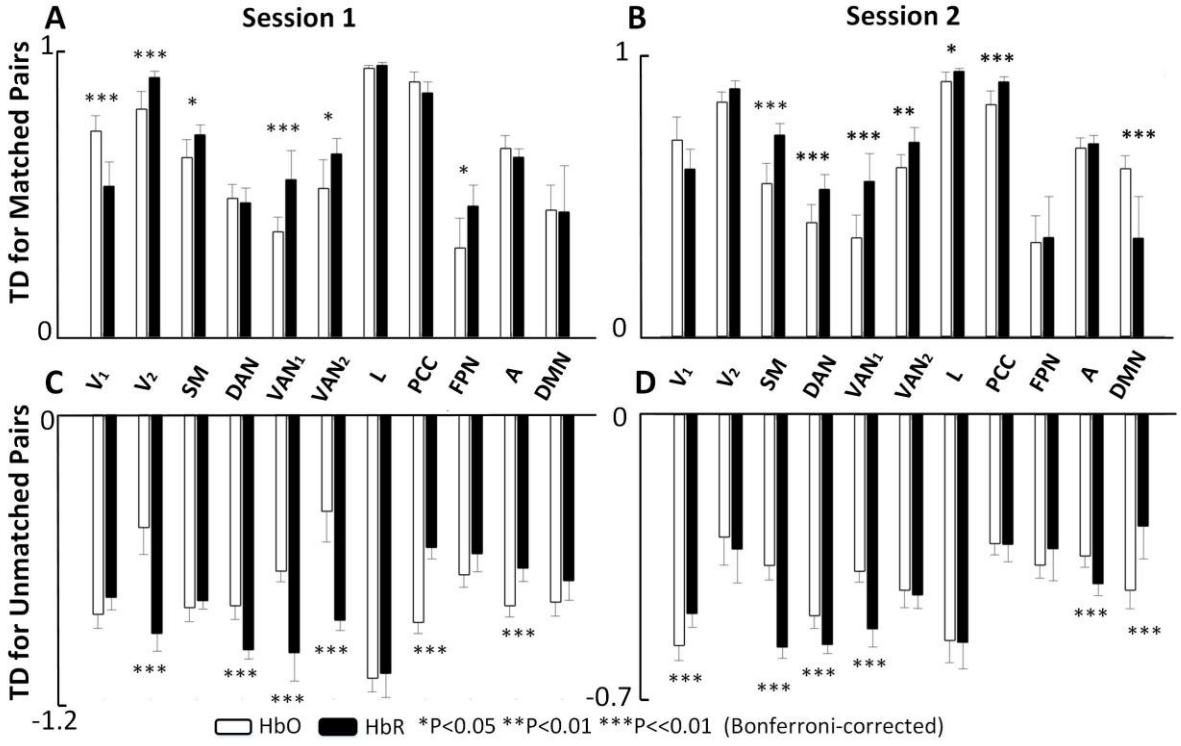

Figure 5-10 Quantitative comparison of participant-level HbO and HbR d-RSNs using TD. Means and standard deviations of TD metric data for HbO d-RSNs (white bars) and HbR d-RSNs (black bars) calculated from participant-level confusion matrices for matched pairs (A-B) and unmatched pairs (C-D) are plotted for the two recording sessions, together with their statistical differences tested using t-test (Bonferroni-corrected).

The direct comparison of reconstructed d-RSNs of the two chromophores using SC and OL metrics yielded the group-level confusion matrices (Figure 5-7, for brevity, only data from one session were presented). High positive values for both SC (Figure 5-7A) and OL (Figure 5-7C) in the diagonal elements of the corresponding confusion, matrices indicate that the HbO and HbR d-

RSNs generally matched with each other, supporting the observations in the indirect comparisons using f-RSN templates as discussed above. Similar to the comparisons against f-RSN templates, the confusions among the closely spaced d-RSNs, i.e., between SM and A, PCC ad V2, and VAN/L and DMN, were similarly observed. Statistically, both SC and OL values from all matched pairs of HbO and HbR d-RSNs (white bars in Figure 5-7B and Figure 5-2D, respectively) were found to be significantly higher ($p < 1e\text{-}41$ and $p < 1e\text{-}18$ respectively, corrected) than metric values from all unmatched pairs (blue bars in Figure 5-7B and Figure 5-2D).

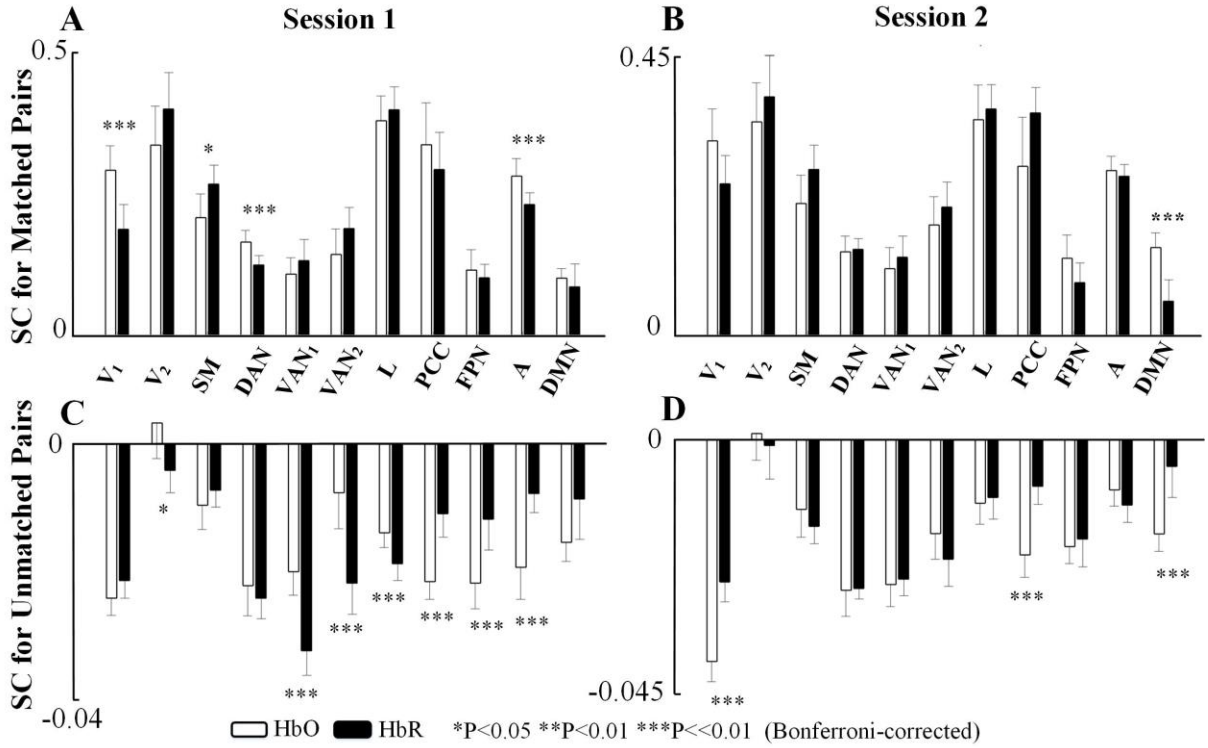

Figure 5-11 Quantitative comparison of participant-level HbO and HbR d-RSNs using SC. Means and standard deviations of SC metric data for HbO d-RSNs (white bars) and HbR d-RSNs (black bars) calculated from participant-level confusion matrices for matched pairs (A-B) and unmatched pairs (C-D) are plotted for the two recording sessions, together with their statistical differences tested using t-test (Bonferroni-corrected).

Furthermore, the SC values from all matched pairs of HbO and HbR d-RSNs were found to be statistically significantly higher ($p < 1e\text{-}8$, corrected) than from positive-only unmatched pairs

(black bar in Figure 5-7B). Beyond indicating similar HbO and HbR d-RSN patterns in general, it was interesting to note that the template matching-based comparisons further indicated that d-RSNs reconstructed from HbR data were better matched to f-RSN templates than HbO d-RSNs (Figure 5-8). For both sessions 1 and 2, the mean TD metric values of HbR were statistically higher than those from HbO in matched pairs ($p < .05$ and $p < 1e\text{-}3$, respectively, corrected). In comparison, the mean values of the TD metric from HbR were statistically lower than those from HbO in unmatched pairs in session 2 ($p < .01$, corrected).

Table 5-1 Two-way ANOVA tests on TD and SC metric values.

	TD				**SC**	
	Source of variation	*F*	*Prob>F*		*F*	*Prob>F*
HbO	Pairs	5914.4	**0**	Pairs	1557.2	**0**
	Sessions	0.16	**0.69**	Sessions	0.15	**0.70**
	Interaction	0.62	**0.43**	Interaction	0.00	**0.96**
		F	*Prob>F*		*F*	*Prob>F*
HbR	Pairs	6631.5	**0**	Pairs	1241.8	**0**
	Sessions	1.06	**0.30**	Sessions	0.25	**0.62**
	Interaction	0.98	**0.32**	Interaction	0.21	**0.65**

A similar trend was also observed when TD data from individuals were grouped into individual RSNs for comparisons (Figure 5-10). Specifically, a total of thirteen significant differences (at least $p < 0.05$, corrected) over TD data between HbO and HbR d-RSNs were observed for matched pairs from the two recording sessions, in which eleven of these showed significantly higher TD values from HbR than those from HbO d-RSNs. For the unmatched pairs, a total of twelve significant differences (at least $p < 1e\text{-}3$, corrected) between HbO and HbR were observed for the two recording sessions, and eight of these indicate significantly lower TD values from HbR than those from HbO. Such statistically significant differences between HbO and HbR were not observed in the metric of SC at the group level (Figure 5-9), and the trend for similar

differences was also not obviously observable at the participant level (Figure 5-11).

5.3.4 Reproducibility of DOT RSNs along time and across participants

The ANOVA analysis (Table 5-1) on TD with samples from individuals showed a strong significant effect of the factor Pairs, i.e., between matched and unmatched pairs, in HbO (F=5914.4, P< .0000) and HbR (F=6631.5, P< .0000) d-RSNs. In contrast, no significant effect was found for the factor Sessions in HbO (F=0.16, P< .69) and HbR (F=1.06, P< .30) d-RSNs.

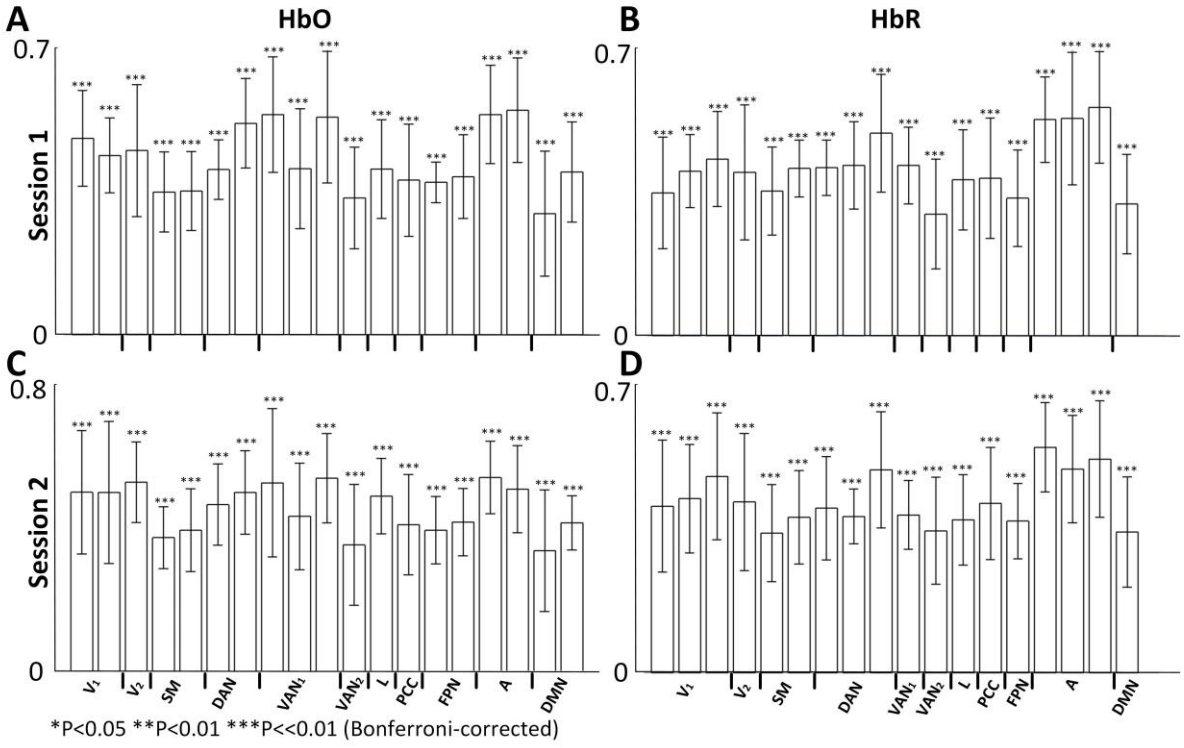

Figure 5-12 Spatial correlations between group-level and participant-level DOT RSNs. Means and standard deviations of SC metric data between unthresholded participant-level d-RSNs and unthresholded group-level d-RSNs for both HbO (A and C) and HbR (B and D) for two recording sessions, together with their statistical differences tested using t-test (Bonferroni-corrected).

Similarly, for SC, the ANOVA test showed a strong significant effect of the factor Pairs in both HbO (F=1557.2, P< .0000) and HbR d-RSNs (F=1241.8, p< .0000). In contrast, no significant effect was found for the factor Sessions in both HbO (F=0.15, p< .70) and HbR d-RSNs (F=0.25,

p< .62). Moreover, no significant interactions were present between these two factors for TD and SC metrics in both HbO and HbR. These data indicated the reproducibility of reconstructed d-RSNs across different datasets and the consistency of reconstructed d-RSNs in different individuals. Furthermore, as described in Sections 5.3.2 and 5.3.3, the differences in TD and SC metric values between d-RSNs with regional and distributed patterns (Figure 5-4, Figure 5-6, and Figure 5-5) and the differences of TD metric values between HbO and HbR d-RSNs (Figure 5-8 and Figure 5-10) were consistently preserved across the two recording sessions (both significant or insignificant differences), which supported the reproducibility of reconstructed d-RSNs across different datasets.

The mean and standard deviation of SC values between the unthresholded participant-level and group-level d-RSNs calculated for session 1 (Figure 5-12A, B) and session 2 (Figure 5-12C, D) for HbO and HbR d-RSNs were all positive-valued and statistically greater (at least $p < 1e\text{-}3$, corrected) than zero correlations (see Section 5.3.3). It was further observed that the SC values across different d-RSNs showed consistent patterns between data from two recording sessions. These facts directly indicated the consistency of reconstructed d-RSNs from both HbO and HbR in different individuals.

5.4 Discussion

The present study tested BW-DOT in reconstructing resting-state brain networks based on near-infrared spectroscopy with a cap-based whole-head optode montage. We uncovered a comprehensive set of RSNs, and their subnetworks based on both HbO and HbR signals, collectively covering the majority of the human neocortex. The spatial patterns of these reconstructed RSNs exhibited high similarities to template maps of fMRI RSNs and between HbO

and HbR. Furthermore, these reconstructed RSNs showed high reproducibility among recording sessions within and across participants.

5.4.1 Reconstruction of multiple brain-wide RSNs

The present study demonstrated the feasibility of reconstructing brain-wide multiple RSNs using a new DOT technology. Our results indicate the similar spatial patterns of DOT-based RSNs to corresponding RSNs from fMRI, consistent with previous DOT-based RSN studies (White et al., 2009, White et al., 2012, Ferradal et al., 2016). Beyond that, due to the use of cap-based, whole-head optode montage, our results also report a large number of simultaneously reconstructed RSNs, which is close to the common number of RSNs, e.g., 10 (Damoiseaux et al., 2006b) or 17 (Yeo et al., 2011), studied with fMRI. In the previous DOT studies, only part of the neocortex was imaged, leading to the investigation of limited RSNs, such as visual networks (White et al., 2012), somatomotor networks (White et al., 2009), and auditory networks (Ferradal et al., 2016). There are also DOT RSN studies that have reported more distributed networks, e.g., DMN, DAN, and FPN (Eggebrecht et al., 2014, Aihara et al., 2020). However, due to the limited spatial coverage of optodes, these studies either reported missing nodes for distributed networks (Eggebrecht et al., 2014) or limited functional connectivity between pre-selected anatomic regions (Aihara et al., 2020).

Our present study is based on the achievements of mapping individual RSNs in these reported DOT studies and, meanwhile, attempts to advance DOT-based technologies in simultaneously mapping a large number of collectively brain-wide RSNs. Specifically, mapping a large number of brain-wide RSNs is significant because 1) it provides a better perspective on the membership of distributed nodes for individual RSNs; 2) it makes it possible to map whole-brain inter-RSN connectivity maps as in fMRI (Bressler and Menon, 2010), which provide insights to basic

neuroscience questions (De Luca et al., 2006, Damoiseaux et al., 2006b) and potential for clinical use (Bressler and Menon, 2010). As an example of defining membership nodes for individual RSNs, our DOT results revealed mPFC and PCC (Figure 5-1 and Figure 5-2), which were both missed in previous DOT RSN studies (Eggebrecht et al., 2014), similar to the anterior and posterior subnetworks of DMN, respectively, as reported in previous fMRI studies. This was achieved as the cap-based whole-head montage has filled the gap in the frontal and medial regions previously unavailable. The identification of these two RSNs is of clinical value as their connectivity changes have been associated with normal aging (Buckner et al., 2008, Andrews-Hanna et al., 2007) and deterioration related to Alzheimer's disease (Sorg et al., 2007).

As mentioned above, the spatial patterns of reconstructed RSNs (Figure 5-1 and Figure 5-2) collectively resemble a comprehensive set of RSNs established in fMRI (Yeo et al., 2011). These networks span regional and distributed cortical areas based on their functional differences. A quantitative comparison between our present results to previously reported DOT RSNs is challenging because of differences in, for example, FOV, optode density, reconstruction methods, statistical methods, and the lack of availability of standard template maps. It is common to validate DOT RSNs with reference to well-established fMRI RSNs (Wheelock et al., 2019). Therefore, the present study has utilized fMRI data from a large-scale study (Yeo et al., 2011) for quantitative assessments of reconstructed DOT RSNs. The adopted quantitative metrics for spatial patterns indicate the spatial similarity between reconstructed DOT RSNs and fMRI RSNs at both group (Figure 5-3) and participant levels (Figure 5-4 and Figure 5-5). These similarities in spatial patterns were consistent in data from two recording sessions.

Beyond quantitative metrics, we observe similarities and differences between reconstructed DOT RSNs and template maps based on visualizations of their spatial patterns (Figure 5-1 and

Figure 5-2). Firstly, while most of the reported fMRI RSNs have bilateral symmetric patterns (Biswal et al., 1995, Damoiseaux et al., 2006b, Yeo et al., 2011, Agosta et al., 2012), our results, on the other hand, reveals that the RSNs are both bilateral as well as lateralized. For example, DANa and DANb are bilateral, while both also indicate hemispheric dominance. Similarly, SMa shows bilateral distributions, while SMb exhibits lateralized patterns. Other bilateral patterns appear in symmetric cortical regions across the two hemispheres that are close to each other, such as V2a, VAN1b, La, and PCCa. On the other hand, other lateralized patterns include V1a, V1b, Aa, Ab, DMNa, and DMNb. It is also important to note that these lateralized d-RSNs appear as pairs with hemisphere-symmetric spatial patterns, e.g., V1a vs. V1b, Aa vs. Ab, and DMNa vs. DMNb. While less reported, lateralized RSN patterns have been reported in fMRI literature (Smith et al., 2009b). Furthermore, the phenomena of hemispheric dominance and localization have been more widely reported in high-sampling rate imaging modalities, e.g., fNIRS (Medvedev, 2014) and EEG source imaging studies (Thatcher et al., 2007, Yuan et al., 2012, Ding et al., 2014, Li et al., 2018).

Secondly, while most previous DOT studies have reported RSNs, our results indicate subnetworks among several RSNs. This is consistent with fMRI literature (Smith et al., 2009b). The reference templates for validating RSNs in the present study also include subnetworks (Yeo et al., 2011). Specifically, our results indicate subnetworks for visual networks and VAN (Figure 5-1 and Figure 5-2), while no subnetworks were detected in RSNs that were otherwise reported in the reference templates. It is worth noting that visual network subnetworks are more prominent than other RSNs, a pattern similar to several fMRI (Smith et al., 2009b) and EEG RSN studies (Li et al., 2018). In fMRI, these subnetworks could be detected more easily with an increased order of components in ICA analysis (Smith et al., 2009b).

The phenomena of differences between DOT and fMRI RSNs on hemisphere symmetry and detectability of subnetworks might potentially be due to the intrinsic dynamic nature of RSNs themselves (Deco et al., 2011). The dynamic nature of brain networks in individual RSNs, and the whole-brain level has been documented in fMRI data of humans (Allen et al., 2014a, Chang and Glover, 2010, Hindriks et al., 2016) and animals (Matsui et al., 2016, Gutierrez-Barragan et al., 2019). Our results, therefore, seem to suggest the dynamic nature of reconstructed RSNs because of the presence of subnetworks for several RSNs, where symmetric lateralized RSNs could also be considered as paired subnetworks. The ability of fNIRS and EEG source imaging to detect subnetworks may also be attributed to the high data sampling rate that enhances the discriminability of subnetworks that dynamically form a network.

5.4.2 HbO vs. HbR DOT RSNs

Previous task-based studies have found differences in using HbO and HbR contrasts (Devor et al., 2005, Culver et al., 2005, Sheth et al., 2004) in mapping brain activations, which have been attributed to different signal-noise-ratios (White et al., 2009) and compartmental sensitivity (Dunn et al., 2005) for these optical contrast signals. However, only small differences have been observed in previous DOT-based RSN studies (White et al., 2012, White et al., 2009, Eggebrecht et al., 2014). Our study extends this similar observation from individual RSNs in previous studies to a set of multiple collectively brain-wide RSNs. Specifically, reconstructed RSNs from both HbO (Figure 5-1) and HbR (Figure 5-2) are similar to each other in general when they are compared as an entire set (Figure 5-7). Individual RSNs are also visually very similar to each other, especially for visual, somatomotor, DAN, limbic, PCC, and auditory networks (Figure 5-1 Figure 5-2). At the same time, the quantitative metrics (Figure 5-8 and Figure 5-11) further reveal that HbR RSNs are slightly but statistically significantly better aligned with fMRI RSNs, which is probably

because the BOLD contrast in fMRI signals is primarily sensitive to paramagnetic HbR molecules (Buxton, 2013). On the other hand, HbO RSNs reconstructed from BW-DOT seem more distributed than HbR RSNs in a few individual networks, i.e., DANa, DANb, and FPNa, which are more consistent with fMRI RSNs. Meanwhile, HbO RSNs also exhibit over-sensitivity in the lateral temporal lobe that is shown up in multiple networks (Figure 5-1), which are not consistent with fMRI RSNs. In summary, HbO- and HbR-based DOT RSNs are, in general, consistent with each other. Some small differences between them indicate complementary benefits of each contrast, which might also suggest the usefulness of total hemoglobin signals, i.e., the combination of HbO and HbR, in mapping RSNs (Devor et al., 2005, Culver et al., 2005, Sheth et al., 2004).

5.4.3 Reproducibility of DOT RSNs

While recent fMRI studies have indicated that RSNs are dynamic (Allen et al., 2014a) and certain parts of the human cortex, e.g., the anterior cingulate cortex, medial prefrontal cortex, hippocampal network, and parietal and temporal networks, show functional variations throughout the day (Park et al., 2012), the fundamental characteristics of RSNs are in general reproducible across time and participants (Damoiseaux et al., 2006b, Chen et al., 2008, Zuo et al., 2010). Our findings support this notion and indicate that generally, HbO and HbR RSNs detected in DOT are consistent in terms of their spatial patterns and contrast differences across different recording sessions (Figure 5-4, and Figure 5-8; Figure 5-6, Figure 5-5, Figure 5-10, Figure 5-11, Figure 5-9; Table 5-1) and participants (Figure 5-12). These facts also suggest the reliability of our proposed framework using a cap-based whole-head optode montage and the high repeatability (consistency across sessions) and robustness (consistency across participants) of HbO and HbR RSNs reconstructed from this framework. In the current DOT RSN literature, quantitative investigations on the reproducibility of RSNs are largely missing. Only a few RSNs, including SM and visual

networks, have been reported to be qualitatively consistent across sessions (White et al., 2009) and participants (White et al., 2012). Our data, therefore, provide important evidence on the reproducibility of RSNs reconstructed from fNIRS signals, which is critical for DOT RSNs to be reliably used as, for example, biomarkers in the monitoring time course of disease progression and/or effects of drugs (Chen et al., 2008).

6. Coactivation pattern analysis of DOT resting-state data

This chapter has been adapted from the following manuscript under review:

Khan, A. F., Fan Zhang, Guofa Shou, Han Yuan, and Lei Ding. " Transient brain-wide coactivations and structured transitions revealed in hemodynamic imaging data."

6.1 Introduction

In Chapter 5, we reconstructed brain-wide DOT RSNs and demonstrated their similarities to fMRI RSNs reported in the literature. These networks were static, i.e., it was assumed that the brain's FC was stationary across the scan. However, the brain's FC is nonstationary and has been studied by hypothesizing different neurophysiological phenomena as the basis for the observed correlation-based FC described in Section 2.3. To further investigate these structured neurophysiological phenomena that are possibly responsible for the formation of FCs in the human brain, the present study utilized the BW-DOT technique to map spatiotemporal structures in hemodynamic signals. The whole-head coverage provides an ability to study brain-wide transient events, e.g., CAPs and global propagating waves, and a means for estimating GS that is not available in patch-based DOT systems. We reasoned that these capacities of BW-DOT, together with other denoising approaches (e.g., 8 SS channels), would also improve our ability to characterize the temporal dynamics of these neuronal events and better distinguish those of neuronal or non-neuronal origins.

The present pilot study investigated the spatiotemporal structures in DOT data from thirteen healthy participants using a CAP framework shown in Figure 6-1. We first estimated cortical RSNs based on HbR, using participant-specific MRI head models and state-of-the-art data preprocessing and reconstructions algorithms. We then adopted a framewise clustering approach on participant-

level spatiotemporal RSN data to obtain CAPs with and without the GS regression. We further analyzed the spatial, temporal, and transitional properties of detected CAPs. Lastly, we investigated the differences in global CAPs (indicating global activity) obtained with and without the GS regression regarding their plausible neural relevance and relationship to GS time series.

6.2 Materials and Methods

6.2.1 Participants, experimental and data protocols

The study was approved by IRB at the University of Oklahoma, and written informed consent was obtained from every participant before the study. A total of 20 participants were recruited for the study without any neurological or neuropsychiatric disorders. Three participants were not able to complete all data recordings. In addition, resting-state data from four participants were excluded from the present study due to poor data quality (primarily excessive motions). Thereafter, resting-state data from thirteen participants (31.7±9.3 years, five females, eight males) were included in the present study. We utilized the participants' data and experiment protocols described in Section 5.2.1.

6.2.2 Preprocessing of fNIRS data

The preprocessing of fNIRS data followed the protocol described in Section 3.4.1 and (Zhang et al., 2021). Briefly, raw channel-wise light intensity data were transformed to optical densities (OD) by measuring their log ratios against the channel-wise means over the entire recording window as baselines (Huppert et al., 2009). Data from each session were preprocessed separately. Power spectral densities (PSDs) of OD data were calculated using Welch's method (window length: 60 s, 50% overlapping) (Huppert et al., 2009). The LS-channel OD data showing no visible heartbeat power peaks in the frequency range of 0.8-1.6 Hz were discarded (possible inadequate optode-scalp contact).

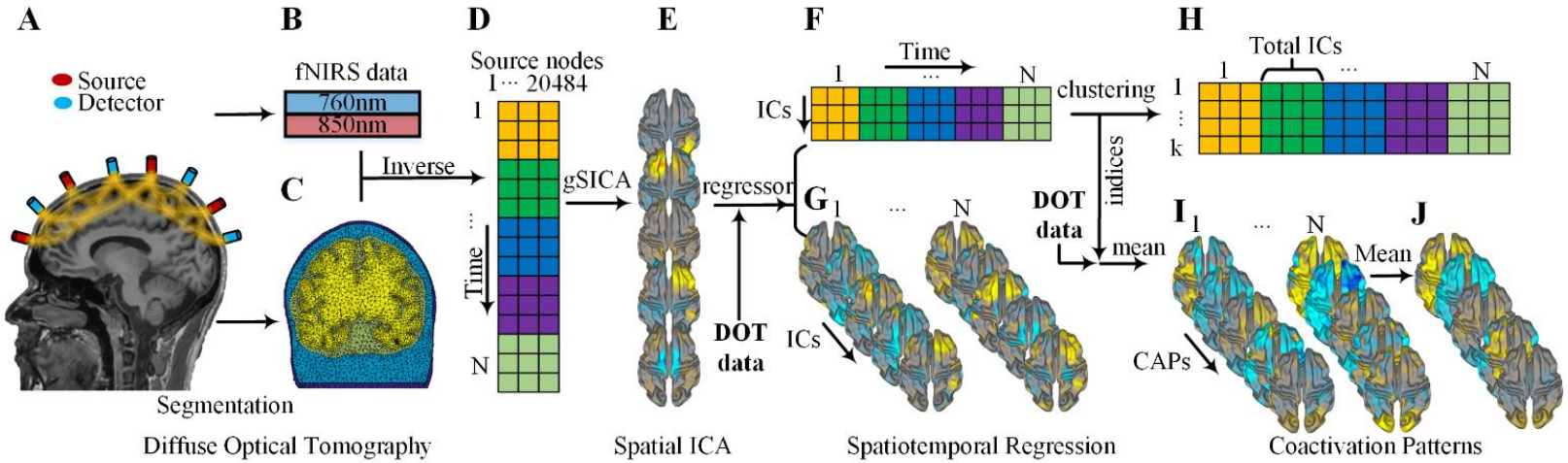

Figure 6-1 CAP framework.

The framework for reconstructing brain-wide CAPs from individual timeframe data of DOT. Diffuse optical tomography (DOT) consists of (A) the cap-based high-density optode placement system; (B) continuous-wave dual-wavelength (760 mm and 850 mm) light intensity fNIRS measurements; (C) realistic finite-element head models segmented from individual participant MRI data; and (D) inversely estimated cortical distribution of HbR concentration changes. (E) group-level Spatial ICA (gSICA) on temporally concatenated DOT data (D) across N participants. Spatiotemporal regression (STR) performs (F) spatial regression to estimate participant-level time courses of ICs (group-level IC spatial maps as regressors and DOT data as responses); and (G) temporal regression to estimate participant-level spatial maps of ICs (participant-level IC time courses as regressors and DOT data as responses). CAPS: The (H) participant-level cluster centroids (k × number of ICs) are obtained via the k-means++ clustering analysis on temporally concatenated IC time courses. The clustering indices are used to average DOT timeframe data to obtain (I) participant-level spatial maps of CAPs; and (J) group-level spatial maps of CAPs.

As the sampling frequency of DOT (6.25 Hz) was sufficiently high, resting OD data were then bandpass filtered at 0.008-0.2 Hz (Huppert et al., 2009), in order to retain useful information in the higher frequency band up to 0.2 Hz (Smith et al., 2012). Bad segments corresponding to excessive head motions were identified based on the metric of GVTD (Sherafati et al., 2020b). After this step, 73.4% ±7.5 of the data in participants were retained. In order to remove the physiological noise related to superficial tissue absorption, motion, and pulse/respiration-related variations (Zhang et al., 2019, Zhang et al., 2021, Khan et al., 2021, Cheong et al., 2020), we computed regressors based on time courses of 8 SS channels that were evenly distributed across the scalp and removed them from LS-channel OD data using general linear model regression (referred to as the SS regression). Note that unlike Section 3.4.1, we did not perform GS regression in the present study as there is evidence of neuronally-relevant information in the GS (Murphy and Fox, 2017).

6.2.3 Brain-wide DOT resting-state networks

DOT forward modeling and the inverse solution was conducted and used as described in Sections 3.2 and 3.3, respectively. The source space was defined as nodes inside the brain (contained by the pial surface) within 45 mm of the scalp. DOT inverse volumetric data of individuals were mapped to individual cortical surfaces defined as the gray and white matter interface. The projected cortical DOT data from individuals were concatenated and subjected to a group-level spatial ICA (Calhoun et al., 2009) (Figure 6-1E). The number of ICs was empirically set to 20 (Khan et al., 2021). The participant-level IC spatial maps (Figure 6-1G) and time courses (Figure 6-1F) were obtained via the back-projection using the dual spatiotemporal regression, STR (Beckmann et al., 2009, Calhoun et al., 2009). Group-level spatial maps of ICs were then obtained by averaging corresponding IC spatial maps from all individuals.

6.2.4 Estimations of CAPs and their spatial, temporal, and transitional properties

Time courses of 20 DOT RSNs (i.e., ICs) from all participants were concatenated and subjected to a k-means clustering analysis to find distinct CAPs with DOT RSNs as building blocks. To remove scale discrepancies between participants and ICs, the time course of each IC was normalized in each participant to obtain z-scores. After that, all participant-level z-score data for corresponding ICs were temporally concatenated (Figure 6-1F). The k-means++ clustering using the Euclidean distance metric (Arthur and Vassilvitskii, 2006) was applied to these concatenated z-scored IC timeframe data (20 ICs × # of time points from all participants) on the time dimension to yield k clusters. The IC timeframes (each is a vector of 20 elements) from the same participant that were classified into the same cluster were firstly averaged to generate the participant-level centroids (Figure 6-1H), which represented the geometric center of the subspace expanded by all timeframe vectors belonging to the same cluster in a 20-dimensional space. Next, the participant-level spatial maps of CAPs (Figure 6-1I) were obtained as an average of the DOT timeframe data using cluster indices obtained from clustering. The group-level spatial maps of CAPs (Figure 6-1J) were obtained via averaging participant-level CAPs across all participants. Note that the participant-level CAPs were obtained in order to perform statistical analyses on spatial, temporal, and transitional metrics discussed in this section to characterize CAPs using participants as samples. To evaluate the spatial link among all CAPs at the group level, the distances between their cluster centroid vectors were calculated and projected onto a 3D space using a multidimensional scaling tool from MATLAB, i.e., cmdscale.m (Seber, 2009). Clustering was repeated with different k values ($6 \leq k \leq 30$) (see most results in Figure 6-4A). The curves of explained variance (i.e., ratio of between-cluster variance to the total variance) and explained variance gain were plotted to help choose an optimal cluster size, i.e., k (Figure 6-4B). With an

elbow area in the range of k=4-7, the explained variance gain between consecutive k values showed a decreasing pattern and was consistently less than 2% beyond k=7. We, therefore, reported results from k=6 as they showed the highest stability (after performing the clustering several times using different seed points) and explained 87.1% of the variance.

Following clustering, entire recording data in each participant were characterized as a sequence of recurring CAP events. To examine dynamic patterns in these sequences, multiple temporal, dynamic, and spectral metrics of CAPs were computed on each participant and then summarized to generate group-level statistics. An occurrence of a CAP was defined as a set of continuous timeframes belonging to the same CAP. The occurrence rate of a CAP was calculated as the ratio of its total occurrences to the total occurrences of all CAPs. The mean dwell time of one type of CAP was calculated as the mean time duration from all its occurrences. The mean interval time of one type of CAP was calculated as the mean time duration between two neighbored occurrences of the CAP. To probe the relationship between a pair of CAPs, the one-step transition probability of one type of CAP to another type of CAP (directional) was calculated as the number of such transitions divided by the total number of transitions in these CAP sequences. To calculate the PSDs of CAPs, we adopted a concept from Gutierrez-Barragan et al. (2019) to construct the continuous-time course of each CAP in each participant. Briefly, these participant-level CAP continuous-time courses were obtained via regressing participant-level normalized (z-scores) cortical DOT data with the group-level CAP spatial maps as regressors. Then CAP PSDs were calculated using the Lomb-Scargle method (Horne and Baliunas, 1986), which could better handle DOT data of temporal discontinuities after preprocessing (Section 6.2.2) than the popular Welch's method (Welch, 1967).

To examine the intra-cluster and inter-cluster spatial similarities among CAPs, the metric of

spatial correlation was used as all CAP spatial maps were defined on the standard cortical surface model. To study temporal correspondences of different CAPs, two types of co-occurrence analyses were utilized. The framewise co-occurrence analysis was applied to two different sets of clustering results usually obtained from the same original data but with different processing conditions (e.g., with or without the SS regression). Specifically, we calculated, at the resolution of single timeframes, the percentage ratio of overlapped occurrences of two CAPs each from different conditions to the total occurrences of one of two CAPs (i.e., the reference CAP of investigational interests). The framewise co-occurrence analysis could not investigate temporal correspondences of different CAPs from single clustering analysis. We, therefore, performed the co-occurrence analysis on predefined time windows, termed windowed co-occurrence analysis, to be distinguished from the one above. Specifically, the ratio between the numbers of occurrences of two investigated CAPs was calculated within a predefined window, termed the windowed co-occurrence ratio (WCOR). These two temporal metrics were calculated in data from each participant, and their statistics were summarized at the group level.

The mixed-effect model with multiple recording sessions (i.e., 2 in the present study) per participant (Holmes, 1988, Beckmann et al., 2003) was adopted to perform statistical analyses on CAP metrics discussed above. Each metric value being tested was separately calculated in each recording session data and then averaged across two sessions for each participant. These participant-level metric values were then tested, unless otherwise mentioned, using two-tail paired t-tests with Bonferroni correction (Bonferroni, 1936).

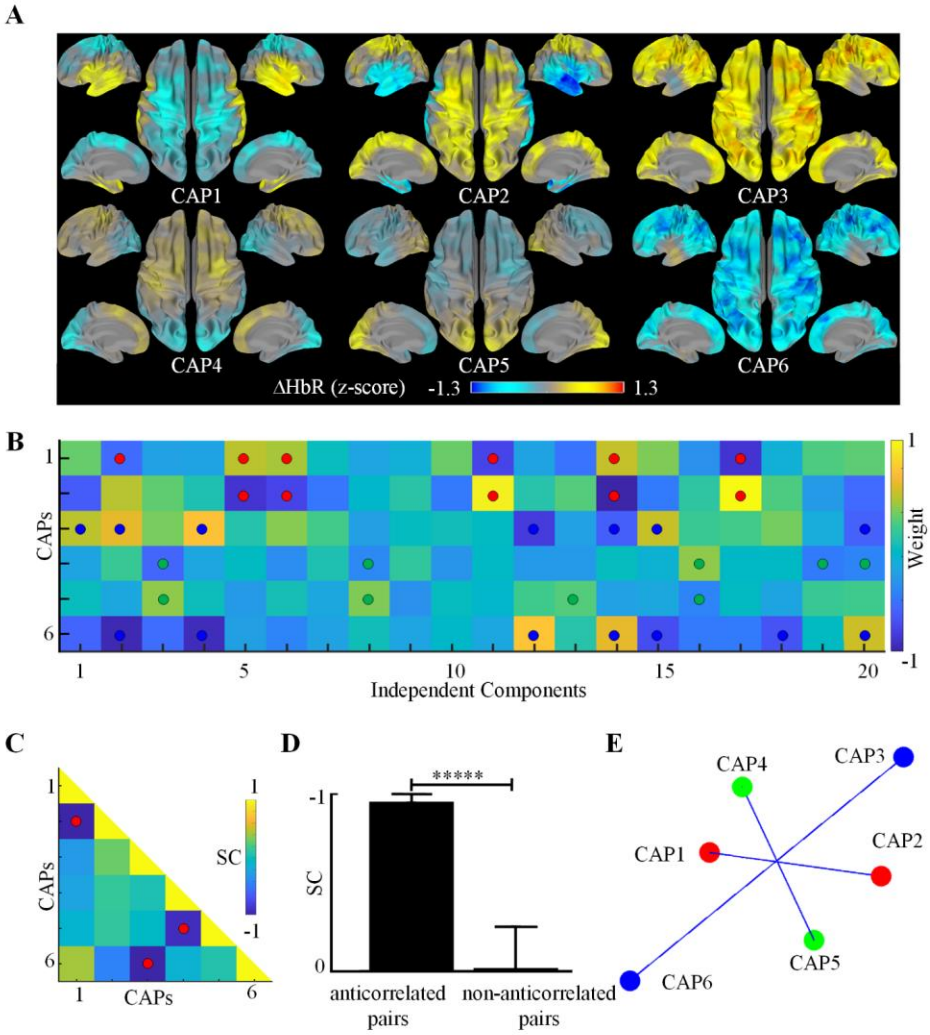

Figure 6-2 Brain-wide DOT CAPs.

(A) Group-level spatial maps of HbR CAPs when k = 6, showing three anticorrelated CAP pairs, i.e., anterior-posterior (CAP4 and CAP5), dorsal-ventral (CAP1 and CAP2), and global pairs (CAP3 and CAP6); (B) group-level cluster centroids of 6 CAPs with ICs as building blocks. Large IC weights in each row (i.e., greater than 60% of the largest absolute value in the row) are denoted by solid circles (same colors used for anticorrelated CAP pairs); (C) spatial correlation (SC) between all possible pairs for the CAPs in (A). solid red dots: SC values < -0.90, indicating three anticorrelated pairs; (D) mean SC values of anticorrelated pairs and non-anticorrelated pairs of CAPs show statistically significant differences using an unpaired t-test (*****: *p<1e-5, corrected*); (E) the 3D distance map of the cluster centroids among 6 CAPs.

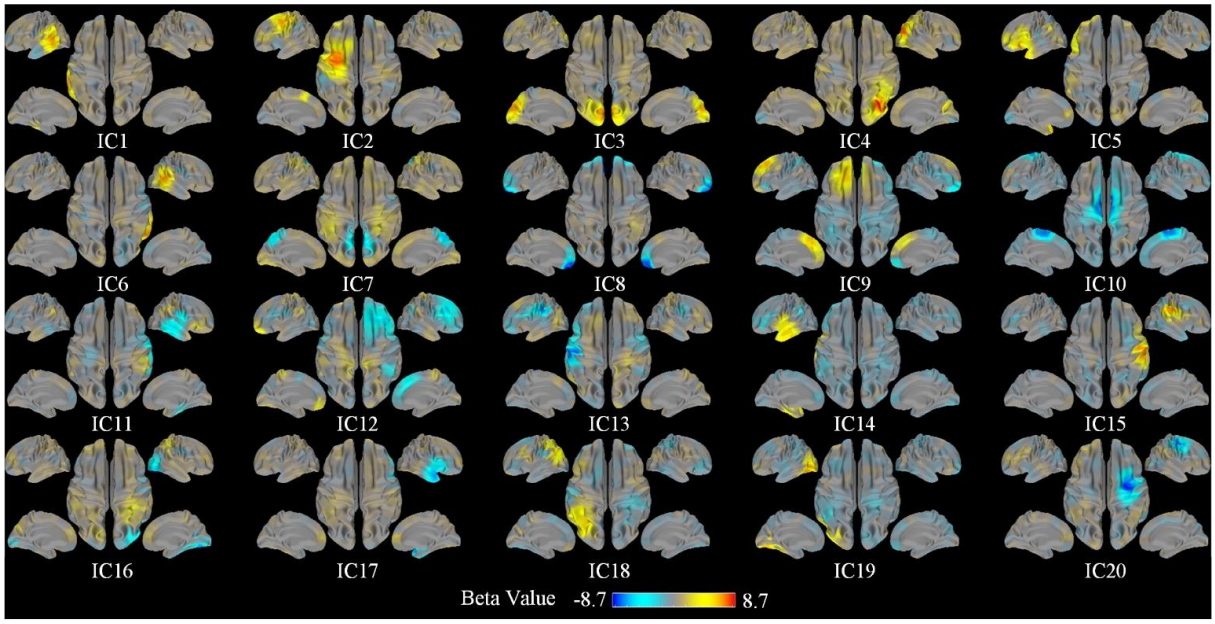

Figure 6-3 Group-level HbR DOT ICs.

Group-level HbR DOT ICs (i.e., 20) obtained via the spatiotemporal regression, visualized on the standard FreeSurfer cortical surface. Most individual ICs exhibit hemisphere-lateralized patterns but also show in complementary pairs with hemisphere-symmetric patterns (e.g., IC1-IC11, IC2-IC20, IC5-IC17; IC13-IC15, IC16-IC19, etc.)

6.2.5 Relationship between CAPs and GS

To probe the relationship between CAPs and GS, we tested whether the occurrences of CAPs locked toward specific phases of GS as such a phase-locking phenomenon had been reported between CAPs and GS in animal fMRI data (Gutierrez-Barragan et al., 2019). Firstly GS was calculated as the mean time course of all cortical node time courses within the source space in each participant (Section 2.3), similar to the calculation of GS in BOLD fMRI data (Zarahn et al., 1997). Secondly, to enhance infraslow activities (Gutierrez-Barragan et al., 2019), the obtained GS time course from each participant was bandpass filtered at 0.01-0.03 Hz and converted into an analytical signal using the Hilbert Transform (Huang et al., 1998) to yield estimations of instantaneous phases and amplitudes. The instantaneous phases were tabulated for each cluster and pooled across

all participants. Then their circular distributions and means were plotted using the MATLAB CircStat toolbox (Berens, 2009).

6.3 Results

6.3.1 Brain-wide DOT CAPs

Figure 6-2A illustrates six coactivation patterns (CAP1-6) obtained with DOT RSNs. The DOT RSNs as building blocks to these CAPs are shown in Figure 6-3. The spatial distributions of these CAPs are structured, brain-wide, and of hemispheric symmetry. Three distinct spatial patterns are identified among them: the dorsal-ventral (DV) pattern (i.e., CAP1, 2), the anterior-posterior (AP) pattern (i.e., CAP4, 5), and the global pattern (i.e., CAP3, 6). The DV CAPs show the opposite HbR changes (positive vs. negative ΔHbR) along the dorsal-ventral axis. In the orthogonal direction of the dorsal-ventral axis, the separation of positive and negative HbR changes approximately runs along the inferior frontal sulcus in the frontal cortex, cuts through the sensorimotor cortex above the deep lateral fissure, and then extends toward the posterior end of the brain roughly along the lateral occipital sulcus. On the middle wall, the separation is on the upper boundary of the inferior temporal cortex. The AP CAPs show the opposite HbR changes along the anterior-posterior axis. The separation of positive and negative HbR changes appears roughly along the postcentral sulcus and cuts through the posterior end of the temporal cortex in the orthogonal direction of the anterior-posterior axis. The global CAPs exhibit either global positive or negative HbR changes with diminished changes toward the tip of the temporal cortex.

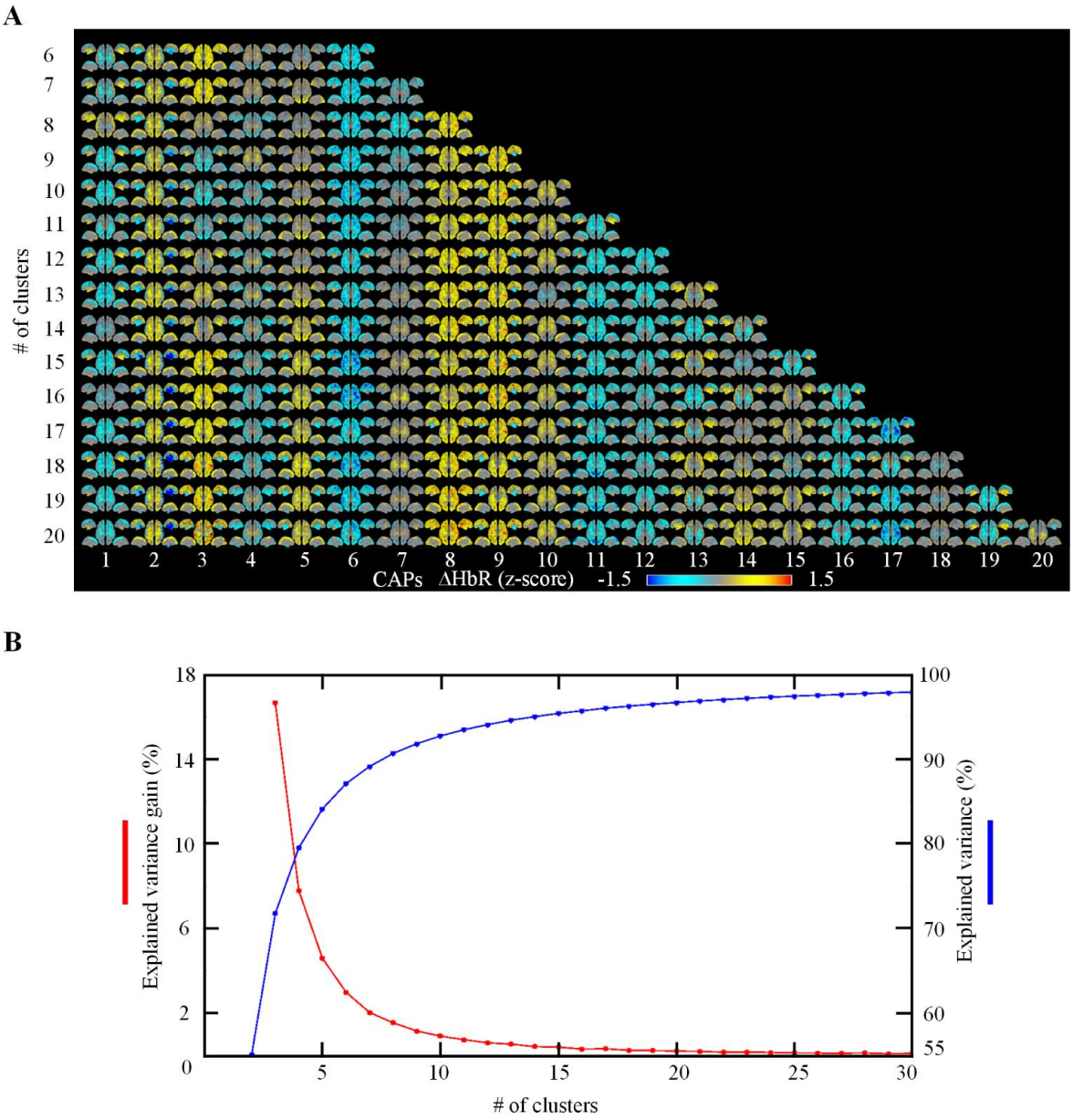

Figure 6-4 Group-level DOT CAPs using different cluster sizes.
(A) Group-level DOT CAPs using different k values (only results for $6 \leq k \leq 20$ are visualized here). (B) Elbow plot of (right y-axis, blue curve) explained variance (%) and (left y-axis, red curve) explained variance gain (%) as the function of the number of clusters ($2 \leq k \leq 30$).

Visual inspections reveal anticorrelated spatial patterns of two CAPs in the DV, AP, or global groups. This is further confirmed by the quantitative metric of pair-wise spatial correlation (SC) between all CAPs (Figure 6-2C). The SC between CAP1 and CAP2, i.e., the pair with DV patterns,

is -0.96, -0.91 for CAP4 and CAP5, i.e., the pair with AP patterns, and -0.97 between CAP3 and CAP6, i.e., the pair with global patterns. The mean SC of these pairs (i.e., -0.95) is statistically significantly (two-sample t-test, $t(13)=6.6$, $p < 1e\text{-}5$, corrected) lower than the mean SC (i.e., -0.01) of all other possible pairs of CAPs (Figure 6-2D). The anticorrelated nature of these pairs is also evident from the weight matrix (Figure 6-2B), wherein each row is the centroid vector for a cluster (i.e., a CAP). Each element in the row represents the weight coefficient of each building block (i.e., IC or DOT RSN). Specifically, the anticorrelated pairs have their significant weight coefficients (i.e., > 60% of the largest) contributed mainly by the same ICs (denoted by solid circles in Figure 6-2B) but with opposite polarity in the paired CAPs.

In addition to characteristic patterns in single CAPs and paired CAPs, the 3D distance map illustrating all cluster centroids reveals a well-structured spatial relationship among all CAPs (Figure 6-2E). Firstly, the three anticorrelated pairs have an almost orthogonal structure. Each CAP pair occupies one of three axes in the 3D space. Secondly, two CAPs in any anticorrelated pair are polarized separately toward either positive or negative directions of the dimensional axis. Lastly, the three-dimensional axes illustrated as the direct links between the three paired CAPs are then across over the same spatial point in the center. This spatial structure indicates that the dynamics of moment-to-moment brain states could be described in a 3D space by this collection of six CAPs, with each of them representing one spatially orthogonal pattern. The Euclidean distance between the projected centroids of the AP pair (2.50) was only about half of those from DV (5.07) and global (4.94) pairs.

For *k* ranging from 6 to 20, all three spatial patterns of CAPs described above (i.e., AP, DV, and global) are retained (Figure 6-4A), albeit with a few changes. Some newly emerged patterns may be due to the sub-patterns split from the original CAPs obtained when *k* equals 6. For example,

the CAP9 from the analysis with k between 9 and 20 shows a close-to-global positive pattern with the temporal pole as moderately negative. This might be a sub-pattern in the original DV pattern with lowered positive/negative boundary. Furthermore, the CAP4 with *k* between 10 and 20 shows a DV pattern with elevated positive/negative boundary compared with the original DV pattern. Some other CAPs are retained, such as DV or AP patterns, but with reduced magnitudes (e.g., CAP18 from k between 18 and 20). The detection of sub-patterns might suggest that there are more detailed ingredients in the space represented by six CAPs but potentially less representative at the group level.

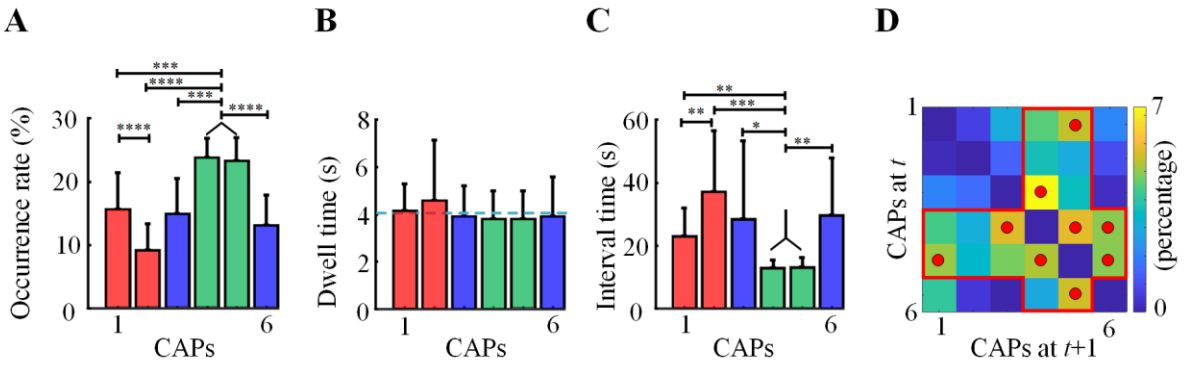

Figure 6-5 Temporal and dynamic measures of DOT CAPs.
Temporal and dynamic measures of DOT CAPs: (A) occurrence rates; (B) dwell time (dashed line: mean of all CAPs); (C) interval time; (D) one-step transition probability matrix of all CAPs from time t to t+1. Red dots: transition probabilities greater than 5%. ****: *p< .0001*, ***: *p< .001*, **: *p< .01* *: *p< .05*, all corrected. Standard deviation bars were calculated across participants.

6.3.2 Temporal, dynamic, and spectral measures of DOT CAPs

The occurrence rates of the AP pair (23.8% and 23.3% for CAP4 and CAP5, respectively) are significantly higher than all other CAPs (paired t-test, $t(12) \geq 4.9$, $p < .001$, corrected, Figure 6-5A). The CAP2 from the DV pair occurs the least at 9.2%, which is significantly lower than all other CAPs (paired t-test, $t(12) \geq 5.5$, $p < .01$, corrected) except the global CAPs. There is no

significant difference in the dwell times among CAPs, which is about 4.02 seconds on average (Figure 6-5B). The interval times of these CAPs are shown in Figure 6-5C. The AP pair's interval times (12.9 s and 13.2 s for CAP4 and CAP5, respectively) are considerably lower than all other CAPs (paired t-test, $t(12) \geq 3.1$, $p < .05$, corrected). Except for the DV pair (paired t-test, $t(12) = 3.5$, $p < .01$, corrected), there was no significant difference in interval times between two CAPs within a pair.

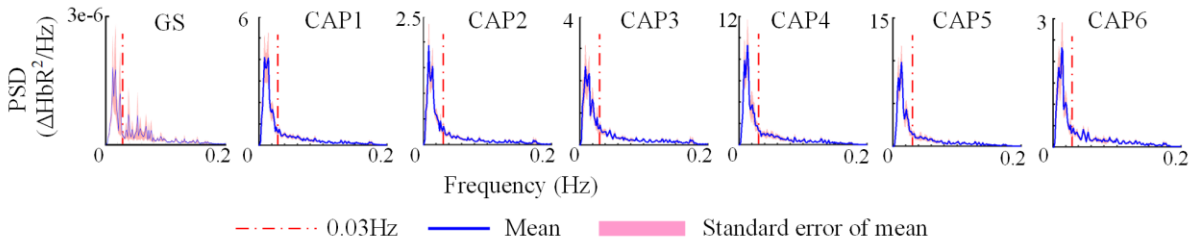

Figure 6-6 PSD of GS and DOT CAPs.

Figure 6-5D illustrates the one-step transition probability matrix among 6 CAPs. Firstly, transitions involving the AP pair of CAPs show higher transition probabilities (enclosed by the solid red lines) than other transitions. Specifically, the top 5% highest CAP transitions all involve either CAP4 or CAP5 (red dots). Furthermore, while the mean transition probability between all possible CAPs is 3.33%, the mean transition rate involving either CAP4 or CAP5 is 4.63%, significantly greater than the overall mean transition rate (two-sample t-test, $t(46) = 2.5$, $p < .05$, corrected). Secondly, except for the AP pair, the mean CAP transitions (1.4%) within the DV pair (between CAP1 and CAP2) and the global pair (between CAP3 and CAP6) were significantly lower than the overall mean transition rate (two-sample t-test, $t(40) = 3.1$, $p < .01$, corrected). The CAP PSDs across all participants revealed a significant amount of power in the infraslow frequency band between 0.005-0.03 Hz (Figure 6-5), overlapping with the frequency band of GSs showing most powers, i.e., 0.008-0.06 Hz (Figure 6-5). It is noted that the cutoff frequency at the

low boundary (i.e., 0.005Hz in CAP PSDs) is caused by the bandpass filter used in the preprocessing. Without it, CAP PSDs should show ~1/f power spectra that are typically observed in BOLD signals (He et al., 2010).

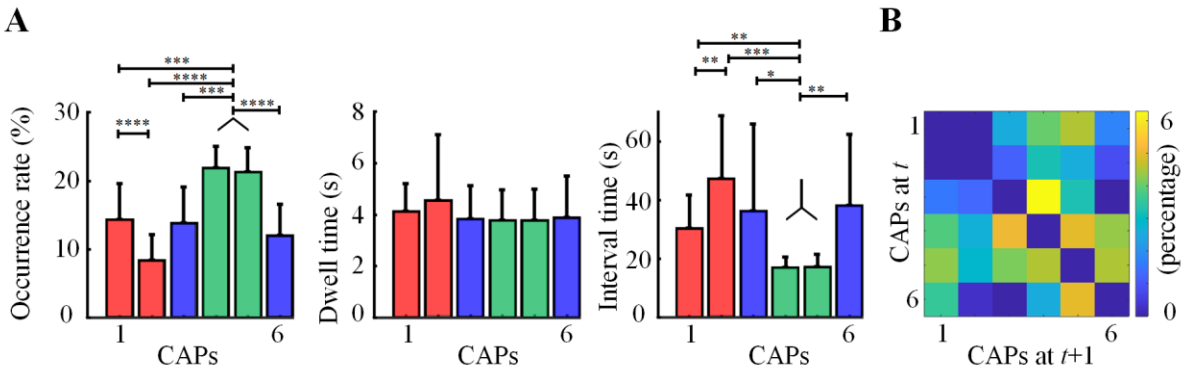

Figure 6-7 Effect of temporal discontinuity on the temporal and dynamic metrics of CAPs. (A) temporal metrics and (B) one-step transition matrix calculated using a dummy CAP (CAP7) in place of the data segments that were removed in the data preprocessing step. Note that we have discarded the metrics corresponding to the dummy CAP.

Temporal discontinuities of DOT data caused by bad segment rejections in preprocessing (see Section 6.2.2) might potentially affect the values of temporal and dynamic metrics of CAPs investigated above. An analysis was performed to investigate the potential effects of temporal discontinuities by creating a dummy CAP (CAP7) in places where data segments were removed. Then all temporal metrics discussed above were re-calculated (Figure 6-7). The results are similar to those in Figure 6-5, which indicates that the effect of missing data on the temporal and dynamic metrics used in the present study does not change the distinct patterns observed in various CAPs.

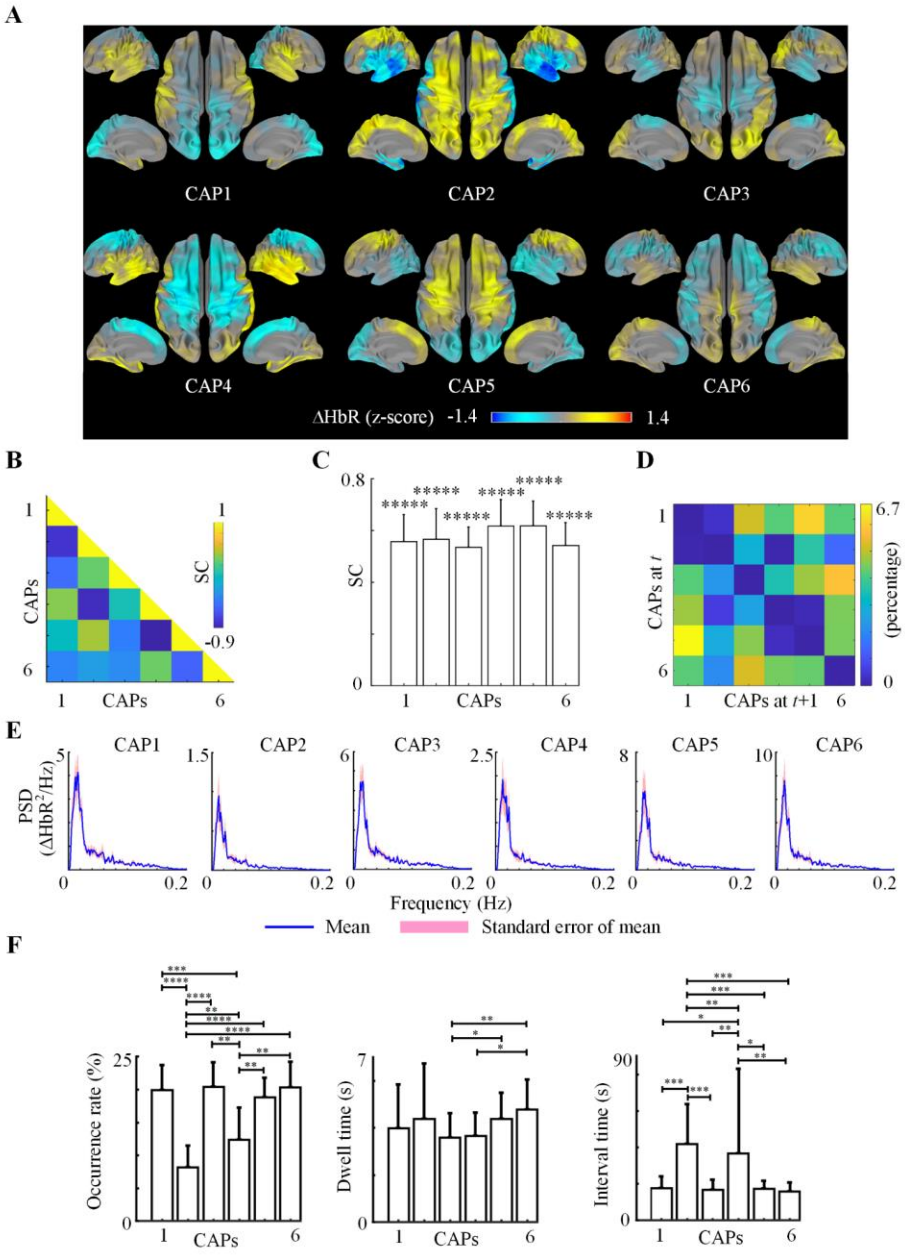

Figure 6-8 The spatiotemporal properties of CAPs (k = 6) in the absence of global signal. (A) Group-level spatial maps of brain-wide DOT CAPs; (B) Spatial correlation (SC) between all possible pairs for the CAPs in (A); (C) Bar plots of means and standard deviations of spatial correlations (SCs) between the group-level and participant-level spatial maps of CAPs. All CAPs show significantly higher SC values than zero (paired t-test, ******: $p < .00001$*, corrected); (D) One-step transition probability matrix of all CAPs from time t to $t+1$; (E) PSD of DOT CAPs; (F) Temporal measures of DOT CAPs (left) occurrence rates (middle) dwell time, and (right) interval time. Paired t-tests are used for testing statistical significances with Bonferroni corrections, *****: $p< .0001$, ***: $p< .001$, **: $p< .01$ *: $p< .05$.*

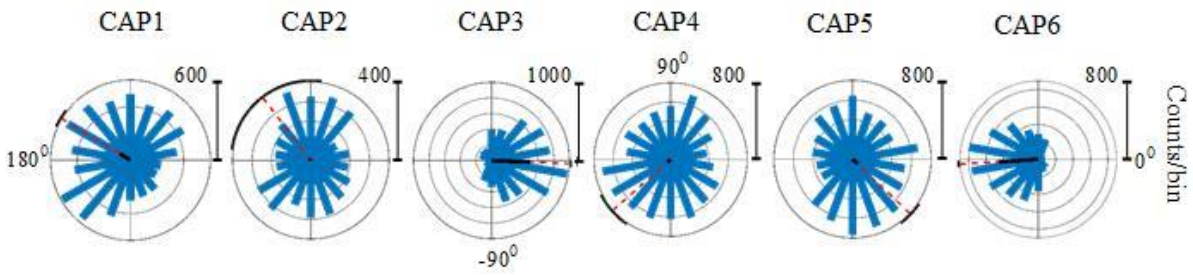

Figure 6-9 GS phase histograms of DOT CAPs.

GS phase histograms of DOT CAPs. Each plot is a circular histogram of occurrences of a CAP pooled from all participants as a function of the GS instantaneous phase at the resolution of 200/bin. Solid black line: magnitude of the resultant mean vector; arc: 95% confidence intervals of estimated mean vectors; 0^0: GS peaks; and 180^0: GS troughs.

6.3.3 Global CAPs phase-locked to GS

We hypothesized a potential linkage between GS and CAPs because 1) GS and all CAPs retain most signal power below 0.1Hz; 2) the occurrences of positive and negative global CAPs are likely leading to GS peaks and troughs; 3) no global CAPs are detected if GS is removed from DOT data in the analysis for all k values (see Figure 6-8A for k = 6). Therefore, we specifically investigated the quantitative correspondences between GS phases and CAP occurrences (Section 6.2.5). Figure 6-9 illustrates the circular occurrence histograms of each CAP across all participants as functions of the instantaneous GS phase. Note that a phase of 0° and 180° represents the peak and trough of GS, respectively. Interestingly, the occurrences of positive and negative global CAP patterns are concentrated most pronouncedly around the GS peaks and troughs, i.e., CAP3 average phase (±std) at -6° ± 55° and CAP6 at 181° ± 55°, respectively, which are significantly different from a uniform circular distribution (Rayleigh test; CAP3: p = 0, CAP6: p <1e-69, corrected). Although the occurrences of the other four CAPs also indicate non-uniform circular distributions, their standard deviations are much wider (CAP1: ±74°, CAP2: ±78°, CAP4: ±79°, and CAP5: ±77°), and their magnitudes of the resultant vectors indicating the average phases are much lower.

The mean normalized magnitude of the resultant vectors at the centered average phases of global CAPs is 0.46, which is significantly greater than the mean magnitude of 0.082 from the other four CAPs (two-sample t-test, $t(4) = 10.7$, $p < .001$, corrected).

6.3.4 Plausible neuronal relevance for global CAPs

Repeating the above ICA and clustering analysis after removing GSs in participant-level data, our results indicate no detection of global CAPs (Figure 6-8A). Due to the debates on the origins of GS in the past decade (Murphy and Fox, 2017), it is important to understand whether the detected global CAPs are of neuronal relevance. Therefore, we have performed further analyses to search for evidence of neuronal relevance for the detected global CAPs.

While removal of GS is a well-established procedure in BOLD fMRI in dealing with non-neuronal systematic fluctuations, it is more difficult in fNIRS, particularly for patch-based systems (Wheelock et al., 2019), due to the absence of whole-brain coverage. On the other hand, non-neuronal hemodynamic systemic fluctuations in fNIRS have been often estimated using the SS channels (ICD: <15 mm) (Gagnon et al., 2012, Goodwin et al., 2014) as such channels are only sensitive to superficial extracerebral tissues, e.g., scalp (Saager and Berger, 2008). The SS regression used in the present study based on such an estimate of systemic fluctuations has been demonstrated to effectively remove non-neuronal signals recorded with LS channels (Zhang et al., 2021). As a result, the detected global CAPs with the SS regression in preprocessing provide the first set of evidence for their potential neuronal relevance.

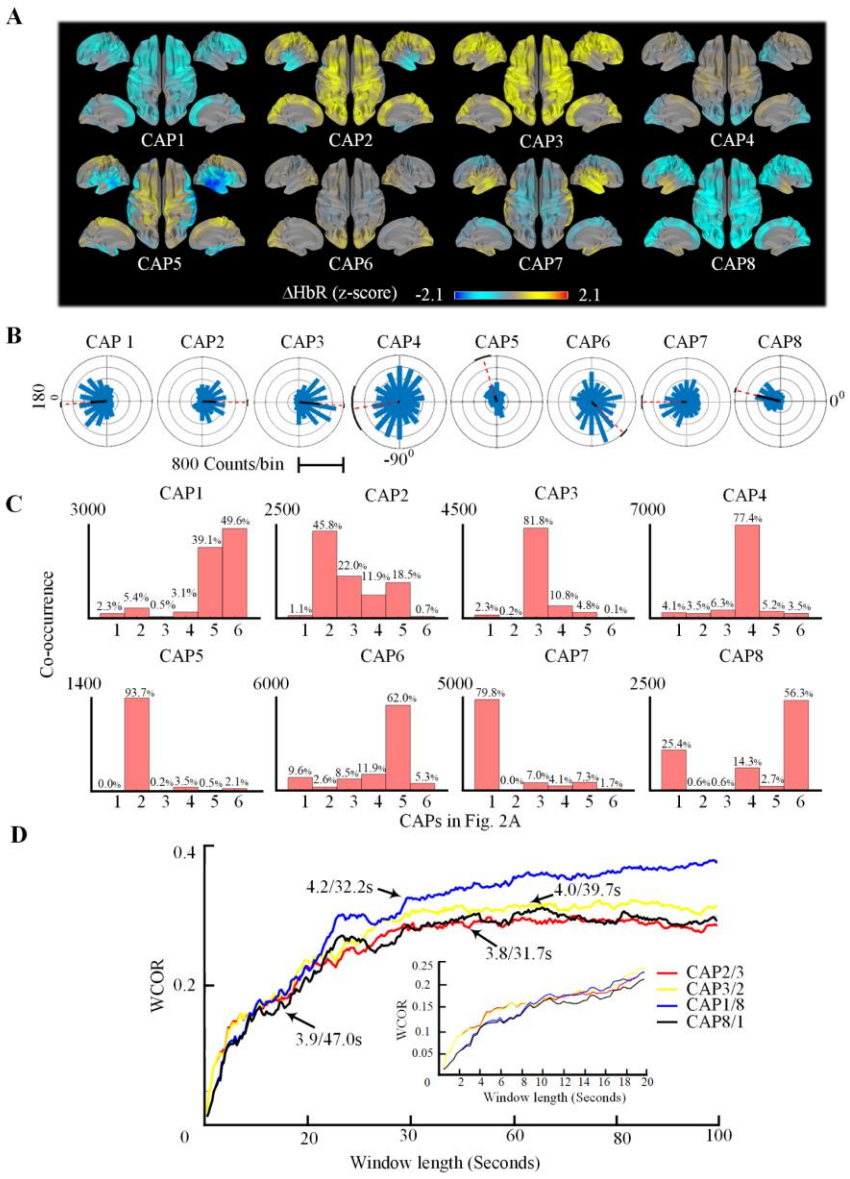

Figure 6-10 Investigation of neuronal origins of global CAPs.

Investigation of neuronal origins of global CAPs. (A) Group-level CAPs without SS regression at k=8; (B) GS phase histograms of these eight CAPs; (C) framewise co-occurrences between 8 CAPs in (A) and 6 CAPs in Figure 6-2A. Percentage value on each bar: the ratio of co-occurrences between a Figure 6-10A CAP (each sub-plot) and a Figure 6-2A CAP (each bar in a sub-plot) to total occurrences of the Figure 6-10A CAP; (D) windowed co-occurrence ratios (WCORs) between the numbers of occurrences of two paired CAPs (CAP2 vs. CAP3 for GS peaks and CAP1 vs. CAP8 for GS troughs) for variable window lengths. The WCOR metric was calculated twice for each pair, each with one of two CAPs as the reference CAP. X/Xs: mean dwell time and mean transit time of each reference CAP. The inset shows an enlarged view of these plots for the window lengths less than 200 seconds.

To further support this evidence, one way is to test whether the absence of SS regression in preprocessing would result in additional global CAPs due to non-neuronal systematic fluctuations and whether these additional global CAPs are separatable from two original global CAPs in Figure 6-2. Therefore, we repeated the same analysis on the same fNIRS dataset but without the SS regression (k=6 to 20). An empirical metric, i.e., the percentage ratio of global CAPs (PRGC) out of all CAPs as a function of k (see details about PRGC in Figure 6-11), was calculated to evaluate the difference in the number of global CAPs with and without the SS regression. The PRGC metric data indicate a large difference in the number of global patterns only with the k value between 8 and 11, supporting our hypothesis that non-neuronal systematic fluctuations lead to additional global CAPs. As our previous results indicate that CAPs primarily exist in anticorrelated pairs (Figure 6-2A), we performed further studies on CAPs obtained without the SS regression at k = 8 (Figure 6-10A). All eight CAPs were consistently observed across participants (Figure 6-14).

From the spatial patterns, CAP4 and CAP6 form the AP pair homologous to CAP4 and CAP5 in Figure 6-2A, respectively, and CAP5 and CAP7 form the DV pair homologous to CAP2 and CAP1 in Figure 6-2A, respectively. The results from the framewise co-occurrence analysis indicate that the occurrences of CAP4 and CAP6 in Figure 6-10 are dominantly overlapped with the occurrences of CAP4 and CAP5 in Figure 6-2A, respectively. Similarly, the occurrences of CAP5 and CAP7 in Figure 6-10A are dominantly overlapped with the occurrences of CAP2 and CAP1 in Figure 6-2A, respectively. These temporal correspondences establish the reliability of DV and AP brain states and the robustness of results from the clustering analysis in detecting them under different conditions (i.e., with or without the SS regression). Such reliability and robustness provide strong confidence in the observations below on global CAPs where changes are expected between the conditions with or without the SS regression.

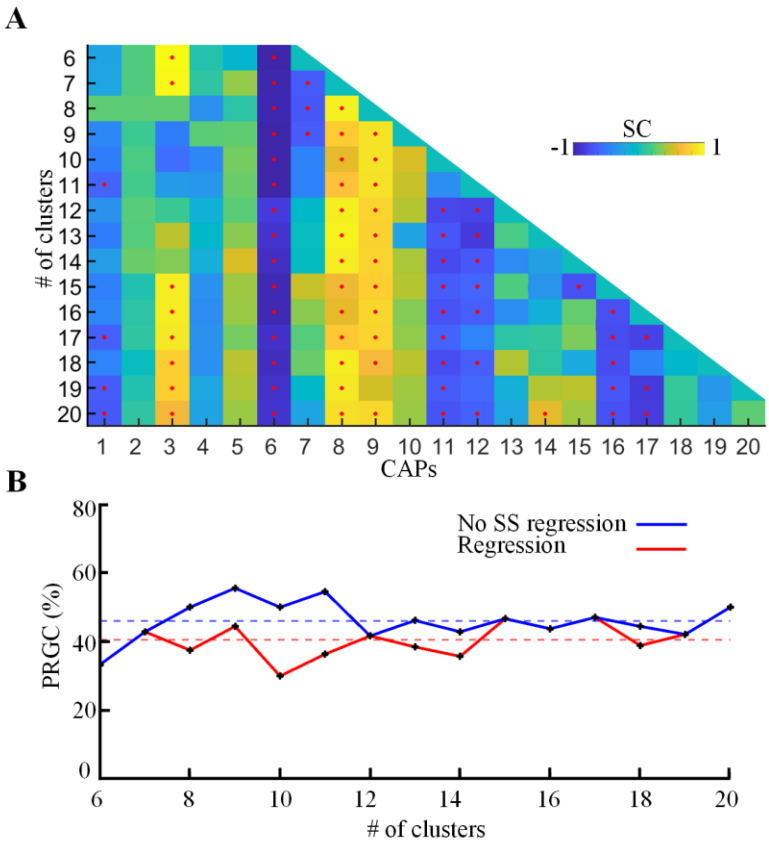

Figure 6-11 Percentage ratio of global CAPs (PRGC).

To evaluate potential changes in the number of global CAPs between different analysis conditions (e.g., with or without SS regressions), an empirical metric, PRGC, was calculated as the ratio of global CAPs to total CAPs in one analysis at different *k* values. CAPs in each analysis were identified as global CAPs if their spatial correlations (absolute values) to a selected global template CAP were higher than 0.55. (A) Illustration of spatial correlation values of CAPs in Figure 6-4A to their selected global CAP template (i.e., CAP3 at k=6); (B) PRGC metric values at different k values for CAPs obtained with and without SS regression. Dotted lines: mean PRGC metric values for these two conditions. We observe that this metric is relatively a constant for different *k* values with the exception in the range between *k*=8 and *k*=11, where DOT data without SS regression exhibit more global CAPs than DOT data with SS regression.

Four CAPs, i.e., CAP1, CAP2, CAP3, and CAP8, exhibit global patterns in Figure 6-10A. Via visual inspections, CAP1 and CAP3 resemble the two original global CAPs in Figure 6-2A (CAP6 and CAP3, respectively). Two additional global CAPs, i.e., CAP2 and CAP8, show

moderately anticorrelated HbR changes at the anterior part of the temporal lobe, which are slightly different from the two global CAPs in Figure 6-2A. The pair of CAP2 and CAP8 in Figure 6-10A also preserved hemispherically symmetric anticorrelated patterns, like all other CAPs in both Figure 6-2A and 6A. Furthermore, the four global CAPs in Figure 6-10A indicate strong phase-locking to GS. In comparison, four non-global CAPs (i.e., AP and DV pairs) are not phase-locked to GS (Figure 6-10B), consistent with those observed in Figure 6-2B. The co-occurrence analysis (Figure 6-10C) indicates that the occurrences of CAP3 in Figure 6-10A are dominantly overlapped with the occurrences of CAP3 in Figure 6-2A. The occurrences of CAP1 in Figure 6-10A primarily overlap with the global state CAP6 and a non-global state CAP5 in Figure 6-2A. On the contrary, both CAP2 and CAP8 in Figure 6-10A significantly overlap with four and three CAPs (>10% for each) in Figure 6-2A, respectively, including global and non-global CAPs. These spatial and temporal correspondences indicate two types of global CAPs in Figure 6-10A that are spatiotemporally distinguishable. Specifically, the pair of CAP1 and CAP3 are potentially of neuronal relevance (like the original global CAPs in Figure 6-2A). In contrast, the two additional global CAPs, i.e., CAP2 and CAP8, are introduced possibly due to non-neuronal systematic fluctuations.

As the two types of global CAP pairs (i.e., the original global CAP pair and the additional global CAP pair) are both phase-locked to GS peaks and troughs, we next investigated if the two types of global CAP pairs occupied different subsets of GS peaks (for the positive global ones: CAP2 vs. CAP3) and troughs (for the negative global ones: CAP1 vs. CAP8) using a windowed co-occurrence analysis. Specifically, we centered a window, which varied from 0.5 to 100 seconds in the step of a single timeframe (0.16 seconds), to a GS peak (or trough) with the original global positive CAP (or the original global negative CAP) as the reference to calculate values of the

metric WCOR and then repeated the calculation with the additional global positive CAP (or the additional global negative CAP) as the reference. We focused the resulted group-level WCOR values (Figure 6-10D) on two window sizes: <=6 seconds which is halfway between the mean dwell time (~4 seconds, Figure 6-5B) of four global CAPs and the mean time between a pair of neighboring peak and trough of GS (8.7 seconds); and >40 seconds as the mean interval time of the four global CAPs is about 40 seconds (Figure 6-5C). The WCOR values corresponding to the window size <=6 seconds are below 12% regardless of the type of the reference CAP, which indicates that each GS peak or trough and its surrounding timeframes are mainly occupied by one type of global CAPs (see examples of overlay of GS peaks, troughs, and CAPs in Figure 6-12).

In other words, two types of global CAPs are phase-locked to different subsets of GS peaks and troughs. For window size >40 seconds, the WCOR values are roughly between 30% and 40% regardless of the type of the reference CAP. Moreover, these values plateau between 40-100 seconds window sizes, which indicates that each type of CAPs largely occurs in clusters. In other words, one type of phase-locked global positive or negative CAP largely occurs consecutively. These observations indicate that the phase-locked occurrences of two types of global CAPs are temporally separable in relation to GS peaks/troughs, which further supports that the two types of global CAPs have different origins.

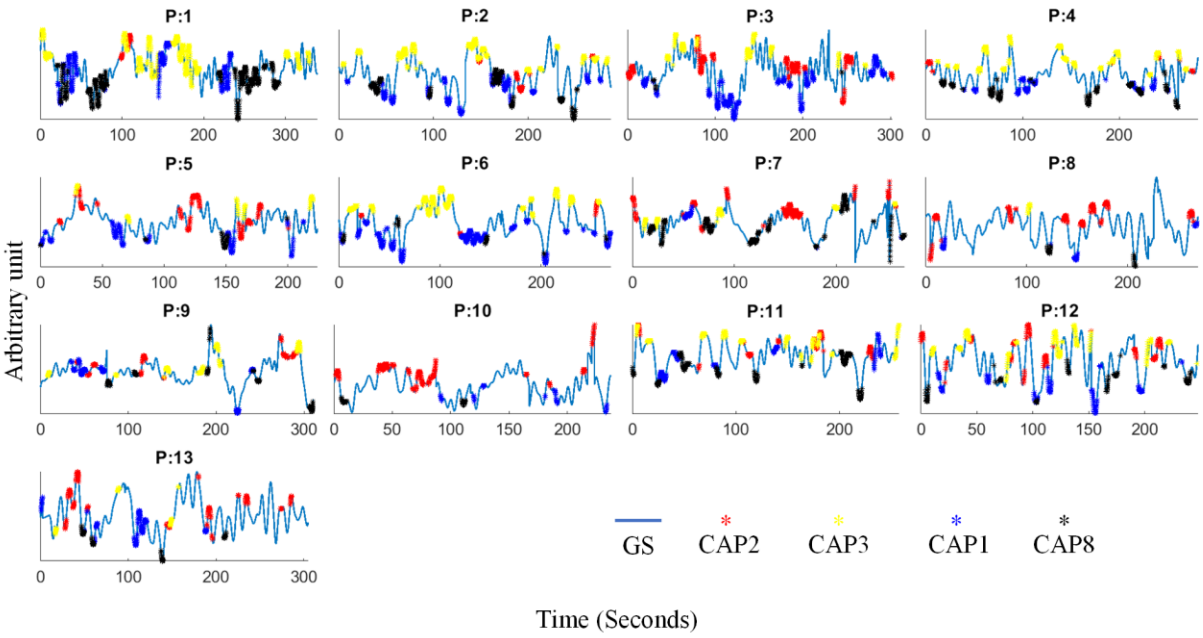

Figure 6-12 Exemplar illustrations of occurrences of four global CAPs in Figure 6-10A. Illustrations of occurrences of four global CAPs in Figure 6-10A on GS time courses from all participants (P1 – P13) from session 1. Only occurrences of these four global CAPs within a window (3.36 s) centered around GS peaks and troughs are shown.

6.3.5 Brain-wide CAPs at individual participants

We investigated if CAPs could be detected at the participant level. Figure 6-13A illustrates the spatial maps of six CAPs obtained from data from one participant. Although spatially noisier, they strongly resemble the group-level CAPs (Figure 6-2A). Three pairs of distinguished patterns are identifiable, including AP (CAP4 and CAP5), DV (CAP1 and CAP2), and global patterns (CAP3 and CAP6), which further indicate anticorrelated features in each pair (Figure 6-13B-C).

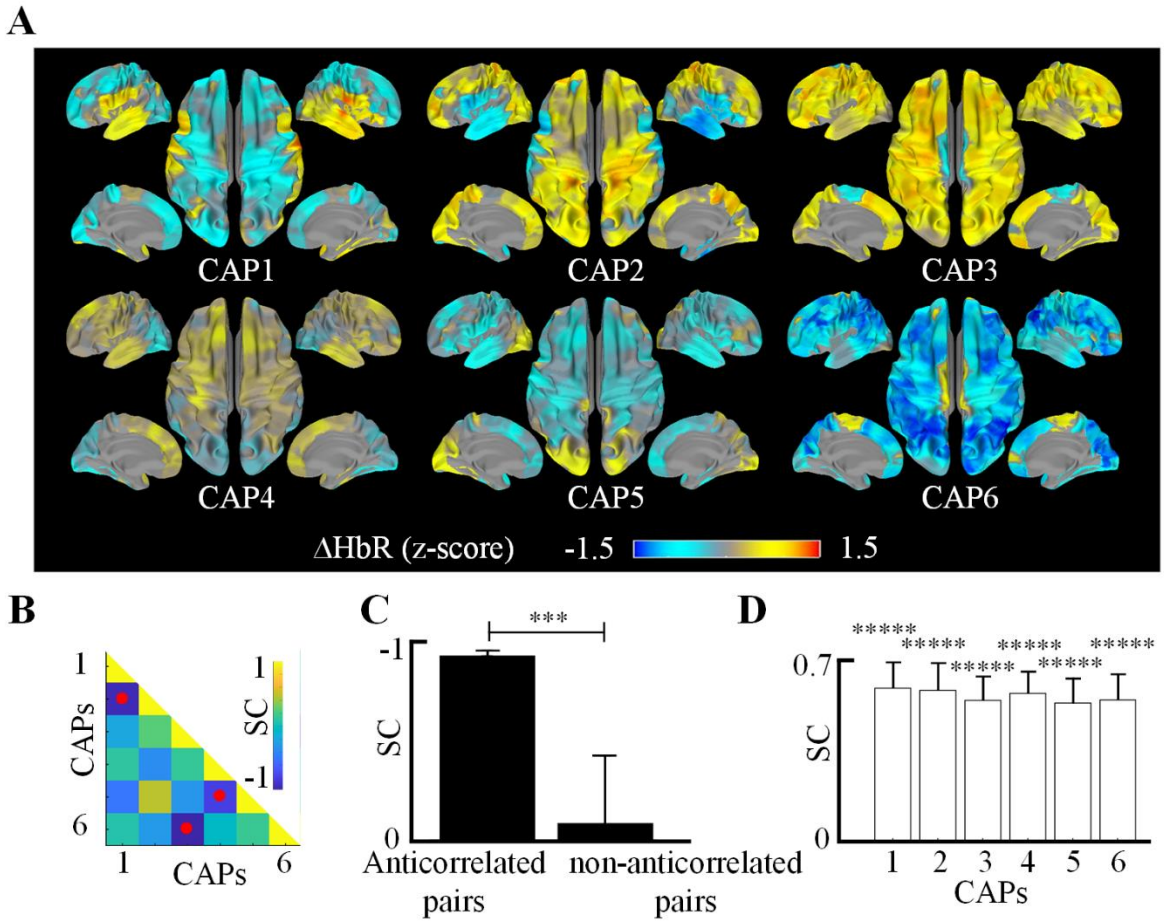

Figure 6-13 Participant-level brain-wide DOT CAPs.

Participant-level brain-wide DOT CAPs. (A) Spatial maps of CAPs from a representative participant corresponding to those in Figure 6-2A; (B) spatial correlation (SC) between all possible pairs for the CAPs in (A); solid red dots: SC values < -0.79, indicating three anticorrelated pairs; (C) mean SC values of anticorrelated pairs and non-anticorrelated pairs of CAPs show statistically significant differences using an two-sample t-test *(***: $p < .001$, corrected*); (D) SCs between the group-level and participant-level spatial maps of CAPs show significantly higher values than zero (paired sampled t-test, *****: $p < .00001$*, corrected).

Moreover, the participant-level spatial maps of all six CAPs are matched with their corresponding group-level maps with statistically significant spatial correlations greater than zero (paired t-test, $p < .00001$, corrected, Figure 6-13D and Figure 6-8C). These findings suggest that FC variations in the brain can be consistently observed at the participant level.

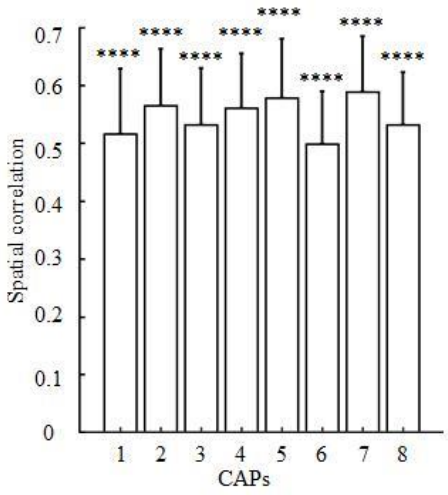

Figure 6-14 Bar plots of means and standard deviations of spatial correlations (SCs) between the group-level and participant-level spatial maps of CAPs in Figure 6-10A.
Bar plots of means and standard deviations of spatial correlations (SCs) between the group-level and participant-level spatial maps of CAPs in Figure 6-10A. All CAPs show significantly higher SC values than zero (paired t-test, *****: $p < .00001$*, Bonferroni corrected).

6.4 Discussion

6.4.1 Brain-wide coactivations indicating recurring brain states

For the first time, the present study reports the detection of brain-wide CAPs in hemodynamic signals recorded with a wearable whole-brain high-density optical imaging system operating in the near-infrared range, known as DOT, on healthy human participants. Our results of DOT CAPs show distinctive spatiotemporal features of CAPs that resemble findings in BOLD fMRI data. Firstly, our data indicate that resting-state fluctuations of whole-brain hemodynamic signals can be accounted for with a relatively small number of brain-wide functional states, i.e., 6 CAPs, which is consistent with the number of CAPs reported in recent fMRI literature, e.g., 6 (Yang et al., 2021) and 8 CAPs (Janes et al., 2020). Small numbers of brain-wide functional states have been similarly reported in animal BOLD data, e.g., 3 (Liang et al., 2015) and 6 CAPs (Gutierrez-Barragan et al., 2019). In comparison to the classical BOLD RSN studies, these CAP numbers are considerably

lower than the number of RSNs, e.g., 10 (Damoiseaux et al., 2006a), 17 (Yeo et al., 2011), and 20 (Smith et al., 2009a), reported with fMRI data, but at a similar level to the number of dynamic brain states estimated from cross-RSN functional connectivity (FC) in resting-state fMRI, e.g., 7 (Allen et al., 2014b). This fact is consistent with the definitions of CAPs in the present study, which are identified as a weighted combination of a set of DOT RSNs (Figure 6-3). Therefore, each CAP represents interactions among multiple RSNs (and transient in nature due to their short dwell times), which is, in concept, similar to the cross-RSN FC (Allen et al., 2014b). However, it is important to note that brain states defined in cross-RSN FCs are estimated based on the metric of correlation over preselected time windows, which are different from the CAP analysis based on individual timeframes. Interestingly, multiple RSNs have been reported to transiently change together in the concept of CAPs in both human (Yang et al., 2021) and animal fMRI data (Gutierrez-Barragan et al., 2019).

On the other hand, large numbers of CAPs have also been reported, e.g., up to 16 (Chen et al., 2015), 20 (Karahanoğlu and Van De Ville, 2015), and 30 CAPs (Liu et al., 2013), from selected fMRI timeframe data showing local intensity peaks in a priori anatomically seeded regions. Moreover, the CAPs based on predetermined regions of interest have established close relationships with RSNs (Liu et al., 2013). The CAPs reported in the present study are identified using a different approach via clustering all timeframe data without being restricted by polarity and intensity of local hemodynamic signals, which allow regionally unbiased detections of transient recurring patterns. Therefore, the CAPs in the present study are believed to be more representative of brain-wide functional states, which has been termed manifold CAPs (Gutierrez-Barragan et al., 2019) as each CAP is defined by a subspace (the mathematical definition of a brain

state) spanned by the collection of timeframes assigned from clustering in the total 20-dimensional space (i.e., 20 ICs as building blocks in the present study).

Secondly, the spatial maps of brain states in CAPs show bilaterally symmetrical patterns. In humans (Yeo et al., 2011, Smith et al., 2009a) and anesthetized monkeys (Vincent et al., 2007b), a hemodynamic resting-state FC often exhibits bilateral symmetry across two cerebral hemispheres, which is even preserved in humans with complete agenesis of the corpus callosum (Tyszka et al., 2011). The majority of coactivation studies with BOLD fMRI have also reported CAPs with symmetrical spatial patterns in humans (Liu et al., 2013, Liu et al., 2018a, Karahanoğlu and Van De Ville, 2015, Chen et al., 2015) and animals (Gutierrez-Barragan et al., 2019, Liang et al., 2015). It is important to note that spatial patterns of ICs, as the building blocks of CAPs, mostly exhibit asymmetrical patterns (Figure 6-3), albeit in complementary pairs (e.g., the IC2-IC20 pair for the dorsal attention network and the IC13-IC15 for the somatomotor network), which is consistent with previously reported DOT RSNs (Khan et al., 2021). This observation indicates that the bilateral symmetry of CAPs could result from temporally coordinated activations of multiple RSNs. It is plausible that the bilateral coordination across hemispheres is transient, which is better detected in the framewise clustering analysis but not in the static ICA analysis. This hemispheric symmetry of CAPs in the present study is preserved despite increasing the k value (Figure 6-4A), ruling out the possibility of it being forced due to a small number of CAPs, e.g., 6.

Thirdly, DOT CAPs show strongly anticorrelated spatial patterns in pairs, i.e., AP, DV, and global pairs (Figure 6-2). In the fMRI literature, strong brain-wide anticorrelation patterns are common in resting-state FCs and CAPs. In humans, the phenomenon of anticorrelation in RSNs has been observed using the conventional windowed correlational method, e.g., between sensory regions and default mode regions (Allen et al., 2014b) and between distributed task-positive and

task-negative brain networks (Fox et al., 2005) (Liu et al., 2013). In animals, the phenomenon of anticorrelation has been reported with CAPs in resting mice (Gutierrez-Barragan et al., 2019). The anticorrelations might be expressed because of separate neuronal processes responsible for competing interests (Fox et al., 2005), such as task focus vs. stimulus-independent thought (Giambra, 1995). Although there have been doubts that the phenomenon of anticorrelation might be artificially introduced due to the GS regression (Murphy et al., 2009), the anticorrelation patterns have been reported in the absence of GS regression (Chai et al., 2012). The results in the present study also show strong anticorrelations in the CAP spatial patterns obtained in the absence of GS regression (Supplementary Figure 3A, B, see more discussions in Section 6.4.3).

Lastly, our results further indicate one pair of DOT RSNs showing global positive and negative patterns, which has been reported when hemodynamic data are analyzed using techniques other than correlation-based methods (Yousefi et al., 2018, Matsui et al., 2019, Ma et al., 2020) . For example, the global coactivation patterns have been identified in human hemodynamic data without removing GS using a quasiperiodic pattern-searching algorithm (Yousefi et al., 2018). Transient global coactivations have been observed in searching globally propagating waves in both hemodynamic and neural signals from rodents (Matsui et al., 2019). A recent human EEG study further identifies global coactivations in electrical signals (Ding et al., 2021).

6.4.2 Spatiotemporal metrics of CAPs indicate structured transitions among brain states

The philosophy of coactivation analysis in studying dynamics of spontaneous brain fluctuations is principally different from conventional correlational-based static/dynamic FC methods. The coactivation analysis utilizes single timeframe data as the basic unit of analysis rather than entire or windowed recordings (Liu et al., 2018b). Even in dFCs, the selection of

windows is limited to the minimal data length mathematically required to warrant the estimation accuracy of correlations, and its non-optimal selection may bias reconstructed brain networks (Liu et al., 2013). Coactivation analysis is, however, independent of the choice of window size. All of our detected CAPs show consistent mean dwell times at 4.02 s (Figure 6-5B), which is significantly lower than window sizes that are usually used in dFC fMRI studies, e.g., 120 s (Savva et al., 2019). The dwell time in the present study is in close agreement with the previous coactivation studies using fMRI, e.g., 4.0-7.6 s in humans (Karahanoğlu and Van De Ville, 2015), 4 s (Gutierrez-Barragan et al., 2019) and ~10 s in rats (Liang et al., 2015).

Beyond the dwell time metric, all other temporal and dynamic metrics indicate significant differences among the six CAPs. These differences are consistent across different metrics, as well as with the spatial metric. They collectively suggest the existence of a structured transition pattern among the six brain states represented by CAPs. Interestingly, the anterior-posterior CAP pair is heavily involved with transitions among all brain states. This important role of the anterior-posterior CAPs in dynamic brain state transitions is supported by their significantly higher occurrence rates and significantly lower interval times than other CAPs. This role is further supported by the 3D distance map (i.e., the spatial metric) between all CAPs (Figure 6-2E), where the distance between two opposite anterior-posterior CAPs is significantly shorter than other anticorrelated CAP pairs. Furthermore, the direct transitions between the two anticorrelated CAPs within the dorsal-ventral and global pairs are among the lowest, further suggesting that the anterior-posterior CAP pair might serve as the intermediate brain states during the transition of brain states in opposite directions.

We speculate that these observed structured transitions among CAPs could indicate the presence of globally propagating waves that have been well reported in fMRI (Raut et al., 2020,

Raut et al., 2021, Majeed et al., 2011), optical data (Matsui et al., 2016, Matsui et al., 2019), MEG data (Takeda et al., 2021), and electrical data (Massimini et al., 2004, Huang et al., 2010, Takeda et al., 2021). Globally propagating waves made up of a sequence of brain-wide CAPs in both hemodynamic and neuronal spiking data predominantly originating from the anterior brain and propagating toward the posterior end of the brain have been reported in mice (Matsui et al., 2016). A cortical traveling wave originating from the prefrontal-orbitofrontal cortical regions and traveling to the posterior cortical regions was observed in sleeping human participants in a high-density (178-186 channels) EEG study (Massimini et al., 2004). Also, a global anterior-to-posterior phase shift in gamma oscillations (40 Hz) was reported with MEG data (Ribary et al., 1991). Our detected anterior-posterior anticorrelated CAPs might be two moment-to-moment snapshots of brain states with the most representative spatial patterns along these anterior-posterior propagating waves. Similarly, we speculate that the detected dorsal-ventral anticorrelated CAPs might reflect representative brain states of cortical dorsoventral propagating waves, e.g., in fMRI of rats and humans (Majeed et al., 2011) and as alpha waves in electrocorticography (Bahramisharif et al., 2013). However, it is cautioned that the present study does not provide direct evidence of propagation. Future studies are needed to integrate the coactivation and other sequence analysis methods (Majeed et al., 2011) to further clarify existing propagation pathways among brain states indicated by CAPs.

6.4.3 Plausible origins of CAPs and GS

We believe that our detected DOT CAPs reflect nonstationary fluctuations in spontaneous neuronal activity in human brains (Foster and Wilson, 2006, Logothetis et al., 2012, Matsui et al., 2019) and, therefore, are of neuronal origins. Firstly, as both CAPs and dFCs study temporal fluctuations in hemodynamic data in resting brains, the neurophysiological evidence of dFC has

been extensively reported in both humans (Chang et al., 2013, Tagliazucchi et al., 2012) and animals (Lu et al., 2007, Thompson et al., 2013b). More recently, a study on lightly anesthetized mice has reported CAPs in simultaneously recorded calcium (i.e., neuronal) and hemodynamic signals and their temporal correspondences, providing direct neuronal evidence of CAPs (Matsui et al., 2019). Studies using other brain signals (i.e., electrical) have directly reported neuronal CAPs in animals (Matsui et al., 2016, Mohajerani et al., 2013, Vanni and Murphy, 2014) and humans (Ding et al., 2021). As discussed above (see Sections 4.1 and 4.2), our present study's spatial, temporal, and transitional data of CAPs corresponds well with hemodynamic CAPs with known neuronal origins.

In addition, our present study has provided indirect evidence about the plausible neuronal relevance of two global CAPs. This evidence includes 1) a pair of original global CAPs (Figure 6-2A) detected with an efficient preprocessing technique in place, i.e., the SS regression, to remove non-neuronal systematic hemodynamic fluctuations (Cheong et al., 2020, Zhang et al., 2019, Zhang et al., 2021); 2) a pair of additional global CAPs observed in the absence of SS regression (corresponding to non-neuronal systematic hemodynamic fluctuations); 3) distinguishable patterns in spatial maps, temporal occurrences, and relations to GS between the pair of original global CAPs and the pair of additional non-neuronal global CAPs; and 4) consistent detections of global CAPs in conditions with a wide range of selection of parameters (Figure 6-2A, Figure 6-10A, Figure 6-13A, and Figure 6-4A). Furthermore, the neuronal relevance of this pair of original CAPs is supported by recent literature on transient electrical global patterns in rats (Schwalm et al., 2017) and electrical global CAPs in humans (Ding et al., 2021).

The present study further indicates that GS contains neuronally relevant information due to the close relationship between GS and global CAPs, i.e., global CAPs phase-locked to GS peaks

and troughs (Figure 6-9 and Figure 6-10B), and no detection of global CAPs after regressing GS out (Figure 6-8A). Given that GS is calculated as the spatial mean of DOT data in each time frame, it is not a surprise that the positive and negative global CAPs correspond to GS peaks and troughs, respectively, as no cancellations between regional activations occur due to the globally same-magnitude polarity. The neuronal relevance of GS has been suggested in recent literature, in which GS of fMRI has been linked to vigilance (Wong et al., 2013, Chen et al., 2020c), glucose metabolism (Thompson et al., 2016), and arousal (Liu et al., 2018a). In addition, our recent whole-head EEG-fNIRS study in humans has shown that the fNIRS GS is negatively associated with EEG vigilance in resting states (Chen et al., 2020). Thus, this finding in the present study suggests that care needs to be exercised when removing GS of hemodynamic data (Schölvinck et al., 2010) in either fMRI or fNIRS.

It is also important to note that, after removing GS, a majority of observations regarding CAPs discussed have been preserved except for the loss of two original global CAPs. Specifically, in results obtained after removing at k=6, the CAP pairs of AP patterns (CAP1, 6) and DV patterns (CAP2, 4) (Figure 6-8A) are still identified. Hemispherical symmetric patterns in all CAPs (Figure 6-8A) and strong anticorrelations within the AP and DV pairs (Figure 6-8B) are also observed. Similarly, the CAP pair of AP patterns have more important roles in the transitions of brain states defined by all CAPs (Figure 6-8D). The CAP pair of DV patterns has the lowest occurrence rates and the highest interval times (Figure 6-8F). All CAPs show similar PSDs (Figure 6-8E) as observed in Figure 6-5 and similar participant-level detections (Figure 6-8C).

6.4.4 Relationship among coactivations, structured propagations, and global activity patterns

Coactivations, brain-wide coordinated transitions, and global activity patterns (or global signals) have been well documented previously in hemodynamic literature, mainly with fMRI as described above. The coexistence of any two of these three phenomena has been reported as well. Matsui et al. (2016) have further demonstrated all three phenomena in both neuronal spiking and hemodynamic data in mice. The present study extends the previous research on animals and reports the coexistence of these phenomena in human brains and their relationship. Specifically, our study initially focuses on investigating coactivation patterns via a framewise clustering technique on independent component sources identified in DOT data, which leads to the detection of brain-wide patterns indicating recurring functional brain states. A pair of identified brain states exhibit global positive (coactivation) and negative (co-deactivation) patterns, leading to the definition of global activity patterns as one kind of recurring functional brain state.

We further demonstrate that these two global activity patterns are phase-locked to global signals and are responsible for generating a significant subset of global signal peaks and troughs, while non-neuronal systematic fluctuations in breathing and circulation are responsible for the generation of other global signal peaks and troughs. Finally, we present evidence about the existence of structured transitions among identified brain states, in which most transitions among brain states involve the pair of anterior-posterior CAPs (Figure 6-5D). Furthermore, brain states with both anterior-posterior and dorsal-ventral patterns might reflect representative spatial patterns during the well-reported globally propagating waves in the anterior-posterior and dorsal-ventral directions, respectively. Global activity patterns have been observed as snapshots of brain states in globally propagating waves (Matsui et al., 2016). It is therefore plausible that all identified CAPs

represent recurring brain states resulting from structured propagations. By showing the relationship between coactivations, brain state transitions, and global activity patterns, the present study brings together a broad range of studies in animals and humans to form the basis for understanding these phenomena on a unified foundation.

7. Spatiotemporal differences between HbO and HbR CAPs

This chapter has been adapted from the following manuscript in preparation:

Khan, A. F., Fan Zhang, Guofa Shou, Han Yuan, and Lei Ding. " Hemoglobin concentration in reduced state captures a more structured spatiotemporal organization of resting-state brain activity than in the oxygenated state."

7.1 Introduction

A majority of the studies investigating networked brain activity (Biswal et al., 1995, Fox et al., 2005) (Tavor et al., 2016, Sheline et al., 2009) (Damoiseaux et al., 2006a, Laumann et al., 2017, Hindriks et al., 2016) (Yeo et al., 2011, Smith et al., 2009a, Laird et al., 2011) have utilized the fMRI BOLD signal. The BOLD signal represents the hemodynamic response in the brain following a neuronal activity that involves a complex interplay of multiple physiological factors, for example, blood oxygenation, blood flow, and volume in the local blood vasculature, also known as neurovascular coupling (NVC) (Iadecola, 2017). Although many explanations of the observed BOLD signal have been provided (Buxton et al., 2004, Buxton et al., 1998, Heinzle et al., 2016, Friston et al., 2000, Marreiros et al., 2008, Friston et al., 2003, Hess et al., 2000), the exact underlying neurophysiology of this observed signal remains unclear.

Sensitive to several contrasts (HbO, HbR, and total hemoglobin concentrations), optical imaging such as fNIRS have helped elucidate some of the mechanisms of NVC (Steinbrink et al., 2006, Schroeter et al., 2006, Strangman et al., 2002, Toronov et al., 2003). Such studies have also provided evidence of several differences between HbO and HbR contrasts. For example, multimodal studies involving fNIRS and fMRI have reported that the BOLD signal is more closely related to the HbR than HbO concentration (Steinbrink et al., 2006, Mehagnoul-Schipper et al., 2002). Secondly, it has also been reported that there is a time lag between the temporal trajectories

of HbO and HbR signals in the motor cortex following a motor task, with HbR leading the HbO response in terms of time to peak from the onset of a stimulus (Lachert et al., 2017, Mackert et al., 2008). Thirdly, it has been reported that there is an initial increase in the relative HbR concentration briefly following a neural activity known as the "fast response," manifesting as an “initial dip” (Frostig et al., 1990, Malonek and Grinvald, 1996, Ernst and Hennig, 1994, Grinvald et al., 1991, Chen et al., 2005, Chen et al., 2011). Due to its close temporal proximity to the neural activity, this initial phase of HbR's temporal trajectory is believed, albeit with controversy, to be more directly related to the metabolic response and hence neural activity (Hu and Yacoub, 2012). These contrast differences among others demonstrate the importance of studying brain function using multiple contrasts for an increased understanding.

Despite the reported differences in temporal trajectories of HbO and HbR signal concentrations described above, there is still a high level of similarity in the spatial topographies of brain networks obtained using these two contrasts under task and resting conditions (Eggebrecht et al., 2012, White et al., 2012, White et al., 2009, Zeff et al., 2007, Ferradal et al., 2016, Khan et al., 2021, Eggebrecht et al., 2014). While it is plausible that a similar networked brain activity resulting from these two contrasts is indeed a genuine phenomenon, it may also be possible that the observed similarity in these networks is because of the limitations in the methodology used. For example, there is an opinion that RSNs obtained using an ICA-based approach may represent more of the spatial parcellation of the brain than the distinct mode of brain activity (Liu and Duyn, 2013). Secondly, previous DOT RSN studies have primarily assumed that the brain's FC remains stationary over the entire scan time, whereas substantial evidence indicates that FC in hemodynamic data is nonstationary (Preti et al., 2017, Allen et al., 2014b, Chang and Glover, 2010, Lurie et al., 2020). It is therefore plausible that modeling the brain's FC using conventional

methods such as the ICA-based approach and using the assumption of stationarity across scan time may not be able to capture the temporal differences in the networked-brain activity of HbO and HbR DOT signals.

Given the existence of separate roles of HbO and HbR concentrations in the NVC, it should be worth investigating the non-stationarity of the brain's FC using both HbO and HbR contrasts rather than studying using only a single contrast as typically done using fMRI BOLD signal. In Chapter 5, we reported several RSNs and their subnetworks based on HbO and HbR contrasts. While HbO and HbR RSNs suggested similarity in terms of the number of RSN types reconstructed and their corresponding spatial patterns, the HbR RSNs higher similarity to fMRI RSNs. We expanded this study by taking into account the non-stationarity of the DOT signals in Chapter 6 using the framework of CAPs in which the spatial, temporal, and transitional properties of detected CAPs were analyzed. However, this study was limited to the HbR contrast to make comparisons to the CAP studies using the fMRI BOLD signal, which is closer to the HbR signal. Given differences in the temporal trajectories of HbO and HbR signals as described above, we hypothesize that the differences in the networked brain activity of HbO and HbR signals should be observable using the CAP analysis. Secondly, since the HbR signal is potentially more closely tied to the neural signal in terms of time than the HbO signal (see above), we further hypothesize that the HbR CAPs should have a more structured transitional organization than the HbO CAPs. Therefore, in the present study, we have investigated the differences between the spatiotemporal properties of DOT CAPs in HbO and HbR contrasts.

7.2 Materials and Methods

7.2.1 Participants, experimental and data protocols

This study was approved by IRB at the University of Oklahoma, and written informed consent

was obtained from every participant before the study. A total of 20 participants were recruited for the study without any neurological or neuropsychiatric disorders. Three participants could not complete the data recording procedures. Resting-state data recorded from two six-minute sessions from thirteen participants (31.7±9.3 years, five females, eight males) with acceptable quality and experiment protocols were used as described in Section 6.2.1.

7.2.2 fNIRS data preprocessing

The preprocessing of fNIRS data followed the protocol described in Section 6.2.2. Data from each session were preprocessed separately. Briefly, the resting-state OD data were calculated (Huppert et al., 2009). The LS-channel OD data showing no visible heartbeat power peaks in the frequency range of 0.8-1.6 Hz were discarded. The OD data were then bandpass filtered at 0.008-0.2 Hz (Huppert et al., 2009) to retain useful information in the higher frequency band up to 0.2 Hz (Smith et al., 2012). Bad segments corresponding to excessive head motions were identified based on the metric of GVTD (Sherafati et al., 2020b), and about 73.4% ±7.5 of the data were retained. In order to remove the physiological noise related to superficial tissue absorption, motion, and pulse/respiration-related variations, we computed regressors based on the time courses of 8 SS channels. We removed them from LS-channel OD data using general linear model regression (referred to as the SS regression). Note, that unlike Section 3.4.1, we did not perform GS regression in the present study as there is evidence of neronally-relevant information in the GS (Murphy and Fox, 2017).

7.2.3 Estimation of brain-wide resting-state networks

DOT forward modeling and the inverse solution was conducted and used as described in Section 3.2 and 3.3, respectively. Briefly, DOT data from participants (two sessions per participant) were temporally concatenated and subjected to a gSICA (Calhoun et al., 2009). The

number of ICs was empirically set to 20. The participant-level IC spatial maps and time courses were obtained via the back-projection using the STR (Calhoun and Adali, 2004, Beckmann et al., 2009). Group-level spatial maps of ICs were then obtained by averaging corresponding IC spatial maps from all participants, resulting in 20 ICs termed DOT RSNs. These networks were visually identified as belonging to putative fMRI RSNs.

7.2.4 Quantitative comparison between HbO and HbR DOT RSN spatial maps

To quantitatively compare the spatial maps of DOT RSNs of the two contrasts as per our first hypothesis (see Section 7.1), we calculated the SC between all HbO and HbR DOT RSNs, resulting in an SC confusion matrix as described in (Section 5.2.3.2). The absolute mathematical operator was used on beta values of spatial maps prior to calculating the SC to accommodate for the differences in the polarities of the maps of HbO and HbR. The diagonal values of the confusion matrix (matched pairs) were compared with the off-diagonal values (unmatched pairs) for statistical significance testing (unpaired t-test with Bonferroni correction). As described in Section 5.2.3.2, spatially matching an HbO RSN to a HbR RSN may also result in a partial match to other networks close to the target network, resulting in positive off-diagonal values in the confusion matrix. Thus, diagonal values from the confusion matrix were further statistically compared with the positive-only off-diagonal values to test whether the similarities of matched pairs were statistically significantly higher than those of unmatched pairs but had spatial closeness.

7.2.5 Estimations of CAPs

Individual DOT RSNs (i.e., ICs) were used to calculate spatiotemporal CAPs described in Section 6.2.4. Briefly, the temporal ICs were temporally z-scored to remove scale discrepancies between participants and ICs and then concatenated along the temporal dimension. The MATLAB's k-means++ clustering using the Euclidean distance metric was applied to these

concatenated z-scored IC data on the time dimension yielding k clusters representing recurring brain states. Previously we have shown the optimal number of clusters for DOT data to be 6 (Section 6.2.4). Therefore, we chose 6 cluster sizes for HbO and HbR. Next, the participant-level spatial maps of CAPs were obtained as the average of participant-level z-scored DOT inverse frames using clustering indices. The group-level spatial maps of CAPs were obtained via averaging participant-level spatial maps of CAPs across all participants. Note that the participant-level CAPs were obtained prior to the group-level CAPs to perform statistical analysis later using participants as samples.

7.2.6 Quantitative comparison between the spatiotemporal properties of HbO and HbR CAPs

Following clustering, each data time frame was allocated to a particular CAP, and entire recording data in participants were characterized as a sequence of recurring CAP events or brain states. We then calculated the spatiotemporal metrics of these CAPs (see Section 6.2.4 for the definition of these metrics) to study hypothesized (see the second hypothesis in Section 7.1) spatiotemporal differences between the HbO and HbR CAPs. To quantitatively match the spatial maps of CAPs, we calculated the SC between the spatial maps of all CAPs, resulting in a 6x6 confusion matrix (also see Section 5.2.3.2). We defined a quantitative metric of bilateral symmetry to evaluate the symmetry of CAP spatial patterns between the left and right hemispheres of the brain's cortical surface. Specifically, for each CAP's spatial map, we thresholded the positive z-scores below the 5% of the maximum z-score to zero and larger positive values to +1. Likewise, we thresholded the negative z-scores greater the 5% of the minimum z-score to zero and larger negative values to -1. This thresholding was done to remove the effect of the small and large z-score values in the calculation of the metric. Next, using a brain parcellation map with 74

bilaterally-defined ROI (74 for each hemisphere)(Destrieux et al., 2010), we calculated the largest occurring +1 or -1, i.e., the mathematical mode operator in each ROI. Next, the ratio between the mode of the left and right ROI was calculated for all ROIs. Finally, the ratio of the total number of +1 to 74 was calculated and defined as the metric of bilateral symmetry. A value of 1 meant that all ROIs of a CAP matched each other, i.e., a highly bilaterally symmetrical spatial pattern. Similarly, smaller values indicated weaker symmetry.

A 3D-distance diagram was calculated using cluster centroids to evaluate the spatial link among all CAPs at the group level, as described in Section 6.2.4. Specifically, the CAP's cluster centroids were visualized by projecting these 20-dimensional vectors onto a 3D space (see Section 6.2.4). The occurrence of a CAP was defined as a set of continuous timeframes belonging to the same CAP. The occurrence rate of a CAP was calculated as the ratio of its total occurrences to the total occurrences of all CAPs. The mean dwell time of a CAP was calculated as the mean time duration from all its occurrences. We also calculated a dynamic metric, i.e., a one-step transition matrix of CAPs of each participant to probe the relationship between a pair of CAPs, the one-step transition probability of one type of CAP to another type of CAP (directional) defined as the number of such transitions divided by the total number of transitions in these CAP sequences. Note that the temporal and dynamic quantitative metrics described above were calculated at the participant level and then averaged using participants as samples to generate group-level statistics.

7.2.7 Reproducibility of spatiotemporal properties of CAPs

We calculated the DOT RSNs and CAPs (k=6) and their spatiotemporal properties for HbR and HbO DOT data from each recording session separately. All parameters were kept the same as above. The results from each session were compared to each other, and the results were obtained using data concatenated from the two sessions to investigate the reproducibility of our results.

7.3 Results

7.3.1 Spatial patterns of HbO and HbR DOT RSNs

Figure 7-1 provides 12 spatial maps of representative HbO and HbR DOT RSNs that demonstrate a high level of similarity in spatial topographies of the two hemoglobin contrasts with SC greater than 0.50. These networks were visually identified from 20 HbO (Figure 7-2) and HbR (Figure 7-3) RSNs.

The spatial patterns of these networks collectively spanned brain-wide cortical areas. The identified limbic network (L17, L20, SC:0.86) primarily covered the anterior part of the medial SFG. The visual network (V5, V6, SC:0.92) primarily covered the lateral part of the visual cortex and part of the ventral visual stream. The SM networks (SM10, SM14, SC:0.71, and SM3, SM11, SC:0.53) primarily covered the ventral parts of the postcentral and precentral gyrus. The auditory networks (A14, A18, SC:0.86, and A4, A12, SC:0.93) covered the auditory cortex and parts of the temporal cortex. The DAN (DAN12, DAN4, SC:0.81, DAN8, DAN1, SC:0.85) covered the left and right FEFs. Several networks were identified belonging to the DMN (DMN7, DMN9, SC:0.84, DMN20, DMN2, SC:0.52). These networks primarily covered parts of the mPFC, the medial part of MFG, and the dorsal part of the IFG. Some spatial extent of the network was also present on the temporal pole. The FPN (FPN18, FPN15, SC:0.53, FPN1, FPN8, SC:0.73) primarily covered parts of the parietal lobe and dorsal part of the SFG. Most networks exhibited hemispheric dominance, but their contralateral symmetrical counterpart also existed. However, bilateral patterns were also observed, for example, in HbO (IC15, 17, and 19 in Figure 7-2) and HbR (IC10 and 16 in Figure 7-3).

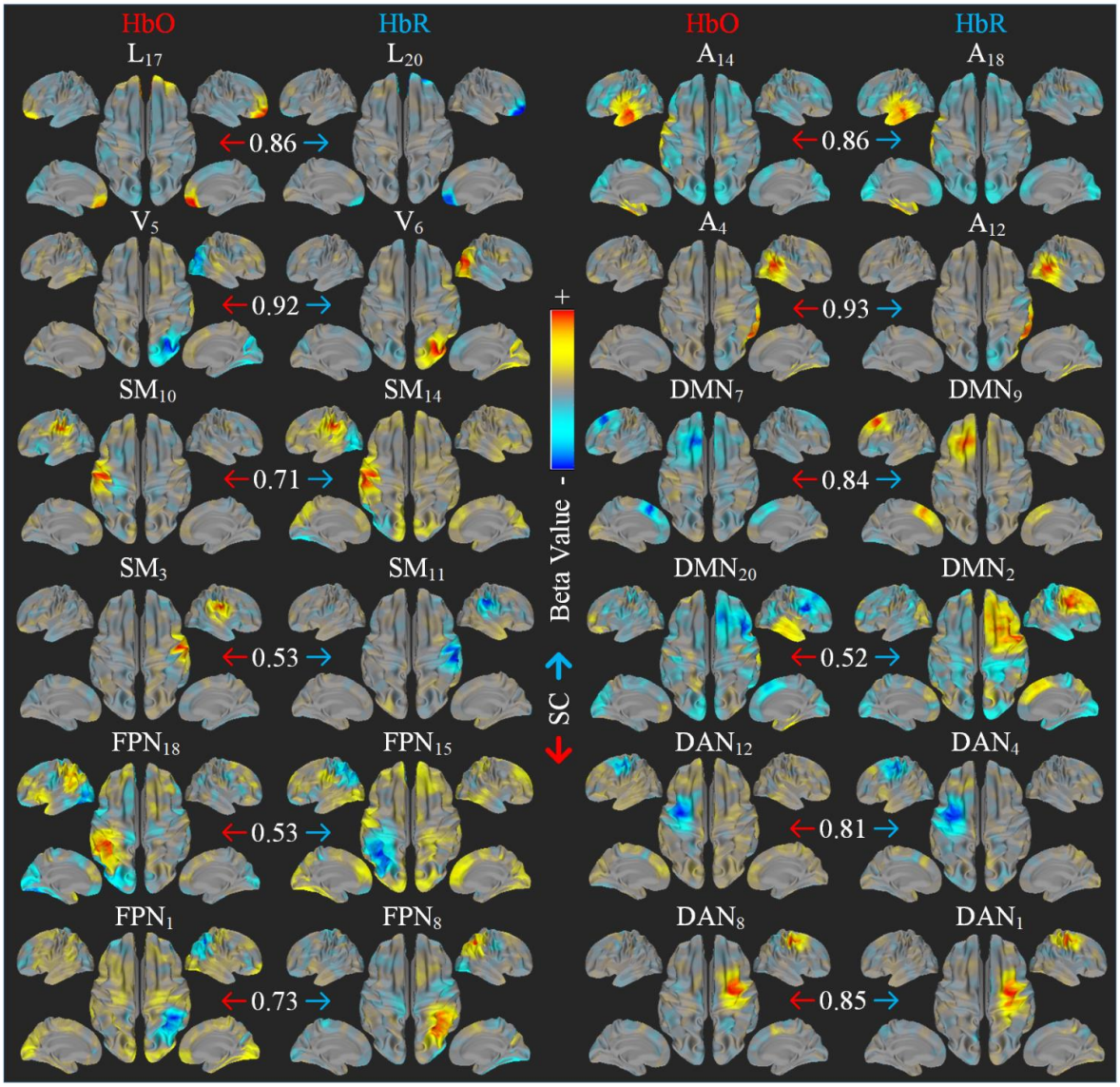

Figure 7-1 ICA-based HbO and HbR DOT RSN maps have similar spatial topographies. Examples of spatial patterns of RSNs obtained from HbO and HbR data that have similar spatial topographies. SC is calculated on the absolute beta values of the RSNs. L=limbic, V = visual, SM = somatomotor, DAN = dorsal attention network, FPN = frontoparietal network, A = auditory, DMN = default mode network. The complete set of 20 HbO and HbR RSNs are provided in Figure 7-2 and Figure 7-3 respectively.

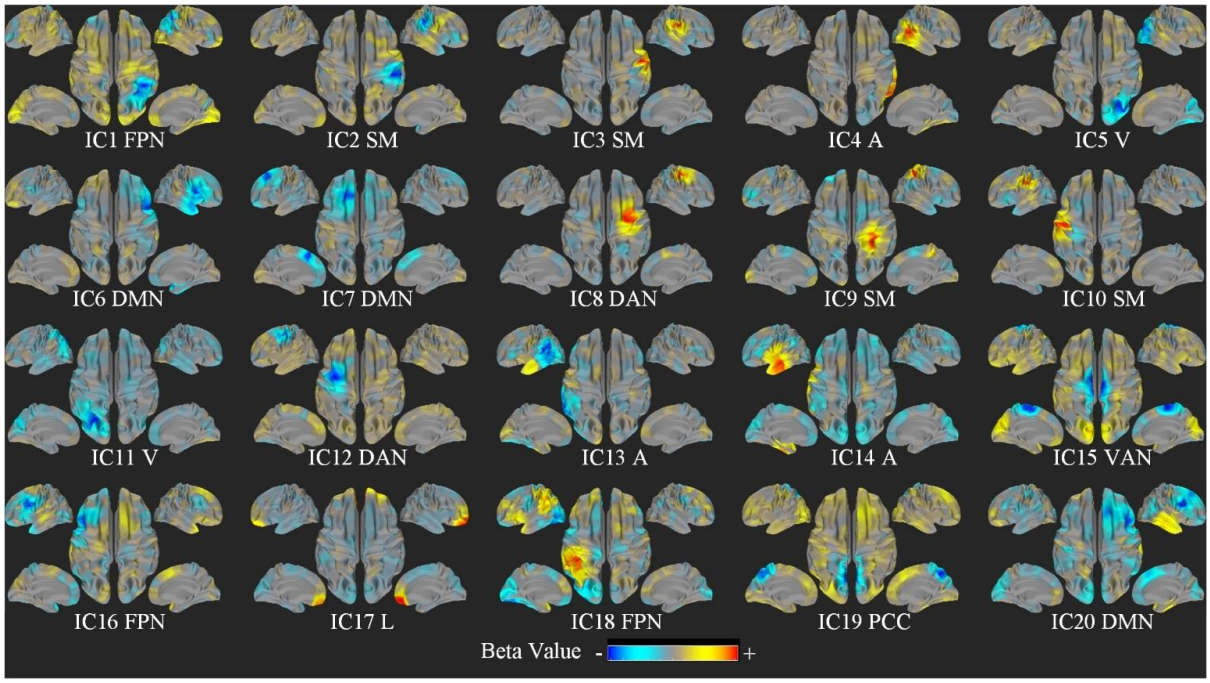

Figure 7-2 Complete set of group-level HbO DOT RSNs.
Group-level HbO DOT RSNs obtained via the spatiotemporal regression, visualized on the standard FreeSurfer cortical surface. VAN = ventral attention network.

Overall, the spatial maps of HbR networks were similar to the HbO networks. This similarity was verified using the quantitative metric of SC calculated on the absolute beta values of all networks (Figure 7-4). This comparison between the reconstructed RSNs of the two chromophores yielded the group-level confusion matrix (Figure 7-4A). High positive metric values in the diagonal elements of the confusion matrix indicate that the HbO and HbR RSNs generally matched with each other. Statistically, SC values from all matched pairs of HbO and HbR RSNs (white bars in Figure 7-4B) were found to be significantly higher (unpaired t-test, $t(398) = 21.1$, $p < 1e\text{-}5$, Bonferroni corrected) than SC values from all unmatched pairs (blue bars Figure 7-4B). Furthermore, the SC values from all matched pairs of HbO and HbR RSNs were found to be statistically significantly higher (unpaired t-test, $t(303) = 20.0$, $p < 1e\text{-}5$, Bonferroni corrected) than from positive-only unmatched pairs (black bar in Figure 7-4B). These results indicate that the DOT

RSNs of the two chromophores (i.e., HbO and HbR) obtained from the ICA-based method have similar spatial topographies.

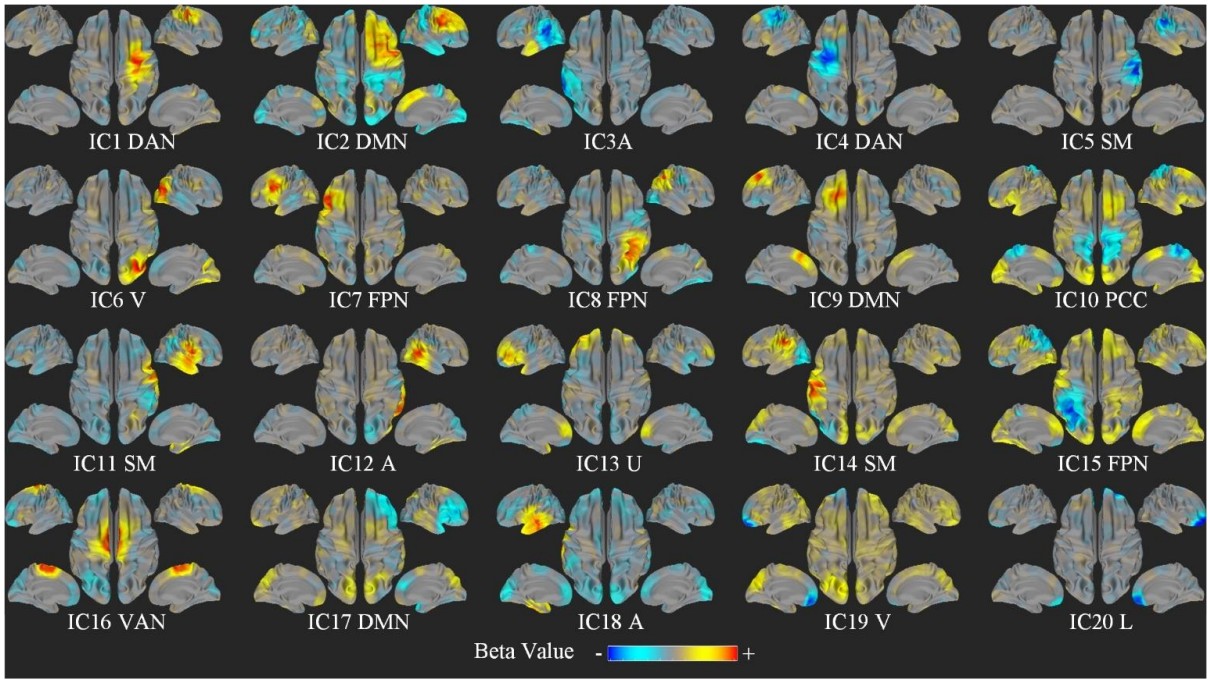

Figure 7-3 Complete set of group-level HbR DOT RSNs.
Group-level HbR DOT RSNs obtained via the spatiotemporal regression, visualized on the standard FreeSurfer cortical surface. U= unidentified network.

7.3.2 Significant differences exist between spatial topographies of HbO and HbR CAPs

A set of six brain-wide spatial maps of CAPs are obtained each for HbO and HbR hemoglobin data representing recurring brain states. The spatial patterns of these CAPs (Figure 7-5) had similarities and differences, as described next. The HbR spatial maps (Figure 7-5A) belonged to either of three bilaterally symmetrical spatial patterns: (1) (DV) (CAP 5,6) exhibiting opposite chromophore changes (positive vs. negative ΔHbR) along the dorsal-ventral axis, (2) the AP (CAP 1,2) exhibiting opposite chromophore changes along the anterior-posterior axis, and (3) global (CAP 3,4) exhibiting either a majority of global positive or global negative chromophore changes.

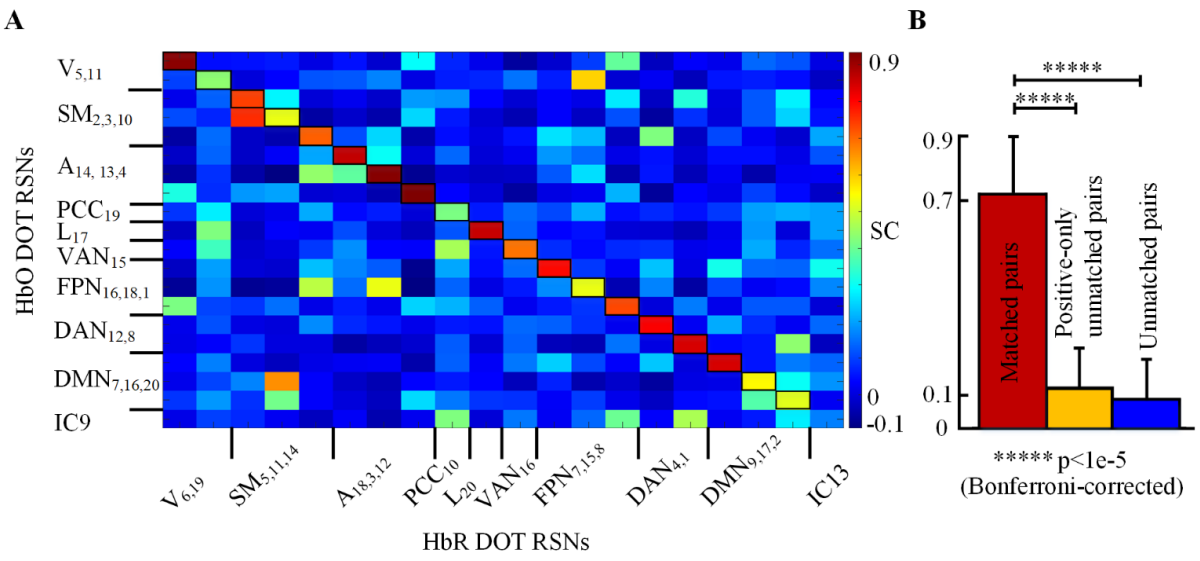

Figure 7-4 Quantitative comparison of spatial maps of HbO and HbR DOT RSNs. (A) Group-level confusion matrix between HbO and HbR DOT RSNs for the quantitative metric of spatial correlation (SC). The subscript on the RSNs denotes the index number of HbO and HbR RSNs as shown in Figure 7-2 and Figure 7-3 respectively. IC=independent component; (B) Means and standard deviations of SC calculated from the confusion matrix for matched pairs (enclosed in solid black lines), positive-only unmatched pairs, and unmatched pairs are plotted for SC together with their statistical differences tested using an unpaired t-test (Bonferroni-corrected).

For DV patterns, the boundary separating the polarity of HbR changes approximately ran along the inferior frontal sulcus, cut through the ventral part of the sensorimotor cortex, and extended posteriorly along the lateral occipital sulcus. For AP patterns, the boundary separating the polarity of HbR changes appeared roughly along the postcentral sulcus and cuts through the posterior end of the temporal cortex. The global CAPs exhibited either global positive or global negative HbR changes with diminished changes toward the anterior part of the temporal lobe.

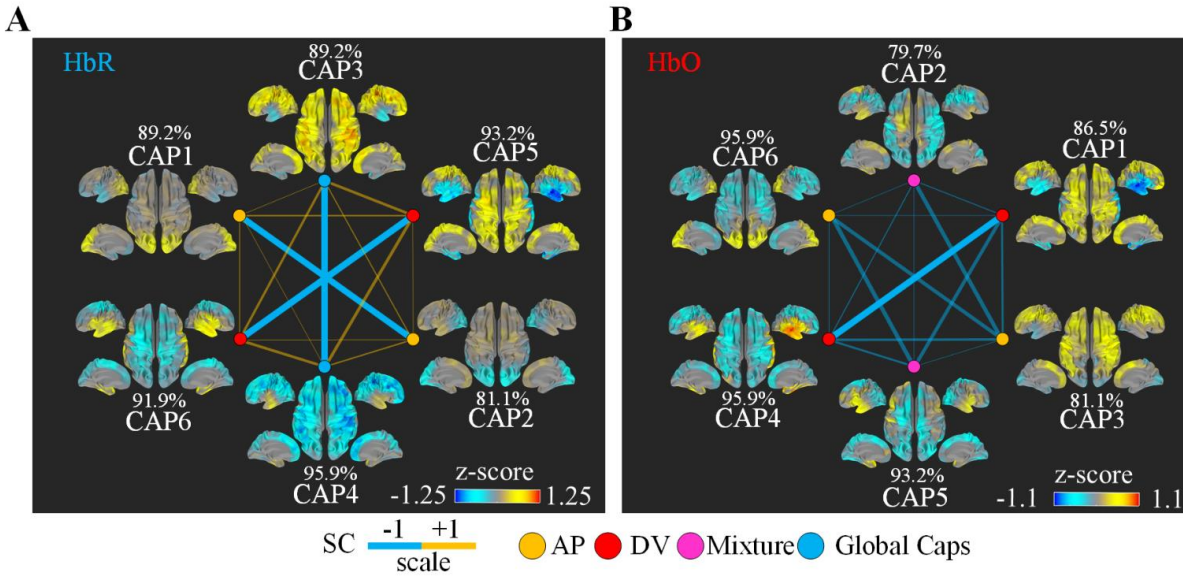

Figure 7-5 Spatial topographies of HbO and HbR DOT CAPs.
Group-level spatial maps of (A) HbR and (B) HbO CAPs for k = 6. Quantitative metric of symmetry for each CAP is shown as a percentage. Spatial correlation (SC) between CAPs is denoted by a line encoded by color (yellow: positive SC, blue: negative SC) and thickness. All lines are made 50% transparent except those with SC values less than -0.90, indicating high anticorrelation between a pair of CAPs.

For HbO, spatial maps (Figure 7-5B) belonged to the DV (CAP 1,4) and AP (CAP3,6) patterns which were similar to the HbR CAPs. Unlike HbR CAPs, we did not observe global CAPs in the HbO data. We could not identify CAP2 and 5 belonging to any pattern observed before in the HbR data. Therefore, we called them the mixture CAPs having a mixture pattern. Most CAPs exhibited high bilateral symmetry except for the mixture CAP2, which had the least bilateral symmetry (79.7%). The mean symmetry of HbR CAPs (mean symmetry: 90.1%) was greater (but not statistically significant) than that of HbO CAPs (mean symmetry: 88.7%).

The HbR CAPs existed in pairs of highly anticorrelated spatial patterns determined from visual inspection and pair-wise SC between all CAPs (Figure 7-5A). CAP1, 2 formed the pair of anticorrelated AP patterns (SC: -0.91), CAP2, 5 formed the pair of DV patterns (SC: -0.97), and CAP3, 4 formed the pair of global patterns (SC: -0.97). The mean SC of these pairs (i.e., -0.95)

was statistically significantly (unpaired t-test, t(13=4.51), p < .01, Bonferroni corrected) lower than the mean SC (i.e., -0.01) of all other possible pairs of CAPs. On the other hand, the HbO CAPs exhibited a strong anticorrelation for only the DV pair, i.e., between CAP1 and 4 (SC: -0.94), whereas there was a weaker anticorrelation for other CAP pairs. Specifically, the SC between the AP and mixture pattern pair CAPs was -0.54 and 0.01, respectively.

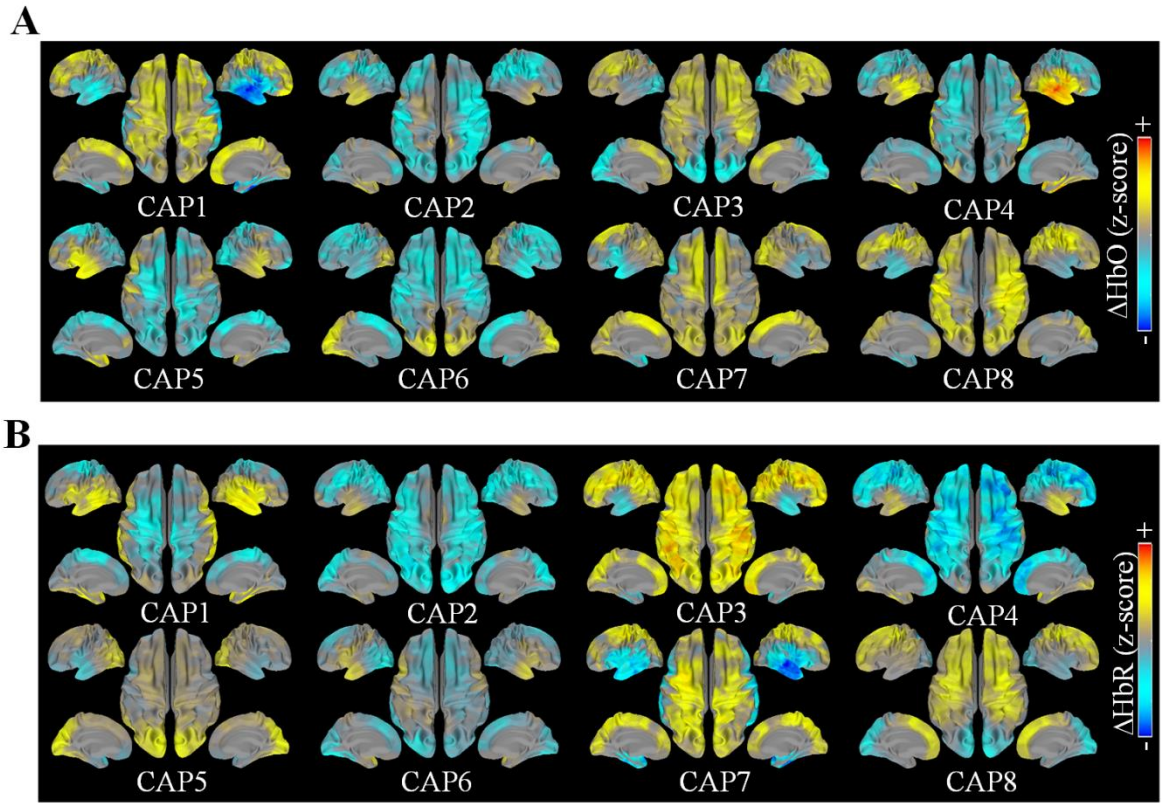

Figure 7-6 HbO and HbR DOT CAPs for k=8.
Group-level spatial maps of (A) HbO and (B) HbR CAPs.

Similar observations and differences were observed for larger cluster sizes. For example, for k=8 (Figure 7-6), all four spatial patterns of CAPs described above (i.e., AP, DV, mixture, and global) are observed. Specifically, for HbR (Figure 7-6B), the AP patterns (CAP5,8), DV patterns (CAP1, 7), global patterns (CAP2, 3, and 4), and one mixture pattern (CAP6) present themselves with strong bilateral symmetry. For HbO (Figure 7-6A), we did not observe any global CAPs but

observed the other three patterns, i.e., AP (CAP3, 6), DV (CAP1, 4), and mixture (CAP2, 5,7, and 8) patterns.

These differences in the spatial topographies of the CAPs of the two chromophores (HbO and HbR) collectively provide evidence that the CAP approach can reveal differences in the brain's FC of HbO and HbR DOT signals, unlike traditional methods like ICA-based RSNs that may instead represent the brain's spatial parcellation. These results thus confirm our first hypothesis.

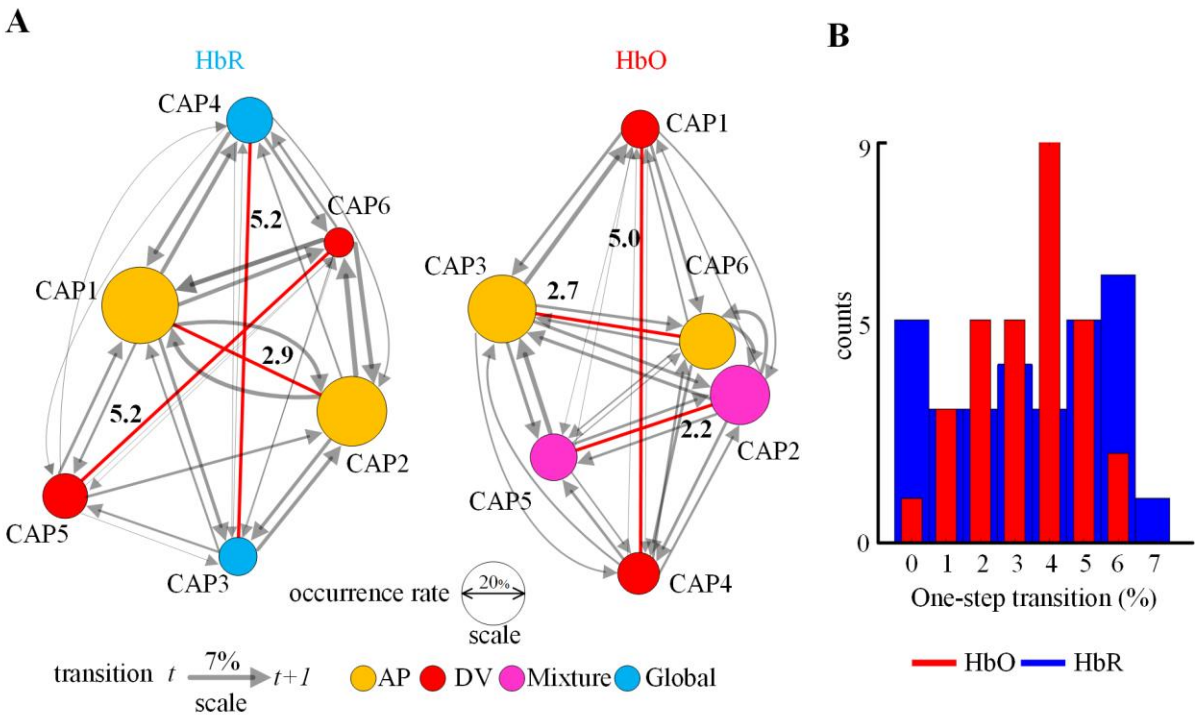

Figure 7-7 HbR CAPs exhibit a structured transitional organization than HbO CAPs. (A) 3D distance maps of the cluster centroids among 6 CAPs of (left) HbR and (right) HbO obtained after multidimensional scaling from a 20-dimensional space to a 3-dimensional subspace. The Euclidean distance between the CAPs is denoted by a red solid line and its value is provided in black and bold. The occurrence rate of a CAP is encoded by the diameter of a circle representing that CAP. One-step transition probability of a CAP from time t to t+1 is denoted using a directed transparent line with its width encoding the transition probability in percentage; (B) histogram of all transition probabilities in (A) for HbR (red bars) and HbO CAPs (blue bars).

7.3.3 HbR CAPs exhibit a more structured transitional organization than HbO CAPs

HbR CAPs show a more structured transitional organization than HbO CAPs, as supported by several observations of the temporal and dynamic properties of HbR and HbO CAPs (Figure 7-7). Firstly, in the HbR CAPs, only one pair of CAPs, i.e., the AP pair, occurred at a higher rate (CAP1: 24.7 %, CAP2: 22.5 %) than all other CAPs. These CAPs have a shorter interval time than other CAPs (data not shown). This high occurrence of the AP CAPs is further supported by a relatively smaller Euclidean distance (2.9) between the cluster centroids of high-occurring CAP1 and CAP2 compared to the distance between less-occurring CAPs, e.g., DV and global (5.2). These distances are shown in a 3D distance map (Figure 7-7) which illustrates all cluster centroids occupying one of the 3D space in an almost orthogonal structure. This structure also indicates that the dynamics of moment-to-moment brain states could be described in a 3D space by this collection of six CAPs, with each of them representing one spatially orthogonal pattern. A closer distance between two brain states represents a higher chance of transitioning between these states. This is supported by the one-step transition probabilities shown as directed arrows in Figure 7-7A. Specifically, a smaller distance between projected centroids in the 3D diagram of HbR CAPs corresponded to a higher transition probability, as shown by relatively thick directed arrows (Figure 7-7A left). For example, the HbR transitions involving the AP pair of CAPs show higher transition probabilities than other transitions resulting in a bimodal histogram of transition probabilities with one peak near zero and another near 6 % (Figure 7-7B) which suggests a heavy involvement of only AP pairs in transitions among all CAPs.

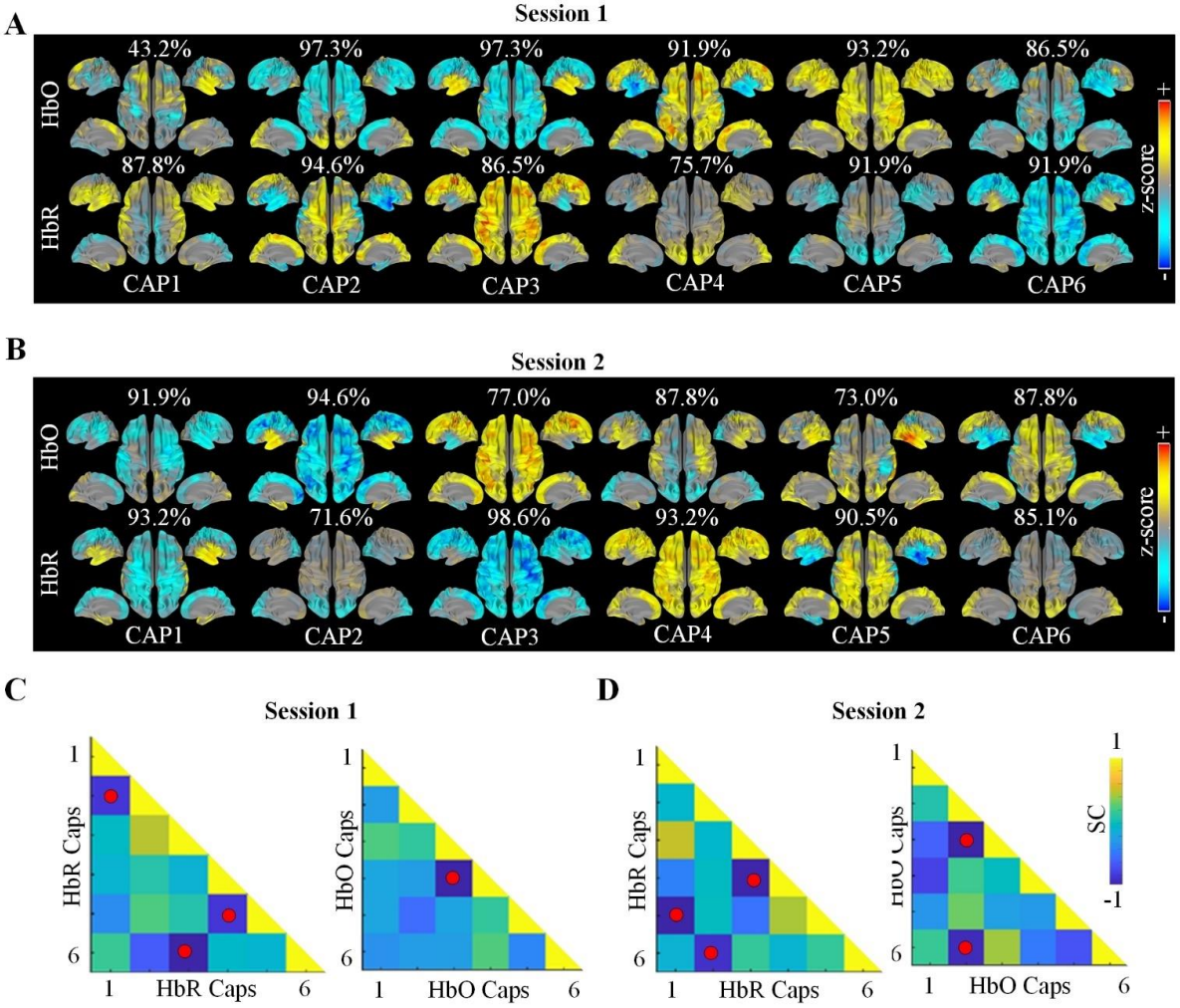

Figure 7-8 Group-level spatial maps of HbO and HbR DOT CAPs for session 1 and session 2. Group-level spatial maps of HbO and HbR CAPs when k = 6 for (A) session 1 and (B) session 2. Percentage of quantitative metric of symmetry for each CAP is shown at its top; spatial correlation (SC) between all possible pairs for the HbO and HbR DOT CAPs for (C) session 1 and (D) session 2 shown in (A) and (B) respectively. Solid red dots: SC values < -0.80, indicating high anticorrelation values between a pair of CAPs.

On the other hand, HbO lacked the structured transitional structure displayed by the HbR resting-state DOT data. Firstly, a smaller distance of 2.2 was observed between a high-occurring CAP (CAP2, 19.2 %) and a less-occurring CAP (CAP5, 15.1 %), in addition to a small distance of 2.7 between high-occurring AP CAPs (CAP3: 21.9 %, CAP6: 18.0 %). Secondly, unlike HbR,

the 3D map of the HbO lacked an orthogonal structure. Thirdly, we did not observe a heavy involvement of only one pair for HbO data. Instead, we observed that the HbO CAP transitions were distributed across several CAPs. Fourthly, overall, the transition probabilities of the HbO CAPs were lower compared to HbR, as indicated by the peak of the histogram of HbO at around 3.5 % (Figure 7-7B). Collectively, these differences in the temporal and dynamic properties of HbO and HbR CAPs confirm our second hypothesis that the HbR CAPs have a more structured transitional organization than HbO CAPs.

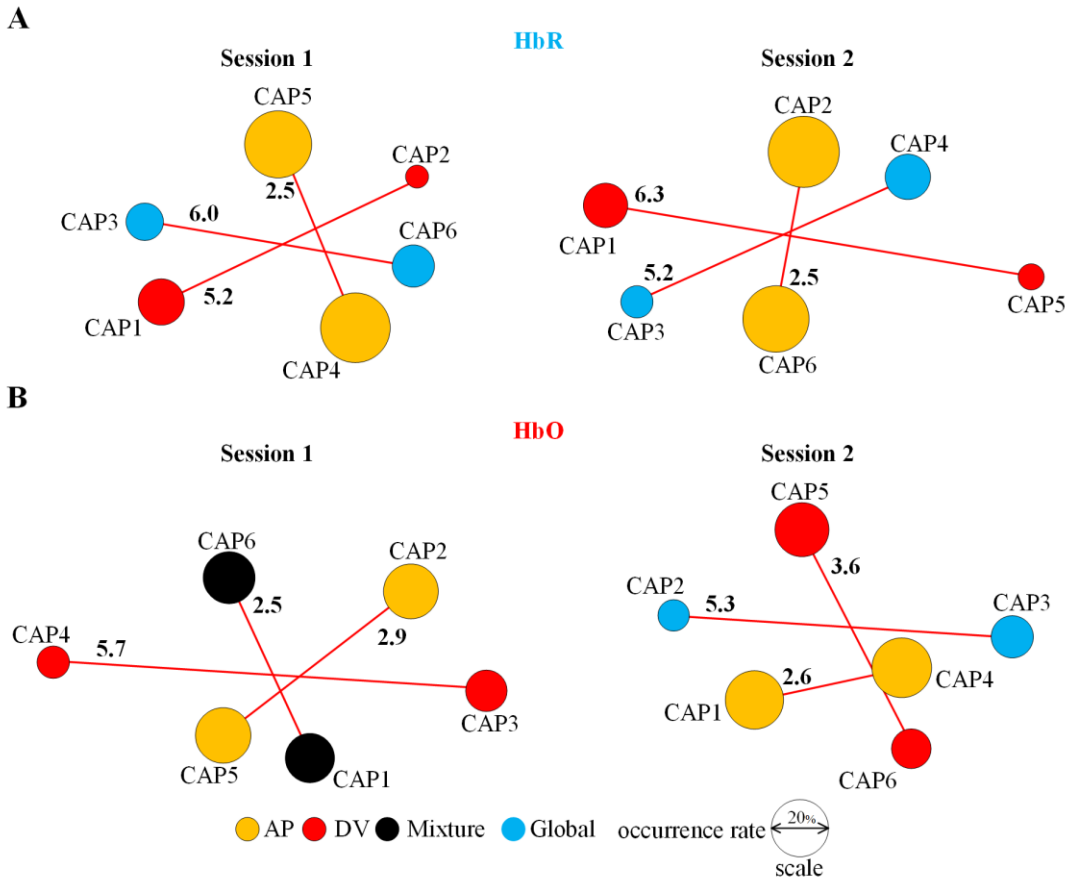

Figure 7-9 3D distance map and occurrence rates of CAPs across sessions.
Differences between the structured organization of CAPs of HbO and HbR are consistent across the two recording sessions. 3D distance maps of the cluster centroids among 6 CAPs and their occurrence rates of (A) HbR and (B) HbO for the two recording sessions.

7.3.4 Reproducibility of HbO and HbR CAPs

We observed differences between the spatiotemporal properties of the HbR and HbO CAPs obtained separately from a recording session. These differences mainly were consistent with those described in Sections 7.3.2 and 7.3.3, in which CAPs were obtained by concatenating data from the two recording sessions prior to clustering. Firstly, for HbR, we observed only AP, DV, and global CAP pairs for both sessions (Figure 7-8 A, B). For HbO, we observed AP, DV, and mixture CAP pairs for session 1. However, for session 2, we observed a global CAP pair (CAP2, 3) instead of a mixture pair. Most CAPs exhibited high bilateral symmetry except for the HbO mixture CAPs (Session 1, CAP1: 43.2 %, Session 2, CAP6: 73.0 %). Interestingly, the bilateral symmetry of an HbO global cap (CAP3) in session 2 (Figure 7-8B) was lower at 77.0 % than global CAPs in all other cases. Similar to the main results, we observed high anticorrelation among HbR CAPs (Figure 7-8C) compared to HbO CAPs (Figure 7-8C) for both sessions.

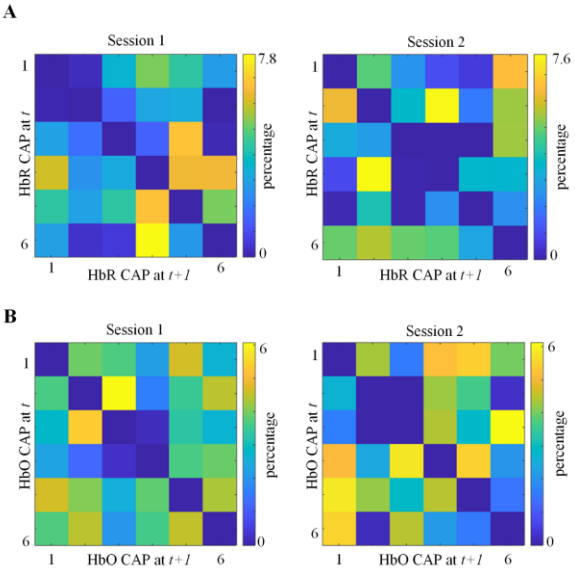

Figure 7-10 One-step transitions of HbO and HbR DOT CAPs for session 1 and session 2. One-step transition probability matrix of all CAPs of (A) HbR and (B) HbR for two recording sessions.

For HbR we observed an almost orthogonal structure in the 3D map for both sessions (Figure 7-9A). However, for HbO, we observed such a structure for only session 1. For HbR, a shorter Euclidean distance was observed between high-occurring CAPs, whereas this was not observed in HbO CAPs in both sessions. Similar to the main results, we saw a heavy involvement of only the AP pair in HbR CAPs, as indicated by the one-step transition probabilities (Figure 7-10A). In contrast, for HbO CAPs, we observed that transitions were distributed across several CAPs with overall lower transition probabilities than the HbR CAPs (Figure 7-10B).

These differences in the spatiotemporal properties of the HbR and HbO CAPs observed consistently across two recording sessions confirm our second hypothesis and suggest that the spontaneous HbR and HbO DOT signals carry different temporal and dynamic information distinguishable using a CAP-based analysis.

7.4 Discussion

In this chapter, we made two hypotheses; (1) that the differences in the resting-state networked brain activity of HbO and HbR signals should be observable using the CAP analysis, and (2) since the HbR signal is potentially more closely tied to the neural activity in terms of time than the HbO signal (see Section 7.1), the HbR CAPs should have a more structured transitional organization than the HbO CAPs. We first demonstrated that the traditional approach of studying networked brain activity via RSNs obtained using the ICA-based approach resulted in spatial patterns of networks with similar topological features (Figure 7-1, Figure 7-4). This spatial similarity between the two chromophores is in agreement with the previously reported HbO and HbR RSNs in the DOT literature obtained using the ICA method (White et al., 2012, Ferradal et al., 2016, Khan et al., 2021) and adds on to the suggestions that RSNs obtained using the ICA-based approach represents more of a spatial parcellation than a distinct mode of brain activity (Liu and Duyn,

2013). Even using the other popular seed-based correlational method to calculate RSNs (Biswal et al., 1995), similarity in spatial maps of the two chromophores has been reported in several DOT studies (Eggebrecht et al., 2012, White et al., 2012, White et al., 2009, Zeff et al., 2007, Ferradal et al., 2016, Eggebrecht et al., 2014). Motivated by the ability of the CAP analysis approach to analyze the distinct mode of brain activity (Liu and Duyn, 2013), we investigated the resting-state networked brain activity of HbO and HbR DOT data using the CAP analysis. Despite a high spatial similarity between the HbO and HbR DOT RSNs (Figure 7-4), we observed several spatiotemporal differences between the CAPs of HbO and HbR, confirming our first hypothesis.

While we observed some CAPs with spatial maps common to both HbO and HbR, such as AP and DV, there were still several differences. For example, we did not observe global patterns in the HbO CAPs and instead observed the mixture CAPs (Figure 7-5B). These mixture CAPs had relatively lower bilateral symmetry and weaker anticorrelations than other CAPs. They were also present in the HbO CAPs in individual recording sessions (Figure 7-8). In humans (Yeo et al., 2011, Smith et al., 2009a) and anesthetized monkeys (Vincent et al., 2007b), hemodynamic resting-state FC often exhibits bilateral symmetry across two cerebral hemispheres. The majority of coactivation studies with BOLD fMRI have also reported CAPs with symmetrical spatial patterns in humans (Liu et al., 2013, Liu et al., 2018a, Karahanoğlu and Van De Ville, 2015, Chen et al., 2015) and animals (Gutierrez-Barragan et al., 2019, Liang et al., 2015). Therefore, the mixture CAPs with lower bilateral symmetry cast doubt on their representation as brain states. While we are still trying to understand these mixture CAPs, we speculate that the heterogeneity in the spatial topography of these CAPs could be because of the oversupply of oxygenated hemoglobin with an increase in hyperemia following the neural activity. This oversupply of oxygen via increased blood flow could generate local hyperoxygenation far exceeding the oxygen

consumption (Hillman, 2014). This oversupply of oxygen occurs after the "initial dip" (Frostig et al., 1990) and is also suggested to supply higher levels of glucose instead of oxygen (Paulson et al., 2010, Fox and Raichle, 1986) and is even suggested to have a role in metabolic waste removal and thermal regulation (Yablonskiy et al., 2000).

On the other hand, deoxygenated hemoglobin is possibly more closely coupled with the brain's metabolic response (Hu and Yacoub, 2012). Its CAPs show a well-structured spatiotemporal organization. Firstly, we observe a high level of bilateral symmetry in all HbR CAPs in concatenated session data (Figure 7-5) and individual session data (Figure 7-8). This bilateral symmetry in CAPs has been reported in numerous studies as described above. Secondly, the HbR CAPs show strongly anticorrelated spatial patterns in all three pairs, i.e., AP, DV, and global pairs (Figure 7-5A, Figure 7-8A). In fMRI literature, strong brain-wide anticorrelation patterns widely exist in resting-state FCs and CAPs. In humans, the phenomenon of anticorrelation in RSNs has been observed using the conventional windowed correlational method, e.g., between sensory regions and default mode regions (Allen et al., 2014b) and between distributed task-positive and task-negative brain networks (Fox et al., 2005) (Liu et al., 2013). In animals, the phenomenon of anticorrelation has been reported with CAPs in resting mice (Gutierrez-Barragan et al., 2019). Although there have been doubts that the phenomenon of anticorrelation might be artificially introduced due to the global signal regression (GSR) (Murphy et al., 2009), the anticorrelation patterns have been reported in the absence of GS regression (Chai et al., 2012).

Moreover, we have shown in our previous CAP-based study that strong anticorrelations in the CAP spatial patterns are observed in the absence of GSR (Khan et al., 2022, under review). Thirdly, the occurrence rate, 3D maps, and transitional data (Figure 7-7) suggest a structured transitional organization of HbR contrast than HbO in which AP CAPs were heavily involved in

transitions involving all CAPs. This adds to our speculation on the temporal proximity of deoxygenated hemoglobin to the metabolic activity as the plausible reason for a superior structured transitional organization of the HbR CAPs than HbO CAPs.

Collectively, these differences between HbO and HbR CAPs confirm our second hypothesis and seem to suggest that deoxygenated hemoglobin is a more representative proxy for studying the temporal nature of networked brain activity than oxygenated hemoglobin. This observation is significant because oxygenated hemoglobin contrast has been historically preferred over deoxygenated hemoglobin contrast due to a high signal-to-noise ratio, especially for task-based experiments (Cui et al., 2010, Strangman et al., 2002, Zhang et al., 2019). Our results, on the other hand, suggest using deoxygenated hemoglobin for interrogating the networked brain activity at rest, especially when assuming nonstationarity across a scan.

8. Summary

This dissertation provides a novel framework for investigating the spatiotemporal properties of networked brain activity of resting-state DOT data. Chapter 2 introduces the field and a literature review of existing DOT RSN studies. Chapter 3 introduces a new computational framework named brain-wide diffuse optical tomography (BW-DOT) for reconstructing RSNs using CW-fNIRS data. Chapter 4 evaluates the BW-DOT framework using simulation and task-based experimental data. Chapter 5 applies the BW-DOT framework to resting-state fNIRS data from healthy participants to reconstruct brain-wide RSNs. Chapter 6 investigates the spatiotemporal properties of resting-state DOT networked brain activity using the method of co-activation patterns. Chapter 7 quantitatively compares the spatiotemporal differences between the HbO and HbR CAPs. In this chapter, we summarize the major work presented in this dissertation and highlight the significance of each contribution. We also discuss the limitations of these studies and provide directions for future work.

8.1 Summary of results

In Chapter 3, we developed a new computational framework of DOT, termed BW-DOT. It uses multiple technologies to investigate brain activity in dual contrasts of HbO and HbR. This work is significant in several ways. Firstly, BW-DOT offers a brain-wide FOV for studying resting-state brain activity, a brain-wide phenomenon. This large FOV is a major improvement to previous DOT RSN studies that primarily reported limited brain coverage, mainly in the form of rectangular optode patches. In addition to a large FOV, we have placed the optodes on a standard 10-5 system. This is an attempt to standardize our system to provide an opportunity to integrate datasets from different researchers for analysis and to standardize the protocol for clinical research. Secondly, the proposed framework mainly utilizes a data-driven approach (i.e., ICA) for pattern

recognition of brain networks. This approach minimizes bias in selecting seed locations otherwise used in SCA methods. ICA can simultaneously reconstruct multiple brain networks and is suitable for cap-based optode placement (see Section 3.8). Thirdly, we have supplemented the ICA with correlation analysis to create statistical correlation tomographic maps (Li et al., 2018), which has not been reported before in the DOT RSN literature. The use of SCT efficiently minimizes the effect of magnitude-causing superficial source reconstructions. It leads to the recovery of brain networks in relatively deep cortical structures. Being able to image deeper cortical areas is of great interest in the DOT functional neuroimaging community because light attenuates considerably with depth.

In Chapter 4, the proposed framework was evaluated using simulated and task-based experimental data. The results using the simulation data provided quantitative spatial resolution metrics of our system. Such an evaluation of these metrics was previously reported using patch-based regional DOT systems using relatively a simple head geometry, i.e., a regional epicortical surface patch (White, 2012). Our current evaluation of these metrics on cap-based whole-head systems provided useful knowledge of the distribution of these metrics on a realistic head geometry with different resolutions and with whole-cap optode montage of different densities. We further investigated the dependence of these metrics on cortical depth and distance from the optodes, which are analyses not reported previously in the literature.

We also evaluated the performance of BW-DOT in reconstructing brain activity elicited by a hand-clenching task. BW-DOT was able to localize motor sources, consistent with previously reported literature accurately. Moreover, these results were reliable because they were consistent over four sessions, and we obtained these results from several participants. Furthermore, timing analysis of reconstructed results was performed, revealing rich temporal information of three brain

areas within the motor network for motor control. This analysis was not previously reported in the DOT literature. These experiments demonstrated that the proposed BW-DOT framework could accurately reconstruct brain activity with a brain-wide FOV. These results gave us confidence that our framework has the spatiotemporal resolution to study brain-wide resting-state activity.

In Chapter 5, we applied BW-DOT to resting-state fNIRS data. This study was significant in several ways. Firstly due to the use of cap-based, whole-head optode montage, our results report a large number of simultaneously-reconstructed RSNs, which is close to the typical number of RSNs, e.g., 10 (Damoiseaux et al., 2006b) or 17 (Yeo et al., 2011), studied with fMRI. In the previous DOT studies, only part of the neocortex was imaged, leading to the investigation of limited RSNs. A large FOV revealed mPFC and PCC (Figure 5-1 and Figure 5-2), which were both missed in previous DOT RSN studies (Eggebrecht et al., 2014), similar to the anterior and posterior subnetworks of DMN, respectively, as reported in previous fMRI studies. This was achieved as the cap-based whole-head montage filled the gap in the previously unavailable frontal and medial regions. The identifications of these two RSNs are of clinical value as their connectivity changes have been associated with normal aging (Buckner et al., 2008, Andrews-Hanna et al., 2007) and deterioration related to Alzheimer's disease (Sorg et al., 2007).

Secondly, while most previous DOT studies have reported RSNs, our results further indicate subnetworks among several RSNs consistent with fMRI literature (Smith et al., 2009b). Thirdly, we have provided a quantitative comparison between HbO and HbR DOT RSNs, missing in the literature. Our quantitative metrics reveal that HbR RSNs are slightly but statistically significantly better aligned with fMRI RSNs, probably because the BOLD contrast in fMRI signals is primarily sensitive to paramagnetic HbR molecules (Buxton, 2013). Overall, HbO- and HbR-based DOT RSNs are, in general, consistent with each other. Some minor differences between them indicate

complementary benefits of each contrast, which might also suggest the usefulness of total hemoglobin signals, i.e., the combination of HbO and HbR, in mapping RSNs (Devor et al., 2005, Culver et al., 2005, Sheth et al., 2004).

In Chapter 6, we, for the first time, report coactivation patterns via a framewise clustering technique on independent component sources identified in HbR DOT data, which leads to the detection of manifold brain-wide patterns indicating recurring functional brain states. The results from this study provide valuable insights and carry significance in several ways. Firstly, we demonstrate that the resting-state fluctuations of whole-brain hemodynamic signals can be accounted for with a relatively small number of brain-wide functional states, i.e., 6 CAPs, which is consistent with the number of CAPs reported in recent fMRI literature, e.g., 6 (Yang et al., 2021) and 8 CAPs (Janes et al., 2020). Secondly, we observe that DOT CAPs show strongly anticorrelated spatial patterns in pairs in which one pair shows global positive and negative patterns. We further demonstrate that these two global activity patterns are phase-locked to global signals (GS) and are responsible for generating a significant subset of global signal peaks and troughs, while non-neuronal systematic fluctuations in breathing and circulation are responsible for the generation of other global signal peaks and troughs.

Thirdly, we present evidence of structured transitions among identified brain states. Most transitions among brain states are mediated via the pair of anterior-posterior CAPs (Figure 6-5D). Furthermore, brain states with both anterior-posterior and dorsal-ventral patterns might reflect representative spatial patterns during the well-reported globally propagating waves in the anterior-posterior and dorsal-ventral directions, respectively. Fourthly, we provide evidence about the plausible neuronal origins of two global CAPs, which further supports that GS contains neuronally relevant information due to the close relationship between GS and global CAPs. These results

collectively indicate the existence and interaction of three phenomena, i.e., CAPs, global brain activity, and brain-wide structured transitions, in human hemodynamic data, which extend existing findings on similar transient neuronal events recently reported in animal fMRI data. Our study has important implications for understanding the spontaneous activities and the fundamental organization of resting-state networked brain activity.

In Chapter 7, we investigated the difference between the spatiotemporal properties of HbO and HbR CAPs. These results have significance in several ways. Firstly, we have demonstrated that the ICA-based method is not suitable for studying the non-stationarity of networked brain activity and that other techniques like CAP analysis are more suitable. Secondly, we demonstrated that CAP analysis could reveal spatiotemporal differences between HbO and HbR DOT signals. Thirdly, our results suggest that the HbR CAPs have a more structured transitional organization compared to CAPs obtained from HbO signals. This observation is significant because fNIRS HbO contrast has been preferred over HbR due to a high signal-to-noise ratio, especially for task-based fNIRS experiments. Our results suggest using HbR contrast as a more appropriate contrast for investigating the non-stationarity of DOT resting-state data.

8.2 Limitations and future work

The present study was limited in the following aspects. Firstly, while the SCT step of the proposed framework has enabled the mapping of relatively deeper cortical activity than what can be done by using spatial ICA alone (see Section 3.5), DOT is still fundamentally limited in mapping deep cortical structures (e.g., the insular cortex) and other deep brain structures (e.g., hippocampus and amygdala), which is primarily constrained by the limited penetration of light and therefore significantly reduced sensitivity in deep parts of the brain (Dehghani et al., 2009b), which is the most significant drawback as compared with fMRI. Secondly, despite having a brain-

wide coverage, a few brain regions still have lower spatial resolution and sensitivity, such as ventral parts of the temporal cortex and dorsal parts of the brain.

Thirdly, the selection of the inverse solution, i.e., MNE, in the present study also contributes to the limited capacity in mapping deep cortical structures. The MNE inverse solution is linear and thus computational efficient. However, its inverse source reconstructions are biased toward superficial source reconstructions (Pascual-Marqui, 1999). It is important to select inverse solutions with accurate reconstructions on source temporal dynamics as the characterization of RSNs in the ICA and SCT steps following the inverse step depends on the accuracy of reconstructed time courses. In order to improve the mapping of sources from deep cortical structures, more advanced inverse imaging techniques could be integrated into the proposed framework (Zhu et al., 2014, Pogue et al., 1999, Cao et al., 2007). Fourthly, while it is not sufficiently noted, optodes connected with optical fibers with high-density placements in our present system are still heavy and of reduced portability. Therefore, much-needed work is required in the direction of miniaturization of the whole-head high-density optode cap.

Fifthly, a relatively low spatial density of optodes might contribute to the small number of brain states (i.e., 6) identified in the present work, which should be investigated in future studies after addressing the technical challenge of having an ultrahigh-density whole-head-coverage DOT system. Sixthly, like fMRI, DOT interrogates human brain activity indirectly on secondary hemodynamic responses of neuronal events and, therefore, neuronal origins of brain-wide CAPs and global brain activity, as well as their propagation characteristics, need to be further investigated using primary response data of neuronal events, i.e., electrical activity (Ding et al., 2021), with technologies like EEG, MEG, and ECoG. In particular, to directly investigate the relationship between brain-wide neuronal events and their hemodynamic correspondences would need

simultaneous recording techniques, including concurrent EEG and fMRI (Yuan et al., 2016, Yuan et al., 2012) or concurrent EEG and fNIRS (Khan et al., 2021, Ahn and Jun, 2017, Chen et al., 2020c). Moreover, the physiological relevance of these global CAPs needs to be established by identifying their behavioral or cognitive correlates (Preti et al., 2017).

Finally, the number of participants in the present study is relatively small compared to some fMRI RSN studies, e.g., about 1000 (Yeo et al., 2011). Therefore, our findings should be validated using a large number of participants.

Bibliography

AGOSTA, F., PIEVANI, M., GEROLDI, C., COPETTI, M., FRISONI, G. B. & FILIPPI, M. 2012. Resting state fMRI in Alzheimer's disease: beyond the default mode network. *Neurobiol Aging,* 33**,** 1564-78.

AGUIRRE, G., ZARAHN, E. & D'ESPOSITO, M. 1998. The inferential impact of global signal covariates in functional neuroimaging analyses. *Neuroimage,* 8**,** 302-306.

AHN, S. & JUN, S. C. 2017. Multi-modal integration of EEG-fNIRS for brain-computer interfaces–current limitations and future directions. *Frontiers in human neuroscience,* 11**,** 503.

AIHARA, T., SHIMOKAWA, T., OGAWA, T., OKADA, Y., ISHIKAWA, A., INOUE, Y. & YAMASHITA, O. 2020. Resting-State Functional Connectivity Estimated With Hierarchical Bayesian Diffuse Optical Tomography. *Front Neurosci,* 14**,** 32.

ALEXANDER, R. A. 1990. A note on averaging correlations. *Bulletin of the Psychonomic Society,* 28**,** 335-336.

ALLEN, E. A., DAMARAJU, E., PLIS, S. M., ERHARDT, E. B., EICHELE, T. & CALHOUN, V. D. 2014a. Tracking whole-brain connectivity dynamics in the resting state. *Cereb Cortex,* 24**,** 663-76.

ALLEN, E. A., DAMARAJU, E., PLIS, S. M., ERHARDT, E. B., EICHELE, T. & CALHOUN, V. D. 2014b. Tracking whole-brain connectivity dynamics in the resting state. *Cerebral cortex,* 24**,** 663-676.

ANDREWS-HANNA, J. R., SNYDER, A. Z., VINCENT, J. L., LUSTIG, C., HEAD, D., RAICHLE, M. E. & BUCKNER, R. L. 2007. Disruption of large-scale brain systems in advanced aging. *Neuron,* 56**,** 924-935.

ARRIDGE, S. R. 1999. Optical tomography in medical imaging. *Inverse Problems,* 15**,** R41-R93.

ARRIDGE, S. R. & SCHWEIGER, M. 1995. Photon-measurement density functions. Part 2: Finite-element-method calculations. *Appl Opt,* 34**,** 8026-37.

ARTHUR, D. & VASSILVITSKII, S. 2006. k-means++: The advantages of careful seeding. Stanford.

BAHRAMISHARIF, A., VAN GERVEN, M. A., AARNOUTSE, E. J., MERCIER, M. R., SCHWARTZ, T. H., FOXE, J. J., RAMSEY, N. F. & JENSEN, O. 2013. Propagating neocortical gamma bursts are coordinated by traveling alpha waves. *Journal of Neuroscience,* 33**,** 18849-18854.

BARTLETT, M. S. 1946. On the theoretical specification and sampling properties of autocorrelated time-series. *Supplement to the Journal of the Royal Statistical Society,* 8**,** 27-41.

BECKMANN, C. F., DELUCA, M., DEVLIN, J. T. & SMITH, S. M. 2005. Investigations into resting-state connectivity using independent component analysis. *Philosophical Transactions of the Royal Society B: Biological Sciences,* 360**,** 1001-1013.

BECKMANN, C. F., JENKINSON, M. & SMITH, S. M. 2003. General multilevel linear modeling for group analysis in FMRI. *Neuroimage,* 20**,** 1052-1063.

BECKMANN, C. F., MACKAY, C. E., FILIPPINI, N. & SMITH, S. M. 2009. Group comparison of resting-state FMRI data using multi-subject ICA and dual regression. *Neuroimage,* 47**,** S148.

BERENS, P. 2009. CircStat: a MATLAB toolbox for circular statistics. *J Stat Softw,* 31**,** 1-21.
BERTERO, M., DE MOL, C. & PIKE, E. R. 1988. Linear inverse problems with discrete data: II. Stability and regularisation. *Inverse problems,* 4**,** 573.
BISWAL, B., ZERRIN YETKIN, F., HAUGHTON, V. M. & HYDE, J. S. 1995. Functional connectivity in the motor cortex of resting human brain using echo-planar MRI. *Magnetic resonance in medicine,* 34**,** 537-541.
BISWAL, B. B., MENNES, M., ZUO, X.-N., GOHEL, S., KELLY, C., SMITH, S. M., BECKMANN, C. F., ADELSTEIN, J. S., BUCKNER, R. L. & COLCOMBE, S. 2010. Toward discovery science of human brain function. *Proceedings of the National Academy of Sciences,* 107**,** 4734-4739.
BLUESTONE, A. Y., ABDOULAEV, G., SCHMITZ, C. H., BARBOUR, R. L. & HIELSCHER, A. H. 2001. Three-dimensional optical tomography of hemodynamics in the human head. *Optics express,* 9**,** 272-286.
BOAS, D. A., CULVER, J. P., STOTT, J. J. & DUNN, A. K. 2002. Three dimensional Monte Carlo code for photon migration through complex heterogeneous media including the adult human head. *Optics express,* 10**,** 159-170.
BOAS, D. A., DALE, A. M. & FRANCESCHINI, M. A. 2004. Diffuse optical imaging of brain activation: approaches to optimizing image sensitivity, resolution, and accuracy. *Neuroimage,* 23 Suppl 1**,** S275-88.
BOAS, D. A., ELWELL, C. E., FERRARI, M. & TAGA, G. 2014. Twenty years of functional near-infrared spectroscopy: introduction for the special issue. Elsevier.
BOAS, D. A., GAUDETTE, T., STRANGMAN, G., CHENG, X., MAROTA, J. J. & MANDEVILLE, J. B. 2001. The accuracy of near infrared spectroscopy and imaging during focal changes in cerebral hemodynamics. *Neuroimage,* 13**,** 76-90.
BONFERRONI, C. 1936. Teoria statistica delle classi e calcolo delle probabilita. *Pubblicazioni del R Istituto Superiore di Scienze Economiche e Commericiali di Firenze,* 8**,** 3-62.
BORTFELD, H. 2019. Functional near-infrared spectroscopy as a tool for assessing speech and spoken language processing in pediatric and adult cochlear implant users. *Developmental psychobiology,* 61**,** 430-443.
BOZKURT, A. & ONARAL, B. 2004. Safety assessment of near infrared light emitting diodes for diffuse optical measurements. *Biomedical Engineering Online,* 3.
BRESSLER, S. L. & MENON, V. 2010. Large-scale brain networks in cognition: emerging methods and principles. *Trends Cogn Sci,* 14**,** 277-90.
BROOKES, M. J., TEWARIE, P. K., HUNT, B. A., ROBSON, S. E., GASCOYNE, L. E., LIDDLE, E. B., LIDDLE, P. F. & MORRIS, P. G. 2016. A multi-layer network approach to MEG connectivity analysis. *Neuroimage,* 132**,** 425-438.
BROOKES, M. J., WOOLRICH, M., LUCKHOO, H., PRICE, D., HALE, J. R., STEPHENSON, M. C., BARNES, G. R., SMITH, S. M. & MORRIS, P. G. 2011. Investigating the electrophysiological basis of resting state networks using magnetoencephalography. *Proceedings of the National Academy of Sciences,* 108**,** 16783-16788.
BUCKNER, R. L., ANDREWS-HANNA, J. R. & SCHACTER, D. L. 2008. The brain's default network: anatomy, function, and relevance to disease.
BUXTON, R. B. 2009. *Introduction to functional magnetic resonance imaging: principles and techniques,* Cambridge university press.

BUXTON, R. B. 2013. The physics of functional magnetic resonance imaging (fMRI). *Rep Prog Phys,* 76**,** 096601.
BUXTON, R. B., ULUDAG, K., DUBOWITZ, D. J. & LIU, T. T. 2004. Modeling the hemodynamic response to brain activation. *Neuroimage,* 23 Suppl 1**,** S220-33.
BUXTON, R. B., WONG, E. C. & FRANK, L. R. 1998. Dynamics of blood flow and oxygenation changes during brain activation: the balloon model. *Magnetic resonance in medicine,* 39**,** 855-864.
CALHOUN, V. & ADALI, T. 2004. Group ICA of fMRI toolbox (GIFT). *Online at http://icatb. sourceforge. net*.
CALHOUN, V. D., ADALI, T., PEARLSON, G. D. & PEKAR, J. J. 2001. A method for making group inferences from functional MRI data using independent component analysis. *Human brain mapping,* 14**,** 140-151.
CALHOUN, V. D., LIU, J. & ADALı, T. 2009. A review of group ICA for fMRI data and ICA for joint inference of imaging, genetic, and ERP data. *Neuroimage,* 45**,** S163-S172.
CALHOUN, V. D., MACIEJEWSKI, P. K., PEARLSON, G. D. & KIEHL, K. A. 2008. Temporal lobe and "default" hemodynamic brain modes discriminate between schizophrenia and bipolar disorder. *Human brain mapping,* 29**,** 1265-1275.
CALVETTI, D., MORIGI, S., REICHEL, L. & SGALLARI, F. 2000. Tikhonov regularization and the L-curve for large discrete ill-posed problems. *Journal of Computational and Applied Mathematics,* 123**,** 423-446.
CAO, N., NEHORAI, A. & JACOB, M. 2007. Image reconstruction for diffuse optical tomography using sparsity regularization and expectation-maximization algorithm. *Optics Express,* 15**,** 13695-13708.
CASE, K. M. & ZWEIFEL, P. F. 1967. Linear transport theory.
CHAI, X. J., CASTAÑÓN, A. N., ÖNGÜR, D. & WHITFIELD-GABRIELI, S. 2012. Anticorrelations in resting state networks without global signal regression. *Neuroimage,* 59**,** 1420-1428.
CHANG, C., CUNNINGHAM, J. P. & GLOVER, G. H. 2009. Influence of heart rate on the BOLD signal: the cardiac response function. *Neuroimage,* 44**,** 857-869.
CHANG, C. & GLOVER, G. H. 2010. Time-frequency dynamics of resting-state brain connectivity measured with fMRI. *Neuroimage,* 50**,** 81-98.
CHANG, C., LIU, Z., CHEN, M. C., LIU, X. & DUYN, J. H. 2013. EEG correlates of time-varying BOLD functional connectivity. *Neuroimage,* 72**,** 227-236.
CHEN, B. R., BOUCHARD, M. B., MCCASLIN, A. F., BURGESS, S. A. & HILLMAN, E. M. 2011. High-speed vascular dynamics of the hemodynamic response. *Neuroimage,* 54**,** 1021-1030.
CHEN, J. E., CHANG, C., GREICIUS, M. D. & GLOVER, G. H. 2015. Introducing co-activation pattern metrics to quantify spontaneous brain network dynamics. *Neuroimage,* 111**,** 476-488.
CHEN, J. Y. E., LEWIS, L. D., CHANG, C. T., TIAN, Q. Y., FULTZ, N. E., OHRINGER, N. A., ROSEN, B. R. & POLIMENI, J. R. 2020a. Resting-state "physiological networks". *Neuroimage,* 213**,** 116707.
CHEN, L. M., FRIEDMAN, R. M. & ROE, A. W. 2005. Optical imaging of SI topography in anesthetized and awake squirrel monkeys. *Journal of Neuroscience,* 25**,** 7648-7659.

CHEN, S., ROSS, T. J., ZHAN, W., MYERS, C. S., CHUANG, K.-S., HEISHMAN, S. J., STEIN, E. A. & YANG, Y. 2008. Group independent component analysis reveals consistent resting-state networks across multiple sessions. *Brain research,* 1239**,** 141-151.

CHEN, W.-L., WAGNER, J., HEUGEL, N., SUGAR, J., LEE, Y.-W., CONANT, L., MALLOY, M., HEFFERNAN, J., QUIRK, B. & ZINOS, A. 2020b. Functional near-infrared spectroscopy and its clinical application in the field of neuroscience: advances and future directions. *Frontiers in Neuroscience,* 14**,** 724.

CHEN, Y., TANG, J., CHEN, Y., FARRAND, J., CRAFT, M. A., CARLSON, B. W. & YUAN, H. 2020c. Amplitude of fNIRS Resting-State Global Signal Is Related to EEG Vigilance Measures: A Simultaneous fNIRS and EEG Study. *Frontiers in Neuroscience,* 14.

CHEONG, D., ZHANG, F., KIM, K., REID, A., HANAN, C., DING, L. & YUAN, H. Task-Related Systemic Artifacts in Functional Near-Infrared Spectroscopy. 2020 42nd Annual International Conference of the IEEE Engineering in Medicine & Biology Society (EMBC), 2020. IEEE, 948-951.

CHUNG, M. K., ROBBINS, S. M., DALTON, K. M., DAVIDSON, R. J., ALEXANDER, A. L. & EVANS, A. C. 2005. Cortical thickness analysis in autism with heat kernel smoothing. *NeuroImage,* 25**,** 1256-1265.

CHUNG, M. K., WORSLEY, K. J., NACEWICZ, B. M., DALTON, K. M. & DAVIDSON, R. J. 2010. General multivariate linear modeling of surface shapes using SurfStat. *Neuroimage,* 53**,** 491-505.

CIFRE, I., ZAREPOUR, M., HOROVITZ, S., CANNAS, S. & CHIALVO, D. 2020. Further results on why a point process is effective for estimating correlation between brain regions. *Papers in Physics,* 12**,** 120003-120003.

COLE, D. M., SMITH, S. M. & BECKMANN, C. F. 2010. Advances and pitfalls in the analysis and interpretation of resting-state FMRI data. *Frontiers in systems neuroscience,* 4**,** 8.

COMON, P. 1994. Independent component analysis, a new concept? *Signal processing,* 36**,** 287-314.

CUI, X., BRAY, S. & REISS, A. L. 2010. Functional near infrared spectroscopy (NIRS) signal improvement based on negative correlation between oxygenated and deoxygenated hemoglobin dynamics. *Neuroimage,* 49**,** 3039-3046.

CULVER, J. P., SIEGEL, A. M., FRANCESCHINI, M. A., MANDEVILLE, J. B. & BOAS, D. A. 2005. Evidence that cerebral blood volume can provide brain activation maps with better spatial resolution than deoxygenated hemoglobin. *Neuroimage,* 27**,** 947-959.

CULVER, J. P., SIEGEL, A. M., STOTT, J. J. & BOAS, D. A. 2003. Volumetric diffuse optical tomography of brain activity. *Optics letters,* 28**,** 2061-2063.

CUTINI, S., MORO, S. B. & BISCONTI, S. 2012. Functional near infrared optical imaging in cognitive neuroscience: an introductory review. *Journal of Near Infrared Spectroscopy,* 20**,** 75-92.

DAMARAJU, E., ALLEN, E. A., BELGER, A., FORD, J. M., MCEWEN, S., MATHALON, D., MUELLER, B., PEARLSON, G., POTKIN, S. & PREDA, A. 2014. Dynamic functional connectivity analysis reveals transient states of dysconnectivity in schizophrenia. *NeuroImage: Clinical,* 5**,** 298-308.

DAMOISEAUX, J. S., ROMBOUTS, S., BARKHOF, F., SCHELTENS, P., STAM, C. J., SMITH, S. M. & BECKMANN, C. F. 2006a. Consistent resting-state networks across healthy subjects. *Proceedings of the national academy of sciences,* 103**,** 13848-13853.

DAMOISEAUX, J. S., ROMBOUTS, S. A., BARKHOF, F., SCHELTENS, P., STAM, C. J., SMITH, S. M. & BECKMANN, C. F. 2006b. Consistent resting-state networks across healthy subjects. *Proc Natl Acad Sci U S A,* 103**,** 13848-53.

DE HAVAS, J. A., PARIMAL, S., SOON, C. S. & CHEE, M. W. 2012. Sleep deprivation reduces default mode network connectivity and anti-correlation during rest and task performance. *Neuroimage,* 59**,** 1745-51.

DE LUCA, M., BECKMANN, C. F., DE STEFANO, N., MATTHEWS, P. M. & SMITH, S. M. 2006. fMRI resting state networks define distinct modes of long-distance interactions in the human brain. *Neuroimage,* 29**,** 1359-67.

DECO, G., JIRSA, V. K. & MCINTOSH, A. R. 2011. Emerging concepts for the dynamical organization of resting-state activity in the brain. *Nat Rev Neurosci,* 12**,** 43-56.

DEHGHANI, H., EAMES, M. E., YALAVARTHY, P. K., DAVIS, S. C., SRINIVASAN, S., CARPENTER, C. M., POGUE, B. W. & PAULSEN, K. D. 2009a. Near infrared optical tomography using NIRFAST: Algorithm for numerical model and image reconstruction. *Communications in numerical methods in engineering,* 25**,** 711-732.

DEHGHANI, H., WHITE, B. R., ZEFF, B. W., TIZZARD, A. & CULVER, J. P. 2009b. Depth sensitivity and image reconstruction analysis of dense imaging arrays for mapping brain function with diffuse optical tomography. *Applied optics,* 48**,** D137-D143.

DELORME, A. & MAKEIG, S. 2004. EEGLAB: an open source toolbox for analysis of single-trial EEG dynamics including independent component analysis. *Journal of neuroscience methods,* 134**,** 9-21.

DELPY, D. & COPE, M. 1997. Quantification in tissue near–infrared spectroscopy. *Philosophical Transactions of the Royal Society of London. Series B: Biological Sciences,* 352**,** 649-659.

DEMIRTAŞ, M., TORNADOR, C., FALCÓN, C., LÓPEZ-SOLÀ, M., HERNÁNDEZ-RIBAS, R., PUJOL, J., MENCHON, J. M., RITTER, P., CARDONER, N. & SORIANO-MAS, C. 2016. Dynamic functional connectivity reveals altered variability in functional connectivity among patients with major depressive disorder. *Human brain mapping,* 37**,** 2918-2930.

DESJARDINS, A. E., KIEHL, K. A. & LIDDLE, P. F. 2001. Removal of confounding effects of global signal in functional MRI analyses. *Neuroimage,* 13**,** 751-8.

DESTRIEUX, C., FISCHL, B., DALE, A. & HALGREN, E. 2010. Automatic parcellation of human cortical gyri and sulci using standard anatomical nomenclature. *Neuroimage,* 53**,** 1-15.

DEVOR, A., ULBERT, I., DUNN, A. K., NARAYANAN, S. N., JONES, S. R., ANDERMANN, M. L., BOAS, D. A. & DALE, A. M. 2005. Coupling of the cortical hemodynamic response to cortical and thalamic neuronal activity. *Proceedings of the National Academy of Sciences,* 102**,** 3822-3827.

DING, L., NI, Y., SWEENEY, J. & HE, B. 2011. Sparse cortical current density imaging in motor potentials induced by finger movement. *Journal of neural engineering,* 8**,** 036008.

DING, L., SHOU, G., CHA, Y.-H., SWEENEY, J. A. & YUAN, H. 2021. Brain-wide neural co-activations in resting human. *bioRxiv***,** 2021.12.03.471116.

DING, L., SHOU, G., YUAN, H. & AL., E. 2014. Lasting modulation effects of rTMS on enrual activity and connectivity as revealed by resting-state EEG. *IEEE Transactions on Biomedical Engineering***,** 2070-2080.

DOULGERAKIS-KONTOUDIS, M., EGGEBRECHT, A. T., WOJTKIEWICZ, S., CULVER, J. P. & DEHGHANI, H. 2017. Toward real-time diffuse optical tomography: accelerating light propagation modeling employing parallel computing on GPU and CPU. *Journal of biomedical optics,* 22**,** 125001.

DU, Y., PEARLSON, G. D., YU, Q., HE, H., LIN, D., SUI, J., WU, L. & CALHOUN, V. D. 2016. Interaction among subsystems within default mode network diminished in schizophrenia patients: a dynamic connectivity approach. *Schizophrenia research,* 170**,** 55-65.

DUNCAN, A., MEEK, J. H., CLEMENCE, M., ELWELL, C. E., TYSZCZUK, L., COPE, M. & DELPY, D. 1995. Optical pathlength measurements on adult head, calf and forearm and the head of the newborn infant using phase resolved optical spectroscopy. *Physics in Medicine & Biology,* 40**,** 295.

DUNN, A. K., DEVOR, A., DALE, A. M. & BOAS, D. A. 2005. Spatial extent of oxygen metabolism and hemodynamic changes during functional activation of the rat somatosensory cortex. *Neuroimage,* 27**,** 279-290.

DYBVIK, H. & STEINERT, M. 2021. Real-World fNIRS Brain Activity Measurements during Ashtanga Vinyasa Yoga. *Brain Sciences,* 11**,** 742.

EGGEBRECHT, A. T., FERRADAL, S. L., ROBICHAUX-VIEHOEVER, A., HASSANPOUR, M. S., DEHGHANI, H., SNYDER, A. Z., HERSHEY, T. & CULVER, J. P. 2014. Mapping distributed brain function and networks with diffuse optical tomography. *Nature photonics,* 8**,** 448-454.

EGGEBRECHT, A. T., WHITE, B. R., FERRADAL, S. L., CHEN, C., ZHAN, Y., SNYDER, A. Z., DEHGHANI, H. & CULVER, J. P. 2012. A quantitative spatial comparison of high-density diffuse optical tomography and fMRI cortical mapping. *neuroimage,* 61**,** 1120-1128.

EHLIS, A.-C., SCHNEIDER, S., DRESLER, T. & FALLGATTER, A. J. 2014. Application of functional near-infrared spectroscopy in psychiatry. *Neuroimage,* 85**,** 478-488.

ERHARDT, E. B., RACHAKONDA, S., BEDRICK, E. J., ALLEN, E. A., ADALI, T. & CALHOUN, V. D. 2011. Comparison of multi-subject ICA methods for analysis of fMRI data. *Human brain mapping,* 32**,** 2075-2095.

ERNST, T. & HENNIG, J. 1994. Observation of a fast response in functional MR. *Magnetic Resonance in Medicine,* 32**,** 146-149.

FANG, Q. & BOAS, D. A. Tetrahedral mesh generation from volumetric binary and grayscale images. 2009 IEEE International Symposium on Biomedical Imaging: From Nano to Macro, 2009. Ieee, 1142-1145.

FERRADAL, S. L., EGGEBRECHT, A. T., HASSANPOUR, M., SNYDER, A. Z. & CULVER, J. P. 2014. Atlas-based head modeling and spatial normalization for high-density diffuse optical tomography: in vivo validation against fMRI. *NeuroImage,* 85**,** 117-126.

FERRADAL, S. L., LIAO, S., EGGEBRECHT, A. T., SHIMONY, J. S., INDER, T. E., CULVER, J. P. & SMYSER, C. D. 2016. Functional Imaging of the Developing Brain at the Bedside Using Diffuse Optical Tomography. *Cerebral Cortex,* 26**,** 1558-1568.

FERRARI, M. & QUARESIMA, V. 2012. A brief review on the history of human functional near-infrared spectroscopy (fNIRS) development and fields of application. *Neuroimage,* 63**,** 921-35.

FISHELL, A. K., ARBELÁEZ, A. M., VALDÉS, C. P., BURNS-YOCUM, T. M., SHERAFATI, A., RICHTER, E. J., TORRES, M., EGGEBRECHT, A. T., SMYSER, C. D. & CULVER,

J. P. 2020. Portable, field-based neuroimaging using high-density diffuse optical tomography. *Neuroimage*, 116541.
FISHER, R. A. 1915. Frequency distribution of the values of the correlation coefficient in samples from an indefinitely large population. *Biometrika,* 10**,** 507-521.
FOSTER, D. J. & WILSON, M. A. 2006. Reverse replay of behavioural sequences in hippocampal place cells during the awake state. *Nature,* 440**,** 680-683.
FOX, M. D. & GREICIUS, M. 2010. Clinical applications of resting state functional connectivity. *Frontiers in systems neuroscience,* 4**,** 19.
FOX, M. D. & RAICHLE, M. E. 2007. Spontaneous fluctuations in brain activity observed with functional magnetic resonance imaging. *Nat Rev Neurosci,* 8**,** 700-11.
FOX, M. D., SNYDER, A. Z., VINCENT, J. L., CORBETTA, M., VAN ESSEN, D. C. & RAICHLE, M. E. 2005. The human brain is intrinsically organized into dynamic, anticorrelated functional networks. *Proceedings of the National Academy of Sciences,* 102**,** 9673-9678.
FOX, M. D., ZHANG, D., SNYDER, A. Z. & RAICHLE, M. E. 2009. The global signal and observed anticorrelated resting state brain networks. *Journal of neurophysiology,* 101**,** 3270-3283.
FOX, P. T. & RAICHLE, M. E. 1986. Focal physiological uncoupling of cerebral blood flow and oxidative metabolism during somatosensory stimulation in human subjects. *Proceedings of the National Academy of Sciences,* 83**,** 1140-1144.
FRANCESCHINI, M. A., JOSEPH, D. K., HUPPERT, T. J., DIAMOND, S. G. & BOAS, D. A. 2006. Diffuse optical imaging of the whole head. *Journal of biomedical optics,* 11**,** 054007.
FRISTON, K. J., HARRISON, L. & PENNY, W. 2003. Dynamic causal modelling. *Neuroimage,* 19**,** 1273-1302.
FRISTON, K. J., HOLMES, A. P., POLINE, J. B., GRASBY, P. J., WILLIAMS, S. C., FRACKOWIAK, R. S. & TURNER, R. 1995. Analysis of fMRI time-series revisited. *Neuroimage,* 2**,** 45-53.
FRISTON, K. J., JEZZARD, P. & TURNER, R. 1994. Analysis of functional MRI time-series. *Human brain mapping,* 1**,** 153-171.
FRISTON, K. J., MECHELLI, A., TURNER, R. & PRICE, C. J. 2000. Nonlinear responses in fMRI: the Balloon model, Volterra kernels, and other hemodynamics. *NeuroImage,* 12**,** 466-477.
FROGEL, J., KOGAN, A., AUGOUSTIDES, J. G., BERKENSTADT, H., FEDUSKA, E., STEYN, J., DWARAKANATH, S., NIR, E. A. & STOHL, S. 2019. The value of cerebral oximetry monitoring in cardiac surgery: challenges and solutions in adult and pediatric practice. *Journal of cardiothoracic and vascular anesthesia,* 33**,** 1778-1784.
FROSTIG, R. D., LIEKE, E. E., TS'O, D. Y. & GRINVALD, A. 1990. Cortical functional architecture and local coupling between neuronal activity and the microcirculation revealed by in vivo high-resolution optical imaging of intrinsic signals. *Proceedings of the National Academy of Sciences,* 87**,** 6082-6086.
GAAB, N., GABRIELI, J. D. & GLOVER, G. H. 2008. Resting in peace or noise: scanner background noise suppresses default-mode network. *Hum Brain Mapp,* 29**,** 858-67.
GAGNON, L., COOPER, R. J., YÜCEL, M. A., PERDUE, K. L., GREVE, D. N. & BOAS, D. A. 2012. Short separation channel location impacts the performance of short channel regression in NIRS. *Neuroimage,* 59**,** 2518-2528.

GAGNON, L., PERDUE, K., GREVE, D. N., GOLDENHOLZ, D., KASKHEDIKAR, G. & BOAS, D. A. 2011. Improved recovery of the hemodynamic response in diffuse optical imaging using short optode separations and state-space modeling. *Neuroimage,* 56**,** 1362-1371.

GERLOFF, C., RICHARD, J., HADLEY, J., SCHULMAN, A. E., HONDA, M. & HALLETT, M. 1998. Functional coupling and regional activation of human cortical motor areas during simple, internally paced and externally paced finger movements. *Brain: a journal of neurology,* 121**,** 1513-1531.

GIAMBRA, L. M. 1995. A laboratory method for investigating influences on switching attention to task-unrelated imagery and thought. *Consciousness and cognition,* 4**,** 1-21.

GIBSON, A. & DEHGHANI, H. 2009. Diffuse optical imaging. *Philosophical Transactions of the Royal Society A: Mathematical, Physical and Engineering Sciences,* 367**,** 3055-3072.

GLANTZ, S. A., SLINKER, B. K. & NEILANDS, T. B. 1990. *Primer of applied regression and analysis of variance,* New York, McGraw-Hill.

GOMAA, W. H. & FAHMY, A. A. 2016. A survey of text similarity approaches. *International journal of computer applications***,** 13-18.

GOODWIN, J. R., GAUDET, C. R. & BERGER, A. J. 2014. Short-channel functional near-infrared spectroscopy regressions improve when source-detector separation is reduced. *Neurophotonics,* 1**,** 015002.

GREICIUS, M. D., FLORES, B. H., MENON, V., GLOVER, G. H., SOLVASON, H. B., KENNA, H., REISS, A. L. & SCHATZBERG, A. F. 2007. Resting-state functional connectivity in major depression: abnormally increased contributions from subgenual cingulate cortex and thalamus. *Biological psychiatry,* 62**,** 429-437.

GREICIUS, M. D., KRASNOW, B., REISS, A. L. & MENON, V. 2003. Functional connectivity in the resting brain: A network analysis of the default mode hypothesis. *Proceedings of the National Academy of Sciences of the United States of America,* 100**,** 253-258.

GRINVALD, A., FROSTIG, R. D., SIEGEL, R. M. & BARTFELD, E. 1991. High-resolution optical imaging of functional brain architecture in the awake monkey. *Proceedings of the National Academy of Sciences,* 88**,** 11559-11563.

GU, Y., SAINBURG, L. E., KUANG, S., HAN, F., WILLIAMS, J. W., LIU, Y., ZHANG, N., ZHANG, X., LEOPOLD, D. A. & LIU, X. 2021. Brain activity fluctuations propagate as waves traversing the cortical hierarchy. *Cerebral Cortex,* 31**,** 3986-4005.

GUTIERREZ-BARRAGAN, D., BASSON, M. A., PANZERI, S. & GOZZI, A. 2019. Infraslow State Fluctuations Govern Spontaneous fMRI Network Dynamics. *Current Biology,* 29**,** 2295-+.

GUYTON, A. 2000. *Textbook of Medical Physiology,* Philadelphia: Saunders, Elsevier.

HABERMEHL, C., HOLTZE, S., STEINBRINK, J., KOCH, S. P., OBRIG, H., MEHNERT, J. & SCHMITZ, C. H. 2012. Somatosensory activation of two fingers can be discriminated with ultrahigh-density diffuse optical tomography. *Neuroimage,* 59**,** 3201-3211.

HALGREN, M., ULBERT, I., BASTUJI, H., FABÓ, D., ERŐSS, L., REY, M., DEVINSKY, O., DOYLE, W. K., MAK-MCCULLY, R. & HALGREN, E. 2019. The generation and propagation of the human alpha rhythm. *Proceedings of the National Academy of Sciences,* 116**,** 23772-23782.

HANSEN, P. C. 2007. Regularization tools version 4.0 for Matlab 7.3. *Numerical algorithms,* 46**,** 189-194.

HANSEN, P. C. & O'LEARY, D. P. 1993. The use of the L-curve in the regularization of discrete ill-posed problems. *SIAM journal on scientific computing,* 14**,** 1487-1503.
HARRELL, F. E. 2015. *Regression modeling strategies: With applications to linear models, logistics and ordinal regressio, and survival analysis*, Springer.
HE, B. J., ZEMPEL, J. M., SNYDER, A. Z. & RAICHLE, M. E. 2010. The temporal structures and functional significance of scale-free brain activity. *Neuron,* 66**,** 353-369.
HEINZLE, J., KOOPMANS, P. J., DEN OUDEN, H. E., RAMAN, S. & STEPHAN, K. E. 2016. A hemodynamic model for layered BOLD signals. *Neuroimage,* 125**,** 556-570.
HESS, A., STILLER, D., KAULISCH, T., HEIL, P. & SCHEICH, H. 2000. New insights into the hemodynamic blood oxygenation level-dependent response through combination of functional magnetic resonance imaging and optical recording in gerbil barrel cortex. *Journal of Neuroscience,* 20**,** 3328-3338.
HILLMAN, E. M. 2014. Coupling mechanism and significance of the BOLD signal: a status report. *Annual review of neuroscience,* 37**,** 161-181.
HINDRIKS, R., ADHIKARI, M. H. & AL., E. 2016. Can sliding-window correlations reveal dynamic functional connectivity in resting-state fMRI? *Neuroimage***,** 242-256.
HOLMES, A. 1988. Generalisability, random effects and population inference. *Neuroimage,* 7.
HORNE, J. H. & BALIUNAS, S. L. 1986. A prescription for period analysis of unevenly sampled time series. *The Astrophysical Journal,* 302**,** 757-763.
HOSHI, Y. & TAMURA, M. 1993. Detection of dynamic changes in cerebral oxygenation coupled to neuronal function during mental work in man. *Neuroscience letters,* 150**,** 5-8.
HU, X. & YACOUB, E. 2012. The story of the initial dip in fMRI. *Neuroimage,* 62**,** 1103-1108.
HUANG, N. E., SHEN, Z., LONG, S. R., WU, M. C., SHIH, H. H., ZHENG, Q., YEN, N.-C., TUNG, C. C. & LIU, H. H. 1998. The empirical mode decomposition and the Hilbert spectrum for nonlinear and non-stationary time series analysis. *Proceedings of the Royal Society of London. Series A: mathematical, physical and engineering sciences,* 454**,** 903-995.
HUANG, X., XU, W., LIANG, J., TAKAGAKI, K., GAO, X. & WU, J.-Y. 2010. Spiral wave dynamics in neocortex. *Neuron,* 68**,** 978-990.
HUPPERT, T. J., DIAMOND, S. G., FRANCESCHINI, M. A. & BOAS, D. A. 2009. HomER: a review of time-series analysis methods for near-infrared spectroscopy of the brain. *Appl Opt,* 48**,** D280-98.
HUTCHISON, R. M., WOMELSDORF, T., ALLEN, E. A., BANDETTINI, P. A., CALHOUN, V. D., CORBETTA, M., DELLA PENNA, S., DUYN, J. H., GLOVER, G. H. & GONZALEZ-CASTILLO, J. 2013a. Dynamic functional connectivity: promise, issues, and interpretations. *Neuroimage,* 80**,** 360-378.
HUTCHISON, R. M., WOMELSDORF, T., GATI, J. S., EVERLING, S. & MENON, R. S. 2013b. Resting-state networks show dynamic functional connectivity in awake humans and anesthetized macaques. *Human brain mapping,* 34**,** 2154-2177.
HYVARINEN, A. 1999. Fast and robust fixed-point algorithms for independent component analysis. *IEEE transactions on Neural Networks,* 10**,** 626-634.
HYVÄRINEN, A., SÄRELÄ, J., SSRELS, J. & VIGÁRIO, R. 1999. Spikes and bumps: Artefacts generated by independent component analysis with insufficient sample size.
IADECOLA, C. 2017. The neurovascular unit coming of age: a journey through neurovascular coupling in health and disease. *Neuron,* 96**,** 17-42.

INGLE JR, J. D. & CROUCH, S. R. 1988. Spectrochemical analysis.
JACQUES, S. L. & POGUE, B. W. 2008. Tutorial on diffuse light transport. *J Biomed Opt,* 13**,** 041302.
JANES, A. C., PEECHATKA, A. L., FREDERICK, B. B. & KAISER, R. H. 2020. Dynamic functioning of transient resting-state coactivation networks in the Human Connectome Project. *Human brain mapping,* 41**,** 373-387.
JOBSIS, F. F. 1977. Noninvasive, infrared monitoring of cerebral and myocardial oxygen sufficiency and circulatory parameters. *Science,* 198**,** 1264-1267.
JOEL, S. E., CAFFO, B. S., VAN ZIJL, P. C. & PEKAR, J. J. 2011. On the relationship between seed-based and ICA-based measures of functional connectivity. *Magnetic Resonance in Medicine,* 66**,** 644-657.
JONES, D. T., VEMURI, P., MURPHY, M. C., GUNTER, J. L., SENJEM, M. L., MACHULDA, M. M., PRZYBELSKI, S. A., GREGG, B. E., KANTARCI, K. & KNOPMAN, D. S. 2012. Non-stationarity in the "resting brain's" modular architecture. *PloS one,* 7**,** e39731.
KAISER, R. H., KANG, M. S., LEW, Y., VAN DER FEEN, J., AGUIRRE, B., CLEGG, R., GOER, F., ESPOSITO, E., AUERBACH, R. P. & HUTCHISON, R. M. 2019. Abnormal frontoinsular-default network dynamics in adolescent depression and rumination: a preliminary resting-state co-activation pattern analysis. *Neuropsychopharmacology,* 44**,** 1604-1612.
KARAHANOĞLU, F. I. & VAN DE VILLE, D. 2015. Transient brain activity disentangles fMRI resting-state dynamics in terms of spatially and temporally overlapping networks. *Nature communications,* 6**,** 1-10.
KATO, T., KAMEI, A., TAKASHIMA, S. & OZAKI, T. 1993. Human visual cortical function during photic stimulation monitoring by means of near-infrared spectroscopy. *Journal of Cerebral Blood Flow & Metabolism,* 13**,** 516-520.
KAUFMANN, T., ELVSASHAGEN, T., ALNAES, D., ZAK, N., PEDERSEN, P. O., NORBOM, L. B., QURAISHI, S. H., TAGLIAZUCCHI, E., LAUFS, H., BJORNERUD, A., MALT, U. F., ANDREASSEN, O. A., ROUSSOS, E., DUFF, E. P., SMITH, S. M., GROOTE, I. R. & WESTLYE, L. T. 2016. The brain functional connectome is robustly altered by lack of sleep. *Neuroimage,* 127**,** 324-332.
KELLY, A. C., UDDIN, L. Q., BISWAL, B. B., CASTELLANOS, F. X. & MILHAM, M. P. 2008. Competition between functional brain networks mediates behavioral variability. *Neuroimage,* 39**,** 527-537.
KHAN, A. F., ZHANG, F., YUAN, H. & DING, L. Dynamic Activation Patterns of the Motor Brain Revealed by Diffuse Optical Tomography. 2019 41st Annual International Conference of the IEEE Engineering in Medicine and Biology Society (EMBC), 2019. IEEE, 6028-6031.
KHAN, A. F., ZHANG, F., YUAN, H. & DING, L. 2021. Brain-wide functional diffuse optical tomography of resting state networks. *Journal of Neural Engineering*.
KIRILINA, E., YU, N., JELZOW, A., WABNITZ, H., JACOBS, A. M. & TACHTSIDIS, I. 2013. Identifying and quantifying main components of physiological noise in functional near infrared spectroscopy on the prefrontal cortex. *Frontiers in human neuroscience,* 7**,** 864.
KOCH, S. P., HABERMEHL, C., MEHNERT, J., SCHMITZ, C. H., HOLTZE, S., VILLRINGER, A., STEINBRINK, J. & OBRIG, H. 2010. High-resolution optical

functional mapping of the human somatosensory cortex. *Frontiers in Neuroenergetics,* 2**,** 12.
KOHNO, S., MIYAI, I., SEIYAMA, A., ODA, I., ISHIKAWA, A., TSUNEISHI, S., AMITA, T. & SHIMIZU, K. 2007. Removal of the skin blood flow artifact in functional near-infrared spectroscopic imaging data through independent component analysis. *Journal of Biomedical Optics,* 12**,** 062111.
KOPTON, I. M. & KENNING, P. 2014. Near-infrared spectroscopy (NIRS) as a new tool for neuroeconomic research. *Frontiers in human neuroscience,* 8**,** 549.
LACHERT, P., JANUSEK, D., PULAWSKI, P., LIEBERT, A., MILEJ, D. & BLINOWSKA, K. J. 2017. Coupling of Oxy-and Deoxyhemoglobin concentrations with EEG rhythms during motor task. *Scientific reports,* 7**,** 1-9.
LAIRD, A. R., FOX, P. M., EICKHOFF, S. B., TURNER, J. A., RAY, K. L., MCKAY, D. R., GLAHN, D. C., BECKMANN, C. F., SMITH, S. M. & FOX, P. T. 2011. Behavioral interpretations of intrinsic connectivity networks. *Journal of cognitive neuroscience,* 23**,** 4022-4037.
LAUMANN, T. O., SNYDER, A. Z., MITRA, A., GORDON, E. M., GRATTON, C., ADEYEMO, B., GILMORE, A. W., NELSON, S. M., BERG, J. J. & GREENE, D. J. 2017. On the stability of BOLD fMRI correlations. *Cerebral cortex,* 27**,** 4719-4732.
LEE, S. H., JIN, S. H. & AN, J. 2019. The difference in cortical activation pattern for complex motor skills: A functional near-infrared spectroscopy study. *Scientific reports,* 9**,** 1-9.
LEI DING, G. S., YOON-HEE CHA, JOHN SWEENEY, HAN YUAN 2021. Brain-wide neural co-activations in resting human. *Bioarxiv*.
LI, C., YUAN, H., SHOU, G., CHA, Y.-H., SUNDERAM, S., BESIO, W. & DING, L. 2018. Cortical statistical correlation tomography of EEG resting state networks. *Frontiers in neuroscience,* 12**,** 365.
LIANG, Z., LIU, X. & ZHANG, N. 2015. Dynamic resting state functional connectivity in awake and anesthetized rodents. *Neuroimage,* 104**,** 89-99.
LIU, T. T., NALCI, A. & FALAHPOUR, M. 2017. The global signal in fMRI: Nuisance or Information? *Neuroimage,* 150**,** 213-229.
LIU, X., CHANG, C. & DUYN, J. H. 2013. Decomposition of spontaneous brain activity into distinct fMRI co-activation patterns. *Frontiers in systems neuroscience,* 7**,** 101.
LIU, X., DE ZWART, J. A., SCHÖLVINCK, M. L., CHANG, C., FRANK, Q. Y., LEOPOLD, D. A. & DUYN, J. H. 2018a. Subcortical evidence for a contribution of arousal to fMRI studies of brain activity. *Nature communications,* 9**,** 1-10.
LIU, X. & DUYN, J. H. 2013. Time-varying functional network information extracted from brief instances of spontaneous brain activity. *Proceedings of the National Academy of Sciences,* 110**,** 4392-4397.
LIU, X., ZHANG, N., CHANG, C. & DUYN, J. H. 2018b. Co-activation patterns in resting-state fMRI signals. *Neuroimage,* 180**,** 485-494.
LLOYD-FOX, S., BLASI, A. & ELWELL, C. 2010. Illuminating the developing brain: the past, present and future of functional near infrared spectroscopy. *Neuroscience & Biobehavioral Reviews,* 34**,** 269-284.
LOGOTHETIS, N. K., ESCHENKO, O., MURAYAMA, Y., AUGATH, M., STEUDEL, T., EVRARD, H., BESSERVE, M. & OELTERMANN, A. 2012. Hippocampal–cortical interaction during periods of subcortical silence. *Nature,* 491**,** 547-553.

LOWE, M., MOCK, B. & SORENSON, J. 1998. Functional connectivity in single and multislice echoplanar imaging using resting-state fluctuations. *Neuroimage,* 7**,** 119-132.

LU, H., ZUO, Y., GU, H., WALTZ, J. A., ZHAN, W., SCHOLL, C. A., REA, W., YANG, Y. & STEIN, E. A. 2007. Synchronized delta oscillations correlate with the resting-state functional MRI signal. *Proceedings of the National Academy of Sciences,* 104**,** 18265-18269.

LUCZAK, A., BARTHÓ, P., MARGUET, S. L., BUZSÁKI, G. & HARRIS, K. D. 2007. Sequential structure of neocortical spontaneous activity in vivo. *Proceedings of the National Academy of Sciences,* 104**,** 347-352.

LURIE, D. J., KESSLER, D., BASSETT, D. S., BETZEL, R. F., BREAKSPEAR, M., KHEILHOLZ, S., KUCYI, A., LIÉGEOIS, R., LINDQUIST, M. A. & MCINTOSH, A. R. 2020. Questions and controversies in the study of time-varying functional connectivity in resting fMRI. *Network Neuroscience,* 4**,** 30-69.

MA, Y., MA, Z., LIANG, Z., NEUBERGER, T. & ZHANG, N. 2020. Global brain signal in awake rats. *Brain Structure and Function,* 225**,** 227-240.

MACKERT, B.-M., LEISTNER, S., SANDER, T., LIEBERT, A., WABNITZ, H., BURGHOFF, M., TRAHMS, L., MACDONALD, R. & CURIO, G. 2008. Dynamics of cortical neurovascular coupling analyzed by simultaneous DC-magnetoencephalography and time-resolved near-infrared spectroscopy. *Neuroimage,* 39**,** 979-986.

MAJEED, W., MAGNUSON, M., HASENKAMP, W., SCHWARB, H., SCHUMACHER, E. H., BARSALOU, L. & KEILHOLZ, S. D. 2011. Spatiotemporal dynamics of low frequency BOLD fluctuations in rats and humans. *Neuroimage,* 54**,** 1140-1150.

MAJEED, W., MAGNUSON, M. & KEILHOLZ, S. D. 2009. Spatiotemporal dynamics of low frequency fluctuations in BOLD fMRI of the rat. *Journal of Magnetic Resonance Imaging: An Official Journal of the International Society for Magnetic Resonance in Medicine,* 30**,** 384-393.

MALONEK, D. & GRINVALD, A. 1996. Interactions between electrical activity and cortical microcirculation revealed by imaging spectroscopy: implications for functional brain mapping. *Science,* 272**,** 551-554.

MARREIROS, A. C., KIEBEL, S. J. & FRISTON, K. J. 2008. Dynamic causal modelling for fMRI: a two-state model. *Neuroimage,* 39**,** 269-278.

MARSHALL, E., NOMI, J. S., DIRKS, B., ROMERO, C., KUPIS, L., CHANG, C. & UDDIN, L. Q. 2020. Coactivation pattern analysis reveals altered salience network dynamics in children with autism spectrum disorder. *Network Neuroscience,* 4**,** 1219-1234.

MASSIMINI, M., HUBER, R., FERRARELLI, F., HILL, S. & TONONI, G. 2004. The sleep slow oscillation as a traveling wave. *Journal of Neuroscience,* 24**,** 6862-6870.

MATHIEU, F., KHELLAF, A., KU, J. C., DONNELLY, J., THELIN, E. P. & ZEILER, F. A. 2020. Continuous near-infrared spectroscopy monitoring in adult traumatic brain injury: a systematic review. *Journal of neurosurgical anesthesiology,* 32**,** 288-299.

MATSUI, T., MURAKAMI, T. & OHKI, K. 2016. Transient neuronal coactivations embedded in globally propagating waves underlie resting-state functional connectivity. *Proc Natl Acad Sci U S A,* 113**,** 6556-61.

MATSUI, T., MURAKAMI, T. & OHKI, K. 2019. Neuronal origin of the temporal dynamics of spontaneous BOLD activity correlation. *Cerebral Cortex,* 29**,** 1496-1508.

MCKENDRICK, R., PARASURAMAN, R., MURTZA, R., FORMWALT, A., BACCUS, W., PACZYNSKI, M. & AYAZ, H. 2016. Into the wild: neuroergonomic differentiation of hand-held and augmented reality wearable displays during outdoor navigation with functional near infrared spectroscopy. *Frontiers in human neuroscience,* 10**,** 216.

MEDVEDEV, A. V. 2014. Does the resting state connectivity have hemispheric asymmetry? A near-infrared spectroscopy study. *Neuroimage,* 85**,** 400-407.

MEEK, J., ELWELL, C., KHAN, M., ROMAYA, J., WYATT, J., DELPY, D. T. & ZEKI, S. 1995. Regional changes in cerebral haemodynamics as a result of a visual stimulus measured by near infrared spectroscopy. *Proceedings of the Royal Society of London. Series B: Biological Sciences,* 261**,** 351-356.

MEHAGNOUL-SCHIPPER, D. J., VAN DER KALLEN, B. F., COLIER, W. N., VAN DER SLUIJS, M. C., VAN ERNING, L. J. T. O., THIJSSEN, H. O., OESEBURG, B., HOEFNAGELS, W. H. & JANSEN, R. W. 2002. Simultaneous measurements of cerebral oxygenation changes during brain activation by near-infrared spectroscopy and functional magnetic resonance imaging in healthy young and elderly subjects. *Human brain mapping,* 16**,** 14-23.

MICHEL, C. M., MURRAY, M. M., LANTZ, G., GONZALEZ, S., SPINELLI, L. & DE PERALTA, R. G. 2004. EEG source imaging. *Clinical neurophysiology,* 115**,** 2195-2222.

MINTZER, J. P. & MOORE, J. E. 2019. Regional tissue oxygenation monitoring in the neonatal intensive care unit: evidence for clinical strategies and future directions. *Pediatric research,* 86**,** 296-304.

MOHAJERANI, M. H., CHAN, A. W., MOHSENVAND, M., LEDUE, J., LIU, R., MCVEA, D. A., BOYD, J. D., WANG, Y. T., REIMERS, M. & MURPHY, T. H. 2013. Spontaneous cortical activity alternates between motifs defined by regional axonal projections. *Nature neuroscience,* 16**,** 1426-1435.

MULLER, L., CHAVANE, F., REYNOLDS, J. & SEJNOWSKI, T. J. 2018. Cortical travelling waves: mechanisms and computational principles. *Nature Reviews Neuroscience,* 19**,** 255.

MURPHY, K., BIRN, R. M., HANDWERKER, D. A., JONES, T. B. & BANDETTINI, P. A. 2009. The impact of global signal regression on resting state correlations: are anti-correlated networks introduced? *Neuroimage,* 44**,** 893-905.

MURPHY, K. & FOX, M. D. 2017. Towards a consensus regarding global signal regression for resting state functional connectivity MRI. *Neuroimage,* 154**,** 169-173.

NASEER, N. & HONG, K.-S. 2015. fNIRS-based brain-computer interfaces: a review. *Frontiers in human neuroscience,* 9**,** 3.

NIU, H. & HE, Y. 2014. Resting-state functional brain connectivity: lessons from functional near-infrared spectroscopy. *The Neuroscientist,* 20**,** 173-188.

NODA, I. & OZAKI, Y. 2005. *Two-dimensional correlation spectroscopy: applications in vibrational and optical spectroscopy,* John Wiley & Sons.

NOVI, S. L., ROBERTS, E., SPAGNUOLO, D., SPILSBURY, B. M., PRICE, D. C., IMBALZANO, C. A., FORERO, E., YODH, A. G., TELLIS, G. M., TELLIS, C. M. & MESQUITA, R. C. 2020. Functional near-infrared spectroscopy for speech protocols: characterization of motion artifacts and guidelines for improving data analysis. *Neurophotonics,* 7**,** 015001.

O'LEARY, M. A., BOAS, D. A., CHANCE, B. & YODH, A. G. 1995. Experimental images of heterogeneous turbid media by frequency-domain diffusing-photon tomography. *Opt Lett,* 20**,** 426-8.

OBRIG, H. & VILLRINGER, A. 2003. Beyond the visible—imaging the human brain with light. *Journal of Cerebral Blood Flow & Metabolism,* 23**,** 1-18.

OOSTENVELD, R. & PRAAMSTRA, P. 2001. The five percent electrode system for high-resolution EEG and ERP measurements. *Clin Neurophysiol,* 112**,** 713-9.

PARK, B., KIM, J. I., LEE, D., JEONG, S.-O., LEE, J. D. & PARK, H.-J. 2012. Are brain networks stable during a 24-hour period? *Neuroimage,* 59**,** 456-466.

PARK, H.-J. & FRISTON, K. 2013. Structural and functional brain networks: from connections to cognition. *Science,* 342.

PASCUAL-MARQUI, R. D. 1999. Review of methods for solving the EEG inverse problem. *International journal of bioelectromagnetism,* 1**,** 75-86.

PATIL, A. V., SAFAIE, J., MOGHADDAM, H. A., WALLOIS, F. & GREBE, R. 2011. Experimental investigation of NIRS spatial sensitivity. *Biomedical optics express,* 2**,** 1478-1493.

PAULSON, O. B., HASSELBALCH, S. G., ROSTRUP, E., KNUDSEN, G. M. & PELLIGRINO, D. 2010. Cerebral blood flow response to functional activation. *Journal of Cerebral Blood Flow & Metabolism,* 30**,** 2-14.

PINTI, P., SCHOLKMANN, F., HAMILTON, A., BURGESS, P. & TACHTSIDIS, I. 2019. Current status and issues regarding pre-processing of fNIRS neuroimaging data: an investigation of diverse signal filtering methods within a general linear model framework. *Frontiers in human neuroscience,* 12**,** 505.

PINTI, P., TACHTSIDIS, I., HAMILTON, A., HIRSCH, J., AICHELBURG, C., GILBERT, S. & BURGESS, P. W. 2020. The present and future use of functional near-infrared spectroscopy (fNIRS) for cognitive neuroscience. *Annals of the New York Academy of Sciences,* 1464**,** 5.

POGUE, B. W., MCBRIDE, T. O., PREWITT, J., OSTERBERG, U. L. & PAULSEN, K. D. 1999. Spatially variant regularization improves diffuse optical tomography. *Appl Opt,* 38**,** 2950-61.

POWER, J. D., COHEN, A. L., NELSON, S. M., WIG, G. S., BARNES, K. A., CHURCH, J. A., VOGEL, A. C., LAUMANN, T. O., MIEZIN, F. M., SCHLAGGAR, B. L. & PETERSEN, S. E. 2011. Functional network organization of the human brain. *Neuron,* 72**,** 665-78.

PRAHL, S. 1999. Optical absorption of hemoglobin. *http://omlc. ogi. edu/spectra/hemoglobin*.

PRETI, M. G., BOLTON, T. A. & VAN DE VILLE, D. 2017. The dynamic functional connectome: State-of-the-art and perspectives. *Neuroimage,* 160**,** 41-54.

PRICE, D. L., DE WILDE, J. P., PAPADAKI, A. M., CURRAN, J. S. & KITNEY, R. I. 2001. Investigation of acoustic noise on 15 MRI scanners from 0.2 T to 3 T. *Journal of Magnetic Resonance Imaging: An Official Journal of the International Society for Magnetic Resonance in Medicine,* 13**,** 288-293.

QUARESIMA, V. & FERRARI, M. A mini-review on functional near-infrared spectroscopy (fNIRS): where do we stand, and where should we go? Photonics, 2019. Multidisciplinary Digital Publishing Institute, 87.

RAICHLE, M. E., MACLEOD, A. M., SNYDER, A. Z., POWERS, W. J., GUSNARD, D. A. & SHULMAN, G. L. 2001. A default mode of brain function. *Proceedings of the National Academy of Sciences,* 98**,** 676-682.

RAO, S. M., BINDER, J., BANDETTINI, P., HAMMEKE, T., YETKIN, F., JESMANOWICZ, A., LISK, L., MORRIS, G., MUELLER, W. & ESTKOWSKI, L. 1993. Functional magnetic resonance imaging of complex human movements. *Neurology,* 43**,** 2311-2311.

RAUT, R. V., MITRA, A., MAREK, S., ORTEGA, M., SNYDER, A. Z., TANENBAUM, A., LAUMANN, T. O., DOSENBACH, N. U. & RAICHLE, M. E. 2020. Organization of propagated intrinsic brain activity in individual humans. *Cerebral Cortex,* 30**,** 1716-1734.

RAUT, R. V., SNYDER, A. Z., MITRA, A., YELLIN, D., FUJII, N., MALACH, R. & RAICHLE, M. E. 2021. Global waves synchronize the brain's functional systems with fluctuating arousal. *Science advances,* 7**,** eabf2709.

REY, G., BOLTON, T. A., GAVIRIA, J., PIGUET, C., PRETI, M. G., FAVRE, S., AUBRY, J.-M., VAN DE VILLE, D. & VUILLEUMIER, P. 2021. Dynamics of amygdala connectivity in bipolar disorders: A longitudinal study across mood states. *Neuropsychopharmacology***,** 1-9.

RIBARY, U., IOANNIDES, A., SINGH, K. D., HASSON, R., BOLTON, J., LADO, F., MOGILNER, A. & LLINAS, R. 1991. Magnetic field tomography of coherent thalamocortical 40-Hz oscillations in humans. *Proceedings of the National Academy of Sciences,* 88**,** 11037-11041.

RIEDL, V., UTZ, L., CASTRILLON, G., GRIMMER, T., RAUSCHECKER, J. P., PLONER, M., FRISTON, K. J., DRZEZGA, A. & SORG, C. 2016. Metabolic connectivity mapping reveals effective connectivity in the resting human brain. *Proc Natl Acad Sci U S A,* 113**,** 428-33.

RONDINONI, C., AMARO, E., JR., CENDES, F., DOS SANTOS, A. C. & SALMON, C. E. 2013. Effect of scanner acoustic background noise on strict resting-state fMRI. *Braz J Med Biol Res,* 46**,** 359-67.

ROSENBERG, M. D., FINN, E. S., SCHEINOST, D., PAPADEMETRIS, X., SHEN, X., CONSTABLE, R. T. & CHUN, M. M. 2016. A neuromarker of sustained attention from whole-brain functional connectivity. *Nature neuroscience,* 19**,** 165-171.

ROY, A. K., SHEHZAD, Z. & AL., E. 2008. Functional connectivity of the human amygdala using resting state fMRI. *Neuroimage***,** 614-626.

SAAGER, R. B. & BERGER, A. J. 2005. Direct characterization and removal of interfering absorption trends in two-layer turbid media. *Journal of the Optical Society of America a-Optics Image Science and Vision,* 22**,** 1874-1882.

SAAGER, R. B. & BERGER, A. J. 2008. Measurement of layer-like hemodynamic trends in scalp and cortex: implications for physiological baseline suppression in functional near-infrared spectroscopy. *Journal of biomedical optics,* 13**,** 034017.

SATO, T., NAMBU, I., TAKEDA, K., AIHARA, T., YAMASHITA, O., ISOGAYA, Y., INOUE, Y., OTAKA, Y., WADA, Y., KAWATO, M., SATO, M. & OSU, R. 2016. Reduction of global interference of scalp-hemodynamics in functional near-infrared spectroscopy using short distance probes. *Neuroimage,* 141**,** 120-132.

SAVVA, A. D., MITSIS, G. D. & MATSOPOULOS, G. K. 2019. Assessment of dynamic functional connectivity in resting-state fMRI using the sliding window technique. *Brain and behavior,* 9**,** e01255.

SCHECKLMANN, M., MANN, A., LANGGUTH, B., EHLIS, A. C., FALLGATTER, A. J. & HAEUSSINGER, F. B. 2017. The Temporal Muscle of the Head Can Cause Artifacts in Optical Imaging Studies with Functional Near-Infrared Spectroscopy. *Frontiers in Human Neuroscience,* 11**,** 456.

SCHMITHORST, V. J. & HOLLAND, S. K. 2004. Comparison of three methods for generating group statistical inferences from independent component analysis of functional magnetic resonance imaging data. *Journal of Magnetic Resonance Imaging: An Official Journal of the International Society for Magnetic Resonance in Medicine,* 19**,** 365-368.

SCHOLKMANN, F., KLEISER, S., METZ, A. J., ZIMMERMANN, R., PAVIA, J. M., WOLF, U. & WOLF, M. 2014. A review on continuous wave functional near-infrared spectroscopy and imaging instrumentation and methodology. *Neuroimage,* 85**,** 6-27.

SCHÖLVINCK, M. L., MAIER, A., FRANK, Q. Y., DUYN, J. H. & LEOPOLD, D. A. 2010. Neural basis of global resting-state fMRI activity. *Proceedings of the National Academy of Sciences,* 107**,** 10238-10243.

SCHROETER, M. L., KUPKA, T., MILDNER, T., ULUDAĞ, K. & VON CRAMON, D. Y. 2006. Investigating the post-stimulus undershoot of the BOLD signal—a simultaneous fMRI and fNIRS study. *Neuroimage,* 30**,** 349-358.

SCHUENKE, M., SCHULTE, E. & SCHUMACHER, U. 2007. *Thieme atlas of anatomy: head and neuroanatomy*, Thieme.

SCHWALM, M., SCHMID, F., WACHSMUTH, L., BACKHAUS, H., KRONFELD, A., JURY, F. A., PROUVOT, P.-H., FOIS, C., ALBERS, F. & VAN ALST, T. 2017. Cortex-wide BOLD fMRI activity reflects locally-recorded slow oscillation-associated calcium waves. *Elife,* 6**,** e27602.

SCHWEIGER, M. & ARRIDGE, S. R. 2014. The Toast++ software suite for forward and inverse modeling in optical tomography. *Journal of biomedical optics,* 19**,** 040801.

SEBER, G. A. 2009. *Multivariate observations*, John Wiley & Sons.

SERRAINO, G. F. & MURPHY, G. J. 2017. Effects of cerebral near-infrared spectroscopy on the outcome of patients undergoing cardiac surgery: a systematic review of randomised trials. *BMJ open,* 7**,** e016613.

SHELINE, Y. I., BARCH, D. M., PRICE, J. L., RUNDLE, M. M., VAISHNAVI, S. N., SNYDER, A. Z., MINTUN, M. A., WANG, S., COALSON, R. S. & RAICHLE, M. E. 2009. The default mode network and self-referential processes in depression. *Proceedings of the National Academy of Sciences,* 106**,** 1942-1947.

SHERAFATI, A., EGGEBRECHT, A. T., BURNS-YOCUM, T. M. & CULVER, J. P. A global metric to detect motion artifacts in optical neuroimaging data (Conference Presentation). Neural Imaging and Sensing, 2017. International Society for Optics and Photonics, 1005112.

SHERAFATI, A., SNYDER, A. Z., EGGEBRECHT, A. T., BERGONZI, K. M., BURNS-YOCUM, T. M., LUGAR, H. M., FERRADAL, S. L., ROBICHAUX-VIEHOEVER, A., SMYSER, C. D. & PALANCA, B. J. 2020a. Global Motion Detection and Censoring in High-Density Diffuse Optical Tomography. *bioRxiv*.

SHERAFATI, A., SNYDER, A. Z., EGGEBRECHT, A. T., BERGONZI, K. M., BURNS-YOCUM, T. M., LUGAR, H. M., FERRADAL, S. L., ROBICHAUX-VIEHOEVER, A., SMYSER, C. D. & PALANCA, B. J. 2020b. Global motion detection and censoring in high-density diffuse optical tomography. *Human brain mapping,* 41**,** 4093-4112.

SHETH, S. A., NEMOTO, M., GUIOU, M., WALKER, M., POURATIAN, N., HAGEMAN, N. & TOGA, A. W. 2004. Columnar specificity of microvascular oxygenation and volume responses: implications for functional brain mapping. *Journal of Neuroscience,* 24**,** 634-641.

SILVER, N. C. & DUNLAP, W. P. 1987. Averaging correlation coefficients: Should Fisher's z transformation be used? *Journal of Applied Psychology,* 72**,** 146.

SMITH, S. M., FOX, P. T., MILLER, K. L., GLAHN, D. C., FOX, P. M., MACKAY, C. E., FILIPPINI, N., WATKINS, K. E., TORO, R. & LAIRD, A. R. 2009a. Correspondence of the brain's functional architecture during activation and rest. *Proceedings of the national academy of sciences,* 106**,** 13040-13045.

SMITH, S. M., FOX, P. T., MILLER, K. L., GLAHN, D. C., FOX, P. M., MACKAY, C. E., FILIPPINI, N., WATKINS, K. E., TORO, R., LAIRD, A. R. & BECKMANN, C. F. 2009b. Correspondence of the brain's functional architecture during activation and rest. *Proc Natl Acad Sci U S A,* 106**,** 13040-5.

SMITH, S. M., MILLER, K. L., MOELLER, S., XU, J., AUERBACH, E. J., WOOLRICH, M. W., BECKMANN, C. F., JENKINSON, M., ANDERSSON, J. & GLASSER, M. F. 2012. Temporally-independent functional modes of spontaneous brain activity. *Proceedings of the National Academy of Sciences,* 109**,** 3131-3136.

SOARES, J. M., SAMPAIO, A., FERREIRA, L. M., SANTOS, N. C., MARQUES, P., MARQUES, F., PALHA, J. A., CERQUEIRA, J. J. & SOUSA, N. 2013. Stress Impact on Resting State Brain Networks. *PLoS One,* 8**,** e66500.

SORG, C., RIEDL, V., MÜHLAU, M., CALHOUN, V. D., EICHELE, T., LÄER, L., DRZEZGA, A., FÖRSTL, H., KURZ, A. & ZIMMER, C. 2007. Selective changes of resting-state networks in individuals at risk for Alzheimer's disease. *Proceedings of the National Academy of Sciences,* 104**,** 18760-18765.

SRINIVASAN, S., POGUE, B. W., JIANG, S., DEHGHANI, H. & PAULSEN, K. D. 2005. Spectrally constrained chromophore and scattering near-infrared tomography provides quantitative and robust reconstruction. *Applied optics,* 44**,** 1858-1869.

STAMATAKIS, E. A., ADAPA, R. M., ABSALOM, A. R. & MENON, D. K. 2010. Changes in resting neural connectivity during propofol sedation. *PloS one,* 5**,** e14224.

STEFANOVSKA, A., BRACIC, M. & KVERNMO, H. D. 1999. Wavelet analysis of oscillations in the peripheral blood circulation measured by laser Doppler technique. *IEEE Trans Biomed Eng,* 46**,** 1230-9.

STEINBRINK, J., VILLRINGER, A., KEMPF, F., HAUX, D., BODEN, S. & OBRIG, H. 2006. Illuminating the BOLD signal: combined fMRI–fNIRS studies. *Magnetic resonance imaging,* 24**,** 495-505.

STERIADE, M., CONTRERAS, D., DOSSI, R. C. & NUNEZ, A. 1993. The slow (< 1 Hz) oscillation in reticular thalamic and thalamocortical neurons: scenario of sleep rhythm generation in interacting thalamic and neocortical networks. *Journal of Neuroscience,* 13**,** 3284-3299.

STRANGMAN, G., CULVER, J. P., THOMPSON, J. H. & BOAS, D. A. 2002. A quantitative comparison of simultaneous BOLD fMRI and NIRS recordings during functional brain activation. *Neuroimage,* 17**,** 719-731.

STRANGMAN, G., GOLDSTEIN, R., RAUCH, S. L. & STEIN, J. 2006. Near-infrared spectroscopy and imaging for investigating stroke rehabilitation: test-retest reliability and review of the literature. *Archives of physical medicine and rehabilitation,* 87**,** 12-19.

STROH, A., ADELSBERGER, H., GROH, A., RÜHLMANN, C., FISCHER, S., SCHIERLOH, A., DEISSEROTH, K. & KONNERTH, A. 2013. Making waves: initiation and propagation of corticothalamic Ca2+ waves in vivo. *Neuron,* 77**,** 1136-1150.

TACHTSIDIS, I. & SCHOLKMANN, F. 2016. False positives and false negatives in functional near-infrared spectroscopy: issues, challenges, and the way forward. *Neurophotonics,* 3**,** 031405.

TAGLIAZUCCHI, E., BALENZUELA, P., FRAIMAN, D., MONTOYA, P. & CHIALVO, D. R. 2011. Spontaneous BOLD event triggered averages for estimating functional connectivity at resting state. *Neuroscience letters,* 488**,** 158-163.

TAGLIAZUCCHI, E., SINIATCHKIN, M., LAUFS, H. & CHIALVO, D. R. 2016. The voxel-wise functional connectome can be efficiently derived from co-activations in a sparse spatio-temporal point-process. *Frontiers in neuroscience,* 10**,** 381.

TAGLIAZUCCHI, E., VON WEGNER, F., MORZELEWSKI, A., BRODBECK, V. & LAUFS, H. 2012. Dynamic BOLD functional connectivity in humans and its electrophysiological correlates. *Frontiers in human neuroscience,* 6**,** 339.

TAKEDA, Y., HIROE, N. & YAMASHITA, O. 2021. Whole-brain propagating patterns in human resting-state brain activities. *NeuroImage***,** 118711.

TAKEUCHI, N., MORI, T., SUZUKAMO, Y., TANAKA, N. & IZUMI, S.-I. 2016. Parallel processing of cognitive and physical demands in left and right prefrontal cortices during smartphone use while walking. *BMC neuroscience,* 17**,** 1-11.

TAVOR, I., JONES, O. P., MARS, R. B., SMITH, S., BEHRENS, T. & JBABDI, S. 2016. Task-free MRI predicts individual differences in brain activity during task performance. *Science,* 352**,** 216-220.

THATCHER, R., BIVER, C. & NORTH, D. 2007. Spatial-temporal current source correlations and cortical connectivity. *Clinical EEG and Neuroscience,* 38**,** 35-48.

THOMPSON, G. J., MAGNUSON, M. E., MERRITT, M. D., SCHWARB, H., PAN, W. J., MCKINLEY, A., TRIPP, L. D., SCHUMACHER, E. H. & KEILHOLZ, S. D. 2013a. Short-time windows of correlation between large-scale functional brain networks predict vigilance intraindividually and interindividually. *Human brain mapping,* 34**,** 3280-3298.

THOMPSON, G. J., MERRITT, M. D., PAN, W.-J., MAGNUSON, M. E., GROOMS, J. K., JAEGER, D. & KEILHOLZ, S. D. 2013b. Neural correlates of time-varying functional connectivity in the rat. *Neuroimage,* 83**,** 826-836.

THOMPSON, G. J., RIEDL, V., GRIMMER, T., DRZEZGA, A., HERMAN, P. & HYDER, F. 2016. The whole-brain "global" signal from resting state fMRI as a potential biomarker of quantitative state changes in glucose metabolism. *Brain connectivity,* 6**,** 435-447.

TIKHONOV, A. N. On the solution of ill-posed problems and the method of regularization. Doklady Akademii Nauk, 1963. Russian Academy of Sciences, 501-504.

TONG, Y., LINDSEY, K. P. & DE, B. F. B. 2011. Partitioning of physiological noise signals in the brain with concurrent near-infrared spectroscopy and fMRI. *J Cereb Blood Flow Metab,* 31**,** 2352-62.

TORONOV, V., WALKER, S., GUPTA, R., CHOI, J. H., GRATTON, E., HUEBER, D. & WEBB, A. 2003. The roles of changes in deoxyhemoglobin concentration and regional cerebral blood volume in the fMRI BOLD signal. *Neuroimage,* 19**,** 1521-1531.

TYSZKA, J. M., KENNEDY, D. P., ADOLPHS, R. & PAUL, L. K. 2011. Intact bilateral resting-state networks in the absence of the corpus callosum. *Journal of Neuroscience,* 31**,** 15154-15162.

VALENCIA, M., PASTOR, M., FERNÁNDEZ-SEARA, M., ARTIEDA, J., MARTINERIE, J. & CHAVEZ, M. 2009. Complex modular structure of large-scale brain networks. *Chaos: An Interdisciplinary Journal of Nonlinear Science,* 19**,** 023119.

VAN DER ZEE, P., COPE, M., ARRIDGE, S., ESSENPREIS, M., POTTER, L., EDWARDS, A., WYATT, J., MCCORMICK, D., ROTH, S. & REYNOLDS, E. 1992. Experimentally measured optical pathlengths for the adult head, calf and forearm and the head of the newborn infant as a function of inter optode spacing. *Oxygen transport to tissue XIII.* Springer.

VAN DIJK, K. R., HEDDEN, T., VENKATARAMAN, A., EVANS, K. C., LAZAR, S. W. & BUCKNER, R. L. 2010. Intrinsic functional connectivity as a tool for human connectomics: theory, properties, and optimization. *Journal of neurophysiology,* 103**,** 297-321.

VANNI, M. P. & MURPHY, T. H. 2014. Mesoscale transcranial spontaneous activity mapping in GCaMP3 transgenic mice reveals extensive reciprocal connections between areas of somatomotor cortex. *Journal of Neuroscience,* 34**,** 15931-15946.

VILLRINGER, A., PLANCK, J., STODIECK, S., BÖTZEL, K., SCHLEINKOFER, L. & DIRNAGL, U. 1994. Noninvasive assessment of cerebral hemodynamics and tissue oxygenation during activation of brain cell function in human adults using near infrared spectroscopy. *Oxygen Transport to Tissue XV.* Springer.

VINCENT, J. L., PATEL, G. H. & AL., E. 2007a. Intrinsic functional architecture in the anaesthitized monkey brain. *Nature***,** 83-86.

VINCENT, J. L., PATEL, G. H., FOX, M. D., SNYDER, A. Z., BAKER, J. T., VAN ESSEN, D. C., ZEMPEL, J. M., SNYDER, L. H., CORBETTA, M. & RAICHLE, M. E. 2007b. Intrinsic functional architecture in the anaesthetized monkey brain. *Nature,* 447**,** 83-86.

VON LÜHMANN, A., ZHENG, Y., ORTEGA-MARTINEZ, A., KIRAN, S., SOMERS, D. C., CRONIN-GOLOMB, A., AWAD, L. N., ELLIS, T. D., BOAS, D. A. & YÜCEL, M. A. 2021. Towards Neuroscience of the Everyday World (NEW) using functional Near Infrared Spectroscopy. *Current opinion in biomedical engineering***,** 100272.

VOSSEL, S., GENG, J. J. & FINK, G. R. 2014. Dorsal and ventral attention systems: distinct neural circuits but collaborative roles. *The Neuroscientist,* 20**,** 150-159.

WANG, L., JACQUES, S. L. & ZHENG, L. 1995. MCML—Monte Carlo modeling of light transport in multi-layered tissues. *Computer methods and programs in biomedicine,* 47**,** 131-146.

WARD, L. M. 2003. Synchronous neural oscillations and cognitive processes. *Trends in cognitive sciences,* 7**,** 553-559.

WELCH, P. 1967. The use of fast Fourier transform for the estimation of power spectra: a method based on time averaging over short, modified periodograms. *IEEE Transactions on audio and electroacoustics,* 15**,** 70-73.

WHEELOCK, M. D., CULVER, J. P. & EGGEBRECHT, A. T. 2019. High-density diffuse optical tomography for imaging human brain function. *Review of Scientific Instruments,* 90**,** 051101.

WHITE, B. 2012. *Developing high-density diffuse optical tomography for neuroimaging.*

WHITE, B. R., LIAO, S. M., FERRADAL, S. L., INDER, T. E. & CULVER, J. P. 2012. Bedside optical imaging of occipital resting-state functional connectivity in neonates. *Neuroimage,* 59**,** 2529-2538.

WHITE, B. R., SNYDER, A. Z., COHEN, A. L., PETERSEN, S. E., RAICHLE, M. E., SCHLAGGAR, B. L. & CULVER, J. P. 2009. Resting-state functional connectivity in the human brain revealed with diffuse optical tomography. *Neuroimage,* 47**,** 148-156.

WONG, C. W., OLAFSSON, V., TAL, O. & LIU, T. T. 2013. The amplitude of the resting-state fMRI global signal is related to EEG vigilance measures. *Neuroimage,* 83**,** 983-990.

WOOLRICH, M. W., RIPLEY, B. D., BRADY, M. & SMITH, S. M. 2001. Temporal autocorrelation in univariate linear modeling of FMRI data. *Neuroimage,* 14**,** 1370-86.

WU, X., EGGEBRECHT, A. T., FERRADAL, S. L., CULVER, J. P. & DEHGHANI, H. 2015. Fast and efficient image reconstruction for high density diffuse optical imaging of the human brain. *Biomedical optics express,* 6**,** 4567-4584.

WYSER, D., MATTILLE, M., WOLF, M., LAMBERCY, O., SCHOLKMANN, F. & GASSERT, R. 2020. Short-channel regression in functional near-infrared spectroscopy is more effective when considering heterogeneous scalp hemodynamics. *Neurophotonics,* 7**,** 035011.

YABLONSKIY, D. A., ACKERMAN, J. J. & RAICHLE, M. E. 2000. Coupling between changes in human brain temperature and oxidative metabolism during prolonged visual stimulation. *Proceedings of the National Academy of Sciences,* 97**,** 7603-7608.

YANG, H., ZHANG, H., DI, X., WANG, S., MENG, C., TIAN, L. & BISWAL, B. 2021. Reproducible coactivation patterns of functional brain networks reveal the aberrant dynamic state transition in schizophrenia. *NeuroImage***,** 118193.

YEO, B. T., KRIENEN, F. M., SEPULCRE, J., SABUNCU, M. R., LASHKARI, D., HOLLINSHEAD, M., ROFFMAN, J. L., SMOLLER, J. W., ZÖLLEI, L. & POLIMENI, J. R. 2011. The organization of the human cerebral cortex estimated by intrinsic functional connectivity. *Journal of neurophysiology*.

YEO, B. T. T., TANDI, J. & CHEE, M. W. L. 2015. Functional connectivity during rested wakefulness predicts vulnerability to sleep deprivation. *Neuroimage,* 111**,** 147-158.

YEUNG, M. K. 2021. An optical window into brain function in children and adolescents: A systematic review of functional near-infrared spectroscopy studies. *Neuroimage,* 227**,** 117672.

YODH, A. & CHANCE, B. 1995. Spectroscopy and imaging with diffusing light. *Physics today,* 48**,** 34-40.

YOUSEFI, B., SHIN, J., SCHUMACHER, E. H. & KEILHOLZ, S. D. 2018. Quasi-periodic patterns of intrinsic brain activity in individuals and their relationship to global signal. *NeuroImage,* 167**,** 297-308.

YUAN, H., DING, L., ZHU, M., ZOTEV, V., PHILLIPS, R. & BODURKA, J. 2016. Reconstructing large-scale brain resting-state networks from high-resolution EEG: spatial and temporal comparisons with fMRI. *Brain connectivity,* 6**,** 122-135.

YUAN, H., ZOTEV, V., PHILLIPS, R., DREVETS, W. C. & BODURKA, J. 2012. Spatiotemporal dynamics of the brain at rest - Exploring EEG microstates as electrophysiological signatures of BOLD resting state networks. *Neuroimage,* 60**,** 2062-2072.

ZARAHN, E., AGUIRRE, G. K. & D'ESPOSITO, M. 1997. Empirical analyses of BOLD fMRI statistics. *Neuroimage,* 5**,** 179-197.

ZEFF, B. W., WHITE, B. R., DEHGHANI, H., SCHLAGGAR, B. L. & CULVER, J. P. 2007. Retinotopic mapping of adult human visual cortex with high-density diffuse optical tomography. *Proceedings of the National Academy of Sciences,* 104**,** 12169-12174.

ZHANG, F., CHEONG, D., CHEN, Y., KHAN, A., DING, L. & YUAN, H. Superficial Fluctuations in Functional Near-Infrared Spectroscopy. 2019 41st Annual International Conference of the IEEE Engineering in Medicine and Biology Society (EMBC), 2019. IEEE, 4779-4782.

ZHANG, F., CHEONG, D., KHAN, A. F., CHEN, Y., DING, L. & YUAN, H. 2021. Correcting Physiological Noise in Whole-Head Functional Near-Infrared Spectroscopy. *Journal of Neuroscience Methods***,** 109262.

ZHANG, H., ZHANG, Y.-J., LU, C.-M., MA, S.-Y., ZANG, Y.-F. & ZHU, C.-Z. 2010. Functional connectivity as revealed by independent component analysis of resting-state fNIRS measurements. *Neuroimage,* 51**,** 1150-1161.

ZHANG, X., NOAH, J. A. & HIRSCH, J. 2016. Separation of the global and local components in functional near-infrared spectroscopy signals using principal component spatial filtering. *Neurophotonics,* 3**,** 015004.

ZHANG, Y., BROOKS, D. H., FRANCESCHINI, M. A. & BOAS, D. A. 2005. Eigenvector-based spatial filtering for reduction of physiological interference in diffuse optical imaging. *J Biomed Opt,* 10**,** 11014.

ZHU, M., ZHANG, W., DICKENS, D. L. & DING, L. 2014. Reconstructing spatially extended brain sources via enforcing multiple transform sparseness. *Neuroimage,* 86**,** 280-93.

ZHUANG, X., WALSH, R. R., SREENIVASAN, K., YANG, Z., MISHRA, V. & CORDES, D. 2018. Incorporating spatial constraint in co-activation pattern analysis to explore the dynamics of resting-state networks: an application to Parkinson's disease. *Neuroimage,* 172**,** 64-84.

ZUBERER, A., KUCYI, A., YAMASHITA, A., WU, C. M., WALTER, M., VALERA, E. & ESTERMAN, M. 2021. Integration and segregation across large-scale intrinsic brain networks as a marker of sustained attention and task-unrelated thought. *NeuroImage***,** 117610.

ZUO, X. N., KELLY, C., ADELSTEIN, J. S., KLEIN, D. F., CASTELLANOS, F. X. & MILHAM, M. P. 2010. Reliable intrinsic connectivity networks: Test-retest evaluation using ICA and dual regression approach. *Neuroimage,* 49**,** 2163-2177.